Femtosecond filamentation in transparent media

A. Couairon[a,*], A. Mysyrowicz[b]

[a]*Centre de Physique Théorique, École Polytechnique, CNRS, F-91128 Palaiseau, France*
[b]*Laboratoire d'Optique Appliquée, École Nationale Supérieure des Techniques Avancées–École Polytechnique, CNRS, F-91761 Palaiseau, France*

Abstract

This paper introduces and discusses the main aspects of ultrashort laser pulse filamentation in various transparent media such as air (gases), transparent solids and liquids. The properties of femtosecond filaments and their applications are presented. Theoretical models developed to explain filaments and the main predictions inferred from these models are reviewed. The various techniques to observe filaments and to measure their characteristics are described. The main measurements of filament features performed so far are reviewed.
© 2007 Elsevier B.V. All rights reserved.

Contents

* Corresponding author.
E-mail addresses: couairon@cpht.polytechnique.fr (A. Couairon), mysyr@ensta.fr (A. Mysyrowicz).

1. Introduction

1.1. Scope of the paper

The aim of this article is to introduce, discuss and review the main aspects of femtosecond laser *filamentation* in various transparent nonlinear and dispersive media. In this review, we do not consider *relativistic filamentation*, corresponding to the propagation of a very intense ($I > 10^{17}$ W/cm^2) laser pulse in a fully ionized medium where electrons oscillate at a velocity approaching c, the light velocity in vacuum. We are concerned with filamentation in a continuous dielectric medium, which becomes weakly ionized by the propagating pulse, of typical peak intensity $\sim 10^{13}$ W/cm^2. The main emphasis will be given to air. However, we will also discuss filamentation in other gases and in condensed media such as transparent solids and liquids.

It has been long believed that intense ultra-short laser pulses are not suited for long range propagation in air. For example, in a linear propagation regime the peak intensity of a femtosecond pulse of initial duration $t_p = 30$ fs (1 fs $= 10^{-15}$ s) with a beam waist of 5 mm is expected to be reduced by a factor of $\sim 5 \times 10^3$ after 1 km of propagation in air due to the combined effect of beam diffraction (factor of 100) and group velocity dispersion (factor of 50). However, experiments using an intense infrared (IR) femtosecond pulse show the opposite trend. In the first experiments carried out by Braun et al. (1995), the intensity of the pulse increased instead of decreasing. It reached sufficiently high values to provoke micro-burns on a hard coated mirror 10 m away from the laser. The same mirror was undamaged if placed immediately close to the laser output, before propagation in air. The researchers from Michigan University correctly explained that a nonlinear effect was responsible for the damage tracks on the mirror: This effect is beam self-focusing. The damage tracks subsisted if the mirror was displaced several meters along the propagation axis. The beam therefore remained focused over an extended distance. This type of propagation was called filamentation or self-guided propagation. Shortly afterwards, filamentation of femtosecond laser pulses was shown to occur over more than 50 m in Laboratoire d'Optique Appliquée, (see Fig. 1, Nibbering et al., 1996) and then over several hundreds of meters (La Fontaine et al., 1999b). Experiments in Spring 2003 at École Polytechnique have revealed an horizontal filamentation over a distance larger than 2 km (Méchain et al., 2004a, 2005a). Experiments of vertical propagation suggest even larger filamentation distances, (see Fig. 2, Wöste et al., 1997 and Rodriguez et al., 2004).

Filamentation aroused a great interest and became a field of intense research activity as shown from the reference list. It is worth stressing at this point that the term "filamentation" may be misleading in the context of ultrashort lasers because it suggests an extended light string whereas the pulse actually shortens in the propagation direction while the beam shrinks and maintains a narrow diameter in the transverse diffraction plane. The term of light bullets would be more appropriate (Silberberg, 1990), although filaments are neither frozen, nor localized structures in time or in space. Throughout this paper, we will nevertheless conform to the custom and continue to use the terms of *filaments* and *filamentation* to denote a dynamic structure with an intense core, that is able to propagate over extended distances much larger than the typical diffraction length while keeping a narrow beam size without the help of any external guiding mechanism. The definition used in the literature is sometimes more strict. The intensity of the core reaching 10^{13}–10^{14} W/cm^2 is sufficient to ionize the molecules or atoms of the medium. The term *filament* is then used to describe the part of the propagation during which the pulse generates a column of weakly ionized plasma in its wake. In our general definition of a filament, ionization is not a necessary condition. Femtosecond filamentation was observed for various laser wavelengths from the ultraviolet to the infrared domain, and for various pulse durations from several tenth of fs to several ps. This generic phenomenon was also observed in transparent solids and liquids and does not critically depend on the initial conditions of the laser or the propagation medium.

1.2. Properties of ultrashort pulse nonlinear propagation

The physical origin of the formation of filaments in air is now well understood. Even if many physical effects come into play during the propagation of the pulse in the filament, the process of its formation can be described by the action
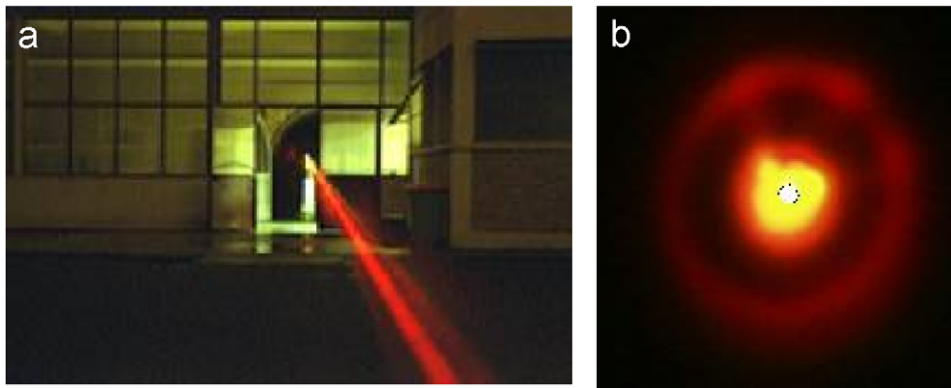
Fig. 1. (a) Propagation of an infrared laser beam (800 nm) in the Laboratory of Applied Optics (École Polytechnique, Palaiseau). The main properties of the filament are a hot core of diameter $\sim 100\,\mu m$ and intensity $\sim 5 \times 10^{13}\,W/cm^2$ generating an electron plasma of density $10^{16}\,cm^{-3}$ and a white continuum. (b) Image of the beam after a propagation over 50 m showing a white core in the center of the filament with a diameter of $100\,\mu m$.

Fig. 2. Vertical propagation in the sky of the teramobile laser beam (peak power of 5 TW at 800 nm, see Section 5.1.1): backward scattering of the beam is recorded using the telescope with a 2 m aperture, located in Tautenburg, Germany. One distinguishes a zone of Mie scattering from a vapor cloud located at an altitude of 9 km.

of mainly two nonlinear physical effects: the optical Kerr effect on the one hand, acts against diffraction and tends to focus the beam on itself. On the other hand, multiphoton absorption limits the intensity. The ensuing ionization of the atmosphere reduces the local refraction index of the medium and leads to beam defocusing. In the following, we briefly review qualitatively these effects as well as other physical effects that play a role in femtosecond filamentation, either in gases or in condensed media. We start by discussing the linear effects, then the nonlinear effects entering the polarization of the medium, and finally the nonlinear effects linked to plasma generation.

1.2.1. Diffraction

Diffraction of laser beams always occurs, even if they propagate in vacuum. The aim of this paragraph is simply to introduce the typical length for diffraction of a laser beam. The laws of Gaussian optics say that the width of a Gaussian

beam with a flat spatial phase increases by a factor of $\sqrt{2}$ when the beam propagates over a typical length, called the Rayleigh length. This length is defined as

$$L_{DF} = \frac{kw_0^2}{2} = \frac{\pi n_0 w_0^2}{\lambda_0}, \tag{1}$$

where w_0 is the beam waist, λ_0 the laser wavelength in vacuum, n_0 the refraction index of the medium at this wavelength, $k \equiv n_0 k_0$ and $k_0 \equiv 2\pi/\lambda_0$, the wavenumbers in the medium and in vacuum, respectively. For example, the Rayleigh length of a beam with $w_0 = 100\,\mu m$ at $\lambda_0 = 800\,nm$ in vacuum ($n_0 = 1$) is $L_{DF} = 3.9\,cm$.

1.2.2. Space–time defocusing

It is generally assumed that a laser pulse propagating in vacuum keeps its duration constant. However, this is not strictly the case. A laser pulse is not monochromatic. In a beam of finite dimension, bluer frequencies diffract less than redder frequencies. Therefore a detector (of limited size) will record a longer pulse after propagation because the spectrum of the pulse reaching the detector has become narrower.

1.2.3. Group velocity dispersion and higher order dispersive effects

Gases, liquids and transparent solids are dispersive media. In a region of normal dispersion, red frequencies are faster than blue frequencies. This means that after propagation, the redder frequencies of a pulse with an initial flat temporal phase will pile up in the leading part of the pulse envelope while the bluer frequencies will be found in the trailing part. This increases the pulse duration and decreases the peak intensity. This effect, called group velocity dispersion, is characterized by the dispersive length

$$L_{GVD} = \frac{t_p^2}{2k''}, \tag{2}$$

where t_p is the pulse duration and $k'' \equiv \partial^2 k/\partial\omega^2|_{\omega_0}$ denotes the coefficient of the quadratic term in the development of the wavenumber as a function of the departure from the central frequency ω_0 of the pulse: $k(\omega) = n(\omega)\omega/c = n_0\omega_0/c + k'(\omega - \omega_0) + k''(\omega - \omega_0)^2/2 + \cdots$. For instance, a $t_p = 10\,fs$ pulse at 800 nm will increase its duration by 40% after only $\sim 2.5\,m$ in air ($k'' = 0.2\,fs^2/cm$) or 1.4 mm in glass ($k'' = 360\,fs^2/cm$).

1.2.4. Self-focusing

The refractive index of air n in the presence of an intense electromagnetic field does not only depend on its frequency, but also on the space and time dependent intensity $I(r, t)$ of the laser according to the law: $n = n_0 + n_2 I(r, t)$. The coefficient of the nonlinear Kerr index n_2 is related to the third order susceptibility $\chi^{(3)}$ by $\chi^{(3)} = 4\epsilon_0 c n_2 n_0^2/3$, where ϵ_0 denotes the permittivity of vacuum. The coefficient n_2 is usually positive, leading to an increase of the refractive index in the presence of intense radiation. We discuss first the monochromatic (or continuous) regime for which the intensity of the laser does not depend on time.

The intensity of a beam being usually highest on axis, at the center of the beam, an effect of curvature of the wavefront similar to that of a lens is involved, with the difference that here the effect is cumulative and can lead, in the absence of other saturating effects, to a catastrophic collapse of the beam on itself. This effect is represented in a diagrammatic way in Fig. 3(a).

The characteristic length L_{SF} for self-focusing is defined as the length over which the cumulated nonlinear phase, measured by the B-integral ($B \equiv k_0 \int_0^z n_2 I \, dz$), varies by a factor of one. It is expressed as a function of the peak intensity I_0:

$$L_{SF} = \frac{1}{n_2 k_0 I_0}. \tag{3}$$

It should be noted that the significant parameter for self-focusing is the initial power P_{in} of the beam and not the initial intensity (power per unit of area). Self-focusing overcomes diffraction and leads to collapse only if the input peak power P_{in} exceeds a critical threshold (Marburger, 1975):

$$P_{cr} \equiv 3.72\lambda_0^2/8\pi n_0 n_2. \tag{4}$$
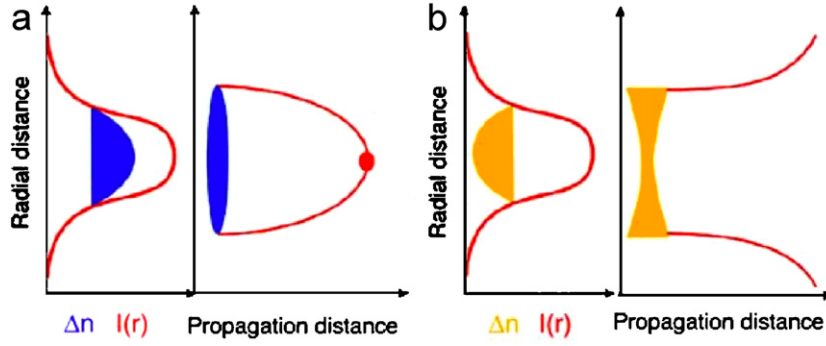
Fig. 3. (a) Self-focusing of a beam by optical Kerr effect. The refractive index of the medium depends on the intensity of the laser and acts as a lens by making convergent an initially collimated beam. Self-focusing prevails over diffraction when the power of the beam exceeds a critical power P_{cr} ($P_{cr} = 3.2$ GW for air at the wavelength of 800 nm) and leads, in the absence of other nonlinear effects, to the collapse of the beam on itself. (b) Defocusing of the beam by the presence of a plasma. The ionization of the medium initially takes place in the center of the beam, where the intensity is most significant. The creation of an under-dense plasma decreases the local index of the medium, which causes beam defocusing.

Eq. (4) is valid for a specific beam shape, sometimes called the Townes beam (Chiao et al., 1964), for which diffraction and self-focusing are balanced. This critical power will be used as a reference throughout this paper; beams with another shape undergo collapse when their power exceeds a threshold usually larger than that given by Eq. (4) (Fibich and Gaeta, 2000). For example the coefficient 3.72 must be replaced by 3.77 to obtain the critical power corresponding to a Gaussian beam.

The propagation length of the self-focusing beam until collapse L_c is rather well approximated by a semi-empirical formula (Marburger, 1975; Dawes and Marburger, 1969):

$$L_c = \frac{0.367 L_{DF}}{\sqrt{[(P_{in}/P_{cr})^{1/2} - 0.852]^2 - 0.0219}},$$ (5)

where L_{DF} is the Rayleigh length of the beam. It is thus seen that L_c, like L_{DF}, varies like the square of the diameter of the laser beam. Eq. (5) is valid for the collapse of Gaussian beams with moderate input powers in purely Kerr media; see e.g., Fibich (1996) for estimations of the collapse position of non-Gaussian beams.

For a collimated beam, at a pulse wavelength of 800 nm, having a power $P_{in} = 10 P_{cr}$ and a waist of $w_0 = 0.5$ cm, the distance to collapse L_c is approximately 15.6 m. At higher input powers (100 P_{cr}), the validity of Eq. (5) breaks down due to modulational instabilities. A transition from a $1/\sqrt{P_{in}}$ to a $1/P_{in}$ scaling was observed both numerically and experimentally (Fibich et al., 2005a).

In the case of a convergent beam (divergent), the position of the collapse $L_{c,f}$ moves before the position of the linear focus of the lens according to

$$\frac{1}{L_{c,f}} = \frac{1}{L_c} + \frac{1}{f},$$ (6)

where f denotes the focal length of the lens.

The critical power given by Eq. (4) is also used as a reference value for ultrashort pulses. In this case, other physical effects as, e.g., group velocity dispersion, or multiphoton absorption and plasma defocusing which will be introduced later, may generally come into play during the self-focusing process and make the scenario of collapse more complex. An additional dimension, here time, is generally involved with these effects, adding a freedom degree to the system. Depending on which physical effect comes into play, the question of the occurrence of collapse in the sense of a singularity at finite distance is still an open question (see Fibich and Papanicolaou, 1999 for a review). For ultrashort pulses, GVD delays the onset of self-focusing since it redistributes the pulse along the temporal axis (Luther et al., 1994a). Due to the absence of any general expression for the critical power for self-focusing in the nonmonochromatic case, it is the habit to consider the peak power of the pulse P_{in} (its energy divided by the duration of the pulse) and to compare this value with that given by Eq. (4) in the monochromatic case. For 100 fs infrared laser pulses, this approach indicates that while the condition $L_{GVD} \gg L_c$ is fulfilled, self-focusing dominates diffraction if $P_{in} > P_{cr}$.

In air at atmospheric pressure, for a laser in the near infra-red domain ($\lambda_0 = 800$ nm), $P_{cr} = 3.2$ GW, which corresponds to a pulse energy of about 0.4 mJ, for a 100 fs laser pulse. It is thus clearly seen that femtosecond pulses launched in air easily reach a strongly nonlinear propagation regime: if the peak power P_{in} is smaller than P_{cr}, the beam diffracts and the pulse duration increases upon propagation, so that the intensity peak quickly becomes negligible. On the other hand, for $P_{in} > P_{cr}$, self-focusing occurs, the pulse duration decreases instead of increasing, the intensity remains high and the propagation regime is strongly nonlinear.

In a real medium, the collapse can be arrested by various mechanisms discussed below. While the relevant mechanism for the arrest of collapse before filamentation in air is multiphoton absorption and the associated plasma defocusing, the physical effect responsible for the arrest of collapse in condensed media is still a debated topics. Among the possible candidates, there are group velocity dispersion (Zharova et al., 1986; Chernev and Petrov, 1992; Rothenberg, 1992b; Fibich et al., 1995; Ranka et al., 1996; Fibich et al., 2003), saturation of n_2 (Fibich and Papanicolaou, 1999; Aközbek et al., 2000; Couairon, 2003a), nonlinear losses (LeMesurier, 2000; Polyakov et al., 2001; Zharova et al., 2002). Vectorial or nonparaxial effects can also, in principle, arrest collapse (Fibich and Papanicolaou, 1997; Fibich and Ilan, 2001a, b).

1.2.5. Self-phase modulation

The temporal variation of the laser intensity involves a temporal variation of the refraction index as $n = n_0 + n_2 I(r, t)$, which in turn corresponds to the appearance of new frequencies in the spectrum of the laser pulse. This effect is called self-phase modulation (SPM). The simplest model accounting for the evolution of the temporal phase links the instantaneous frequencies to the pulse intensity as:

$$\omega(t) = -\frac{\partial \phi}{\partial t} \sim \omega_0 - \frac{n_2 \omega_0}{c} z \frac{\partial I(r, t)}{\partial t}. \tag{7}$$

The generation of new frequencies thus depends on the slope of the pulse $\partial I / \partial t$, the propagation distance z in the Kerr medium and its nonlinear index coefficient n_2. In a purely Kerr medium, the front part of the pulse generates redder frequencies, the back part bluer frequencies. Self-phase modulation plays a significant role in the appearance of a continuum of emission covering the visible and extending towards the infra-red domain.

1.2.6. Raman contribution to the Kerr effect

The optical Kerr effect can originate from two contributions, a pure electronic response with a time constant below 1 fs, and a slower response due to the nuclear motion (Stolen et al., 1989; Stolen and Tomlison, 1992). The optical Kerr coefficient is therefore dependent on the pulse duration. If the pulse duration is shorter than the Raman response time, only the electronic (quasi-instantaneous) response of electrons contributes. This is the case in air for a 10 fs pulse. In gaseous or liquid media with anisotropic molecules, orientation of the molecules in response to the incident fields makes a major contribution to the nonlinear index. Typical response times due to reorientation of the molecules are of the order of picoseconds to several hundred of picoseconds or even more in liquids.

1.2.7. Self-steepening

Laser pulse self-steepening occurs because the velocity of the peak intensity of the pulse is smaller than that of the trailing edge of the pulse, due to the intensity dependent change of refractive index $\Delta n = n_2 I$ (DeMartini et al., 1967). For Δn positive and instantaneous, the light velocity decreases with increasing laser intensity. Starting from a Gaussian pulse, the peak is slowed down with respect to the pulse group velocity while the trailing part catches up with the peak, leading to the formation of a steep edge in the trailing part of the pulse. This effect leads to a faster self-focusing of the trailing part of the pulse (in comparison with the leading part) and to an increase of the bluer frequencies generated in the steep trailing part (see e.g. Rothenberg, 1992b, and Fig. 4). Self-steepening also leads to asymmetric pulse splitting (Fibich and Papanicolaou, 1997; Ranka and Gaeta, 1998).

1.2.8. Photo-ionization

Filamentation requires a nearly lossless initial Kerr region followed by an abrupt onset of multiphoton absorption and plasma defocusing. For filamentation to occur, it is therefore necessary that the energy of the laser photons undergoing filamentation is a small fraction of the ionization potential U_i of the gas. For a small ionization potential $U_i < 3\hbar\omega_0$, the gradual attenuation of the pulse (due to two-three photon absorption) is too important to allow the formation of a narrow filament. The condition $\hbar\omega_0 \ll U_i$ is fulfilled for instance in air at 800 nm: $\hbar\omega_0 = 1.5$ eV, $U_i \sim 12$ eV since
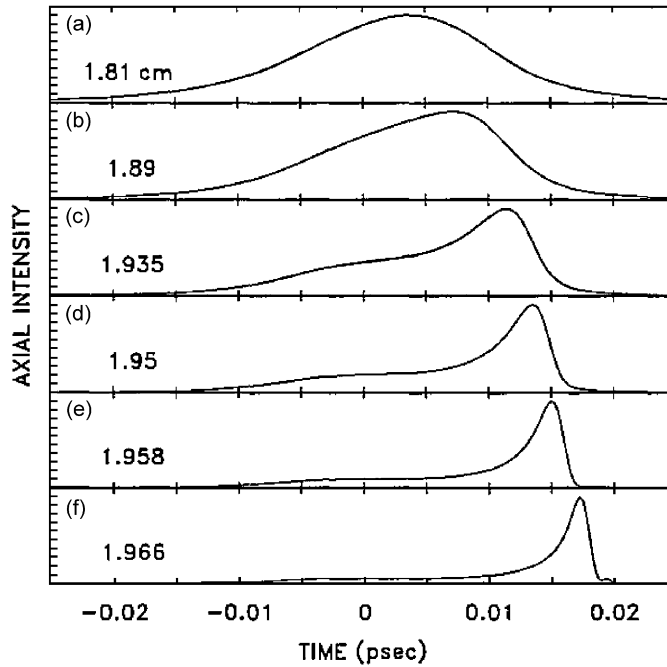
Fig. 4. Calculated intensity on axis (normalized units) as a function of time for a self-focusing and self-steepening pulse in a normally dispersive medium (xenon gas at 40 atm). The propagation distances are indicated on the graphs in cm. From Rothenberg (1992b).
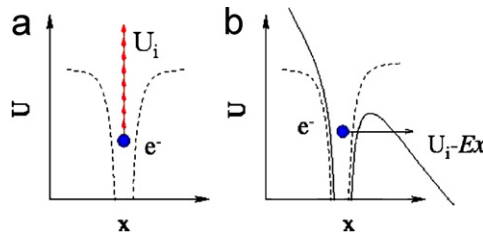
Fig. 5. Schematic diagram of: (a) multiphoton and (b) tunnel ionization.

oxygen is the first ionized constituent. Ionization of the medium requires the simultaneous absorption of a large number of photons $\sim U_i/\hbar\omega_0$, a process highly improbable at low intensity. However, when the beam approaches collapse, the pulse intensity increases enormously and ionization becomes possible. Ionization steps in very abruptly because its probability strongly depends on the light intensity. Photo-ionization or optical-field-ionization (OFI) covers both the so-called multiphoton and tunnel regimes: multiphoton ionization (MPI) is described by perturbation theory and is the first process to set in, in terms of increasing intensities. The ionization rate scales as I^K where $K \sim 8$ for air (oxygen) at 800 nm. Tunnel ionization occurs at higher intensities. It is described by the tunnel escape of an electron across the barrier formed by the combined action of the electromagnetic field and the Coulomb potential tying the electron to the nucleus (see Fig. 5). At even higher intensities, the potential barrier is suppressed and the electron is born in the ionization continuum at each oscillating cycle of the field. The corresponding attenuation of the beam is mentioned below in Section 1.2.11.

1.2.9. Plasma defocusing

The generation of a plasma involves a local reduction in the refraction index (Feit and Fleck, 1974), according to the law

$$n \simeq n_0 - \frac{\rho(r,t)}{2\rho_c}, \tag{8}$$

where $\rho(r, t)$ is the density of free electrons and $\rho_c \equiv \epsilon_0 m_e \omega_0^2 / e^2$ denotes the value of the critical plasma density above which the plasma becomes opaque (m_e and e denote the electron mass and charge, $\rho_c \sim 1.7 \times 10^{21}\,\mathrm{cm}^{-3}$ at 800 nm). The characteristic length L_{PL} for plasma defocusing is defined as the length over which the B-integral ($B = -k_0 \int_0^z \rho / 2n_0\rho_c\,\mathrm{d}z$) corresponding to the integrated nonlinear phase induced by a fully ionized plasma ($\rho = \rho_{\mathrm{at}}$) only changes by a factor of one. Following the same reasoning as for the derivation of Eq. (3), L_{PL} is expressed a function of the neutral atom density ρ_{at}:

$$L_{\mathrm{PL}} = \frac{2n_0\rho_c}{k_0\rho_{\mathrm{at}}}. \tag{9}$$

For a weakly ionized medium of density ρ, the length scale for plasma defocusing is therefore $L_{\mathrm{PL}}\rho_{\mathrm{at}}/\rho$. For a gas of density $\rho_{\mathrm{at}} = 2 \times 10^{19}\,\mathrm{cm}^{-3}$, and an electron density $\rho = 10^{16}\,\mathrm{cm}^{-3}$, we obtain $L_{\mathrm{PL}} \sim 22\,\mu\mathrm{m}$ and $L_{\mathrm{PL}}\rho_{\mathrm{at}}/\rho \sim 44\,\mathrm{cm}$. The reduction in the refraction index acts as a divergent lens, preventing the complete collapse of the beam on itself. This effect is schematically shown in Fig. 3(b). However, it should be stressed that the forward part of the pulse generates the electron plasma which in turn defocuses mainly the trailing part of the pulse. In addition to the purely spatial aspect illustrated in Fig. 3, plasma defocusing acts locally in time and leads to a strong asymmetry in the pulse temporal profile, which is partly at the origin of the dynamics in filamentation and temporal compression effects discussed in Sections 1.3.6, 3.2.4 and 4.1.5.

When an electron plasma is generated in the wake of the pulse, this also contributes to a spectral broadening and shift towards blue in the leading part of the pulse, similarly to the phenomenon of spectral broadening in a laser breakdown plasma (Yablonovitch, 1974a, b). In the presence of ionization, the simplest model relates the instantaneous frequency to the time dependent plasma density ρ as

$$\omega(t) = -\frac{\mathrm{d}\phi}{\mathrm{d}t} \sim \omega_0 + \frac{\omega_0 z}{c}\left(-n_2\frac{\partial I(r, t)}{\partial t} + \frac{1}{2n_0\rho_c}\frac{\partial \rho(r, t)}{\partial t}\right). \tag{10}$$

This is the counterpart of Eq. (7) when self-phase modulation induced by the plasma is also included. Plasma induced SPM was proposed as a mechanism to generate pulses of a few optical cycles (Yablonovitch, 1974a).

In addition to self-phase modulation, the plasma generated in the wake of the propagating pulse was also recently shown to modify the dispersive properties of the medium (Koprinkov, 2004). In particular, in air at infrared wavelength, the changes in group velocity dispersion induced by the plasma are sufficient to counteract locally the normal GVD and leave the medium nearly nondispersive.

1.2.10. Losses due to plasma absorption

Electrons produced by multiphoton or tunnel ionization can be further accelerated by the electric field of the remaining part of the pulse in an inverse Bremsstrahlung effect. If the electrons acquire enough kinetic energy, they give rise to a second generation of electrons by impact ionization of other molecules or atoms, in an avalanche like process. This process is at the origin of electric breakdown of long pulses in air or transparent solids, preventing long range propagation of laser energy.

To first approximation, plasma absorption can be formulated following the Drude model, in which the electron plasma is treated as a fluid. The collective electron velocity $\mathbf{v}$ is supposed to respond to the optical field and, consequently, the total current density $\mathbf{j} = -\rho e\mathbf{v}$ is governed by

$$\frac{\mathrm{d}\mathbf{j}}{\mathrm{d}t} = \frac{e^2}{m_e}\rho\mathbf{E} - \frac{\mathbf{j}}{\tau_c}, \tag{11}$$

where τ_c is the electron collision time. In the frequency domain, this leads to a current density:

$$\mathbf{j} = \frac{\tau_c(1 + i\omega\tau_c)}{1 + \omega^2\tau_c^2}\frac{e^2}{m_e}\rho\mathbf{E}. \tag{12}$$

Absorption of the laser pulse due to the plasma is given by

$$\frac{1}{2}\,\mathrm{Re}\,(\mathbf{j}\cdot\mathbf{E}^*) = \frac{\tau_c}{1 + \omega^2\tau_c^2}\frac{e^2}{2m_e}\rho|\mathbf{E}|^2 \equiv \sigma\rho I, \tag{13}$$
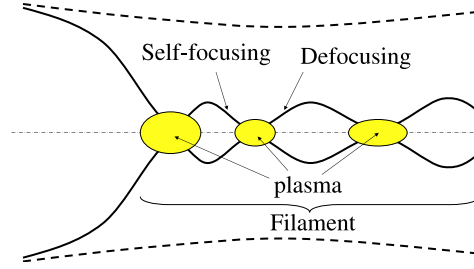
Fig. 6. Schematic representation of the focusing–defocusing cycles undergone by the intense core of the beam. The solid curves indicate the diameter of the intense core. The filamentation length is the distance covered by these cycles. The dashed line indicates the root mean square radius of the full beam.

where $I \equiv \frac{1}{2}\epsilon_0 c n_0 |\mathbf{E}|^2$ and σ denotes the cross section for inverse Bremsstrahlung (Raizer, 1965) which reads

$$\sigma = \frac{e^2}{\epsilon_0 m_e c n_0} \frac{\tau_c}{(1 + \omega^2 \tau_c^2)}. \tag{14}$$

1.2.11. Losses due to multiphoton absorption

Optical field ionization (OFI) is associated with energy losses. The beam attenuation due to multiphoton absorption can be generally described as a dissipative current J_i satisfying:

$$\mathbf{J}_i \cdot \mathbf{E} = \sum_k \rho_k W_k^{\mathrm{OFI}}(I) U_{i,k}, \tag{15}$$

where ρ_k, $W_k^{\mathrm{OFI}}(I)$ and $U_{i,k}$ denote the atom or ion density, the field dependent ionization rate and the ionization potential of species k in the medium. For multiphoton ionization of a single constituent, the ionization rate scales as $W^{\mathrm{OFI}}(I) = \sigma_K I^K$, where $K \equiv \langle U_i/\hbar\omega_0 + 1 \rangle$ denotes the number of photons at the frequency ω_0 necessary to liberate an electron, and σ_K the ionization cross section. The typical length for multiphoton absorption, defined as the length over which a pulse of intensity I is attenuated by a factor $[(K+1)/2]^{1/(K-1)}$, reads:

$$L_{\mathrm{MPA}} = \frac{1}{2K\hbar\omega_0 \sigma_K I^{K-1} \rho_{\mathrm{at}}}. \tag{16}$$

For a filamented pulse at 800 nm in air ($K = 8$, $\sigma_8 = 3.7 \times 10^{-96}\,\mathrm{cm}^{16}/\mathrm{W}^8/\mathrm{s}^1$), typical values are $L_{\mathrm{MPA}} \sim 160\,\mu\mathrm{m}$ for $I = 5 \times 10^{13}\,\mathrm{W/cm}^2$ and $L_{\mathrm{MPA}} \sim 12.6\,\mathrm{m}$ for $I = 10^{13}\,\mathrm{W/cm}^2$.

1.2.12. Refocusing cycles

It is primarily the combined action of the optical Kerr effect, multiphoton absorption and ionization which are at the origin of the formation of filaments preserving an average diameter of about 100 μm over long distances in air, even if other effects, like diffraction, group velocity dispersion, self-phase modulation and pulse self-steepening contribute to this self-guiding process. This process is shown in Fig. 6. A pulse with peak power above P_{cr} should undergo a collapse. However, when the beam becomes sufficiently intense, MPA attenuates the core of the beam and a plasma is generated near the collapse location, which defocuses the beam core. Once defocused, the beam may still contain a power above critical and undergo another focusing–defocusing cycle. The repetition of this scenario sustains a long range, self-guided propagation in the form of a filament. The interplay between self-focusing, MPA and ionization is therefore a highly dynamic process, with recurrent, aperiodic strings or spikes of ionization surging whenever the beam starts collapsing again (Mlejnek et al., 1998a). The recurrence of these cycles depends among other things on the peak power of the input pulse.

At this point, it should be stressed again that *self-guiding* or *self-channeling* is nothing else than a terminology meaning that no external waveguide sustains this long range propagation. By these terms, it is not assumed by any means that the filament is a soliton-like structure or that there is a delicate balance between the index variations attributed to each physical effect. Rather, a dynamic competition between self-focusing and defocusing effects (plasma defocusing among others) involves successive focusing–defocusing cycles in the global dynamics.

These physical effects couple space and time since self-phase modulation (the temporal counterpart of self-focusing), simultaneously competes with group velocity dispersion, self-steepening and shock formation due to plasma defocusing. This leads to strong pulse distortions during propagation. Multiphoton and plasma absorption also indirectly participate in this complex coupling by attenuating the peak intensity.

1.2.13. Modulational instability

When the laser pulse power is well above P_{cr}, the beam starts collapsing over many spots, each forming its own filament. The appearance of many filaments is related to the growth of components of the beam intensity profile with specific transverse spatial frequencies. The growth rate k_i of spatial modulation structures is a function of the transverse wave number of the perturbations which reads as $k_i(k_\perp) = (k_\perp/2k_0)\sqrt{8\pi I_0/P_{cr}^G - k_\perp^2}$, where $P_{cr}^G \equiv \lambda_0^2/2\pi n_0 n_2$ denotes an estimation of the critical power for self-focusing associated to a Gaussian beam and I_0 denotes the intensity of the laser field. The maximum growth rate of spatial modulation structures occurs at a transverse wavenumber $k_\perp^{opt} = 2\sqrt{\pi I_0/P_{cr}^G}$ (Campillo et al., 1973, 1974). After a growth of the instability waves as $\sim \exp[k_i(k_\perp^{opt})z]$, saturation occurs in the form of filaments with a transverse spacing between the filaments equal to $d_{fil} = 2\pi/k_\perp^{opt} = \sqrt{\pi P_{cr}^G/I_0}$. Assuming a regular filamentation pattern, one can roughly estimate the individual power that a filament should be able to carry as $P_{fil} = 2\pi \int_0^{d_{fil}} I_0 r \, dr \sim (\pi^2/4) P_{cr}^G$ (Couairon and Bergé, 2000). From these energy considerations, a beam with power P_{in} well above critical leads to a number of filaments $N \sim P_{in}/P_{fil}$. It should not be forgotten that these considerations rely on several assumptions, among which the fact that the instability analysis is performed on plane and monochromatic waves. For Gaussian pulses, the threshold for modulational instability initiated by noise was found to lie around 100 P_{cr} (Fibich et al., 2005a). In addition, the nonlinear saturation of the growth of filaments after the linear stage of the instability is assumed not to destroy the filamentation pattern. Therefore, the estimated number of filaments should not be expected to be accurate. The above considerations are not qualitatively modified when other physical effects such as multiphoton ionization or absorption are accounted for; in this case the spatial growth rate is reduced with respect that obtained in a purely Kerr medium (Couairon and Bergé, 2000; Marklund and Shukla, 2006).

1.2.14. Filaments in condensed media

Filamentation in condensed media is not only interesting for applications (see Section 5.2.8), but also constitute a remarkable system where all the physical effects and properties presented above are observed on a reduced scale. Dense transparent dielectrics have a nonlinear refraction index about 3 orders of magnitude larger than in gases. As a result, the critical power for self-focusing is in the Megawatt range while it is in the Gigawatt range for gases. Only 1 µJ energy is required for a laser pulse of 100 fs in order to self-focus the beam in a solid. Remarkably, the peak intensity in the filament is almost the same as in gases. As will be shown later, a filament carries about one critical power for self-focusing. From the peak intensity and the carried power, the filament diameter is estimated to be about a few microns to a few tens of microns, i.e. 30 times narrower than in gases (Yablonovitch and Bloembergen, 1972; Tzortzakis et al., 2001d). It is worth underlining here that the ionization mechanism generating free electrons in gases is replaced in solids by the promotion of electrons from valence to conduction band. The electron density reaches typically 10^{18}–10^{20} cm^{-3} which is three orders of magnitude larger than that reached in air but still corresponds to a low density plasma.

The Rayleigh length of an 800 nm laser beam corresponding to $w_0 = 10$ µm is about 390 µm. With the same intensity but a much higher electron density, energy losses are much higher in condensed media. This quickly exhausts the laser energy reservoir and filamentation stops because the peak power of the pulse quickly goes below the critical power for self-focusing.

Another important difference between condensed media and gases is the higher GVD. As will be shown in Section 1.2.15, GVD is an efficient mechanism to arrest the collapse.

1.2.15. Arrest of collapse

From the previous presentation, one might draw the conclusion that plasma defocusing alone is responsible for the arrest of collapse that would occur in a purely Kerr medium when the input beam power is above the critical power for self-focusing. Several mechanism, however, are able to play this role. Among them, there are saturation of the nonlinear index by a higher order (defocusing) nonlinearity (Aközbek et al., 2000; Couairon, 2003a), nonlocal effects
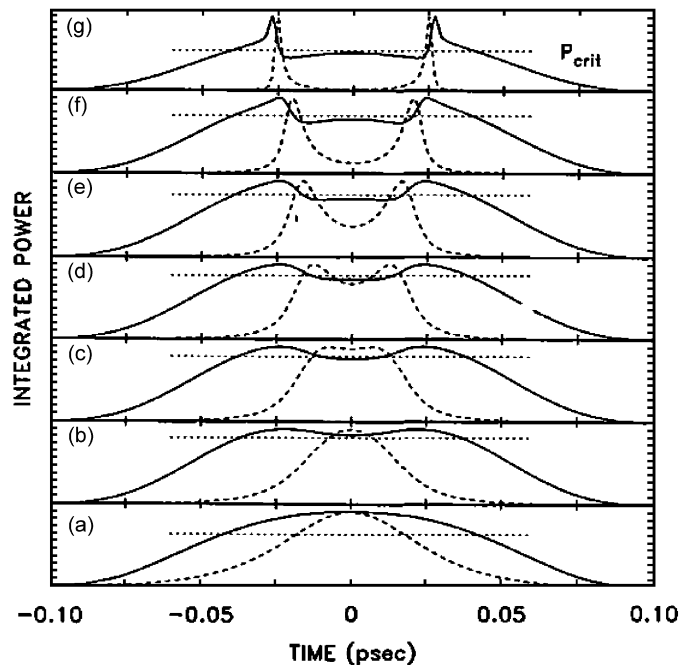
Fig. 7. Pulse splitting due to the competition between the optical Kerr effect and GVD in a 40 atm Xe gas. The 600 nm input pulse has a FWHM duration of 50 fs and peak power of 45 MW. The beam of 500 μm FWHM is focused with $f = 25$ cm. The solid curves show the spatially integrated power at successive propagation distances. (a) 17.53 cm; (b) 18.6 cm; (c) 18.79 cm; (d) 18.86 cm; (e) 18.92 cm; (f) 18.98 cm; (g) 19.04 cm. The dashed curves are the axial intensities. The dotted lines indicate the critical power level (15 MW). According to Rothenberg (1992a).

(plasma defocusing, Raman Kerr effect) (Bang et al., 2002; Turitsyn, 1985) or nonlinear absorption (Vlasov et al., 1989; Kosmatov et al., 1991; Dyachenko et al., 1992; LeMesurier, 2000; Couairon et al., 2006c).

While in gases, GVD is too small to play a significant role in the arrest of collapse, several authors have pointed out that GVD, which is much stronger in solids, leads to pulse splitting into two components moving in opposite directions in the frame of the input pulse (see Fig. 7) (Zharova et al., 1986, 2002; Chernev and Petrov, 1992; Rothenberg, 1992a; Fibich et al., 1995, 2003; Fibich and Papanicolaou, 1997). With GVD alone, these authors describe pulse propagation beyond the nonlinear focus. Ranka et al. (1996) have shown that GVD is an efficient mechanism arresting the collapse. This mechanism, however, is relevant for pulses having a sufficiently low peak power, since the critical power threshold for collapse in dispersive media, determined analytically by Luther et al. (1994a) increases with dispersion. We remind that for pulses with powers largely exceeding the critical power for self-focusing, multiphoton absorption is an even more efficient mechanism than GVD in arresting the collapse and it leads to multiple splitting beyond the nonlinear focus (see Vlasov et al., 1989; Kosmatov et al., 1991; Dyachenko et al., 1992; LeMesurier, 2000; Couairon et al., 2006c). Pulse splitting is therefore not systematically induced by GVD, although GVD as well as space–time focusing and self-steepening must often be taken into account so as to correctly describe the propagation beyond the nonlinear focus in the slowly varying envelope approximation (Ranka and Gaeta, 1998).

1.3. Properties of light filaments

1.3.1. Robustness of filaments

A remarkable feature of filaments is their universality: they appear in many transparent media whatever their solid, liquid or gaseous nature, provided that the photon energy is much less than the fundamental electronic transition energy. This suggests that a robust attractor of the propagation dynamics might exist in the nonlinear regime. Filaments are even regenerated when a central stopper blocks their propagation (Courvoisier et al., 2003; Kolesik and Moloney, 2004b; Dubietis et al., 2004b; Liu et al., 2005e). This property was called self-healing by Kolesik and Moloney (2004b). Filaments are actually rebuilt from the laser energy reservoir (Mlejnek et al., 1999a). As a result filaments can traverse
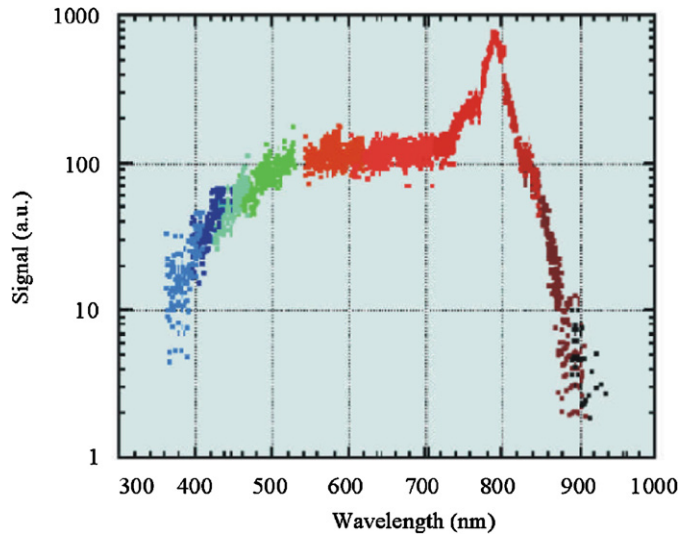
Fig. 8. Spectrum of a femtosecond laser beam ($\lambda_0 = 800$ nm; $\tau_{\text{FWHM}} = 70$ fs, $P_{\text{in}} = 3$ TW) after propagation over a distance of 10 m in air. The fast fall between 800 and 900 nm corresponds to the fall of the detectivity of the measuring apparatus (see Kasparian et al., 2000b).

adverse atmospheric conditions such as foggy or rainy atmosphere (Méchain et al., 2005b). This property is interesting for all applications where a large amount of laser energy must be conveyed over extended distances in the sky (see Section 5).

1.3.2. Long range propagation

One of the most spectacular properties of filamentation is its ability to convey high intensities over extended distances. Peak intensities exceeding 10^{12} W/cm^2 have been observed over several kilometers via filamentation (Méchain et al., 2005a). Energy losses during filamentation in air are minimized because: (a) the intensity is always maintained at the verge or below the value corresponding to ionization threshold via the clamping mechanism; (b) the short pulse duration prevents significant pulse attenuation through its interaction with the generated plasma (via inverse Bremsstrahlung).

1.3.3. Spectral broadening

Filamentation is accompanied by a strong spectral broadening, which depends on the strong reorganization of the temporal shape of the pulse. Several effects combine to cause spectral broadening: self-phase-modulation, self-steepening and ionization of the medium. In particular, the sharp trailing part of the pulse is due to self-steepening as well as ionization, which add preferentially new frequencies on the high energy side of the spectrum (see Fig. 8). Thus, an initial pulse centered in the near infrared at 800 nm partially converts into a continuum covering the entire visible part of the spectrum when propagating in air. On the low energy side, continuum generation has been observed up to 5 μm in the IR (Kasparian et al., 2000b) but with a much lower intensity. The conversion rate into white light varies from a few tenth of percent for an initially collimated beam up to an appreciable fraction of the initial energy, for a convergent beam. A similar phenomenon forming a so-called white light laser was reported in transparent solids (Petit et al., 2000b).

1.3.4. Intensity clamping

As we have seen, filamentation results predominantly from a dynamic competition between the optical Kerr effect, multiphoton ionization and associated multiphoton absorption. Multiphoton ionization sets in once the beam intensity reaches a sufficiently high value. The multiphoton ionization rate scales first as I^K, with K, the number of photons simultaneously absorbed, typically greater than 5 for infrared wavelengths. The generated electron density has therefore a threshold like response, which saturates self-focusing locally and limits the peak intensity inside the filament by defocusing the beam. This simple idea allows an estimation of the clamping intensity according to Braun et al. (1995),
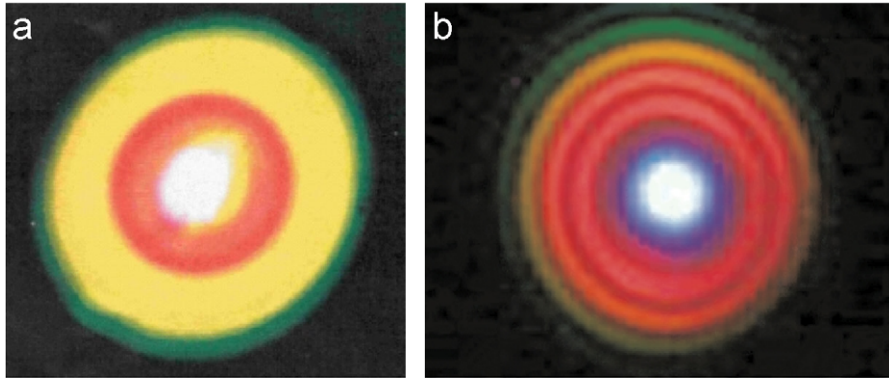
Fig. 9. Conical emission accompanying a self-guided pulse. (a) A central white core (the filament) is surrounded by Newton's rings having a divergence of the order of the mrad (Nibbering et al., 1996). (b) Conical emission measured at 25 m from a 5 mJ, 45 fs, 800 nm pulse (Chin, 2004).

Kasparian et al. (2000a), Becker et al. (2001a):

$$n_2 I = \frac{\rho(I)}{2\rho_c}. \tag{17}$$

In air, by using the rough estimate $\rho(I) \sim \sigma_K I^K \rho_{at} t_p$, where ρ_{at} denotes the density of neutral atoms, we obtain

$$I \sim \left(\frac{2n_2\rho_c}{\sigma_K t_p \rho_{at}} \right)^{K-1}, \tag{18}$$

which yields the clamping intensity $I \sim 1.8 \times 10^{13} \, \text{W/cm}^2$ for a pulse duration $t_p = 100 \, \text{fs}$ at 800 nm. The filament contains a fixed amount of power, roughly equal to P_{cr} (Braun et al., 1995). Following Yablonovitch and Bloembergen (1972), the transverse size of the filament corresponding to the above power ($P_{cr} = 3.2 \, \text{GW}$) and intensity given by Eq. (18) is $w_0 = 105 \, \mu\text{m}$.

Liu et al. (2002c) have found also evidence of the clamping phenomenon from an analysis of the supercontinuum generated by filamentation of 170 fs, 800 nm laser pulses in condensed media (water, chloroform and glass). The maximum blueshift due to self-phase modulation was found to be independent of the pulse energy above a critical value, which was interpreted from Eq. (10) as a manifestation of the clamping phenomenon.

1.3.5. Conical emission of white light and colored rings

The white light beam generated during filamentation in gases or condensed media generally consists of a white central part surrounded by a rainbow-like conical emission (see Fig. 9). The radial order of the spectral components is inverse of diffraction with bluer frequencies appearing on the outside rings. This phenomenon is a signature of filamentation. Several mechanism have been invoked to explain this still not entirely understood phenomenon: Cerenkov radiation (Golub, 1990; Nibbering et al., 1996), self-phase modulation (Kosareva et al., 1997a, b), four-wave mixing (Xing et al., 1993; Luther et al., 1994b), X-waves (Di Trapani et al., 2003; Conti et al., 2003; Faccio et al., 2006b). The reader is referred to Aumiler et al. (2005) for a review of tentative interpretations of conical emission in dense atomic vapors. Conical emission accompanying filamentation is discussed in more details in Section 2.1.7.

1.3.6. Pulse self-compression

In the filamentation process, several effects compete to reshape the pulse time profile. This leads to a significant shortening of the pulse duration. Recent calculations have shown that nearly single optical cycle pulses can be obtained in this way, starting with pulses of a few tens of femtoseconds duration. Fig. 10 shows a sequence of space time profiles of a femtosecond laser pulse at various stages as it progresses through a gas volume (Couairon et al., 2006a). Intense single cycle pulses in the visible or infrared are extremely important for producing attosecond pulses in the far UV via high-order harmonics generation (Brabec and Krausz, 2000). Pulse self-compression via filamentation may
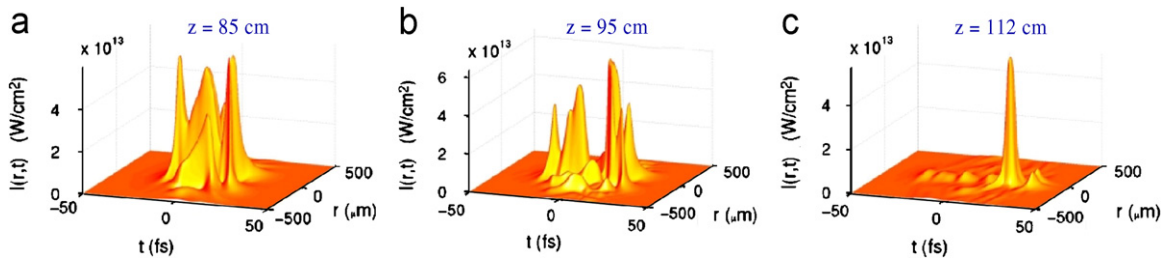
Fig. 10. Numerical simulations show the self-shortening and single cycle pulse generation of a 1 mJ, 25 fs infrared laser pulse undergoing filamentation in a gas cell filled with argon at 0.8 atm. According to Couairon et al. (2006a).
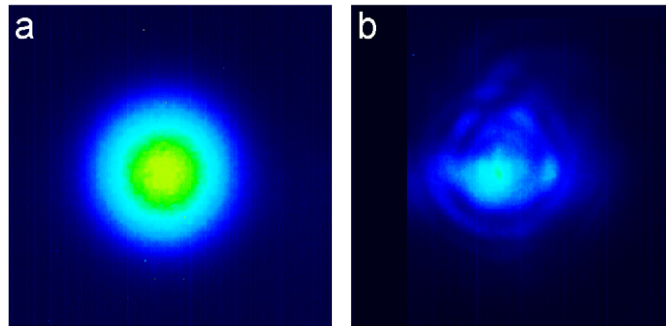
Fig. 11. Conical emission and laser pattern measured after 20 m of propagation in air from a 400 nm laser pulse. (a) Surrounding conical emission only, with the power spectrum close to that of the incident laser pulse removed by a colour filter. The external diameter of the blue ring is about 1 cm. (b) Strongly attenuated total laser beam at the same distance. From Prade et al. (2006a).

considerably simplify the experimental procedure to generate attosecond XUV pulses via high-harmonic generation with phase-stabilized single cycle laser pulses (Hauri et al., 2004; Chakraborty et al., 2006).

1.3.7. Pulse mode self-cleaning

By examining the far-field pattern of the conical emission surrounding a filament core generated from a 400 nm laser pulse, Prade et al. (2006a) noticed a significant improvement of the beam quality. The spatial conical emission associated with the filament corresponds to a single transverse radiation mode while the remnant of the incident pulse around 400 nm, which does not couple into the filament, exhibits a poorer beam quality (Prade et al., 2006a, b). This is shown in Fig. 11 which compares the spatial profile of the conical emission (with the wavelengths around the central laser frequency removed by a color filter placed at $z = 15$ m) with the total beam profile at the same distance comprising the remnant of the nonfilamentary part of the beam, the filament core and the much weaker conical emission. A striking feature is the excellent quality of the conical emission which takes the form of a single transverse mode. Filaments bear therefore remarkable properties in the time domain (pulse self-compression), frequency domain (spectrum broadening) and spatial domain (mode improvement) making it a unique source for applications (Chin et al., 2007).

1.3.8. Filaments in optical parametric amplifiers

A nice application of the unique properties of filaments is illustrated by the possibility to design optical parametric amplifiers where a filament acts as a pump source. Théberge et al. (2006a) have shown that a signal beam tunable over the entire visible spectrum is obtained with excellent beam quality. It corresponds to a diffraction limited Gaussian beam ($M^2 < 1.01$), translating the self-cleaning effect of a filament. When compared to an OPA system operating with the same laser as a pump except that it is not in a filament form, the signal beam has also a shorter pulse duration translating the self-compression effect of filaments. Finally, the signal beam exhibits a distinct improvement in beam stability interpreted as an effect of the intensity clamping phenomenon (see Fig. 12).
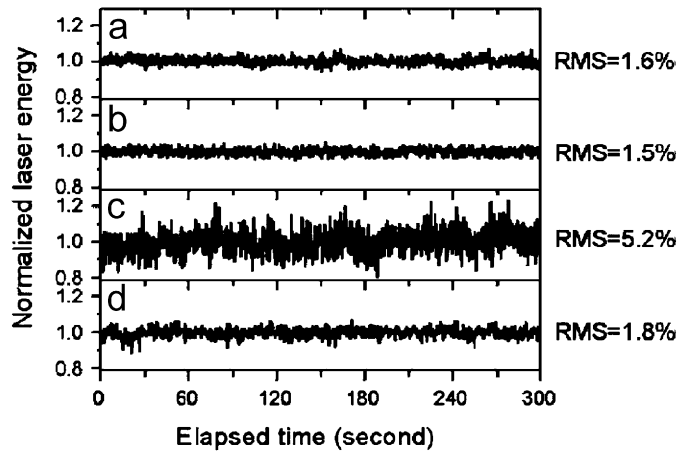
Fig. 12. Temporal evolution of energy per pulse normalized over the mean energy for (a) the infrared seed ($1.1\,\mu m < \lambda < 1.6\,\mu m$), (b) the near infrared pump pulse (807 nm), (c) the generated signal pulse for near infrared pump power (10 times below P_{cr} in air), and (d) the generated signal pulse for pump power of 2.5 P_{cr}. The rms energy fluctuations are indicated on the right-hand side. From Théberge et al. (2006a).

1.3.9. Superluminal velocity

One of the interesting properties of filamentation is that the pulse envelope undergoes strong temporal and spatial deformations. The motion of the peak intensity can even exceed the light velocity in the medium, a phenomenon called superluminal propagation.

Experimental evidence for superluminal propagation during filamentation has been reported by Tzortzakis et al. (2003) in an experiment on filament concatenation. It is possible to connect two spatially separated plasma strings by sending a sequence of two laser pulses with different curvatures and an appropriate delay. It was found that the chronological coincidence of the two pulses, which leads to the connection, could only be obtained by delaying the pulse with the smaller beam curvature (see Section 4.1.22 for details). This pulse which has undergone filamentation has an advance over its nonfilamented twin. This advance is exacerbated by introducing a thin fused silica plate in its path (see Fig. 13).

1.3.10. Generation of THz radiation

Plasma channels formed by femtosecond laser filaments in air radiate electromagnetic THz pulses (EMP), in a frequency range at the border region between optical sources and radio sources. This is an exciting property since it gives rise to a coherent emission from an ubiquitous medium in a challenging part of the electromagnetic spectrum. Since the location of filaments can be varied to a large extent, it provides a coherent THz source at a remote, selected location. THz and sub-THz emission have important applications in medical and other domains.

Heterodyne detection of sub-THz radiation emitted radially by plasma strings after filamentation in air was recently reported (Tzortzakis et al., 2002). Very recently, Houard et al. (2007a) and D'Amico et al. (2007b) reported a stronger sub-THz radiation emitted by the filament in a narrow forward cone.

1.3.11. Two-colored filamentation and third harmonic generation

As we have seen, the nonlinear response initiating filamentation is the optical Kerr effect described by the real part of the third order susceptibility of the medium. Third harmonic generation, a process associated with the imaginary part of $\chi^{(3)}$ will also take place. As shown by Aközbek et al. (2002b) the generated coherent wave at $3\omega_0$ is coupled with the fundamental wave ω_0 via cross-phase modulation (the refractive index $n_2(3\omega_0)$ is modified by the field at ω_0 and vice versa). This leads to the formation of a UV filament at $3\omega_0$. Cross-phase modulation couples the fundamental and the third harmonic pulse together, imposing a constant phase difference of π inside the two-colored filament. The cofilamentation of the high intensity fundamental and third harmonic pulses over long distances opens the way to promising applications for atmospheric remote sensing (Théberge et al., 2005a–d).
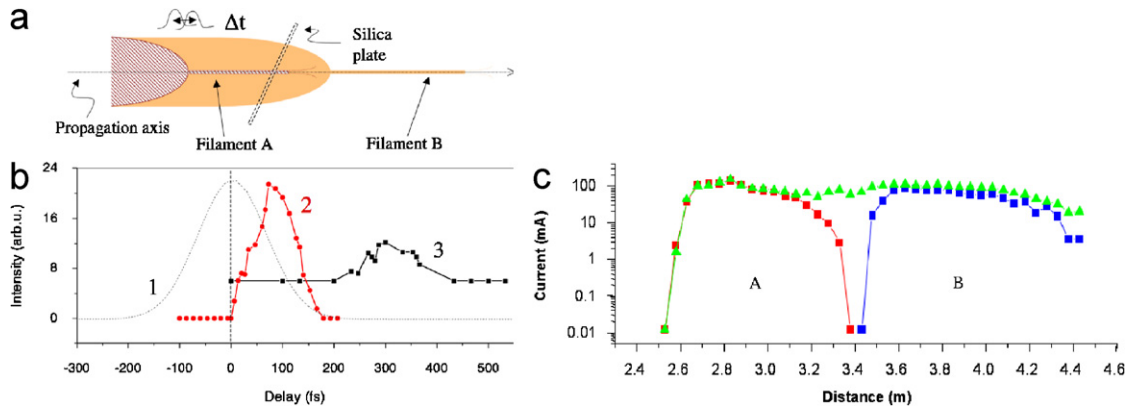
Fig. 13. (a) Schematic representation of the experiment. Two filaments A and B are generated along the same axis by using two pulses A and B with different beam convergence. A silica plate can be introduced in a region where only pulse A is a filament. For a well suited delay between pulses A and B, it is possible to connect the filaments in order to give rise to only one filament of constant density. (b) Curve 1 represents the second harmonic autocorrelation trace of the initial laser pulses. Curve 2 corresponds to the conduction signal measured at the junction region between the two filaments as a function of delay between pulses A and B: in the absence of the silica plate, it is necessary to advance pulse B by 100 fs (curve 2) in order to have chronological coincidence between pulses A and B in the junction region. Curve 3 is the signal measured in the presence of the silica plate. In this case, pulse B must be advanced by 300 fs. According to Tzortzakis et al. (2003). (c) Measurements of the conductivity of air for the two individual filaments A and B and the concatenated filament (Tzortzakis et al., 2003; Couairon et al., 2003).
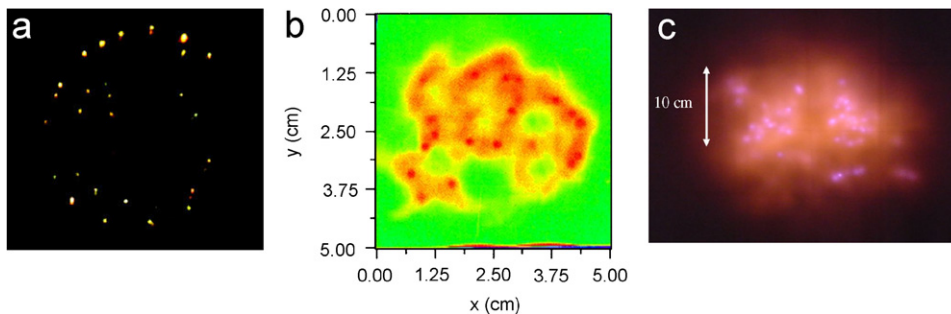
Fig. 14. (a) Image of a beam profile recorded on a screen at 50 m with the camera shutter opened immediately after the laser pulse. The spots corresponds to the long lasting phosphorescence of the screen induced by the filament spots. (b) Image of another beam profile recorded on the same screen at 50 m with the camera shutter open during the laser pulse. (c) Image of the beam profile recorded on a white screen at 600 m showing multifilamentary structure. For the three cases, the pulse of initial duration 100 fs has been stretched to 1.7 ps with a negative chirp (Méchain et al., 2005a).

1.3.12. Multiple filamentation

When the input peak power is far above the critical power for self-focusing, the modulational instability breaks up the beam into a large number N ($N \simeq P_{in}/P_{cr}$) of filaments (see Fig. 14(a)) (Vidal and Johnston, 1996). For large powers above $\sim 100 P_{cr}$, multiple filamentation occurs at a distance scaling as $1/P_{in}$. For smaller powers, modulational instability can also lead to multiple filamentation but this occurs beyond the beam collapse at a distance scaling as $1/\sqrt{P_{in}}$ (Fibich et al., 2005a). These filaments, which grow from the small fluctuations in the beam intensity profile, can be seemingly randomly distributed in a given transverse plane z or organized into specific patterns (Mlejnek et al., 1999a; Méchain et al., 2004b; Dubietis et al., 2004c; Fibich et al., 2004; Schroeder et al., 2004). Each filament is likely to take a power about P_{cr}. When the power of an individual filament becomes smaller than P_{cr}, the filament restores the main part of its energy to a common photon bath; this energy reservoir can feed narrow filaments, which further leads to a new distribution of filaments becoming quickly random. The number of filaments N decreases gradually with the propagation distance due to energy losses by plasma or multiphoton absorption, until containing only one filament. Numerical simulations of the propagation must clearly be handled in $(3 + 1)$ dimensions in this case (three spatial dimensions + time) to capture the full dynamics of filamentation.

1.3.13. Energy reservoir

Fig. 14 shows two photographs of a screen intercepting the laser beam at a distance of 50 m. The laser beam contains about 200 mJ. After 50 m, more than 90% of the initial laser energy is still present inside the 1 cm diameter beam. Fig. 14(a) is recorded several ms after the pulse. The small spots still observable correspond to the long lasting fluorescence of the screen induced by the very intense filaments which have been formed. By contrast, Fig. 14(b) is recorded during the pulse. One sees again the bright spots corresponding to multiple filaments but in addition, one observes a more diffused illuminated area. This diffuse area forms an energy reservoir for the filament. Since the energy in each filament is at most one mJ, the total energy content of the filaments is around 30 mJ, a factor 10 below the total energy measured at that distance. Most of the energy is distributed in the reservoir. As can be seen, this energy tends to link different filaments through ducts joining adjacent filaments. The energy reservoir plays a very important role in the persistence of filament formation and regeneration over long distances as first pointed out by Mlejnek et al. (1999a).

2. Modeling filamentation

2.1. Model scenarii

The history of filamentation traces back to the early days of nonlinear optics (Askar'yan, 1962) where long narrow fluorescence or damage tracks were seen in solids and liquids (Hercher, 1964; Lallemand and Bloembergen, 1965; Shen and Shaham, 1965; Garmire et al., 1966). Two models were advocated to explain this phenomenon: one is the self-trapping model where a strict equilibrium between diffraction and self-focusing is proposed (Chiao et al., 1964, 1966; Talanov, 1964, 1965). This equilibrium is interpreted as a mode, often referred to as the Townes mode (Chiao et al., 1964), which was later shown to represent the self-similar blowup solution reached during the collapse of a self-focusing beam regardless of its initial shape (Landman et al., 1991, 1992; Fibich and Papanicolaou, 1999). The self-trapping model explains certain features such as the quality of the emerging mode and the associated considerable spectral broadening (Gustafson et al., 1969; Svelto, 1974) or the self-focusing distance (Kelley, 1965; Marburger and Dawes, 1968). The other model called the moving focus model considers the filament as an illusion, as explained in Section 2.1.1. A large part of the nanosecond pulse experiments were consistently explained by the moving focus model (Lugovoi and Prokhorov, 1968; Shen, 1984; Giuliano and Marburger, 1971; Loy and Shen, 1969, 1973; Korobkin et al., 1970). However, a more complete description (Shen, 1984) shows that a short pulse deforms into a horn-shape as it propagates, which can be viewed as a self-trapped appendix to the moving focus; this horn structure corresponds to the descending part of the pulse which sees a larger refractive index induced by the leading part. It is not astonishing that the same concepts have been invoked in the case of femtosecond laser pulses.

2.1.1. Moving focus model

In the moving focus model (Lugovoi and Prokhorov, 1968; Shen, 1984; Brodeur et al., 1997), the laser pulse is stacked into time slices that are considered to be independent from each other. This picture relies on the assumption that the influence of collapsed time slices on the subsequent propagation can be neglected. This approximation is valid when the physical effects coupling the various time slices together, such as e.g. GVD, remains weak. In air, the typical distance for GVD for a $t_p = 100$ fs infrared pulse is $z = 250$ m, much larger than the typical self-focusing and collapse distances. The approximation of independent time slices seems therefore justified at first sight. Each time slice contains a specific power. All the central slices of a pulse with peak power above critical are self-focused at distances that become larger as the corresponding power is closer to critical value. The slices with power below P_{cr} diffract. In this picture, the perception of a filament is constituted by the collection of nonlinear focii corresponding to the different temporal slices of the pulse comprised between the time slices t_A and t_B which correspond to a power P_{cr} on the ascending (resp. descending) slope of the pulse envelope. Fig. 15(A) shows the predicted locations of the moving focus as a function of time. Following the original model (see e.g. Lugovoi and Prokhorov, 1968; Shen, 1984), the velocities and propagation directions refer here to the laboratory frame and not to the reference frame moving at the pulse group velocity usually used in optics. Applying Eq. (5) to $P_{in} = P(\tau = t - z/v_g)$ yields a focus for each time slice in the pulse. Two branches appear: the upper branch starting from the earliest focus B describes the forward motion of the focus due to the forward part of the pulse $t_A < t \leqslant t_B$. This branch has a superluminal velocity. The lower branch BCD describes the backward motion of the focus from B to C, the time slice t_C with maximum power focusing at the closest position to the laser, followed by the forward motion from C to D, corresponding to the trailing part of the pulse.
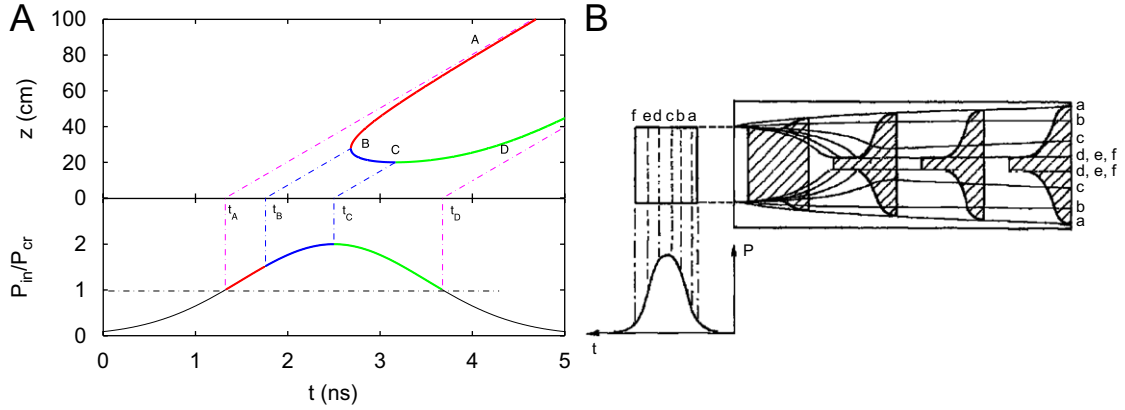
Fig. 15. (A) Prediction of the moving focus location as a function of time and input pulse power (adapted from Shen, 1984). The time slice with the maximum power collapse at the shortest distance from the laser. The time slices with smaller power, provided $P_{in} \geqslant P_{cr}$, collapse farther on the propagation axis, leading to the illusion of a filament. (B) Transient self-focusing for pulses shorter than the response time. The descending parts of the pulse (d, e, f) are trapped by the change of index induced by (a, b, c) giving rise to the horn-shaped appendix. After Shen (1984).

It is instructive to apply the moving focus model to the case of a converging beam. The succession of nonlinear focii, found by applying the lens transformation to the collapse positions of the various slices, all lie before the geometric focus (Lange et al., 1998c). One does not expect in this case any significant forward propagation of energy beyond the geometric focus. This is clearly in contradiction with many experimental results concerning femtosecond filamentation.

In fact, the cartoon of the moving focus model must be modified as soon as the intensity is sufficient to ionize the medium, because it induces a strong coupling between the various time slices in the trail of the pulse. This coupling delays the collapse of the slices in the trail of the pulse, and allows energy to propagate beyond the linear focus of a lens. Applying the required modifications is equivalent to describe a transient self-focusing as shown in Fig. 15(B) and leads to the fusion of the model with others models described in Sections 2.1.2 and 2.1.3 (Couairon, 2003c).

2.1.2. Self-guiding model

The terminology of *self-guiding* refers to nothing else than the absence of any external guiding mechanism, such as a waveguide. Yet, the notion of *self-guiding* is not necessarily understood in the same way in the literature. Among the reasons, there is certainly the fact that it is seemingly equivalent to several other terminologies (*self-trapping, self-channeling*). In the first report of femtosecond filamentation in air, Braun et al. (1995) proposed the *self-channeling* model as a stable balance between self-focusing from the intensity dependent refractive index and the combined effects of natural diffraction and refraction from the plasma generated by the intense laser pulse. In this picture, unbalance eventually occurs due to nonlinear energy losses during the generation of the plasma. Thus, *self-channeling* is an extension of *self-trapping* (Chiao et al., 1964) in the sense that it includes the effect of plasma defocusing. This is necessary since the self-trapping mechanism relying on an equilibrium between self-focusing and diffraction is unstable and leads to either diffraction for low power pulses or collapse for high power pulses (Shen, 1984). Braun et al. (1995) performed a Javan–Kelley analysis to estimate several characteristics of the filament such as its size, peak intensity and the generated electron density (Javan and Kelley, 1966). This can be expressed in terms of an equilibrium of the index variations corresponding to the three involved mechanisms:

$$n_2 I = \frac{\rho(I)}{2\rho_c} + \frac{(1.22\lambda_0)^2}{8\pi n_0 w_0^2}. \tag{19}$$

It seems now clear that the self-channeling model cannot be reduced to Eq. (19). In fact both the intensity and the electron density vary with time and space, and thus, the balance can only be local. However, Eq. (19) is remarkably predictive for the orders of magnitudes of the peak intensity or electron densities with respect to the measured counterparts. In air, for $n_2 = 3.2 \times 10^{-19} \, \text{cm}^2/\text{W}$ and $\lambda_0 = 800 \, \text{nm}$, the critical power for self-focusing is equal to $P_{cr} = 3.2 \, \text{GW}$; Since $P_{cr} \sim P_{cr}^G$, a filament carrying one P_{cr}^G has a size of $w_0 = (2P_{cr}^G/\pi I)^{1/2}$. A pulse with duration t_p generates a plasma

with a peak density roughly estimated by $\rho(I) \sim \sigma_K I^K \rho_{at} t_p$, where σ_K denotes the cross section for multiphoton ionization involving K photons and ρ_{at} the density of neutral molecules. For the pulse under consideration, this leads to the following scaling laws:

$$I \sim \left(\frac{0.76 n_2 \rho_c}{\sigma_K t_p \rho_{at}} \right)^{1/(K-1)}, \tag{20}$$

$$\rho(I) \sim \left[\frac{(0.76 n_2 \rho_c)^K}{\sigma_K t_p \rho_{at}} \right]^{1/(K-1)}, \tag{21}$$

$$w_0 \sim \left(\frac{2 P_{cr}^G}{\pi} \right)^{1/2} \left(\frac{\sigma_K t_p \rho_{at}}{0.76 n_2 \rho_c} \right)^{1/2(K-1)}. \tag{22}$$

For $t_p = 100$ fs, $\lambda_0 = 800$ nm and ionization of oxygen with $K = 8$, $\sigma_8 = 2.8 \times 10^{-96}$ cm^{16}/W^8/s^1, Eqs. (20,21,22) give a peak intensity of 1.6×10^{13} W/cm^2, an electron density of 6.8×10^{15} cm^{-3} and a filament size of $w_0 = 110$ µm.

Becker et al. (2001a) have analyzed the fluorescence spectra of nitrogen molecules at different gas pressures and impinging laser pulse energies. From the saturation of the signal, they obtained evidence of an intensity clamping in agreement with the rough estimation given by Eq. (20). Kasparian et al. (2000a) used a similar model to estimate the saturation intensity within a filament, the only difference being that they neglect the contribution of diffraction, which is valid when the pulse input peak power exceeds several P_{cr}.

Nibbering et al. (1996) introduced the model of self-guiding to explain the conical emission characterizing femtosecond filaments as a Cerenkov radiation in a leaky waveguide. Originally, the self-guiding model referred to the unbalanced competition between self-focusing and plasma defocusing, due to the energy losses. It was interpreted in terms of a leaky waveguide consisting in a weakly ionized inner core surrounded by a dynamic cladding. The cladding was proposed to bring an additional supply of energy to compensate the leakage in the core.

The main extensions of these models are detailed below: The dynamic spatial replenishment model (Mlejnek et al., 1998a) proposes an unsteady balance between the nonlinear physical effects involved in filamentation while two conical wave models were proposed as complementary interpretations of filamentation highlighting the key roles of GVD (Conti et al., 2003) and nonlinear losses (Dubietis et al., 2004a) in reshaping the pulse into a stationary wavepacket. Up to date, these effects have been considered separately. This led to the discovery of nonlinear X-waves which constitute stationary nonlinear wavepackets in dispersive but lossless media (Conti et al., 2003), and to the discovery of unbalanced Bessel beams which are stationary and nonlinear monochromatic wavepackets fully supporting an energy flow directed toward the core of the beam, where nonlinear losses occur (Dubietis et al., 2004a; Porras et al., 2004).

2.1.3. Dynamic spatial replenishment

The dynamic spatial replenishment was initially proposed by Mlejnek et al. (1998a, b) as an elucidation of the self-guiding and the moving focus models (Mlejnek et al., 1999b). Since the cartoon shown in Fig. 6 only deals with spatial effects induced by self-focusing and plasma generation, it somewhat oversimplifies the phenomena occurring in filamentation. Numerical simulations of pulse filamentation uncovered its full dynamical picture. Self-focusing forms a leading peak in the pulse which generates a plasma in its wake. The trail of the pulse is then defocused and the leading peak simultaneously becomes less intense owing to multiphoton absorption. Subsequently plasma generation is turned off, thus allowing the beam to shrink again upon itself due to the still active self-focusing effect (Mlejnek et al., 1998a, 1999b, c, 2001; Moloney et al., 2000). This scenario can repeat many times until the pulse power becomes insufficient for refocusing, thereby allowing a long range propagation (see Fig. 16).

2.1.4. Spatial soliton and light bullets

A temporal optical soliton is a nonlinear wave for which self-phase modulation exactly compensate dispersion during its propagation. In addition, it has specific particle-like interaction properties. Laser pulses taking the shape of temporal solitons are well known to exist in one-dimensional systems such as optical fibers. The concept of spatial solitons is similar to that of temporal solitons except that nonlinear spatial effects compensate diffraction. It has long been recognized that self-focusing can compensate for the spreading of the beam owing to diffraction: the Townes mode represents the equilibrium solution (Chiao et al., 1964). The resulting balance, however, is unstable in more that one
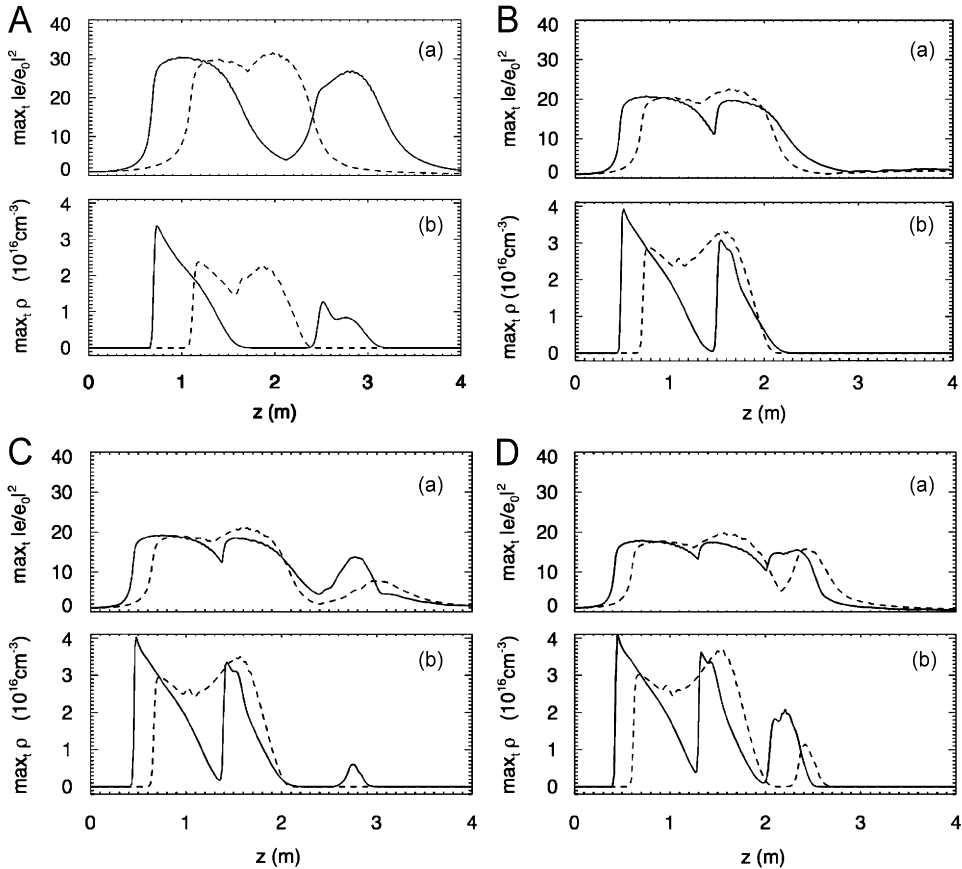
Fig. 16. (a) On-axis peak intensity and (b) peak electron density vs. propagation distance for $P_{in}/P_{cr} = 4$ (A), 6 (B), 6.5 (C) and 7 (D). The continuous curves correspond to the inclusion of the Raman–Kerr contribution in the model while for the dashed curves, it is omitted. From Mlejnek et al. (1999c).

dimension, in the sense that either the beam diffracts at low power or it collapses or breaks into multiple filaments at higher power (Shen, 1984). Before the break-up of a beam with power above the critical power, the collapse of a self-focusing beam in a Kerr medium is a self-similar process during which the beam takes the form of a Townes mode as recently observed by Moll et al. (2003), without reaching an equilibrium. When the beam is sufficiently intense, additional defocusing mechanisms such as plasma defocusing or high order saturation of the nonlinear index compete with the self-focusing due to the Kerr effect, therefore suggesting the possibility of the formation of a steady spatial soliton if a strict balance between these effects is achieved. Extending this idea, it has been proposed that the nonlinear propagation of powerful laser pulses in cubic Kerr media could form the so-called spatiotemporal solitons or light bullets (see Wise and Di Trapani, 2002 for a review), which generalizes the notion of spatial solitons. In this case, under suitable conditions, the nonlinearity acting in space through self-focusing and in time through self phase modulation, might compensate diffraction and dispersion simultaneously to produce a soliton in space and time. Despite these predictions, no spatio-temporal soliton has ever been observed yet in any real physical system. The claim made by Koprinkov et al. (2000) turned out to be unjustified (Gaeta and Wise, 2001; Koprinkov et al., 2001). Although the concept is obviously interesting, several reasons make the observation of such structures rather unlikely. First, the formation of a spatiotemporal soliton competes with modulational instabilities that can occur in one or several dimensions and tend to destroy the structure. Second, even if a spatio-temporal soliton constitutes a specific solution to a given model, neglected physical effect always present in real physical systems such as e.g. absorption can prevent the structure to propagate over more than a typical length for diffraction or dispersion (Chen et al., 2004). Despite its long range propagation property with a long living hot core, the self-channeling of intense laser pulses is a dynamical process
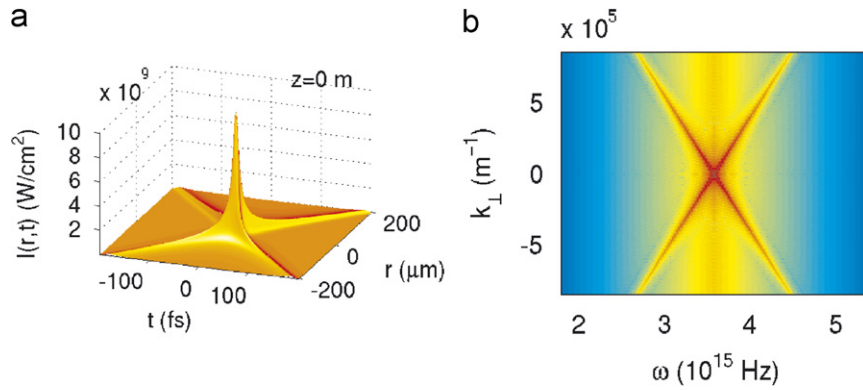
Fig. 17. (a) Near field (r, t) profile of an X-wave. (b) Far-field $(k_\perp, \omega)$ of the X-wave shown in (a).

involving a strong reorganization of the pulse structure and is therefore incompatible with the notion of spatiotemporal soliton. A nearly spatial soliton could be identified in the self-channeling process, i.e., a specific time slice of the pulse seems to be frozen over long distances when dispersion is sufficiently weak; This time slice, however was shown to be structurally unstable, i.e. destroyed by realistic dispersion, and the remaining part of the pulse diffracts (Bergé and Couairon, 2001a), which rules out the possibility of a genuine soliton propagation.

2.1.5. Conical X-waves

X-waves are peculiar wavepackets propagating without undergoing the natural spreading due to diffraction or dispersion. They are known in the context of linear acoustics (Lu and Greenleaf, 1992a, b, 1994; Stepanishen and Sun, 1997; Stepanishen, 1999; Salo et al., 1999) or electromagnetic propagation (Salo et al., 2000; Reivelt and Saari, 2000), and constitute the polychromatic generalization of diffraction-free Bessel beams (Durnin et al., 1987). Measurements of the whole three-dimensional distribution of the field of optical X waves in free space were performed by Saari and Reivelt (Saari and Reivelt, 1997). These waves are called Bessel-X waves or conical waves in general because they possess an intense core surrounded by extended feet storing a large amount of energy and their feet are shaped as a cone (or an X if only one transverse dimension is considered) both in the near field (r–t domain) and in the far field (k–ω domain). It has been long believed that conical waves are intrinsically nonparaxial objects because all known solutions were obtained for nonparaxial propagation equations while the corresponding paraxial approximations involved some loss of stationarity (Salo et al., 2000). Paraxial envelope X-waves were recently reported (Porras et al., 2003a,b), however, as stationary solutions to the paraxial propagation equation in a dispersive medium:

$$\frac{\partial \mathcal{E}}{\partial z} = \frac{i}{2k} \varDelta_\perp \mathcal{E} - i\frac{k''}{2}\frac{\partial^2 \mathcal{E}}{\partial t^2}, \tag{23}$$

where the first term on the right hand side accounts for diffraction in the transverse plane and the second term accounts for GVD, t being the retarded time in the reference frame of the pulse. Solutions in the form

$$\mathcal{E}(r, t) = \frac{1}{2\pi} \int d\omega\, f(\omega) J_0(\sqrt{kk''}|\omega|r) \exp(-i\omega t), \tag{24}$$

where $f(\omega)$ is any narrow spectral function, constitutes a weakly localized stationary solution of Eq. (23). In the space–time domain, this solution possesses a narrow core and extended feet forming a cone with angle determined by the material dispersion (see Fig. 17(a)). In the far field, the solution is also conical since its $(k_\perp, \omega)$ spectrum follows:

$$k_\perp^2 = kk''\omega^2, \tag{25}$$

where ω here denotes the frequency detuning from the central frequency (see Fig. 17(b)). A more general family of envelope linear modes in the form of X-waves was shown to exist (Porras and Di Trapani, 2004), having a stationary intensity in some reference frame (possibly different from that traveling at the group velocity of the carrier frequency) and the two branches of the X in the $(k_\perp, \omega)$ space separated by either a gap in frequency or a gap in wavenumber.
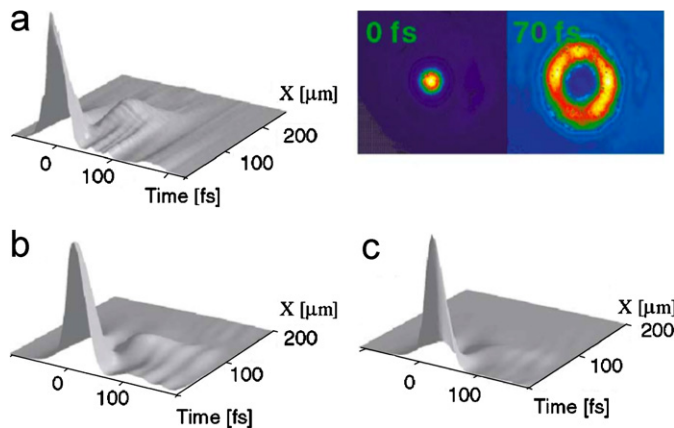
Fig. 18. (a) Measured spatiotemporal intensity profile exhibiting the spontaneous formation of an X-shaped nonlinear conical wave in a Lithium triborate crystal. The profile was measured 5 mm beyond the output face of the 22 mm long crystal. The inset shows the transverse intensity patterns measured for the time slices at peak ($t = 0$ fs) and at $t = 70$ fs. (b) counterpart of the profile in (a), obtained from numerical simulation. (c) As in (b), calculated right on crystal output. From Di Trapani et al. (2003).

The recent understanding of the unique and unexpected theory of space–time focusing in quadratic media giving rise to second harmonic generation allowed an extension of the concept of X-waves in the nonlinear regime (see Dubietis et al., 2006b; Conti et al., 2007, for a review). X-waves were shown to be spontaneously generated from conventional localized pulses in $\chi^{(2)}$ media (Valiulis et al., 2001; Di Trapani et al., 2003) as well as in Kerr media (Faccio et al., 2005a, b). Fig. 18 shows the first measurements of nonlinear X-waves in the field of nonlinear optics. These measurements were corroborated by the theoretical identification of stationary conical wavepackets in the form of X-shaped nonlinear waves (Conti et al., 2003).

Femtosecond filaments share many of the features of X-waves. X-shaped waves both in the far-field and in the near field were measured in experiments on filamentation in liquids and solids (Faccio et al., 2005a, b). Numerical integration of models for filamentation which will be presented below uncovered the possible role of X-waves as attractors within a more complicated dynamics during filamentation (Kolesik et al., 2004, 2005; Couairon et al., 2006c). The concept of X-waves plays therefore an important role since it looks very promising for the interpretation of filamentation.

2.1.6. Conical unbalanced Bessel beams

Recently, Dubietis et al. (2004a) proposed an interpretation of filamentation in condensed media based on a scenario featuring a long range stationarity of the hot core of the beam despite the presence of losses. The model describes the propagation of a monochromatic laser pulse undergoing self-focusing, diffraction and multiphoton absorption only, without considering any saturating nonlinearity, plasma defocusing or dispersive effects which were usually introduced to counteract the Kerr self-focusing. Sirutkaitis et al. (2003) showed from numerical simulations that this model is relevant to capture the robustness of the filament against nonlinear losses and its long range propagation, even if the defocusing action of the plasma is neglected. The role of the energy reservoir, which surrounds the hot core, as a loss replenishment mechanism was already pointed out from simulation results by Mlejnek et al. (1999a) or from experiments by Courvoisier et al. (2003). However, the active role of nonlinear losses in producing a locally balanced regime and a seemingly stationary propagation of the hot core was identified by Dubietis et al. (2004a). Nonlinear losses generate a flux of radiation towards the core of the beam and a nonlinear phase shift, mediated by propagation, which precisely counteracts that produced by Kerr self-focusing. Overall, this model interprets the filamentation dynamics as leading to a conical beam structure composed of a central hot core which experiences nonlinear interaction with matter, and of a slowly decaying Bessel like tail which provides the large energy reservoir. In contrast with conventional Gaussian beams, energy flows from a cone shaped surface toward the center and replenishes the hot core owing to a coherent interference effect similar to the Arago spot experiment. Nonlinear losses can be considered as a smooth stopper extended along the optical axis which continuously adds conical components to the beam while it propagates (see Gaižauskas et al., 2007, for a review). The stationary beam supported by the refilling process which drives the

energy from the tails to the intense core was identified as a nonlinear unbalanced Bessel beam (Porras et al., 2004). Other effects such as plasma defocusing, chromatic dispersion, nonlinearity saturation, usually considered to counteract the Kerr-induced SPM are not strictly necessary for the establishment of the stationary regime proposed in this model. However, this does not mean that they play a negligible role in real settings. The previous section showed that nonlinear X-waves were introduced as the stationary wavepackets of an analogously simplified model accounting for Kerr self-focusing, diffraction and chromatic dispersion only. Both scenarios are characterized by a stationary solution in the form of a conical wavepacket. NLX waves indicate the key role of GVD while UBB indicate the key role of nonlinear losses. A stationary wavepacket also accounting for the other effects mentioned above, presumably playing the role of an attractor for the dynamics of ultrashort pulse filamentation, has not been found yet. It is however expected to belong to the family of conical wavepackets since this conjecture is true by considering separately either nonlinear losses or GVD among the effects playing a role.

2.1.7. Interpretations of the conical emission

Several interpretations of the conical emission (CE) associated with filamentation have been proposed in the literature. As for the various interpretations of the self-guiding mechanism itself, the authors believe that all interpretations of the conical emission present a different facet of the problem and should combine into a unified description. Here, four different interpretations are reviewed.

In the early nineties, several theoretical studies were performed to demonstrate the arrest of collapse by normal GVD leading to pulse splitting. To this aim, the minimal model capturing the essence of the physics is a nonlinear Schrödinger equation including a cubic Kerr nonlinearity and normal GVD. Luther et al. (1994b) predicted that this model induce a four wave interaction that promotes a transport of energy from the band of wave trains $(\mathbf{k}, \omega)$ to sidebands $(\mathbf{k} \pm k_\perp, \omega \pm \Omega)$, closely related to those of the modulational instability of the uniform plane-wave solutions (Liou et al., 1992; Couairon and Bergé, 2000). Phase matching for a maximum instability growth rate requires that the linear diffraction and dispersion terms cancel for the signal and the idler, which yields precisely Eq. (25). A consequence of the growth of these new spectral features is the appearance of frequency-shifted off-axis radiation in the far-field of the pulse which appears as a colored ring. Thus, this four-wave mixing process was shown to be responsible for the pulse splitting due to GVD and to induce a spatio-temporal dynamics resulting in conical emission. According to Golub (1990), the phase matching conditions of the four wave mixing process $2\mathbf{k}(\omega) = \mathbf{k}_{\text{blue}} + \mathbf{k}_{\text{red}}$ predict an inverse spatial order of the emitted photons in the observed conical emission.

On the other hand, a Čerenkov type process was proposed to interpret conical emission (Golub, 1990). In this case, the polarization generated by the filament in the medium, propagating at the laser pulse group velocity v_{gr} results in an emission at frequencies fulfilling a Čerenkov condition at conical angle θ given by $\cos \theta = v_{\text{ph}}/v_{\text{gr}}$, where $v_{\text{ph}} \equiv c/n(\omega)$ is the phase velocity of the emitted light. The dispersive properties of the medium select each Fourier component of the nonlinear polarization to emit at a specific angle. In fact, a similarity exist between the condition for Čerenkov emission by a source moving along the interface between the plasma channel and the gas and the refraction laws of light at this boundary. This is the origin of the proposition of a leaky waveguide by Nibbering et al. (1996) to explain simultaneously the self-guiding and the conical emission phenomena associated with filamentation. The leaky waveguide has a weakly ionized core (the plasma channel) and a surrounding cladding. The refractive index of the core is smaller than that of the cladding due to the sharp interface of the plasma whose density scales as the eighth power of the intensity. The core is narrower than the cladding by a factor of three ($\sqrt{8} \sim 2.8$).

An interpretation relying only on self-phase modulation was proposed by several authors (Kosareva et al., 1997a, b; Chin et al., 1999a; Kandidov et al., 1997a; Golubtsov et al., 2000, 2001). The measured conical emission angle was found to be increasing with decreasing wavelength and to be independent of the position along the filament. These features were qualitatively reproduced by simulations considering the optical Kerr effect and plasma generation as the single polarization sources, see Fig. 19 and Kosareva et al. (1997a). Eq. (10) and its counterpart (26) below allowed the following qualitative interpretation of CE:

$$\delta k_\perp(t) = \frac{\mathrm{d}\phi}{\mathrm{d}r} \sim \frac{\omega_0 z}{c} \left(-n_2 \frac{\partial I(r, t)}{\partial r} + \frac{1}{2n_0 \rho_c} \frac{\partial \rho(r, t)}{\partial r} \right). \tag{26}$$

The front of the pulse, where plasma can be neglected, induces a redshift associated with a positive $\delta k_\perp(t)$, i.e. converging toward the filament axis, while the contribution of the plasma in the trail of the pulse leads to a blue-shift associated with a negative radial phase derivative. Hence the CE is interpreted as a divergence of the anti-Stokes components of
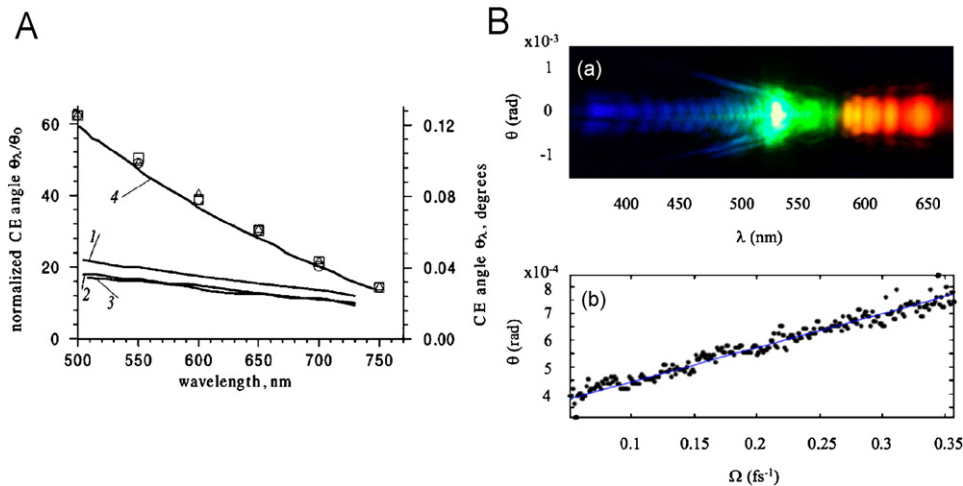
Fig. 19. (A) Measured (symbols) and calculated (curves) conical emission angles at various positions along the filament generated by a 10 mJ, 250 fs, 800 nm laser pulse: triangles: 40 m; circles: 50 m; squares: 60 m. A smaller beam was used in the simulations (170 μm instead of 3.5 mm); the CE angle in curves 1–3 was calculated at distances giving the same ratio with the diffraction length as in the experiment. From the computed distribution of the electric field in space and time, multiplication of the temporal phase by a factor of 2 led to Curve 4 and to a good agreement between calculations and experiments. According to Kosareva et al. (1997a). (B) (a) Measured θ, λ spectra (in real colors) for a filament in air with an input pulse of 200 fs duration, 527 nm central wavelength and $E_{in} = 3$ mJ. (b) points of maximum CE gain taken from (a). The solid line corresponds to the best linear fit. From Faccio et al. (2006c).

the supercontinuum induced by the plasma (Kandidov et al., 2004b; Kosareva et al., 2003). No conical emission was found at Stokes shifted wavelengths (Kosareva et al., 1997a). Note that the good agreement between measurements and simulations (curve 4 in Fig. 19) was obtained by artificially increasing the temporal dependence of the nonlinear phase, for example by using larger ionization rates. Although the dispersive properties of the medium do not enter in this interpretation, a better agreement was later obtained by including dispersion in the model (Golubtsov et al., 2001; Kandidov et al., 2003a), while the contribution of other effects directly modifying SPM such as the Raman–Kerr effect or the self-steepening effect is modifying the cone angle obtained from numerical simulations by a few percent only (Golubtsov and Kosareva, 2002).

Finally, the phenomenon of conical emission was revisited and reinterpreted using the paradigm of X-waves. The claim of the connection between conical emission and Nonlinear X-waves was proposed for the first time by Conti et al. (2003). The angular dispersion of colored conical emission associated with filamentation was measured for different media (water, lithium-triborate and air) by Faccio et al. (2006c). The chromatic dispersion of the material was shown to play a key role in the determination of the cone angle of CE that follows Eq. (25). These measurements are in complete agreement with the interpretation of CE as a manifestation of the spontaneous generation of nonlinear X-waves (Conti et al., 2003; Faccio et al., 2005a, b). In addition, this interpretation supported by the results of numerical simulations (Kolesik et al., 2004; Couairon et al., 2006c), was shown to be consistent with the interpretation in terms of a Čerenkov like process, i.e. leading to the same prediction for the frequency dependence of the cone angle (Faccio et al., 2006c).

2.2. Model equations governing the nonlinear propagation of laser pulses and filamentation

In order to capture the physics of filamentation of ultrashort laser pulses in air and more generally in gases, solids and liquids, several teams have developed propagation codes based on various unidirectional propagation equations (see e.g. Moloney and Kolesik, 2007; Couairon and Mysyrowicz, 2006; Chin et al., 2005, for a review). The first numerical simulations in this field started with a minimal model in the form of a nonlinear Schrödinger equation describing the pulse propagation and catching the essential of the physics without developing heavy numerical tools. The influence of various physical effects were later on studied theoretically and numerically by adding source terms to this model. Here, the presentation follows the historical development of this model, which has become a standard in the field.

Recently, Kolesik and Moloney (2004a) have shown that a general unidirectional pulse propagation equation allows the derivation of all models that have been previously used in femtosecond filamentation as well as in other fields dealing with the propagation of laser pulses.

From Maxwell equations and constitutive equations for the medium, a vector wave equation governing the evolution of the laser pulse in a transparent nonlinear medium reads:

$$\nabla^2 \mathbf{E} - \nabla(\nabla \cdot \mathbf{E}) - \frac{1}{c^2} \frac{\partial^2}{\partial t^2} \int_{-\infty}^{t} n^2(\mathbf{r}, t - t') \mathbf{E}(t') \, \mathrm{d}t' = \mu_0 \left(\frac{\partial^2 \mathbf{P}_{\mathrm{nl}}}{\partial t^2} + \frac{\partial \mathbf{J}_{\mathrm{p}}}{\partial t} \right),$$ (27)

where $n^2 = 1 + \epsilon_0 \chi^{(1)}$ is the linear index of refraction due to vacuum and bound electrons, $\chi^{(1)}$ is the linear susceptibility, $\mathbf{P}_{\mathrm{nl}}$ is the nonlinear polarization associated with bound electrons, $\mathbf{J}_{\mathrm{p}}$ is the plasma current density associated with the free electrons (Newell and Moloney, 1992; Liu et al., 2002a; Couairon et al., 2002; Sprangle et al., 2002).

2.2.1. Reduced model

When the laser field is and remains linearly polarized along $\mathbf{e}_x$, the electric field can be decomposed into a carrier wave and an envelope as $\mathbf{E}(x, y, z, t) = \frac{1}{2} \mathcal{E}(x, y, z, t) \exp[\mathrm{i}(kz - \omega_0 t)] \mathbf{e}_x + c.c.$, where z is the propagation direction, k and ω_0 are the central wavenumber and frequency of the laser pulse. A scalar equation of nonlinear Schrödinger type is then obtained by neglecting the vectorial operator $\nabla(\nabla \cdot)$ and using the reference frame of the pulse ($z, t = t_{\mathrm{lab}} - z/v_g(\omega_0)$) where $v_g(\omega_0) \equiv \partial \omega / \partial k|_{\omega_0}$ denotes the group velocity:

$$\frac{\partial \mathcal{E}}{\partial z} = \frac{\mathrm{i}}{2k} \Delta_\perp \mathcal{E} + \mathrm{i} k_0 n_2 |\mathcal{E}|^2 \mathcal{E} - \mathrm{i} \frac{k_0}{2n_0} \frac{\rho}{\rho_c} \mathcal{E}.$$ (28)

Here, the linear refraction index n_0 has been assumed to be constant. Eq. (28) describes the forward propagation of the slowly varying envelope $\mathcal{E}(x, y, z, t)$ of the pulse in the paraxial approximation, i.e., the terms $\partial^2/\partial z^2$ and $\partial^2/\partial z \partial t$ have been neglected. The first term on the right hand side (rhs) of Eq. (28) accounts for diffraction within the transverse plane with $\Delta_\perp \equiv \partial^2/\partial x^2 + \partial^2/\partial y^2$. The second term accounts for the optical Kerr effect. Its dependence comes from the nonlinear polarization $\mathbf{P}_{\mathrm{nl}}$ which reads at the dominant third order for a centro-symmetric medium:

$$\mathbf{P}_{\mathrm{nl}} \equiv \epsilon_0 \chi^{(3)} |\mathbf{E}|^2 \mathbf{E} \quad \text{where } \chi^{(3)} = 4\epsilon_0 c n_2 n_0^2 / 3.$$ (29)

The Kerr term in Eq. (28) is obtained by introducing the carrier-wave decomposition in Eq. (29). To obtain the plasma defocusing term in Eq. (28), this decomposition is also introduced in the evolution equation for the plasma current density:

$$\frac{\partial \mathbf{J}_{\mathrm{p}}}{\partial t} = -\frac{e^2}{m_e} \rho \mathbf{E},$$ (30)

where ρ denotes the electron density and $\rho_c \equiv \epsilon_0 m_e \omega_0^2 / e^2$, the critical plasma density above which the plasma becomes opaque ($\rho_c = 2 \times 10^{21} \, \mathrm{cm}^{-3}$ at 800 nm). Therefore, the model takes into account the main physical effects proposed to be responsible for the *self-channeling* of ultrashort laser pulses in air by Braun et al. (1995). We adopt the convention that $I \equiv |\mathcal{E}|^2$ is an intensity expressed in W/cm^2 so as to make the product $n_2|\mathcal{E}|^2$ dimensionless. Eq. (28) must be solved simultaneously with the equation describing the evolution of the density of electrons mainly generated by photoionization:

$$\frac{\partial \rho}{\partial t} = \sigma_K |\mathcal{E}|^{2K} \rho_{\mathrm{at}},$$ (31)

where it is assumed here that photoionization occurs in the multiphoton regime. The quantity σ_K denotes the coefficient of the multiphoton ionization rate $W_{\mathrm{MPI}} = \sigma_K I^K$ involving K photons, where $K \equiv \langle U_i/\hbar\omega_0 + 1 \rangle$, U_i denotes the ionization potential of the medium and ρ_{at}, the density of neutral atoms.

Since Eq. (28) generally describes the propagation of a laser pulse in a Kerr medium coupled to ionization of the medium, this model was actually proposed before the discovery of femtosecond *self-channeling* (Braun et al., 1995). For instance, it was used to study laser induced breakdown in water (Feng et al., 1995) where, instead of Eq. (31), an evolution equation accounting for avalanche ionization and recombination was proposed. For short pulses,

multiphoton ionization constitutes the prevailing mechanism for plasma generation. Model (28–31) was therefore used in the early numerical works on femtosecond filamentation (Braun et al., 1995; Brodeur et al., 1997; Kosareva et al., 1997a; Kandidov et al., 1997b; Lange et al., 1998c; Chiron et al., 1999; La Fontaine et al., 1999b).

2.2.2. Initial pulse

Initial conditions must be given to start the propagation. The most common input pulses are Gaussian with a temporal half width t_p. The input beams are modeled by collimated or focused Gaussian profiles with peak input intensity I_0, transverse waist w_0, input peak power $P_{in} = \pi w_0^2 I_0/2$ and energy $E_{in} = P_{in} t_p \sqrt{\pi/2}$.

$$\mathcal{E}(x, y, t, 0) = \sqrt{I_0} \exp\left[-\frac{x^2 + y^2}{w_0^2} - i\frac{kr^2}{2f} - \frac{t^2}{t_p^2} - iCt^2\right]. \tag{32}$$

When the beam is focused, the curvature radius f of the beam and the focusing distance d are related by the relation:

$$f = d + z_f^2/d, \tag{33}$$

where $z_f = kw_f^2/2$ denotes the Rayleigh length associated with the beam waist w_f and

$$w_f \equiv \frac{w_0}{\sqrt{1 + L_{DF}^2/f^2}}. \tag{34}$$

A chirp C may be added to the pulse. It is linked to the pulse temporal duration $t_p(C)$ and the pulse minimal duration $t_p(0)$ by

$$C = \pm\frac{\sqrt{[t_p(C)/t_p(0)]^2 - 1}}{t_p^2(C)}. \tag{35}$$

Different input beams have been used to mimic experiments including super-Gaussian beams (Couairon et al., 2002; Fibich et al., 2005b), flat Gaussian beams (Gori, 1994), diaphragmed beams (Couairon et al., 2006b; Méchain et al., 2004b), possibly with perturbations or noise (Méchain et al., 2004a; Fibich et al., 2005a), or measured beam profiles (Couairon et al., 2002; Méchain et al., 2004a, 2005a). Various temporal profiles for the input pulses have also been considered. Note that for non-Gaussian beams or pulses, the relation between waist, power, energy and pulse duration must be adapted, and the collapse distance given by Eq. (5) is no longer valid. For example with a super Gaussian beam $\mathcal{E}(x, y, t, 0) = \sqrt{I_0} \exp(-r^n/w_0^n)$, where $r^2 = x^2 + y^2$, the input power is given by $P_{in} = 2\pi w_0^2 I_0 \Gamma(2/n)/n2^{2/n}$ where Γ denotes the gamma function (Abramowitz and Stegun, 1972)

2.2.3. Raman–Kerr effect

With femtosecond pulses which have inherent large bandwidths, an ensemble of low-frequency rotational and/or vibrational modes are excited. This mechanism is described by a three-level nonresonant process for the interaction of the laser field with a molecule, between a nonpopulated higher energy state and two lower energy rotational states. It is similar to two parametrically excited bound nonlinear oscillators, which leads to a noninstantaneous optical polarization. In this case, the interaction of the laser with the dipole moments of the molecular constituents of air generates the same frequency dependent nonlinear refraction index as that obtained quantum mechanically (Ackerhalt and Milonni, 1986; Hickman and Bischel, 1988; Peñano et al., 2003; Azarenkov et al., 1991, 1993).

For sufficiently long pulses, it can be shown that the nonlinear polarization can be represented as

$$\mathbf{P}_{nl} = \epsilon_0 Q_R(t)\mathbf{E},$$

where the Raman response function $Q_R(t)$ is determined by

$$\frac{\partial^2 Q_R}{\partial t^2} + 2\Gamma\frac{\partial Q_R}{\partial t} + \Omega^2 Q_R = \omega_R\frac{\Omega_R^2}{\Omega_0}\frac{|E|^2}{E_0^2}, \tag{36}$$

where $\Omega^2 = \omega_R^2 + \Gamma^2$, ω_R is the fundamental rotational frequency, Γ is the phenomenological damping rate, with $\Omega_R = \mu E_0/\hbar$, the Rabi frequency associated with the peak laser amplitude E_0, μ is the dipole transition moment matrix

element associated with transitions to the excited state and Ω_0 is the frequency associated with transition from the higher to one of two lower energy states. The validity range of this description is $t_p \gg \Omega_R^{-1}$. The Raman response function reads as

$$Q_R(t) = 2\alpha n_2 n_0 \int_0^t \mathcal{R}(t - t')|E(t')|^2 \, dt',$$ (37)

where $\mathcal{R}(t) = \Omega^2 \omega_R^{-1} \sin(\omega_R t) \exp(-\Gamma t)$ and $\alpha n_2 = \omega_R \Omega_R^2/n_0 \Omega^2 \Omega_0 E_0^2$ denotes the fraction of the delayed Raman–Kerr component in the Kerr effect. The third order nonlinear polarization $\mathbf{P}_{nl}(t)$ can be approximated in the electric dipole approximation by including the instantaneous as well as the delayed Kerr response:

$$\mathbf{P}_{nl}(t) = \epsilon_0 2n_0 n_2 \left[(1 - \alpha)I(t) + \alpha \int_0^{+\infty} I(t - \tau)\mathcal{R}(\tau) \, d\tau \right] \mathbf{E}(t).$$ (38)

Another interesting effect associated with the Raman–Kerr effect is the revival of the nonlinear Kerr effect. The short pulse initially excites a limited number of in phase ortho-vibrational quantum modes. Each mode evolves according to its eigenfrequency, leading to a fast decay of the retarded response, the exponential term above (free induction decay). However, because of the limited number of modes, a spontaneous revival of the nonlinear response due to the rephasing of the orthovibrational modes occurs several picoseconds after the pump (Ripoche et al., 1997; Nibbering et al., 1997).

2.2.4. Model including group velocity dispersion, Raman contribution, plasma and multiphoton absorption, avalanche and recombination

Model (28)–(31) was extended by taking into account additional physical effects as source terms for the propagation equation as well as for the electron generation equation:

$$\frac{\partial \mathcal{E}}{\partial z} = \frac{i}{2k} \left(\frac{\partial^2}{\partial x^2} + \frac{\partial^2}{\partial y^2} \right) \mathcal{E} - i\frac{k''}{2} \frac{\partial^2 \mathcal{E}}{\partial t^2} + N(|\mathcal{E}|^2, \rho)\mathcal{E},$$ (39)

$$N(|\mathcal{E}|^2, \rho) = N_{\text{Kerr}}(|\mathcal{E}|^2) + N_{\text{Plasma}}(\rho) + N_{\text{MPA}}(|\mathcal{E}|^2),$$ (40)

$$N_{\text{Kerr}}(|\mathcal{E}|^2) = ik_0 n_2 (1 - \alpha)|\mathcal{E}(x, y, z, t)|^2 + ik_0 n_2 \alpha \int_{-\infty}^t \mathcal{R}(t - \tau)|\mathcal{E}(x, y, z, \tau)|^2 \, d\tau,$$ (41)

$$N_{\text{Plasma}}(\rho) = -\frac{\sigma}{2}(1 + i\omega_0 \tau_c)\rho,$$ (42)

$$N_{\text{MPA}}(|\mathcal{E}|^2) = -\frac{\beta_K}{2}|\mathcal{E}|^{2K-2} \left[1 - \frac{\rho}{\rho_{\text{at}}} \right].$$ (43)

The evolution of the electron density entering in Eq. (42) is governed by

$$\frac{\partial \rho}{\partial t} = \sigma_K |\mathcal{E}|^{2K}(\rho_{\text{at}} - \rho) + \frac{\sigma}{U_i}\rho|\mathcal{E}|^2 - a\rho^2.$$ (44)

For clarity, the dependence of the electric field envelope $\mathcal{E}$ and electron density ρ on (x, y, z, t) was explicitly mentioned only in Eq. (41). The second term on the rhs of Eq. (39) accounts for group velocity dispersion with coefficient $k'' \equiv \partial^2 k/\partial \omega^2|_{\omega_0}$. The last term on the rhs of Eq. (39) accounts for nonlinearity induced by the optical Kerr effect, the plasma and multiphoton absorption (MPA) [see Eq. (40)]. The Kerr term (41) is split into an instantaneous component due to the electronic response in the polarization and a delayed component, of fraction α, due to stimulated molecular Raman scattering (Ripoche et al., 1997). The function $\mathcal{R}(t)$ mimics the molecular response with a characteristic time Γ^{-1} and frequency ω_R:

$$\mathcal{R}(t) = \mathcal{R}_0 \exp(-\Gamma t) \sin \omega_R t,$$ (45)

where $\mathcal{R}_0 = (\Gamma^2 + \omega_R^2)/\omega_R$. In air at 800 nm, $\Gamma^{-1} = 70$ fs and $\omega_R = 16$ THz. The plasma term (42) accounts for plasma absorption (real part) and plasma defocusing (imaginary part). The cross section σ for inverse Bremsstrahlung follows

the Drude model (Yablonovitch and Bloembergen, 1972) and reads:

$$\sigma = \frac{k_0}{n_0 \rho_c} \frac{\omega_0 \tau_c}{(1 + \omega_0^2 \tau_c^2)}, \tag{46}$$

where τ_c is the electron collision time. In air, $\tau_c = 350$ fs and $\sigma = 5.1 \times 10^{-18}$ cm^2. Therefore $\tau_c \gg \omega_0^{-1}$, and in this limit, the defocusing term can be expressed as a function of the critical plasma density as in Eq. (28) $\sigma \omega_0 \tau_c \rho \simeq k_0 \rho / n_0 \rho_c$. The MPA term in Eq. (43) accounts for energy absorption due to multiphoton ionization; the coefficient $\beta_K = K \hbar \omega_0 \rho_{at} \sigma_K$ is related to the multiphoton ionization coefficient.

Eq. (44) describes the generation of the plasma by multiphoton ionization with rate $\sigma_K |\mathcal{E}|^{2K}$ and avalanche (multiplication of the electrons in the laser field) with rate $(\sigma/U_i)|\mathcal{E}|^2$. The last term in Eq. (44) represents the mechanisms of plasma recombination (electron captured by ion).

Although it contains several additional physical effects, this model is more simple than Eqs. (28)–(31) to deal with numerically. The reason is that in Eq. (28) plasma defocusing stops the collapse of the beam on itself but generates very steep temporal gradients requiring a high numerical resolution whereas the additional effects, even small, are sufficient to regularize the propagation. The model (39)–(44) is therefore extensively used (Mlejnek et al., 1998a, b, 1999a–c, 2001; Moloney et al., 2000; Aközbek et al., 2000; Schwarz et al., 2000; Tzortzakis et al., 2001a).

2.2.5. Model including shock terms, photoionization

Brabec and Krausz (1997) proposed an envelope equation modeling the propagation of pulses of a few optical cycles (2.7 fs at 800 nm). The main idea in the derivation of this equation, called the *nonlinear envelope equation* consists in assuming that the pulse envelope is slowly varying in the propagation direction z, but not in time. In this way the cross derivative $\partial^2/\partial z \partial t$ (appearing in the wave equation (27) when the change of reference frame $t = t_{lab} - z/v_g$ is performed), is kept whereas $\partial^2/\partial z^2$ is still neglected. This introduces additional terms corresponding to optical shocks (Zozulya et al., 1998, 1999; Gaeta, 2000). An equivalent formulation in the frequency domain was proposed by Bespalov et al. (2002). All high-order dispersive terms can be also retained in the propagation equation when it is written in the frequency domain corresponding to the retarded time $t \equiv t_{lab} - z/v_g$ (Gaeta, 2000; Tzortzakis et al., 2001d; Couairon et al., 2002; Sprangle et al., 2002; Méchain et al., 2004b):

$$U \frac{\partial \hat{\mathcal{E}}}{\partial z} = \frac{i}{2k} \left[\Delta_\perp + \frac{n^2(\omega)\omega^2}{c^2} - k^2 U^2 \right] \hat{\mathcal{E}} + \mathcal{F}\{N(|\mathcal{E}|^2, \rho)\mathcal{E}\}. \tag{47}$$

Here $\hat{\mathcal{E}}(x, y, z, \omega) = \mathcal{F}\{\mathcal{E}(x, y, z, t)\}$, where $\mathcal{F}$ denotes Fourier transform, $U \equiv 1 + (\omega - \omega_0)/kv_g$. It can be readily seen by a small ω expansion that: $(n^2(\omega)\omega^2/c^2 - k^2 U^2)/2kU \simeq k''(\omega - \omega_0)^2/2 + k'''(\omega - \omega_0)^3/6 + \cdots$, which shows that the second term in the rhs of Eq. (47) accounts for GVD at second and higher-orders. The nonlinear terms in Eq. (47) read as

$$N(|\mathcal{E}|^2, \rho) = T^2 N_{Kerr}(|\mathcal{E}|^2) + N_{Plasma}(\rho) + T N_{MPA}(\mathcal{E}). \tag{48}$$

The comparison of Eqs. (47) and (48) with Eqs. (39) and (40) shows that the nonlinear terms are modified by the presence of the operator $T \equiv 1 + i\omega_0^{-1}\partial/\partial t$, which accounts for space–time focusing and self-steepening of the pulse. It describes deviations from the slowly varying envelope approximation (Brabec and Krausz, 1997; Gaeta, 2000; Couairon et al., 2002). This equation is then able to treat pulses of a few fs.

The plasma term is slightly modified so as to include a frequency dependence:

$$N_{Plasma}(\rho) = -\frac{k_0}{2n_0 \rho_c} \frac{\omega_0 \tau_c}{(1 + \omega^2 \tau_c^2)} (1 + i\omega \tau_c)\rho. \tag{49}$$

Another modification concerns the multiphoton absorption term which can be generalized to take into account a photoionization rate $W(|\mathcal{E}|^2)$ that may differ from its multiphoton expression scaling as $|\mathcal{E}|^{2K}$, as indicated in the following expression:

$$N_{MPA}(|\mathcal{E}|^2) = -\frac{W(|\mathcal{E}|^2)U_i}{2|\mathcal{E}|^2}(\rho_{at} - \rho). \tag{50}$$
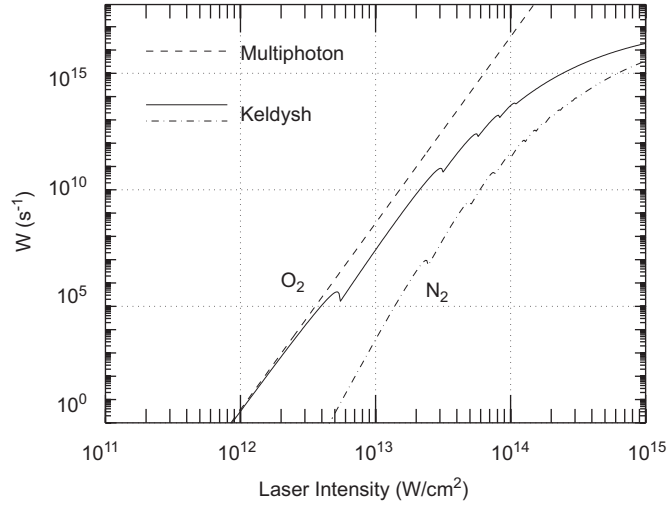
Fig. 20. Ionization rates for oxygen (continuous curve) and nitrogen (dash-dotted curve) vs. laser intensity at 800 nm. The dashed line shows the multiphoton ionization rate of oxygen.

2.2.6. Plasma generation by optical field ionization

Consistently, the evolution equation for the electron density may be slightly generalized in order to describe photoionization not only in the multiphoton regime but also in the tunnel regime valid for high intensities.

$$\frac{\partial \rho}{\partial t} = W(|\mathcal{E}|^2)(\rho_{\text{at}} - \rho) + \frac{\sigma}{U_i}\rho|\mathcal{E}|^2. \tag{51}$$

In Eq. (51), the photoionization rate $W(|\mathcal{E}|^2)$ describes the probability of ionization of an atom with potential U_i (the forbidden band in a solid). For this quantity, the generalized Keldysh–PPT formula (Keldysh, 1965; Perelomov et al., 1966) as well describes the ionization rate in the multiphoton regime, valid for $I \leqslant 10^{13}$ W/cm^2, and the tunnel regime when $I \geqslant 10^{14}$ W/cm^2 (Ammosov et al., 1986). It also covers the intermediate regime which actually is the regime in which infrared femtosecond filamentation takes place. Fig. 20 shows the ionization rates for oxygen and nitrogen computed from the full Keldysh–PPT formulation with a recently determined prefactor for diatomic molecules (Mishima et al., 2002).

The multiphoton ionization rate is plotted in dashed line. Ionization rates from the complete Keldysh–PPT formulation are shown by the continuous curve for oxygen and by the dash-dotted curve for nitrogen. Around 10^{13} W/cm^2 the multiphoton ionization rate for oxygen shown in dashed line exceeds by two decades its counterpart computed from the full Keldysh–PPT formulation.

It should be stressed that Talebpour et al. (1999b) have shown that the PPT formulation applied to oxygen and nitrogen can fit measured ionization rates in the tunnel regime ($10^{13} < I < 10^{15}$ W/cm^2) with a very good agreement by replacing the charge parameter with an effective charge equal to $Z_{\text{eff}} = 0.53$ for oxygen and 0.9 for nitrogen.

2.2.7. Multispecies, multilevel ionization

Kandidov et al. (1993, 1994, 1997b) solved numerically the self-consistent problem of the propagation of a laser pulse in a gas even before the first experiments on femtosecond filamentation were reported. They developed for this pioneering work a model involving multilevel ionization and avalanche, similar to the studies about blueshifting in noble gases (Wood et al., 1991; Rae and Burnett, 1992; Penetrante et al., 1992; Augst et al., 1991; Wood et al., 1993). The evolution equations for the densities ρ_l of the lth ions of charge le read:

$$\frac{\partial \rho_l}{\partial t} = -W_l(|\mathcal{E}|^2)\rho_l + W_{l-1}(|\mathcal{E}|^2)\rho_{l-1} - \sigma_l v_e \rho_e \rho_l + \sigma_{l-1} v_e \rho_e \rho_{l-1}, \quad l = 1, 2 \ldots, \tag{52}$$

where $W_l(|\mathcal{E}|^2)$ denotes the ionization rate of the corresponding species, σ_l is the impact ionization cross-section of the lth ion empirically given by Lotz (1967a, b; 1968a–c), v_e is the oscillatory velocity of an electron in the laser field and the total electron density is given by

$$\rho_e = \sum_l l\rho_l. \tag{53}$$

One of the important results obtained by Kandidov et al. (1994) concerns the saturation phenomenon occurring when a laser pulse propagates in a ionizing medium: When plasma defocusing is described self-consistently as in the models (28), (39) and (47), the peak intensity cannot grow above a few 10^{13} W/cm^2 for infrared wavelengths. Later, this phenomenon was also called *intensity clamping* (Becker et al., 2001a). This intensity is too small to generate a plasma with a ionization degree larger than a few percent for a gas at atmospheric pressure. Therefore, the probability of multiple ionization of a gas and of impact ionization remains low in the conditions of infrared femtosecond filamentation, unless high pressure gradients (gas cell, gas jets) and/or strongly focusing geometries are used.

Multispecies ionization has also been considered in gases such as air. Eq. (51) is replaced by a set of evolution equations for the densities of neutral atoms in the gas. For example in air, simultaneous ionization of oxygen and nitrogen with densities ρ_O and ρ_N are considered:

$$\frac{\partial \rho_O}{\partial t} = -W_O \rho_O, \tag{54}$$

$$\frac{\partial \rho_N}{\partial t} = -W_N \rho_N, \tag{55}$$

where the initial atom densities are $\rho_O(t \to -\infty) = 0.2\rho_{air}$ and $\rho_O(t \to -\infty) = 0.8\rho_{air}$. The electron density is then obtained from $\rho = \rho_{at} - \rho_O - \rho_N$.

Couairon et al. (2002) have found that optical field ionization of air in filamentation regime is modelled by the system (54), (55) or by Eq. (51) with $\rho_{at} = 0.2\rho_{air}$ (the density of oxygen molecules 5×10^{18} cm^{-3} at atmospheric pressure) without significant difference in the resulting electron density. This holds in both cases where the Keldysh–PPT formulation or its multiphoton limit is used for the ionization rates. The reason is that mainly oxygen is ionized in air, modeled as a mixture of oxygen and nitrogen, using Eqs. (54,55). Oxygen is indeed easier to ionize. For instance, for multiphoton ionization of oxygen molecules with the potential $U_i = 12.1$ eV, $K = 8$ photons are necessary to liberate an electron. The coefficient $\sigma_8 = 2.8 \times 10^{-96}$ s^{-1} cm^{16}/W^8 was computed from Keldysh's theory (Keldysh, 1965). A similar calculation for nitrogen with potential $U_i = 15.6$ eV leads to a number of $K = 11$ photons and a coefficient of $\sigma_{11} = 6 \times 10^{-140}$ s^{-1} cm^{22}/W^{11}.

2.2.8. Model including cross phase modulation for elliptically polarized laser pulses

Schjødt-Eriksen et al. (2001) have shown that the polarization state of an elliptically polarized intense femtosecond pulse propagating in a Kerr medium with normal group velocity dispersion affects the arrest of collapse, via pulse splitting, as well as the subsequent propagation. This study raised the question of the influence of the polarization state in femtosecond filamentation. Kolesik et al. (2001) have extended the model (39) to describe filamentation of elliptically polarized pulses. The model was then extended by generalizing Eq. (47) to describe the filamentation of successive, linearly or orthogonally polarized, laser pulses (Couairon et al., 2003).

$$\frac{\partial \mathcal{E}^{\pm}}{\partial z} = \frac{i}{2k} \nabla^2_{\perp} \mathcal{E}^{\pm} - i\frac{k''}{2}\frac{\partial^2 \mathcal{E}^{\pm}}{\partial t^2} + N(|\mathcal{E}^{\pm}|^2, |\mathcal{E}^{\mp}|^2)\mathcal{E}^{\pm}, \tag{56}$$

where $\mathcal{E}^{\pm}$ denote the complex amplitudes of the two circularly polarized components of the electric field. The nonlinear terms read as in Eq. (40) except that the Kerr term is replaced by its counterpart for elliptic polarization:

$$N_{Kerr}(|\mathcal{E}^{\pm}|^2, |\mathcal{E}^{\mp}|^2) = ik_0 n_2 \left\{ (1-\alpha)\left[\frac{2}{3}|\mathcal{E}^{\pm}(t)|^2 + \frac{4}{3}|\mathcal{E}^{\mp}(t)|^2 \right] \right.$$
$$\left. + \alpha \int_{-\infty}^{t} \mathcal{R}(t-\tau)\left[\frac{2}{3}|\mathcal{E}^{\pm}(\tau)|^2 + \frac{4}{3}|\mathcal{E}^{\mp}(\tau)|^2 \right] d\tau \right\}. \tag{57}$$

This model was coupled with Eq. (44) despite experimental evidence that multiphoton ionization rates depend on the polarization state of the light (Petit et al., 2000a), i.e., in the absence of a simple but polarization dependent model for ionization, an isotropic ionization was assumed by Kolesik et al. (2001). This was done by merely introducing the total intensity $|\mathcal{E}|^2 \equiv |\mathcal{E}^+|^2 + |\mathcal{E}^-|^2$ in Eqs. (42), (43) as well as in the ionization rates $W(|\mathcal{E}|^2)$ entering Eq. (44) though the latter were derived for linearly polarized electric fields.

2.2.9. Model including nonparaxial terms and vectorial effects

Fibich and Ilan (2001a, b) have shown that even a small deviation from the assumption that the electric field remains transverse can strongly affect propagation. Therefore:

(i) they reintroduced in the wave equation (27) the usually neglected term $\nabla \cdot \mathbf{E}$ which satisfies

$$\nabla \cdot \mathbf{E} = -\frac{1}{\epsilon_0 n_0^2} \nabla \cdot \mathbf{P}_{\mathrm{nl}};$$
(58)

(ii) they also used a fully vectorial formulation for $\mathbf{P}_{\mathrm{nl}}$,

$$\mathbf{P}_{\mathrm{nl}} = \epsilon_0 \chi^{(3)} [|\mathbf{E}|^2 \mathbf{E} + \frac{\gamma}{\gamma + 1} (\mathbf{E} \times \mathbf{E}^*) \times \mathbf{E}],$$
(59)

where $\gamma = 1/2$ for the case of the optical Kerr effect considered in the other models of this section;
(iii) they took into account the nonparaxial component $\partial_{zz}^2 \mathbf{E}$;
(iv) they finally derived a scalar beam propagation model for the transverse component $\mathcal{E}_1$ of the envelope of the electric field, assumed to be along the x-axis. Note that alternatively, it is also possible to use a vector Hertz formulation of Maxwell equations to describe the vectorial effects as proposed by Milsted Jr and Cantrell (1996). The scalar equation derived by Fibich and Ilan (2001a, b) includes the optical Kerr effect, nonparaxial and vectorial effects:

$$\frac{\partial \mathcal{E}_1}{\partial z} = \frac{\mathrm{i}}{2k} \Delta_\perp \mathcal{E}_1 + \mathrm{i} k_0 n_2 |\mathcal{E}_1|^2 \mathcal{E}_1 + N_{\mathrm{nonparaxial}}(\mathcal{E}_1) + N_{\mathrm{vectorial}}(\mathcal{E}_1),$$
(60)

where

$$N_{\mathrm{nonparaxial}}(\mathcal{E}) = -\mathrm{i} \left[\frac{1}{8k^3} \Delta_\perp^2 \mathcal{E} + k_0 n_2 |\mathcal{E}|^2 \Delta_\perp \mathcal{E} + \frac{n_2}{2n_0 k} (\nabla_\perp \mathcal{E}) \cdot (\nabla_\perp \mathcal{E}^*)(2\mathcal{E} + \mathcal{E}^*) + \frac{k_0 n_2^2}{2n_0} |\mathcal{E}|^4 \mathcal{E} \right],$$
(61)

$$N_{\mathrm{vectorial}}(\mathcal{E}) = \mathrm{i} \frac{n_2}{n_0 k} \left[\frac{4 + 6\gamma}{1 + \gamma} \left| \frac{\partial \mathcal{E}}{\partial x} \right|^2 \mathcal{E} + \left(\frac{\partial \mathcal{E}}{\partial x} \right)^2 \mathcal{E}^* + \frac{1 + 2\gamma}{1 + \gamma} \left(|\mathcal{E}|^2 \frac{\partial^2 \mathcal{E}}{\partial x^2} + \mathcal{E}^2 \frac{\partial^2 \mathcal{E}^*}{\partial x^2} \right) \right].$$
(62)

The vectorial and nonparaxial terms break the revolution symmetry in the propagation equation and are likely to induce a polarization instability leading to multiple filamentation, as shown in Section 3.2.9.

2.2.10. Model including third harmonic generation

Aközbek et al. (2002b) derived a model accounting for third harmonic generation in a filament. The model presented below is an extension of the Aközbek et al. (2002b) model, written in the frequency domain so as to account for space–time focusing and shock terms. The model constitutes a two envelope model with a propagation equation describing the evolution of the fundamental pulse at ω_0 and another describing the evolution of the third harmonic pulse at $3\omega_0$. Nonlinear terms are related to the coupling between the fundamental and its third harmonic.

Let us define the dispersion relation: $k(\omega) = n(\omega)\omega/c$, the wavenumber at the fundamental frequency: $k_{\omega_0} \equiv k(\omega_0)$ and its derivatives $k_{\omega_0}^{(m)} \equiv \frac{\partial^m k}{\partial \omega^m}|_{\omega_0}$, the harmonic frequency $3\omega_0$ the wavenumber of the third harmonic $k_{3\omega_0} \equiv k(3\omega_0)$, and the derivatives $k_{3\omega_0}^{(m)} \equiv \frac{\partial^m k}{\partial \omega^m}|_{3\omega_0}$. The propagation equations for the fundamental and the third harmonic read:

$$\hat{U} \frac{\partial \hat{\mathcal{E}}_{\omega_0}}{\partial z} = \frac{\mathrm{i}}{2k_{\omega_0}} [\nabla_\perp^2 + (k^2(\omega) - k_{\omega_0}^2 \hat{U}^2)] \hat{\mathcal{E}}_{\omega_0} + \mathcal{F}\{N_{\omega_0}(\mathcal{E}_{\omega_0}, \mathcal{E}_{3\omega_0})\},$$
(63)

where $\hat{U}(\omega) \equiv 1 + \frac{k_{\omega_0}^{(1)}}{k_{\omega_0}}(\omega - \omega_0)$.

$$\hat{V}\frac{\partial\hat{\mathcal{E}}_{3\omega_0}}{\partial z} = \frac{i}{2k_{3\omega_0}}[\nabla_\perp^2 + (k^2(\omega) - k_{3\omega_0}^2\hat{V}^2)]\hat{\mathcal{E}}_{3\omega_0} - i\Delta k\hat{\mathcal{E}}_{3\omega_0}$$
$$+ \mathcal{F}\{N_{3\omega_0}(\mathcal{E}_{\omega_0}, \mathcal{E}_{3\omega_0})\}, \tag{64}$$

where

$$\hat{V}(\omega) \equiv 1 + \frac{k_{\omega_0}^{(1)}}{k_{3\omega_0}}(\omega - 3\omega_0), \quad \Delta k = k_{3\omega_0} - k_{\omega_0}. \tag{65}$$

Besides the Kerr, plasma and multiphoton absorption terms given by Eqs. (41), (43), (49) applied to each component, the nonlinearity also includes a cross-phase modulation term (XPM):

$$N_{\omega_0}(\mathcal{E}_{\omega_0}, \mathcal{E}_{3\omega_0}) = [T^2 N_{\text{Kerr}}(|\mathcal{E}_{\omega_0}|^2) + N_{\text{Plasma},\omega_0}(\rho) + TN_{\text{MPA},\omega_0}(|\mathcal{E}_{\omega_0}|^2)]\mathcal{E}_{\omega_0}$$
$$+ T^2 N_{\text{XPM},\omega_0}(\mathcal{E}_{\omega_0}, \mathcal{E}_{3\omega_0}), \tag{66}$$

$$N_{3\omega_0}(\mathcal{E}_{\omega_0}, \mathcal{E}_{3\omega_0}) = [T_{3\omega_0}^2 N_{\text{Kerr}}(|\mathcal{E}_{3\omega_0}|^2) + N_{\text{Plasma},3\omega_0}(\rho) + T_{3\omega_0}N_{\text{MPA},3\omega_0}(|\mathcal{E}_{3\omega_0}|^2)]\mathcal{E}_{3\omega_0}$$
$$+ T_{3\omega_0}^2 N_{\text{XPM},3\omega_0}(\mathcal{E}_{\omega_0}, \mathcal{E}_{3\omega_0}), \tag{67}$$

where $T_{3\omega_0} \equiv 1 + i(3\omega_0)^{-1}\partial/\partial t$ and

$$N_{\text{XPM},\omega_0}(\mathcal{E}_{\omega_0}, \mathcal{E}_{3\omega_0}) = ik_{\omega_0}n_2(2|\mathcal{E}_{3\omega_0}|^2\mathcal{E}_{\omega_0} + \mathcal{E}_{\omega_0}^{*2}\mathcal{E}_{3\omega_0}), \tag{68}$$

$$N_{\text{XPM},3\omega_0}(\mathcal{E}_{\omega_0}, \mathcal{E}_{3\omega_0}) = i3k_{\omega_0}n_2(2|\mathcal{E}_{\omega_0}|^2\mathcal{E}_{3\omega_0} + \mathcal{E}_{\omega_0}^3/3). \tag{69}$$

Recently, Kolesik et al. (2006) highlighted the limits of a two-envelope decomposition to describe third harmonic generation and propagation. Specifically, this decomposition becomes ambiguous when the supercontinuum generated by the pump overlap with the third harmonic. A single unidirectional propagation equation resolving the carrier frequencies was proposed to cure the problem (see Section 2.2.11 and Kolesik et al., 2006).

2.2.11. Unidirectional pulse propagation equation

Ideally, one wishes to solve Maxwell equations in two or three dimensions, including the nonlinear polarization response of the medium, over an extended propagation distance. However, this constitutes an extremely difficult computational task because two propagation directions in the forward and in the backward direction must be delt with simultaneously. Kolesik et al. (2002), Kolesik and Moloney (2004a), and Moloney and Kolesik (2007) proposed a model that makes a bridge between various nonlinear envelope equations and Maxwell equations. The model includes nonparaxial terms and vectorial effects. It is called unidirectional optical pulse propagation equation (UPPE) and can be expressed either as a time t-propagated version, where t denotes time in the reference frame of the laboratory, or as a distance z-propagated version like all the previously presented models. There is not a unique way to define a unidirectional pulse propagation equation; the reader is referred to Kinsler et al. (2005) for a review of the theory leading from Maxwell equations to UPPEs. Here, we present only one of the possibilities chosen by Kolesik and Moloney (2004a). Both the t-propagated and the z-propagated versions are not envelope equations but describe the propagation of the fast oscillating electric field. The t propagation version is expressed in the Fourier domain as:

$$\frac{\partial \mathbf{D}(\mathbf{k}, t)}{\partial t} = -i\omega(\mathbf{k})\mathbf{D}(\mathbf{k}, t) + \left[1 - \frac{\mathbf{kk}}{k^2}\right] \cdot \left[\frac{i}{2}\omega(k)\mathbf{P}_{\text{nl}}(\mathbf{k}, t) - \frac{\mathbf{J}(\mathbf{k}, t)}{2}\right], \tag{70}$$

where $\mathbf{D}$ denotes the forward propagating complex amplitude of the depolarization vector $\mathbf{D} = \epsilon_0 n^2\mathbf{E} + \mathbf{P}_{\text{nl}}$, $\mathbf{k}$ is a 3D wave vector satisfying the linear dispersion relation of the medium $\mathbf{k}^2 = \kappa^2(\omega) \equiv n^2\omega^2/c^2$. The factored out transverse projection operator $1 - \mathbf{kk}/k^2$ shows that the initial transversality condition $\nabla \cdot \mathbf{D} = 0$ is preserved during the propagation. The z propagated version describes the upward propagation of the transverse components of the electric field:

$$\frac{\partial \mathbf{E}_\perp(\omega, k_\perp, z)}{\partial z} = ik_z\mathbf{E}_\perp(\omega, k_\perp, z) + \sum_{s=1,2}\mathbf{e}_s^\perp\mathbf{e}_s \cdot \left\{\mu_0\frac{\omega}{2k_z}[i\omega\mathbf{P}_{\text{nl}}(\omega, k_\perp, z) - \mathbf{J}(\omega, k_\perp, z)]\right\}, \tag{71}$$

where the upper $\perp$ index denotes the transverse component,

$$k_z = \sqrt{\frac{n^2\omega^2}{c^2} - k_\perp^2} \tag{72}$$

and $\mathbf{e}_s$ denote the polarization vectors, implicitly depending on the wave vector. The longitudinal z component of the field can be obtained from the transverse components if it is needed for the calculation of the nonlinear polarization $\mathbf{P}_{nl}$ or the current density $\mathbf{J}$. A similar propagation equation holds for the backward propagation component of the electric field. In practice, the backward component is neglected and the nonlinear polarization $\mathbf{P}_{nl}$ and current density $\mathbf{J}$ may be computed from the forward propagating field only.

This fully vectorial equation reduces to a nonlinear envelope equation under suitable approximations, i.e., by (i) replacing the sum over the polarization vectors $\sum_{s=1,2} \mathbf{e}_s^\perp$ by the identity operator in the transverse plane; (ii) developing the electric field into a carrier and an envelope $\mathbf{E}(x, y, z, t) = \frac{1}{2}\mathcal{E}(x, y, z, t)\exp[\mathrm{i}(kz - \omega_0 t)]\mathbf{e}_x + c.c.$ and similarly for $\mathbf{P}_{nl}$ and $\mathbf{J}$ with $k = \kappa(\omega_0)$; (iii) approximating $k_z \simeq kU(\omega)(1 + \frac{1}{2k^2U^2}(\kappa^2 - k^2U^2 - k_\perp^2))$. The envelope equation obtained after these three steps reads:

$$\frac{\partial\tilde{\mathcal{E}}(\omega, k_\perp, z)}{\partial z} = -\mathrm{i}\frac{k_\perp^2}{2kU}\tilde{\mathcal{E}} + \frac{\mathrm{i}}{2kU}(\kappa^2 - k^2U^2)\tilde{\mathcal{E}} + \mathrm{i}\frac{k_0}{2\epsilon_0 n_0}T\tilde{\mathcal{P}}(\omega, k_\perp, z) - \frac{1}{2\epsilon_0 n_0}\tilde{\mathcal{J}}(\omega, k_\perp, z), \tag{73}$$

where $\tilde{\mathcal{E}}(\omega, k_\perp, z)$ denotes the Fourier transform of $\mathcal{E}(x, y, z, t)$ (the tilde denotes 3D Fourier transform), $U \equiv 1 + (\omega - \omega_0)/kv_g$, $v_g \equiv 1/\kappa'(\omega_0)$, $T \equiv 1 + (\omega - \omega_0)/\omega_0$. For an instantaneous Kerr effect ($\mathcal{P} = 2\epsilon_0 n_0 n_2|\mathcal{E}|^2\mathcal{E}$), and the plasma contribution as in Eq. (12), we obtain

$$\frac{\partial\tilde{\mathcal{E}}(\omega, k_\perp, z)}{\partial z} = -\mathrm{i}\frac{k_\perp^2}{2kU}\tilde{\mathcal{E}} + \frac{\mathrm{i}}{2kU}(\kappa^2 - k^2U^2)\tilde{\mathcal{E}} + \mathrm{i}k_0 Tn_2\mathcal{F}\{|\mathcal{E}|^2\mathcal{E}\} - \frac{k_0}{2\rho_c n_0}\frac{\omega_0\tau_c}{1 + \omega^2\tau_c^2}(1 + \mathrm{i}\omega\tau_c)\mathcal{F}\{\rho\mathcal{E}\}. \tag{74}$$

The main advantages of formulation (71) over (73) is that it fully accounts for nonparaxiality and captures the chromatic dispersion of the medium over an arbitrary wide frequency range. For instance, in order to describe third harmonic generation in the framework of Eq. (71) without using a two-envelope model, Kolesik et al. (2006) showed that it is sufficient to replace the nonlinear polarization in Eq. (70) by

$$P_{nl} = 2\epsilon_0 n_0 n_2\left[(1 - \alpha)E^2 + \alpha\int_{-\infty}^{t}\mathcal{R}(t - \tau)E^2(\tau)\,\mathrm{d}\tau\right]E(t), \tag{75}$$

where $\mathcal{R}$ denotes the Raman response with fraction α.

2.3. Numerical techniques for the integration of these models

Several numerical methods can be used to solve the models presented above. Although an extensive description of these methods is beyond the scope of this review, we will briefly describe the standard possibilities. All the models of Section 2.2 are basically paraxial propagation equations, possibly extended in some cases. Any numerical scheme valid for solving advection-diffusion equations is therefore convenient (Press et al., 1992). The easiest scheme to implement is probably a split-step scheme in which all linear terms (diffraction and dispersion) are computed in Fourier space (FSS for Fourier split step) over a half step while the nonlinear terms are computed directly in the physical space over a second half-step using an Adams–Bashforth or a Runge–Kutta procedure.

Typically a few hours of calculation on a workstation are necessary to compute the pulse propagation over a few meters in $(2 + 1)$ dimensions. In the general $(3 + 1)$D case, it is necessary to use powerful means of calculations. Alternatively, computational time or grid points may be saved by a specific choice of the numerical scheme according to the model to be solved. For example when a revolution symmetry around the propagation axis is assumed, it is very convenient for the computation of the linear part to couple the Fourier decomposition in the direction of time to the standard Crank–Nicholson scheme in the transverse direction (FCN). Another interesting choice can be the use of the standard alternating direction implicit (ADI) method with alternate time and space directions (Press et al., 1992),

Table 1
References for the physical parameters of several media (see models in Section 2.2)

	$n_2, \alpha, \Gamma, \omega_R$	β_K, σ_K	$n(\omega), k'', k'''$
Air	(Shimoji et al., 1989)	(Talebpour et al., 1999b)	(Galkin and Tatevian, 1997)
N₂	(Ripoche et al., 1997)		
O₂	(Nibbering et al., 1997) (Mizrahi and Shelton, 1985) (Shaw et al., 1993)	(Schwarz et al., 2001)	
Noble gases	(Shelton, 1990) (Nurhuda et al., 2002c, b, 2004) (Ripoche et al., 1997) (Nibbering et al., 1997) (Lehmeier et al., 1985)	(Perry et al., 1988) (Augst et al., 1991) (L'Huillier et al., 1983) (Lompre et al., 1976) (Lompre et al., 1976)	(Dalgarno and Kingston, 1966) (Mansfield and Peck, 1969) (Peck, 1983)
Condensed media	(Nikogosyan, 1997)	(Liu et al., 1978) (Nathan et al., 1985)	
Water	(Nikogosyan, 1997) (Smith et al., 1977)	(Kennedy, 1995) (Feng et al., 1997) (Williams et al., 1976) (Migus et al., 1987)	(Van Engen et al., 1998) (Kou et al., 1993) (Khashan and Nassif, 2000)
Fused silica	(Olivier et al., 2004)	(Lenzner et al., 1998) (Li et al., 1999)	(Khashan and Nassif, 2000)

although high order dispersive terms are less easy to implement in the latter method. The numerical schemes may then even be easily modified so as to introduce mappings between the physical space and the computational space, which transform a regular computational grid into a nonuniform grid in the physical domain. The advantage of this procedure is to enable an efficient resolution of the propagation equation on grids suited to the intensity gradients of the wave, with possibilities to adapt the grid during the calculation. $(3 + 1)$D numerical simulations of multiple filamentation were performed on a workstation by this method (Méchain et al., 2004a, b, 2005a). Pseudo-spectral decomposition scheme using Chebishev polynomials is a method inherently designed to use these mappings (Canuto et al., 1988) and can also be applied efficiently to most models in Section 2.2 by simply using split steps. Couairon et al. (2002) have tested the efficiency of these different methods. In general, the FCN method is very efficient. The ADI method can be made completely implicit and is more stable but each step is longer. The split step Chebishev spectral method is slower than FCN or ADI but it is extremely accurate when very high gradients must be described. An adaptive mesh refinement technique was used by Mlejnek et al. (1999a), Moloney et al. (2000) to increase the resolution around each peak intensity in $3 + 1$ dimensions. More recently, Ando and Fujimoto (2005) have developed an efficient method based on Suzuki's exponential-product expansion (Suzuki, 1985, 1990, 1991, 1993) applied to the evolution operator, which allowed them to perform $(3 + 1)$D numerical simulations of filamentation without large scale calculations.

As for Eq. (51), it is an ordinary differential equation which can be solved by the Runge–Kutta method or by direct integration (analytically at each time step) when it is possible (Couairon et al., 2002; Chiron et al., 1999; Kandidov et al., 1994).

Finally, it is worth underlining that parameters characterizing the medium must be introduced in the models presented in Section 2.2, besides parameters for the input pulse. The results of numerical simulations sensitively depend on the correct estimation of these parameters, even if the physics is restricted to a given set of physical effects. The main parameters needed are the following: among the nonlinear effects to be considered, there are the optical Kerr effect with its possible Raman contribution (nonlinear index coefficient n_2, fraction of the delayed component α, damping Γ and frequency ω_R of the molecular response), multiphoton absorption (β_K) and plasma generation (σ_K, U_i), while the description of the dispersive properties of the medium needs either the second and higher dispersive coefficients ($k'', k''', \ldots$) at the laser wavelength, or a dispersion relation valid in the frequency domain under consideration. Below, we indicate in Table 1 a few references including measurements in various media, which we found particularly useful for the determination of these parameters.

Ionization rates: Once the ionization potential U_i of the medium and the laser wavelengths are known, it is possible to calculate easily the ionization rates and associated multiphoton absorption cross sections by using the Keldysh formulation (Keldysh, 1965) and its subsequent development (Perelomov et al., 1966; Ilkov et al., 1992; Mishima et al., 2002). It allows the determination of the optical field ionization rates of singly ionized atoms in gases or in condensed media, for an electromagnetic wave for which the photon energy is lower than the ionization potential. It was revisited by several authors. In particular we find it useful to cite the paper by Talebpour et al. (1999b) which gives a semi-empirical model for the rate of tunnel ionization of nitrogen and oxygen molecule in an intense Ti:sapphire laser pulse, and the paper by Ilkov et al. (1992) which defines the undetermined preexponential coefficient in the multiphoton limit of Keldysh's theory by continuity with the tunnel ionization rates (Ammosov et al., 1986). Below, we detail the model we use in our numerical simulations for gases and condensed media.

Optical field ionization rates for gases: For an atom with ionization potential U_i in a linearly polarized laser field with frequency ω_0 and peak electric field E, the adiabaticity parameter is defined as the square root of the ratio of the ionization potential U_i by the ponderomotive energy of the electron

$$\gamma = \frac{\omega_0}{eE}\sqrt{2mU_i} \tag{76}$$

and distinguishes whether OFI occurs in the tunnel regime $\gamma \ll 1$ or in the multiphoton regime $\gamma \gg 1$. Keldysh's formulation and its subsequent developments by Perelomov et al. (1966) led to a general formula for OFI rates valid for any atom or ion with quantum numbers l and m and charge state Z:

$$W(\omega_0, E) = \omega_{\mathrm{a.u.}}\sqrt{\frac{6}{\pi}}|C_{n^*,l^*}|^2 f(l,m)\frac{U_i}{2U_\mathrm{H}}A_m(\omega_0,\gamma)\left(\frac{2E_0}{E\sqrt{1+\gamma^2}}\right)^{2n-|m|-3/2}\exp\left(-\frac{2E_0}{3E}g(\gamma)\right), \tag{77}$$

where $n = Z(U_0/U_\mathrm{H})^{-1/2}$, U_H is the ionization potential of hydrogen, $\omega_{\mathrm{a.u.}} = eE_\mathrm{H}/\sqrt{2mU_\mathrm{H}} \simeq 4.1 \times 10^{16}\,\mathrm{s}^{-1}$ (defined by $\gamma = 1$ for hydrogen or by $\hbar\omega_{\mathrm{a.u.}} = 2U_\mathrm{H}$), $E_\mathrm{H} = e^5 m^2/\hbar^4(4\pi\epsilon_0)^3 \simeq 514\,\mathrm{GV/m}$ and $E_0 = E_\mathrm{H} \times (U_i/U_\mathrm{H})^{3/2}$. For a given atom, the dimensionless constant C_{n^*,l^*} is adapted from the formula known for the hydrogen atom (Perelomov et al., 1966) by replacing the principal n and orbital l quantum numbers by their effective counterparts $n^* = n - \delta_l$ and $l^* = l - \delta_l$, respectively, and $\delta_l = n - (U_i/U_\mathrm{H})^{-1/2}$ is the quantum defect:

$$|C_{n^*,l^*}|^2 = \frac{2^{2n^*}}{n^*\Gamma(n^*+l^*+1)\Gamma(n^*-l^*)}, \tag{78}$$

where Γ is the gamma function (Abramowitz and Stegun, 1972). The constant $f(l,m)$ reads

$$f(l,m) = \frac{(2l+1)(l+|m|)!}{2^{|m|}(|m|)!(l-|m|)!}, \quad f(0,0) = 1. \tag{79}$$

The other functions entering formula (77) read as

$$A_m(\omega_0,\gamma) = \frac{4}{\sqrt{3\pi}}\frac{1}{|m|!}\frac{\gamma^2}{1+\gamma^2} \times \sum_{\kappa \geqslant v}^{+\infty}\exp[-\alpha(\kappa-v)]\Phi_m(\sqrt{\beta(\kappa-v)}), \tag{80}$$

$$\Phi_m(x) = \frac{x^{2|m|+1}}{2}\int_0^1\frac{\mathrm{e}^{-x^2 t}t^{|m|}}{\sqrt{1-t}}\,\mathrm{d}t = \mathrm{e}^{-x^2}\int_0^x(x^2-y^2)^{|m|}\mathrm{e}^{y^2}\,\mathrm{d}y, \tag{81}$$

$$\beta(\gamma) = \frac{2\gamma}{\sqrt{1+\gamma^2}}, \tag{82}$$

$$\alpha(\gamma) = 2\left[\sinh^{-1}\gamma - \frac{\gamma}{\sqrt{1+\gamma^2}}\right] = \begin{cases} 2\gamma^3/3 & \text{when } \gamma \ll 1, \\ 2(\log 2\gamma - 1) & \text{when } \gamma \gg 1, \end{cases} \tag{83}$$

Table 2
Cross sections for multiphoton ionization computed from Eq. (89) for several gases at various wavelengths

			248 nm	400 nm	527 nm	800 nm	1055 nm
	U_i (eV)	$K; \sigma_K$ (s^{-1} cm^{2K}/W^K)					
O_2	12.063	3; 1.35×10^{-28}		4; 2.52×10^{-42}	6; 5.98×10^{-70}	8; 2.81×10^{-96}	11; 7.71×10^{-136}
N_2	15.576	4; 3.22×10^{-44}		6; 3.15×10^{-72}	7; 1.40×10^{-85}	11; 6.31×10^{-140}	14; 2.03×10^{-179}
He	24.587	5; 3.42×10^{-61}		8; 2.03×10^{-104}	11; 1.32×10^{-146}	16; 2.60×10^{-215}	21; 8.16×10^{-283}
Ne	21.564	5; 2.04×10^{-60}		7; 5.93×10^{-89}	10; 5.21×10^{-131}	14; 1.55×10^{-185}	19; 1.16×10^{-252}
Ar	15.759	4; 2.98×10^{-44}		6; 2.79×10^{-72}	7; 1.14×10^{-85}	11; 5.06×10^{-140}	14; 1.61×10^{-179}
Kr	13.999	3; 4.95×10^{-29}		5; 3.38×10^{-57}	6; 5.15×10^{-71}	10; 4.35×10^{-125}	12; 4.09×10^{-151}
Xe	12.130	3; 1.31×10^{-28}		4; 2.20×10^{-42}	6; 5.65×10^{-70}	8; 2.40×10^{-96}	11; 6.91×10^{-136}

$$g(\gamma) = \frac{3}{2\gamma} \left[\left(1 + \frac{1}{2\gamma^2}\right) \sinh^{-1} \gamma - \frac{\sqrt{1+\gamma^2}}{2\gamma} \right] = \begin{cases} 1 - \dfrac{\gamma^2}{10} + \dfrac{9\gamma^4}{280} & \text{when } \gamma \ll 1, \\ \dfrac{3}{2\gamma} \left(\log 2\gamma - \dfrac{1}{2} \right) & \text{when } \gamma \gg 1, \end{cases} \tag{84}$$

$$v = \frac{U_i}{\hbar\omega_0}\left(1 + \frac{1}{2\gamma^2}\right), \quad v_0 = \frac{U_i}{\hbar\omega_0}. \tag{85}$$

Below, we give explicitly the tunnel and multiphoton limits separately for single ionization of atoms in the fundamental state with $l = m = 0$, $n^* = (U_i/U_H)^{-1/2}$ and $|C_{n^*,l^*}|^2 = 2^{2n^*}/n^* \Gamma(2n^*)$:

Tunnel limit: OFI rates in the tunnel regime are obtained when $\gamma \ll 1$. In this case, $A_0(\omega_0, \gamma) \to 1$ and the probability of tunnel ionization is independent of the frequency of the wave:

$$W(E) = \omega_{\text{a.u.}} |C_{n^*,l^*}|^2 \frac{U_0}{2U_H} \sqrt{\frac{6}{\pi}} \left(\frac{2E_0}{E}\right)^{2n^*-3/2} \exp\left(-\frac{2E_0}{3E}\right). \tag{86}$$

In Fig. 20, the solid curve shows the OFI rate for oxygen and nitrogen obtained from the general formula (77) at 800 nm, which is asymptotic to tunnel ionization rates (86) when $I > 10^{14}$ W/cm^2.

Multiphoton limit: the multiphoton approximation of the OFI rates is obtained when $\gamma \gg 1$, by taking into account only the term $\kappa = K \equiv \text{mod}\,(v_0 + 1)$ in the series for $A_m(\omega_0, \gamma)$ [Eq. (80)] and by using the relation $v_0 \equiv U_i/\hbar\omega_0 = E_0/2E\gamma$,

$$W(\omega_0, E) = \omega_{\text{a.u.}} \frac{4^{2n^*}}{\pi\sqrt{2}} |C_{n^*,l^*}|^2 \frac{U_i}{2U_H} v_0^{2n^*+2K-3/2} e^{2K-v_0} \Phi_0(\sqrt{2(K-v_0)}) \left(\frac{E}{E_0}\right)^{2K}. \tag{87}$$

It can be readily seen that the ionization rates become proportional to a power of the laser intensity $I \equiv \epsilon_0 n_0 c |E|^2/2$:

$$W(\omega_0, I) = \sigma_K I^K \tag{88}$$

and

$$\sigma_K = \omega_{\text{a.u.}} \frac{4^{2n^*}}{\pi\sqrt{2}} |C_{n^*,l^*}|^2 \frac{U_0}{2U_H} v_0^{2K+2n^*-3/2} e^{2K-v_0} \times \Phi_0(\sqrt{2(K-v_0)}) \times \frac{1}{I_0^K}, \tag{89}$$

where $I_0 = \epsilon_0 n_0 c E_0^2/2$.

The general formula (77) is asymptotic to the MPI rate (88) at low intensity, plotted as a dashed curve in Fig. 20 for oxygen at 800 nm. Below, we give in Table 2 a few MPI coefficients computed from Eq. (89) for several gases at various wavelengths.

Recently, Mishima et al. (2002) have revisited the Keldysh theory by the electron momentum dependence in the preexponential factor and by evaluating the ionization rates with another method (residue theorem instead of saddle-point integration). The authors have found ionization rates for the atomic case that are a factor of 4 larger than those determined by Keldysh while in the molecular case (for example N_2, O_2):

$$W_{\text{mol}} = \frac{16}{3} \frac{(2\gamma^2 + 3)}{1 + \gamma^2} W_{\text{atom}} = 4 \times \frac{16}{3} \frac{(2\gamma^2 + 3)}{1 + \gamma^2} W_{\text{Keldysh}}. \tag{90}$$

The electron momentum dependence can simply be accounted for by changing β into $B\beta$, $\alpha/2$ into $\alpha/2 + C$ and A_m into $A_m/\sqrt{B}$ in Eqs. (80), (82) and (83), where B and C depend on U_i, ω and γ as indicated in Appendix B of (Mishima et al., 2002).

Optical field ionization rates for condensed dielectrics: For transparent condensed media, the Keldysh formulation relies on a different definition of the adiabaticity parameter:

$$\gamma = \frac{\omega_0}{eE}\sqrt{m^*U_i}, \tag{91}$$

where U_i is the gap between the valence and the conduction band and m^* denotes the reduced mass between the electron and the hole. The transition rate for the generation of electron–hole pairs (Keldysh, 1965) reads as

$$W(\omega_0, E) = \frac{2\omega_0}{9\pi}\left(\frac{\omega_0 m^*}{\hbar\sqrt{\Gamma}}\right)^{3/2} Q(\gamma, x)\exp(-\alpha\langle x+1\rangle), \tag{92}$$

where

$$\Gamma = \frac{\gamma^2}{1+\gamma^2}, \quad \Xi = \frac{1}{1+\gamma^2}, \tag{93}$$

$$Q(\gamma, x) = \sqrt{\frac{\pi}{2K(\Xi)}} \times \sum_{n=0}^{\infty} \exp(-n\alpha)\Phi(\sqrt{\beta(n+2v)}), \tag{94}$$

$$\alpha = \pi\frac{K(\Gamma) - E(\Gamma)}{E(\Xi)}, \quad \beta = \frac{\pi^2}{4K(\Xi)E(\Xi)}, \tag{95}$$

$$x = \frac{2}{\pi}\frac{U_i}{\hbar\omega_0}\frac{E(\Xi)}{\sqrt{\Gamma}}, \quad v = \langle x+1\rangle - x, \tag{96}$$

$\langle .\rangle$ denotes the integer part, K and E in Eqs. (94)–(96) denote the complete elliptic integral of the first and second kind and Φ the Dawson function $\Phi(z) = \int_0^z \exp(y^2 - z^2)\,\mathrm{d}y$. Eqs. (92) and (94) are written with complete elliptic integral functions as defined by Abramowitz and Stegun (1972) and do not differ from Eq. (39) by Keldysh (1965) that contains $K(X^{1/2})$ and $E(X^{1/2})$ whereas Eqs. (92)–(96) contain $K(X)$ and $E(X)$. In agreement with these definitions and with (Tien et al., 1999), our quantity β is divided by 4 in Eq. (95) whereas the corresponding quantity in the Keldysh (1965) formula is divided by 2.

Nathan et al. (1985) reviewed measurements of two and three photon absorption coefficients for various materials. There is usually a great dispersion of values found in the literature for the multiphoton transition rates. These rates can be found by the low intensity limit of Eq. (92): $W_{\mathrm{MPI}} = \beta_K I^K/K\hbar\omega_0$. For example for fused silica at 800 nm: $\sigma_6 = 1.5 \times 10^{-71}$ s^{-1} cm^{12}/W^6 (Li et al., 1999), $\sigma_6 = 3 \times 10^{-67\pm0.9}$ s^{-1} cm^{12}/W^6 (Lenzner et al., 1998). In fact, there is also a dispersion even for values of the gap. For fused silica, a gap of 9 eV is reported by several authors (Fischetti et al., 1985; Junnarkar, 2001; Li et al., 1999; Lenzner et al., 1998; Stuart et al., 1995, 1996). A lower gap of 7.8 eV is reported by Nathan et al. (1985), Liu et al. (1978, 1979). Recently a gap of 7.1 eV has also been reported (Joglekar et al., 2003). A recent paper by Gruzdev (2004) shows, however, that these multiphoton transition rates not only depend on the gap but also on the band structure assumed to be nonparabolic in Keldysh's formulation.

Avalanche ionization and plasma absorption. Ionization cross sections of atoms and ions by electron impact were tabulated by Tawara and Kato (1987). Measurements as well as analytical laws fitting the measurements can be found in this reference for most media in which femtosecond filaments are usually generated. For water, the breakdown threshold was measured by several authors leading to the evaluation of useful absorption parameters (Noack and Vogel, 1999; Fan et al., 2002; Kennedy, 1995).

2.4. Semi-analytical approach

Several semi-analytical models were developed to study the nonlinear propagation of high power laser beams. Despite their inherent limitations, these models have the merit to give an intuitive approach of the filamentation process. The main idea of these models is to describe the pulse propagation by means of averaged quantities such as the beam power,

radius and curvature. Specific assumptions are usually made to simplify the physics or to make the models analytically tractable. For example a self-similar evolution of the beam and pulse profiles is often assumed. This assumption constitutes a severe limitation of the models since it can lead to a strong disagreement with the results of full numerical simulations of the pulse propagation. Yet, simple evolution equations may be derived for the beam power and width by different methods which are thus extremely powerful tools to investigate propagation regimes that are still out of reach for direct numerical simulations. These semi-analytical tools have been developed in several fields and rely on different methods, namely, the paraxial ray approximation (Sodha et al., 1976; Max, 1976) and three methods leading to equivalent results: moment theories (Lam et al., 1977), variational methods (Anderson and Bonnedal, 1979) and self-similar solution formalism. These semi-analytical methods may become unreliable in the case of tightly focused beams (Fibich and Ilan, 2000). In this case, an alternative is to use a modulational theory (Fibich and Papanicolaou, 1999). In the following, the moment formalism will be reviewed and the main differences with the other equivalent methods will only be briefly indicated.

2.4.1. Moment formalism

Although the moment formalism was first applied to cw laser beams, the method can be extended to short laser pulses by considering time dependent quantities such as the pulse power and width:

$$P(z, t) = \int |\mathcal{E}(r, z, t)|^2 \, d\mathbf{r}, \tag{97}$$

$$W^2(z, t) = \frac{1}{P(z, t)} \int r^2 |\mathcal{E}(r, z, t)|^2 \, d\mathbf{r}, \tag{98}$$

where the integration is performed in the transverse direction only. The eikonal formalism can be applied by introducing $\mathcal{E} = \mathcal{A} \exp(i\mathcal{S})$ in one of the evolution equations for the laser pulse presented in Section 2.2 and written as

$$2ik \frac{\partial \mathcal{E}}{\partial z} = -\nabla_\perp^2 + \mathcal{M}\mathcal{E}. \tag{99}$$

We limit the presentation of the moment formalism to the case where no nonparaxial, vectorial or cross polarization term is present in the propagation equation. Following Marburger (1975), this leads to

$$\left[2k \frac{\partial S}{\partial z} + (\nabla_\perp S)^2 \right] \mathcal{A} = \nabla_\perp^2 \mathcal{A} - \mathcal{M}_r \mathcal{A}, \tag{100}$$

$$k \frac{\partial \mathcal{A}^2}{\partial z} = -\nabla_\perp \cdot (\mathcal{A}^2 \nabla_\perp S) + \mathcal{M}_i \mathcal{A}^2, \tag{101}$$

where $\nabla_\perp$ denotes the transverse gradient, $\mathcal{M}_r$ and $\mathcal{M}_i$ denote the real and imaginary parts of $\mathcal{M}(r, t, z)$, respectively. Multiplication of Eq. (100) by $\mathcal{A}$ or $r^2 \mathcal{A}$ and integration in the transverse direction, associated with similar operations with Eq. (101) leads to the general system of four equations governing the evolution of power, beam width, beam curvature and phase:

$$k \frac{\partial P}{\partial z} = \int \mathcal{M}_i \mathcal{A}^2 \, d\mathbf{r}, \tag{102}$$

$$k \frac{\partial (W^2 P)}{\partial z} = 2 \int r \mathcal{A}^2 \frac{\partial S}{\partial r} \, d\mathbf{r} + \int r^2 \mathcal{M}_i \mathcal{A}^2 \, d\mathbf{r}, \tag{103}$$

$$2k \int \mathcal{A}^2 \frac{\partial S}{\partial z} \, d\mathbf{r} = - \int [(\mathcal{A} \nabla_\perp S)^2 + (\nabla_\perp \mathcal{A})^2] \, d\mathbf{r} - \int \mathcal{M}_r \mathcal{A}^2 \, d\mathbf{r}, \tag{104}$$

$$2k \int r^2 \mathcal{A}^2 \frac{\partial S}{\partial z} \, d\mathbf{r} = - \int \left(r^2 \mathcal{A}^2 (\nabla_\perp S)^2 + r^2 (\nabla_\perp \mathcal{A})^2 + r \frac{\partial \mathcal{A}^2}{\partial r} + r^2 \mathcal{M}_r \mathcal{A}^2 \right) \, d\mathbf{r}. \tag{105}$$

The eikonal is then sought in the form

$$S(r, z, t) = r^2 b(z, t) + \phi(z, t), \tag{106}$$

where b is linked to the beam curvature and ϕ denotes the beam phase on axis. Eqs. (103), (104), (105) may then be rewritten as

$$k\frac{\partial P}{\partial z} = PF_i^{(0)},$$ (107)

$$k\frac{\partial W^2}{\partial z} = 4bW^2 + W^2 H_i,$$ (108)

$$2k\frac{\partial b}{\partial z} = \frac{Q_1}{W^4} - 4b^2 + \frac{G_r}{W^2},$$ (109)

$$2k\frac{\partial \phi}{\partial z} = \frac{Q_2}{W^2} - (G_r + F_r^{(0)})$$ (110)

where the dimensionless quantities

$$Q = \frac{m_4}{m_2^2}, \quad Q_1 = \frac{d_0 m_2 - d_2}{Q - 1}, \quad Q_2 = \frac{d_2 - m_4 d_0/m_2}{Q - 1}$$ (111)

are expressed in terms of the moments

$$m_j = \frac{\int \xi^j \mathcal{A}^2 \, d\vec{\xi}}{\int \mathcal{A}^2 \, d\vec{\xi}}; \quad d_j = \frac{\int \nabla_\xi \mathcal{A} \cdot \nabla_\xi (\xi^j A) \, d\vec{\xi}}{\int \mathcal{A}^2 \, d\vec{\xi}},$$ (112)

which involve the scale $w(z, t)$, the rescaled additional variable $\xi = r/w(z, t)$ and the shape of the pulse. Note that in general, the moments $m_j(z, t)$ and $d_j(z, t)$ depend on z and t and the width $W(z, t)$ is linked to the scale $w(z, t)$ by the relation $W^2(z, t) = w^2(z, t)m_2(z, t)$. The subscript r or i denotes real or imaginary parts of the functions $F^{(n)}$, G and H, which have dimensions of W^{-2} and are defined as

$$F^{(n)}(z, t) = \frac{\int \xi^n \mathcal{M}\mathcal{A}^2 \, d\vec{\xi}}{\int \xi^n \mathcal{A}^2 \, d\vec{\xi}},$$ (113)

$$H = F^{(2)} - F^{(0)},$$ (114)

$$G = \frac{H}{1 - Q}.$$ (115)

The set of Eqs. (107)–(115) defines the evolution of the beam power, radius, curvature and phase as a function of the propagation distance. It is valid for an arbitrary beam profile. Finally, by combining Eqs. (108) and (109), a second order differential equation is found for the beam width:

$$\frac{\partial^2 W}{\partial z^2} = \frac{Q_1 + W^2 G_r}{k^2 W^3} - \frac{W}{4k^2} H_i^2 + \frac{1}{2kW} \frac{\partial (W^2 H_i)}{\partial z}.$$ (116)

Together with Eq. (102), it allows the determination of the beam width and power as a function of the propagation distance provided a beam profile is assumed to be preserved along propagation and initial conditions are given for the input power $P(z = 0, t)$, the width $W(z = 0, t)$ and the curvature of the input beam, i.e., its derivative $\partial_z W(z = 0, t)$.

This moment theory is quite general but the moment equations involve high-order moments and must be closed. This is done by assuming a self-similar beam evolution, most often associated with a Gaussian ansatz in the form

$$\mathcal{A} = \sqrt{\frac{2P(z, t)}{\pi w^2(z, t)}} \exp(-\xi^2).$$ (117)

This choice yields $m_2 = 1/2$, which amounts to using a normalization scale $w(z, t) = \sqrt{2}W(z, t)$ for the beam width, larger than the root mean square beam width $W(z, t)$. In this case, we have $Q = 2$, $Q_1 = 1$ and $Q_2 = -2$. To proceed with an example, the method is applied to the model of filamentation (39)–(44) which involves the optical Kerr effect

with a delayed contribution of fraction α, MPI and MPA. Other effects are neglected for the purpose of illustration. This yields Eq. (99) with nonlinearity below:

$$\mathcal{M} = -2kk_0 n_2 \left[(1-\alpha)\mathcal{A}^2 + \alpha \int_{-\infty}^{t} \mathcal{R}(t'-t)\mathcal{A}^2(t')\,dt' \right] + 2kL_{pl}^{-1} \int_{-\infty}^{t} \sigma_K \mathcal{A}^{2K}(t')\,dt' - ik\beta_K \mathcal{A}^{2K-2} \tag{118}$$

with $L_{pl}^{-1} = \sigma \omega_0 \tau_c \rho_{at}/2 = L_{PL}^{-1}\omega_0^2\tau_c^2/(1+\omega_0^2\tau_c^2)$ and L_{PL} defined by Eq. (9).

$$\frac{\partial P}{\partial z} = -\frac{\beta_K P}{K}\left(\frac{2P}{\pi w^2}\right)^{K-1}, \tag{119}$$

$$\begin{aligned}
\frac{\partial^2 w}{\partial z^2} = {} & \frac{4}{k^2 w^3}\left(1 - (1-\alpha)\frac{P(z,t)}{P_{cr}^G} - 4\alpha w^4 \int_{-\infty}^{t} \frac{P'}{P_{cr}^G}\frac{\mathcal{R}(t'-t)}{(w^2+w'^2)^2}\,dt'\right) \\
& + \frac{4K\sigma_K}{kL_{pl}}w \int_{-\infty}^{t}\left(\frac{2P'}{\pi w'^2}\right)^K \frac{w'^2}{(Kw^2+w'^2)^2}\,dt' - \beta_K\left(\frac{2P}{\pi w^2}\right)^{K-1}\left(c_1 w\beta_K\left(\frac{2P}{\pi w^2}\right)^{K-1} - c_2\frac{dw}{dz}\right),
\end{aligned} \tag{120}$$

where $P' \equiv P(z,t')$ and $w' \equiv w(z,t')$, w in the integral terms depends on z and t,

$$c_1 = \frac{(K-1)^2(2K-1)}{4K^4}, \quad c_2 = \frac{(K-2)(K-1)}{K^2}. \tag{121}$$

Eq. (120) describes the evolution of the beam width associated to each time slice of the pulse. The moment formalism is quite powerful since it allows the derivation of the evolution equation (116) for the time dependent beam width, under the assumption of an arbitrary prescribed beam shape. At this point, it should be stressed that the temporal profile of the pulse is not assumed to be Gaussian even if the initial pulse is Gaussian or if the prescribed beam shape is chosen as Gaussian. In addition, physical effects that couple various time slices in the pulse, such as multiphoton ionization or the delayed Kerr effect which are crucial in the physics of femtosecond filamentation, are fully included in the model without assuming independent time slices. Eq. (116) preserves the coupling between the time slices as shown by Couairon (2003c) where Eq. (120) was obtained in the case of a Gaussian initial pulse with power conservation (no multiphoton absorption). The method, however, can be applied in general even if the power is not preserved. It describes the evolution of the pulse profile similarly to that of a set of damped coupled nonlinear oscillators.

2.4.2. Variational method

The problem of self-focusing of laser beams in media with various nonlinearity was reformulated in terms of a variational principle by Anderson and Bonnedal (1979), who used Gaussian test functions. Several approximations which are discussed below make this type of analysis possible. The application of this method, as briefly presented below, allows a quick and intuitive understanding of the phenomenon of filamentation. We first present the method before discussing the validity of the approximations made in the context of filamentation.

All nonlinear evolution equations derived in Section 2.2 are written in the form

$$2ik\frac{\partial \mathcal{E}}{\partial z} = P(\mathcal{E}) + R(\mathcal{E}), \tag{122}$$

where $P(\mathcal{E})$ denotes a nonlinear evolution operator that can be obtained from a Lagrangian, L, and $R(\mathcal{E})$, a nonlinear operator that cannot. When $R\mathcal{E} \equiv 0$, Eq. (122) is equivalent to the variational problem $\delta \int \mathcal{L}\,dz \equiv 0$ where $\mathcal{L} = \int L\,d\mathbf{r}$. From this variational formulation, the Rayleigh-Ritz procedure consists in finding a trial function $\mathcal{E}_T(\mathbf{r},t,z)$ for the evolution of $\mathcal{E}$, with a prescribed dependence on certain parameter functions, $q_j(z)$ that characterize crucial features of the solution, as e.g., the beam width or curvature. Inserting this trial function in the Lagrangian $\mathcal{L}$ allows the derivation of evolution equations for the parameter functions by means of the Euler–Lagrange equations (where z is the evolution

variable):

$$\frac{\delta \mathcal{L}}{\delta q_j} \equiv \frac{\partial \mathcal{L}}{\partial q_j} - \frac{d}{dz} \frac{\partial \mathcal{L}}{\partial p_j} = 0, \quad p_j = \frac{dq_j}{dz}, \quad j = 1, 2, \dots . \tag{123}$$

This standard formulation must be extended in situations where a Lagrangian cannot be found for the original equation, i.e., when $R\mathcal{E} \neq 0$ as for example when physical effects like damping, higher order dispersion, or self-steepening are taken into account in the models. In such a case, the generalization of Eq. (123) becomes (Anderson et al., 2001)

$$\frac{\delta \mathcal{L}}{\delta q_j} = -2 \operatorname{Re} \left[\int R(\mathcal{E}_T) \frac{\partial \mathcal{E}_T^*}{\partial q_j} \, d\mathbf{r} \right] \tag{124}$$

and it is sufficient to use the Lagrangian

$$\mathcal{L}(z) = \int_0^\infty r \, dr \left[ik \left(\mathcal{E} \frac{\partial \mathcal{E}^*}{\partial z} - \mathcal{E}^* \frac{\partial \mathcal{E}}{\partial z} \right) + |\nabla_\perp \mathcal{E}|^2 \right] \tag{125}$$

and to put in $R(\mathcal{E})$ the remaining terms even if some of them such as the instantaneous part of the Kerr effect could have entered the Lagrangian. The advantage of this procedure is the possibility to apply the method not only to a continuous laser field, but also to a time dependent laser pulse. The method can indeed be generalized to study the propagation of femtosecond laser pulses in transparent media by allowing the parameters functions $q_j(z, t)$ to depend also explicitly on time. As for the moment theory, the method will be applied to a specific test function in the form

$$\mathcal{E}(z, r, t) = \mathcal{E}_0(z, t) \mathcal{A} \left(\frac{r^2}{w^2(z, t)} \right) \exp(ib(z, t)r^2 + i\phi(z, t)), \tag{126}$$

where $\mathcal{E}_0(z, t)$ denotes the amplitude on-axis, $\mathcal{A}(z, t)$ is a real amplitude, $w(z, t)$ the beam width, $b(z, t)$ the curvature parameter and $\phi(z, t)$ the phase. With this ansatz, the Lagrangian (125) becomes

$$\mathcal{L}(z, t) = \left(\int \mathcal{A}^2 \, d\vec{\xi} \right) \mathcal{E}_0^2 \left[2kw^2 \left(\frac{\partial b}{\partial z} w^2 m_2 + \frac{\partial \phi}{\partial z} \right) + d_0 + 4m_2 w^4 b^2 \right]. \tag{127}$$

The variation of $\mathcal{L}$ with respect to ϕ, b, $\mathcal{E}_0$ and w as derived from Eqs. (124) leads to the evolution equations for these parameters:

$$k \frac{\partial P}{\partial z} = P F_i^{(0)}, \tag{128}$$

$$k \frac{\partial w}{\partial z} = 2wb + \frac{w}{2} H_i, \tag{129}$$

$$2k \frac{\partial b}{\partial z} = \frac{q_1}{w^4} - 4b^2 + \frac{g_r}{w^2}, \tag{130}$$

$$2k \frac{\partial \phi}{\partial z} = \frac{q_2}{w^2} - (2F_r^{(0)} + D). \tag{131}$$

$$\tag{132}$$

Here the on axis pulse amplitude $\mathcal{E}_0$ was expressed as a function of the power $P(z, t) \propto \mathcal{E}_0(z, t)^2 w^2(z, t)$ and we introduced the quantities

$$D = \frac{\int \xi \mathcal{M}(\partial \mathcal{A}/\partial \xi) \, d\vec{\xi}}{\int \mathcal{A}^2 \, d\vec{\xi}}, \tag{133}$$

$$g = \frac{D + F^{(0)}}{m_2}, \tag{134}$$

$$q_1 = d_0/m_2, \quad q_2 = -2d_0. \tag{135}$$

The resulting set of equations is formally the same but in general differs from that obtained by the moment theory (107)–(110), i.e. different coefficients are obtained except for the case of a Gaussian test function defined by (117), for which $d_0 = 2$, $m_2 = 1/2$, $q_1 = 4$, $q_2 = -4$, $D_r = -F_r^{(2)}$ and $G_r = g_r$.

Combining Eqs. (129) and (130), the evolution equation for the beam radius reads

$$\frac{\partial^2 w}{\partial z^2} = \frac{(q_1 + w^2 g_r)}{k^2 w^3} - \frac{w H_i^2}{4k^2} + \frac{1}{2kw}\frac{\partial(w^2 H_i)}{\partial z}, \tag{136}$$

and coincides with Eq. (116) for a Gaussian test function, which leads to the evolution equation (120) when applied to the propagation model involving the nonlinearity (118).

Sprangle et al. (2002) have developed a method called Source Dependent Expansion method which is similar to the variational procedure and have obtained an evolution equation for the beam width of a filamenting pulse similar to Eq. (136). Their final evolution equation for the beam width is retrieved from Eq. (120) by assuming that $w' = w$ in the integral term corresponding to plasma defocusing in Eq. (120), which amounts to neglecting the coupling effect between the different time slices in the pulse due to multiphoton ionization or the Raman–Kerr effect, an assumption implicit in the derivation done by Sprangle et al. (2002).

A slightly different approach was pursued by Henz and Herrmann (1996), Aközbek et al. (2000) and by Jisha et al. (2005). In order to apply the variational method to the problem of femtosecond filamentation, which involves physical effects such as plasma defocusing and the delayed Kerr effect that cannot, in principle, enter in the Lagrangian, these authors have made the assumption that the test function has separable variables and can be chosen as $\mathcal{E}(z, r, t) = \mathcal{B}(z, r)\mathcal{T}(t)$. Under this assumption, it is possible to apply the variational method as presented above or by generalizing the Lagrangian so as to include the instantaneous Kerr effect and plasma defocusing in the form

$$L = ik\left(\mathcal{B}\frac{\partial \mathcal{B}^*}{\partial z} - \mathcal{B}^*\frac{\partial \mathcal{B}}{\partial z}\right)\mathcal{T} + |\nabla_\perp \mathcal{B}|^2\mathcal{T} - kk_0 n_2|\mathcal{B}|^4\mathcal{T}^3 + \frac{2k\sigma_K}{(K+1)L_{pl}}|\mathcal{B}|^{2K+2}\mathcal{T}n(t) \tag{137}$$

with $n(t) = \int_\infty^t \mathcal{T}^{2K}(t')\,dt'$. A Gaussian test function is then chosen in the form

$$\mathcal{B}(z, r) = \mathcal{E}_0(z)\exp\left(-\frac{r^2}{w^2(z)} + ib(z)r^2 + i\phi(z, t)\right). \tag{138}$$

The reduced Lagrangian is obtained as

$$\mathcal{L} = \int_0^\infty Lr\,dr = \frac{1}{4}\mathcal{E}_0^2\mathcal{T}\left[kw^2\left(w^2\frac{db}{dz} + 2\frac{d\phi}{dz}\right) + 2 + 2w^4 b^2 + kk_0 n_2 w^2\mathcal{E}_0^2\mathcal{T}^2 - \frac{2k}{L_{pl}}w^2\mathcal{E}_0^{2K}n(t)\right]. \tag{139}$$

It is then possible to derive an evolution equation for the beam width which is nearly that obtained by Sprangle et al. (2002) when the instantaneous Kerr effect and multiphoton ionization are the only nonlinear effects considered. Note that the dependence on time of the parameters w, b, $\mathcal{E}_0$ and ϕ is made apparent by the time dependence in the reduced Lagrangian (139); each time slice in the pulse has therefore its own beam width, curvature, phase and power. The power $P(t)$ of each time slice is preserved and the evolution of the beam widths $w(z, t)$ is given by

$$P(t) = \pi\mathcal{E}_0(z, t)^2\mathcal{T}^2(t)w(z, t)^2/2 = \pi I_0\mathcal{T}^2(t)w_0^2/2, \tag{140}$$

$$\frac{\partial^2 w}{\partial z^2} = \frac{4}{k^2 w^3}\left(1 - \frac{P(t)}{P_{cr}^G}\right) + \frac{4K\sigma_K I_0^K}{(K+1)^2 kL_{pl}w_0}\left(\frac{w_0}{w}\right)^{2K+1}n(t). \tag{141}$$

Comparing Eqs. (141) and (120) shows that the assumption of uncoupled time slices has been made, i.e. Eq. (141) is retrieved by assuming $w' = w$ in the integral term accounting for plasma defocusing in Eq. (120). This amounts to describing the pulse as a collection of independent nonlinear oscillators whereas the coupling between the various time slices due to ionization or the delayed Kerr effect is properly taken into account in Eq. (120).

It is important to note that the variational method and the moment theory do not yield completely equivalent results. This is due to the fact that the moment and variational models treat the width in different ways, even without considering the time dependence of the width. In the moment analysis the squared width is a fundamental variable and the width

is a derived variable, whereas in the variational analysis the width is a fundamental variable: The orders of squaring and radial-averaging are reversed (Kozlov et al., 2005). The beam widths obtained from both methods are therefore not equivalent. For specific test-functions including the Gaussian beam with quadratic curvature or chirp, however, both systems can lead to identical results.

Finally, we stress that numerous extensions of this variational approach have been made to describe semi-analytically the propagation of pulsed beams in various conditions. In particular, the case of two interacting and copropagating beams was investigated by Wu et al. (2004) for cross polarized pulses and by Couairon et al. (2002) for two filaments with the same polarization. The link between the variational method and the moment method was investigated by Bergé and Couairon (2001b). The moment method can be viewed as a perturbative approach that amounts to accounting for radiation losses caused by deviations from exact self-similarity of the test function chosen in the variational approach. The case of beam propagation in a nonlocal nonlinear medium (e.g. under the effect of ionization or delayed Kerr effect) was investigated by means of a variational method by Guo et al. (2006). The case of the extension of the variational approach beam propagation in media with nonlinear absorption was investigated by Hermann (2003).

2.4.3. Paraxial ray approximation

Lehner and Auby (2000) among others (Schwarz and Diels, 2001; Hua, 2005) have applied the paraxial ray approximation to the problem of femtosecond filamentation.

The paraxial ray approximation consists in introducing a self-similar beam profile in any propagation equation derived in Section 2.2, for example in Eq. (28). By performing a small r-expansion in the transverse diffraction plane, evolutions equation are derived for the beam width and power at leading orders in r. This method is known to suffer from an underestimation of the influence of the feet of the beam if it is not applied with care. As an example, considering the problem of the collapse due to the optical Kerr effect, i.e., keeping in Eq. (28) only diffraction and Kerr self-focusing, we have $\mathcal{M}_r = 2k_0^2 n_0 n_2$ and the evolution equation for the beam width obtained by this method reads (Lehner and Auby, 2000; Schwarz and Diels, 2001):

$$\frac{\partial^2 w}{\partial z^2} = \frac{4}{k^2 w^3} \left(1 - \frac{P_{\text{in}}}{P_{\text{cr}}^{\text{parax}}} \right), \tag{142}$$

where $P_{\text{cr}}^{\text{parax}} \equiv P_{\text{cr}}^{\text{G}}/4$. According to the variational or moment theory, the beam width should vanish at finite distance on axis, i.e., a catastrophic collapse should occur for $P_{\text{in}} > P_{\text{cr}}^{\text{G}} = \lambda_0^2/2\pi n_0 n_2$ whereas the paraxial ray approximation predicts that collapse should occur for $P_{\text{in}} > P_{\text{cr}}^{\text{G}}/4$. It is seen that the threshold $P_{\text{cr}}^{\text{parax}}$ for the collapse singularity predicted by the paraxial theory is underestimated by a factor of four with respect to the threshold P_{cr}^{G} obtained from the variational or the moment theory.

Actually, the paraxial ray approximation has been shown to give results equivalent to the moment or the variational theory by Subbarao et al. (1998, 2003). The authors have shown that the refractive index should be carefully estimated to obtain correct results. To this aim, application of the paraxial ray approximation should be done in the transverse momentum coordinate, i.e., in the transverse Fourier variable of the transverse coordinate.

3. Theoretical results

3.1. Main results obtained by the analytical approaches (beam–particle analogy)

All semi-analytical methods presented in Section 2.2 lead to evolution equations for the power and beam width.

In the simplest cases, the main results obtained from these methods can be very easily figured out by using the beam–particle analogy: Eq. (141) shows that the beam is confined in its own potential well, formed by the combined action of the optical Kerr effect and multiphoton ionization (or generically, any saturating nonlinearity) (Henz and Herrmann, 1996; Aközbek et al., 2000; Lehner and Auby, 2000; Schwarz et al., 2000; Yu et al., 2004). Integration of Eq. (141) indeed leads to

$$\frac{1}{2}\left(\frac{\partial w}{\partial z}\right)^2 - \frac{1}{2}\left(\frac{\partial w}{\partial z}\right)_0^2 = -[U(w, t) - U(w_0, t)], \tag{143}$$
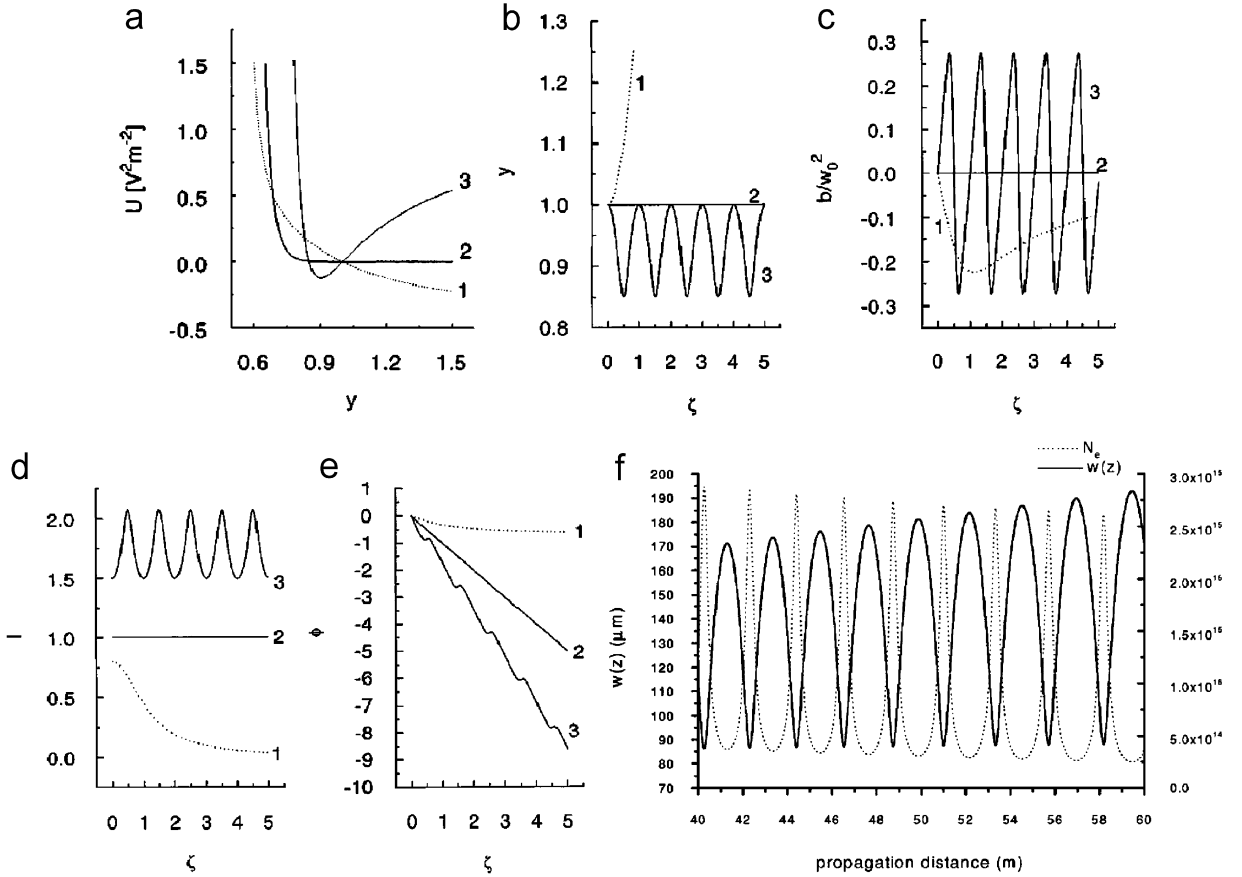
Fig. 21. (a) Potential as a function of the normalized beam radius $y \equiv w/w_0$. (b) Normalized beam radius $y \equiv w/w_0$ and (c) normalized curvature parameter as functions of the normalized propagation distance $\zeta = z/kw_0^2$. (d) Normalized intensity and (e) phase. curve 1 : $P_{\text{in}} < P_{\text{cr}}^{\text{G}}$. Curve 2: $P_{\text{in}} = P_{\text{cr}}^{\text{G}}$. curve 3: $P_{\text{in}} > P_{\text{cr}}^{\text{G}}$. According to Henz and Herrmann (Henz and Herrmann, 1996). (f) Beam size w and electron density versus distance for a UV laser beam with initial power of 49.5 MW. Significant ionization occurs only over short lengths at each refocusing stage, leading to a dashed plasma channel. According to Schwarz and Diels (2001).

$$U(w, t) = \frac{2}{k^2 w^2}\left(1 - \frac{P(t)}{P_{\text{cr}}^{\text{G}}}\right) + \frac{2\sigma_K I_0^K}{(K+1)^2 k L_{pl}} n(t) \frac{w_0^{2K}}{w^{2K}}. \tag{144}$$

The evolution of the beam width is therefore interpretable as the motion of a collection of particles whose positions are given by $w(z, t)$ in a field with potential $U(w, t)$. Here, the time t links each time slice of the pulse to a given particle. The beam width $w(z, t)$ corresponds to the depth of the particle t in its potential well. The curvature parameter b is linked to the particle velocity $\partial w/\partial z$ by the relation $b = (k/2w)\partial w/\partial z$ and the propagation distance z corresponds to time for the particles. The form of the potential depends on the initial power (of the height of the particle). The initial speed of the particle corresponds to the initial convergence of the beam $(\partial w/\partial z)_0 = 2w_0 b_0$.

Let us first consider a pulsed beam stacked into independent time slices. Fig. 21(a) shows the potential $U(w, t)$ for parameters corresponding to the propagation of an infrared laser pulse in air (Henz and Herrmann, 1996). Three possible cases are considered: (i) The beam width of the time slices with power below critical can only increase. (ii) The beam diameter of the time slices with power above critical will oscillate with a period all the faster as the initial power is high. The oscillation frequency also depends on the initial diameter of the beam and its convergence. (iii) If the initial diameter of the laser beam corresponds to the minimum of the potential, the beam keeps a constant diameter

given by

$$w_0(t) = \frac{K k \sigma_K I_0^K}{(K+1)^2 L_{pl}} \frac{n(t)}{(P(t)/P_{cr}^G - 1)}. \tag{145}$$

This condition that the potential have its minimum at $w(z = 0, t) = w_0(t)$ (beam with zero curvature) corresponds to the relation for a self-trapped solution, which can be satisfied only for the time slices with power above critical and a specific initial time dependent beam width. In contrast with the Townes mode, this self-trapped solution was proposed to be structurally stable (Aközbek et al., 2000). However, temporal modulational instability should destroy this solution as is the case for spatial solitons in more than one transverse dimension.

This semi-analytical approach has the merit to be rather easily tractable numerically and to give a global picture of the beam propagation qualitatively close to observations. It is necessary, however, to be careful with the interpretation of numerical results obtained from this method because this approach does not correctly treat the space–time coupling due to ionization of air, even if the losses due to the ionization of the medium are taken into account. Actually, several physical effects couple the various time slices in the pulse, which makes dependent the potential well of a slice on the dynamics of the preceding slices. Couairon (2003c) showed in particular that this simplified model represents femtosecond filamentation as an intrinsically periodic propagation. In the presence of dissipation, the same model leads to damped pseudo-periodic oscillations which systematically leads to overestimations of the filamentation distances.

In the general case, the power is not preserved and the time slices are not independent from each other. This amounts to interpreting the evolution of the beam widths corresponding to the different time slices as the damped motion on a deformable surface of interacting particles. Each temporal slice of the pulsed beam makes damped oscillations with a pseudo-period which is modified along the propagation. The various slices, initially in phase rapidly make incoherent oscillations, leading in principle to a totally chaotic behavior. Integration in time allows the superposition of all the temporal slices to obtain the fluence distribution of the beam as a function of the propagation distance which is primarily determined by the most focused part of the beam and may exhibit a beam of practically constant diameter in good agreement with observations of filamentation. It should not be forgotten, however, that all these semi-analytical models are usually applied with a prescribed Gaussian beam shape in the transverse direction and are therefore inherently unable to reproduce the possible ring-like structure generated by beam defocusing of a filamenting pulse, unless a different test function is chosen from the beginning. One of the possible approach in this direction is a perturbative approach (Fibich, 1996; Arevalo and Becker, 2005b) accounting for the excess power which is not kept in the inner part of the self-focusing beam and enters an outer component reintroduced via the spatial phase of the beam.

3.2. Main results obtained by numerical simulations

3.2.1. Numerical simulations of filamentation in air

Fig. 22 gives typical results of numerical simulations obtained with a simulation code which has been shown to reproduce experimental results accurately in several experimental situations (Couairon et al., 2002, 2003, 2005b, 2006c; Tzortzakis et al., 2001a; Méchain et al. 2004a, b; Sudrie et al., 2002; Couairon, 2003c; Faccio et al., 2005b; Dubietis et al., 2006a). Fig. 22(a,b) show the beam width as a function of the propagation distance for an ultraviolet ($\lambda_0 = 248$ nm) and an infrared ($\lambda_0 = 800$ nm) pulse ($R(z)$ is the half width at half maximum (HWHM) of the fluence distribution $F(r, z) \equiv \int_{-\infty}^{+\infty} I(r, z, t) \, dt$). The results exhibit a first part (purely Kerr compression) where the beam is self-focused and collapses on itself at the end of this stage. The local intensity of the electric field strongly increases and becomes sufficient to ionize the molecules of air. Ionization of the molecules of oxygen and of nitrogen requires the simultaneous absorption of 3–4 ultraviolet or 8–11 infra-red photons. A non-negligible ionization of air requires a threshold intensity and therefore appears very abruptly, in the center of the beam, as indicated by the dashed curves in Fig. 22(c,d). The generation of a plasma of free electrons and ions by multiphoton ionization acts like a saturating mechanism. Actually, two effects are efficient simultaneously in the saturation process: plasma defocusing only acts on the trailing part of the pulse but multiphoton absorption, the energy losses associated with plasma generation, act on the high intensity part of the beam. These effects limit the peak intensity of the laser in the filament to a value in the vicinity of a few 10^{13} W/cm^2 for infrared (800 nm) pulses, with an associated electron density of a few 10^{16} cm^{-3}, and less for UV pulses. These saturation levels depend on the ionization rates which are used in the computation.
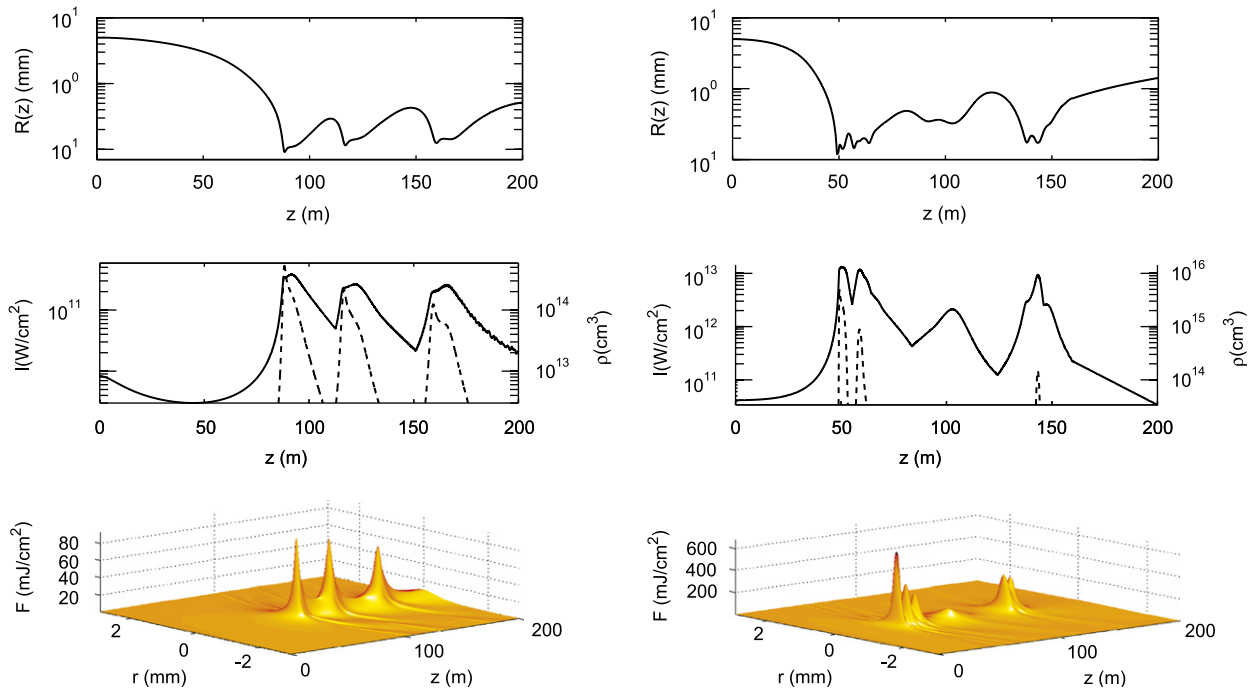
Fig. 22. Propagation of a collimated beam (diameter of 1 cm) in air for an ultraviolet laser pulse (first column: $\lambda = 248$ nm, $\tau_{\text{FWHM}} = 100$ fs, 1 mJ) and for an infrared laser pulse (second column: $\lambda = 800$ nm, $\tau_{\text{FWHM}} = 100$ fs, 3 mJ). The initial power of the pulse is slightly larger than the critical power for self-focusing $P_{\text{cr}}^{\text{UV}} = 0.12$ GW, $P_{\text{cr}}^{\text{IR}} = 3.2$ GW. The beam radius $R(z)$, the maximum intensity (solid curve, left axis), the density of free electrons on-axis (dashed curve, right axis) and the fluence distribution are plotted as a function of the propagation distance. According to Couairon and Mysyrowicz (2006).

Here, the Mishima et al. (2002) formulation has been used. Higher intensities up to 10^{14} W/cm^2 and electron densities up to 10^{17} cm^{-3} can be obtained with different ionization rates (Couairon et al., 2002; Couairon and Bergé, 2002). While a complex space–time dynamics occurs, the numerical simulations show a competition between focusing and defocusing effects taking place in the transverse diffraction plane, which leads to the formation of a filament with an average diameter of a few hundreds of μm. Each pinching of the beam by the optical Kerr effect causes multiphoton absorption and ionization (mainly oxygen is ionized), which involves defocusing and an increase in the beam width. This process persists in principle as long as the power of the beam exceeds the critical power for self-focusing. The intense core of the beam contains a fraction of a few percent of the beam energy. Most of the beam energy is contained in the feet which feed the core. During the self-guided propagation, the energy losses are weak and the pulse undergoes important structural modifications. Indeed, the pulse tends to adjust its size in the vicinity of an intensity close to the ionization threshold. The number and the frequency of the rebounds of ionization, intensity and fluence (Fig. 22(e,f)) depend on the initial conditions, in particular of the convergence of the beam and its size.

Fig. 23 shows another example where a 5 mJ, 50 fs, 800 nm laser pulse was shown to generate a long self-guided channel of light although the plasma is generated by bursts and does not form a continuous channel (Couairon et al., 2002). Ionization of nitrogen is almost negligible with respect to ionization of oxygen since there is a departure of two decades in their respective contribution to the total electron density. Similar $(2 + 1)$D simulation results that show the space–time reshaping of infrared laser pulses undergoing filamentation in air can be found in several publications (Kandidov et al., 1997b, 2003a, b; Lange et al., 1998c; Mlejnek et al., 1998a; Chiron et al., 1999; Bergé and Couairon, 2000; Couairon and Bergé, 2002). These results are generic in the sense that the details of the model such as the importance of a specific physical effect can change the overall stability of the generated filament or some features such as the periodicity of the refocusing cycles but not the general scenario. In particular, Nurhuda and van Groesen (2005) have shown that modifying the balance between the instantaneous and the delayed contribution in the Kerr effect does not affect this filamentation scenario.
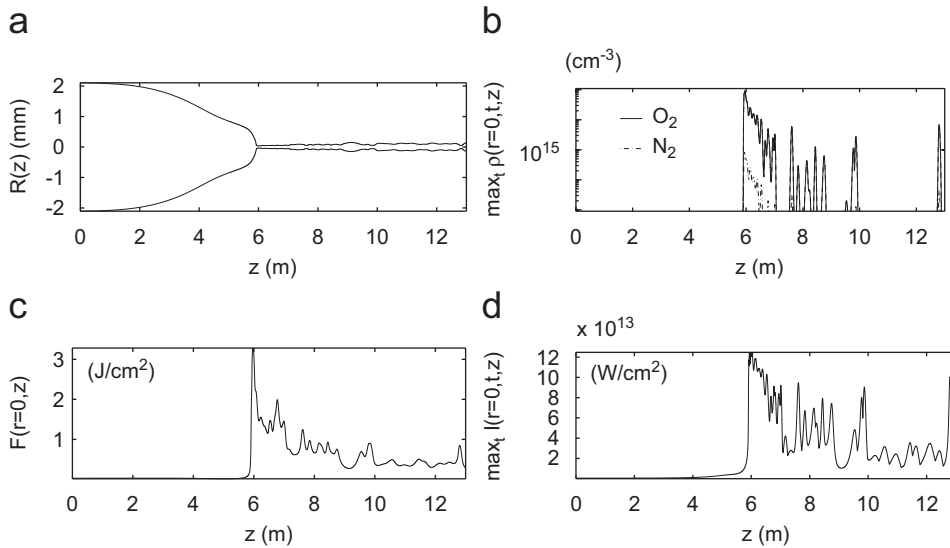
Fig. 23. Propagation of a collimated beam in air. The initial power of the pulse ($\lambda = 800$ nm, duration $= 50$ fs) is about 25 P_{cr}. (a) The diameter of the beam $2R$, (b) the maximum density of free electrons, (c) the on axis fluence and (d) the peak intensity on axis are plotted as functions of the propagation distance. From Couairon et al. (2002).
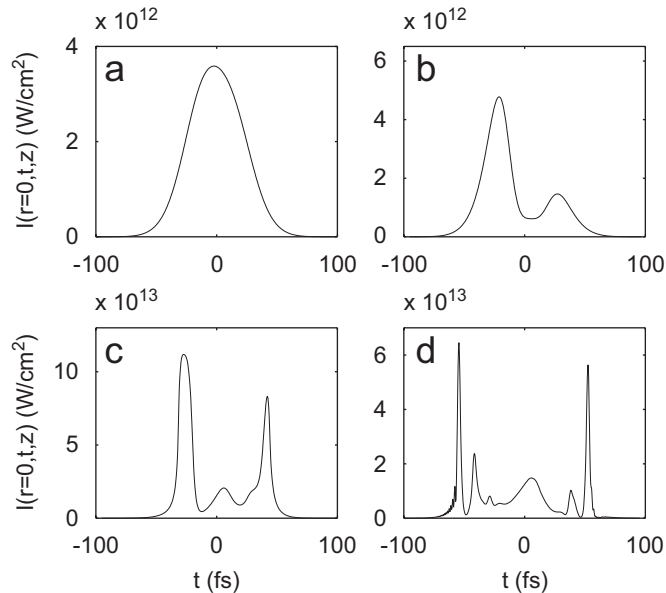
Fig. 24. Pulse temporal profile at successive propagation distances during filamentation. (a) The initial pulse. (b) The pulse splits into two when it propagates beyond the nonlinear focus. (c) The substructures are shortened and stiffened. (d) Shortening and stiffening are reinforced and accentuated during the propagation in the form of a filament. From Couairon et al. (2002).

Fig. 24 shows the evolution of the temporal profile of the pulse in the case $P_{in} \simeq P_{cr}$. At the beginning of the filament, the pulse is split into two shorter pulses. This temporal splitting originates from two contributions: The energy depletion of the center of the beam due to multiphoton absorption leads to an inherent splitting in time when the collapse is arrested (LeMesurier, 2000). To a lesser extent, the splitting in time also follows from the arrest of collapse by GVD (more efficient in the UV). The second contribution arise from a spatial effect due to the plasma defocusing of the
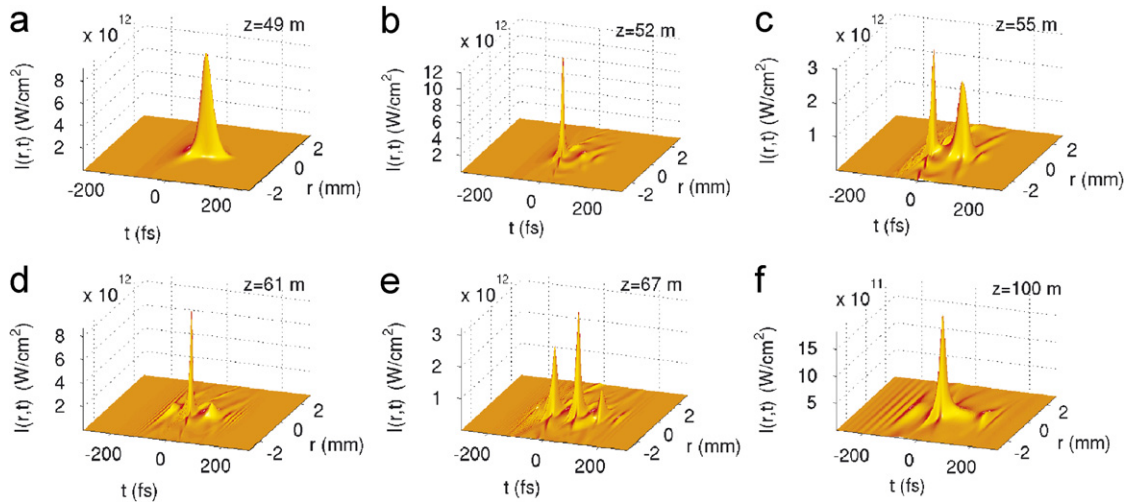
Fig. 25. Evolution of the temporal profile of the pulse during the nonlinear propagation of the same IR pulse as in Fig. 22. The initial pulse (a) undergoes contraction in the transverse diffraction plane (b) plasma defocusing of its trailing part (c) which is subsequently refocused by the optical Kerr effect (apparent splitting beyond the nonlinear focus) (d,e,f) During the propagation in the form of a filament, successive focusing–defocusing cycles reinforce and accentuate the shortening and the stiffening of the pulse beyond the nonlinear focus. From Couairon and Mysyrowicz (2006).

trail of the pulse and its subsequent refocusing by the optical Kerr effect. This effect has been called *Dynamic Spatial Replenishment* (Mlejnek et al., 1998a, 1999b, c, 2001; Moloney et al., 2000) and constitutes the main reason of the asymmetry in time. The sequence of Fig. 25 shows the dynamic evolution of the pulse with the appearance of shorter subpulses through these recurrent splitting in time. In this example, the temporal profile of the pulse is multipeaked. In general, it can be rather complex during the filamentation process. Chegotov (2002a, b) predicted that an ultrashort laser pulse penetrating an ionizing gas should undergo strong space–time modulation of its intensity distribution due to the depletion induced by multiphoton absorption. Kandidov et al. (2000) have shown numerically that the filamenting pulse decays into a train of spikes as it propagates. However, as will be seen below, clean isolated pulses can be generated at specific locations and under well controlled conditions, their duration can be as short as a single cycle.

3.2.2. Numerical simulations of UV filaments in air

Ultraviolet filamentation has attracted considerable interest for long range propagation. Some authors have pointed out that by using UV pulses, one should obtain kilometer long continuous ionization channels (Zhao et al., 1995b). The basic argument is the following: the propagation loss due to inverse bremsstrahlung scale as $I\lambda^2$; therefore, an order of magnitude reduction is expected in the UV (Schwarz and Diels, 2001; Schwarz et al., 2002). Taking into account the higher multiphoton absorption losses of a UV pulse as compared to an infrared pulse, the authors estimate global losses of 40 μJ/m of propagation. To achieve long distances, long pulses might compensate the energy losses For instance, with a ns pulse of 200 mJ energy, one expects a plasma channel generation over a distance of 5 km (200 mJ/(40 μJ/m)) (Schwarz et al., 2000). According to this argument, filamentation should be sustained even with a nanosecond pulse because of the weaker laser plasma interaction. Schwarz and Diels (2001) predict quasicontinuous plasma channels generated over a kilometer. Note, however that this argument assumes that all the energy in the input beam is used for ionization in the filament core and that continuous filaments are stable. More recently, Niday et al. (2005) have tackled the same problem and have addressed the stability of such ns filaments. The authors have used three different approaches: First, following Couairon and Bergé (2000) and Bian and Antonsen (2001), they performed a linear spatiotemporal stability analysis of plane and monochromatic waves supported by the model (28) and (31), in which plasma absorption and recombination were added as in Eqs. (42) and (44). Second, they transformed the model into a monochromatic propagation equation by changing the plasma contribution into a high order saturation term and found the ground state, or stationary solution, in the absence of MPA and plasma absorption. They solved numerically the evolution equations of the perturbations around this ground state. Third, Niday et al. (2005) performed direct numerical simulations of the original model initiated by a 400 ps super-Gaussian pulse with a Gaussian beam
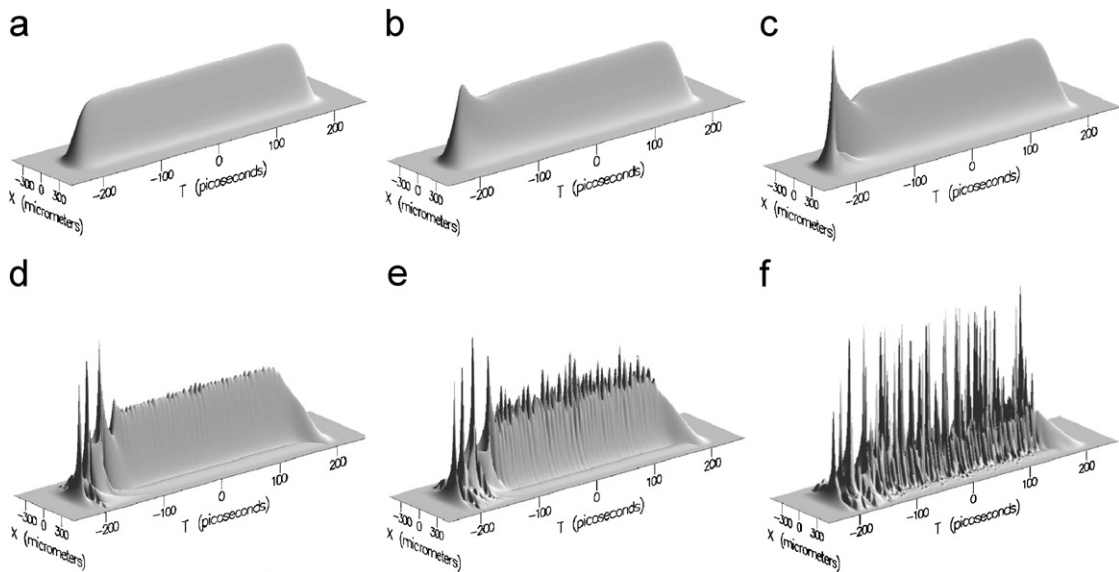
Fig. 26. Development of the modulational instability in the filamented ns pulse, leading to a train of shorter pulses (Niday et al., 2005).

width of $120\,\mu m$ and a noise seed (0.01% random amplitude variations). The spatial and temporal bandwidth covered the bands of unstable wavenumbers and frequencies identified from the previous analyses. The results of the three methods indicate that a ns continuous filament seeded by noise should temporally split into substructures (see Fig. 26) and eventually undergo diffraction and beam defocusing after propagation over a length scale in the meter range, thus making unlikely the existence of a stable continuous long duration filament.

Tzortzakis et al. (2000b, 2001b) have simulated numerically the filamentation of 248 nm, 450 fs laser pulses. They found that the optical Kerr effect and multiphoton absorption play crucial antagonistic roles, the first by acting as an intensity amplifier by means of beam self-focusing and the second by acting as an intensity limiter. With UV pulses, in which the ionization cross section is much higher, since it requires 3–4 photons instead of 8–10 at infrared wavelengths, beam self-focusing is hindered much earlier. The resulting situation is simpler than that predicted by the multiple focusing–defocusing cycles, and closer to a true equilibrium, with a lower clamping intensity in the UV filament. Fig. 27 shows the beam width, using a UV laser (248 nm) (Tzortzakis et al., 2001b). Filamentation and intensity clamping occurs earlier than at IR wavelengths during the collapse of the beam on its axis. The width of resulting filament is larger than for an infrared filament. The fluence profiles exhibit a ring formation during self-focusing, due to the fact that the input beam was super-Gaussian so as to mimic experimental beams.

3.2.3. Infrared filamentation in argon

From numerical simulations in argon at various pressures, Mlejnek et al. (1998b) identified several propagation regimes. For high pressures ($p \gg 1\,atm$), self-focusing, normal GVD and multiphoton absorption are the prevailing physical effects and lead to superbroadening, and pulse splitting owing to the arrest of collapse by GVD. For low pressures ($p \ll 1\,atm$), plasma defocusing and tunnel ionization becomes the prevailing physical effects resulting in plasma induced blueshifting. This regime was also studied by means of analytical models described in Section 2.4.3 (Liu and Tripathi, 2000; Gupta and Sharma, 2003). At intermediate pressures, both self-focusing and plasma induced effects compete and make long propagation distances possible. This regime was the first identification of the *dynamic spatial replenishment* process as a mechanism generating multiple subpulses, which clearly differs from that of pulse splitting due to GVD. Once split, the remaining power in a subpulse may exceed P_{cr} and lead to subsequent self-focusing and propagation in the form of a filament. Nurhuda et al. (2002a) confirmed this scenario and demonstrated pulse splitting and pulse shortening from 200 to 35 fs (see the computed temporal profiles in Fig. 28).

The result is important for two reasons: first, it shows that the dynamic spatial replenishment process is valid in argon where there is no delayed contribution to the Kerr effect. Second it shows that the sub-pulses generated by this multiple
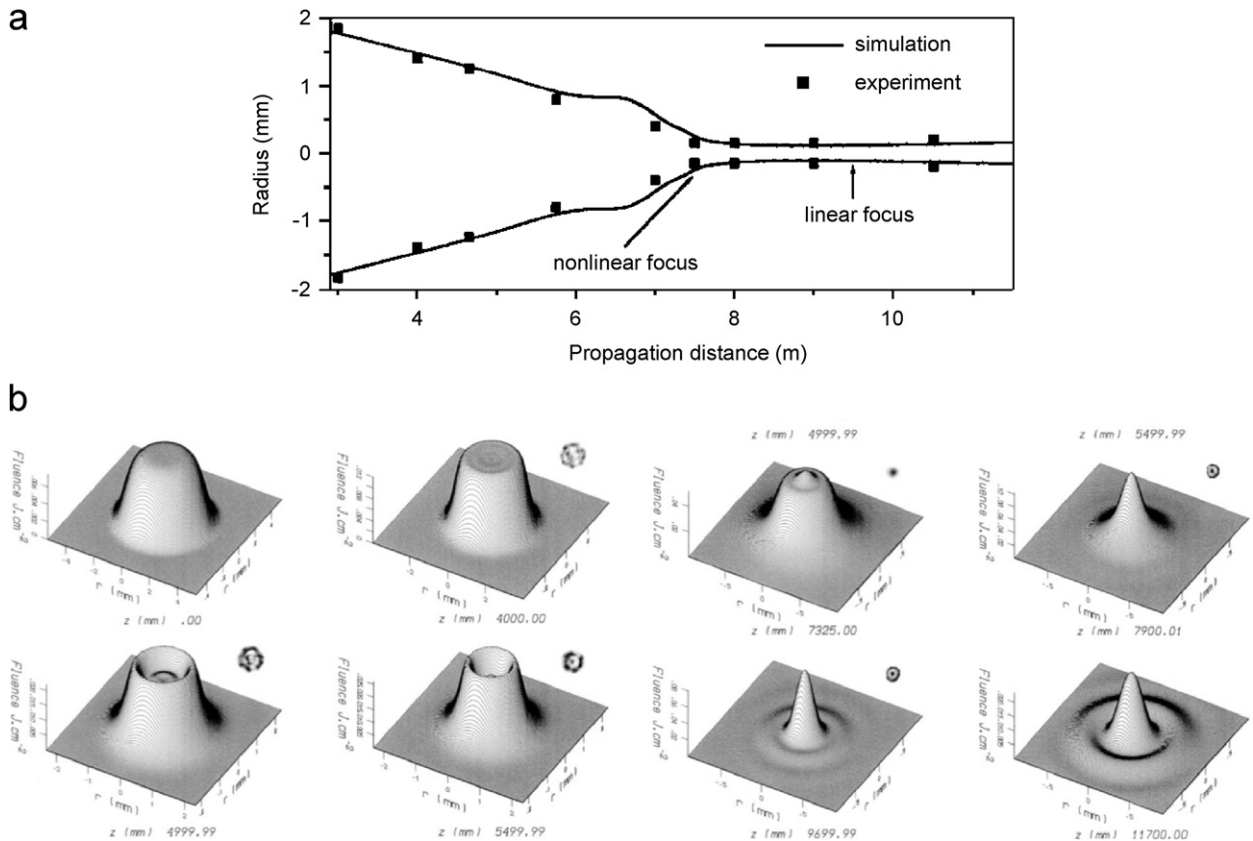
Fig. 27. (a) Comparison between the diameter of a UV filament (248 nm) and simulations, according to Tzortzakis et al. (2001b). (b) Three-dimensional fluence simulated profiles for different distances. Insets: experimental burning spots of the laser on photographic paper at the same distances. The sizes of the burning spots are not to scale. From Tzortzakis et al. (2000b, 2001b).
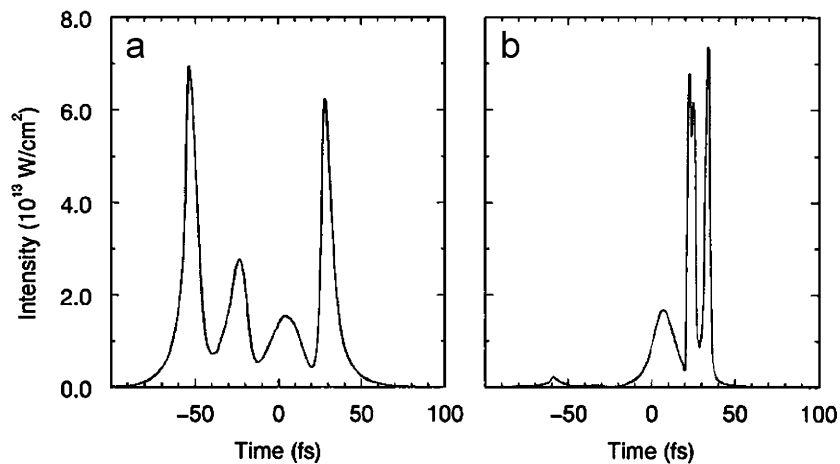
Fig. 28. On-axis pulse temporal profiles obtained by numerical simulations of filamentation in argon at 2.5 atm for a focused ($f = 2$ m), 60 fs, 1.2 mJ, 789 nm input pulse. (a) At the focal point and (b) 10 cm beyond the focus. According to Nurhuda et al. (2002a).
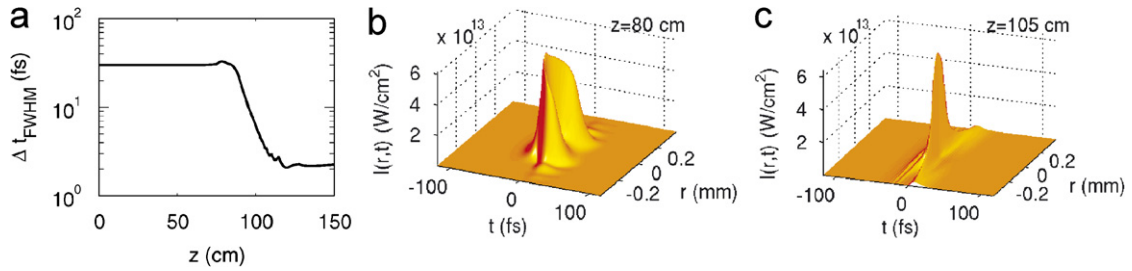
Fig. 29. (a) Pulse duration (FWHM) computed on the intensity integrated radially over 100 μm during the filamentation of a 25 fs laser pulse in an argon pressure gradient. According to Couairon et al. (2005a). (b–c) Intensity distributions computed at the beginning (b) and at the end (c) of the pressure gradient.

splitting process can lead to nearly isolated, intense short pulses, a process opening the way to pulse shortening via filamentation.

3.2.4. Pulse self-compression by filamentation

Going one step further, very recently, the possibility to generate isolated nearly single cycle pulses by filamentation in noble gases has been demonstrated both theoretically (Couairon et al., 2006a) and experimentally (Hauri et al., 2004), a result that might impact several domains related to high-field physics and attophysics. Fig. 10 in Section 1.3.6 shows the computed evolution of a 1 mJ, 25 fs infrared laser pulse focused in the middle ($z = 95$ cm) of a gas cell filled with argon at 0.8 atm. The complex structure in space and time reflects the highly nonlinear filamented regime which leads to successive splitting in time and eventually forms a 3 fs isolated structure at the end of the filament, with a peak intensity of about 5×10^{13} W/cm^2. This pulse self-shortening process can even be simplified by using a gas density gradient, achieved by a control of the pressure along the propagation distance. In this case, numerical simulations show that three parameters (maximum gas density, length of the density gradient and position with respect to the focus of the lens) are available to switch on and off the filamentation process, and finally ensure the generation of a single cycle pulse in vacuum. Fig. 29(a) shows the evolution of the pulse duration as a function of the propagation distance when the gas pressure increases up to 0.5 atm at 85 cm and decreases back to zero, the FWHM length of the pressure gradient being 18 cm (Couairon et al., 2005a). The dynamics in the filament is limited to the self-focusing stage followed by the plasma defocusing stage in the center and trailing part of the pulse, which typically produces the fishbone structure shown in Fig. 29(b) in the (r, t) space. Finally, the decrease of the pressure is equivalent to switch off all nonlinear effects, which leads to the pancake pulse structure shown in Fig. 29(c), i.e., to a 2 fs pulse with peak intensity of a few 10^{13} W/cm^2 at the end of the filamentation stage. The self-shortening process by filamentation is similar to the erosion of the trailing part of the pulse by the generated plasma associated with the steepening of the front part as predicted by Sergeev et al. (1992), Kim et al. (1990).

3.2.5. Simulations of supercontinuum generation

Filamentation leads to extremely short structures of a few fs duration. Correspondingly a large spectrum is generated. Fig. 30 shows a typical example of the spectral broadening which occurs during filamentation. The spectral range of the pulse is broadened by a factor 10 (or more) leading, in the case of the IR pulse (Fig. 30(b)), to the appearance of a continuum of emission covering the visible and extending towards the infra-red domain. The UV pulse (Fig. 30(a)) undergoes a smaller, yet important spectral broadening. This strong spectral broadening is due to self phase modulation, which corresponds to the generation of new frequencies in the spectrum of the laser pulse caused by the temporal variation of the refraction index as $n = n_0 + n_2 I(r, z, t)$. The simplest model accounting for the evolution of the temporal phase links the instantaneous frequencies to the pulse intensity [see Eq. (7)].

Aközbek et al. (2001) have shown that when the self-steepening terms are accounted for in the model, a shock is formed in the trailing part of the pulse which causes strong blue shifting of the spectrum and generates a white light continuum. Kolesik et al. (2003b) have recently shown that the chromatic dispersion of the medium is a key player in determining the spectral extent of supercontinuum generation, thus going beyond the simple SPM theory which states that the spectral extent of supercontinuum is mainly obtained from the Kerr induced spectral broadening and the blueshifting induced by plasma generation. As can be readily seen from Eqs. (10) and (31), the maximum broadening
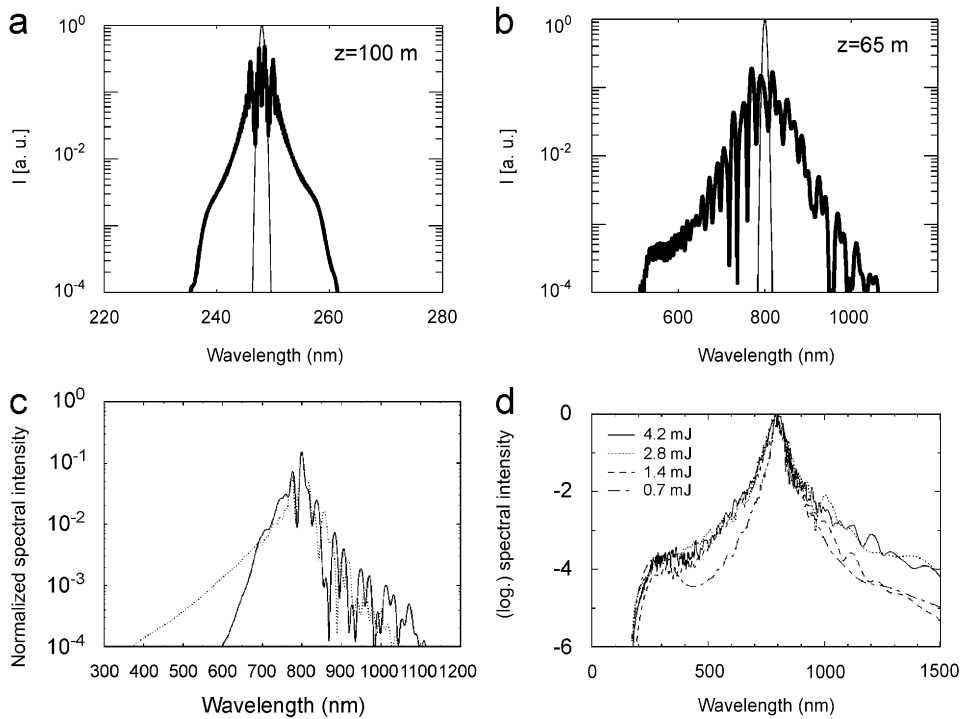
Fig. 30. Spectral Broadening obtained during filamentation of (a) the UV pulse and (b) the IR pulse with the same parameters as in Fig. 22. From Couairon and Mysyrowicz (2006). (c) The power spectra of a filamented pulse at 1.1 Rayleigh lengths are compared in the absence (continuous curve) and in the presence (dashed curve) of self-steepening. From Aközbek et al. (2001). (d) Simulated supercontinuum generation in air at 800 nm for a range of initial pulse energies and a pulse duration $t_p = 144$ fs. From Kolesik et al. (2003b).

scales as $\Delta\omega_{max} \propto I_{max}^K$, where I_{max} is the clamping intensity in the filament. Taking account of the correct chromatic dispersion of the medium is thus an important requirement for quantitative predictions of the spectral broadening in filaments.

Kandidov et al. (2003a) have shown that the supercontinuum generation in air strongly depends on the spatio-temporal phase gradients of the complex amplitude of the electric field. The relative contribution of self-steepening to the spectral broadening is less pronounced in the case of integrated spectra over the whole transverse aperture than in the case of the on-axis spectra. This is due to the high-frequency spectral components generated at the off-axis positions due to the laser-induced plasma production. As shown in Fig. 31, at the beginning of the filamentation the blue wing is mainly formed in the ring at the leading edge of the pulse. Therefore, the conical divergence of high-frequency components dominates in the pulse spectrum (Fig. 31(a)). Later on, the pulse breaks up into two subpulses. At the trailing edge of the second subpulse, the self-steepening is pronounced on the beam axis (Fig. 31(d)). As a result, the high-frequency components that appear in the pulse spectrum do not have the angular divergence and propagate mainly along the axis (Fig. 31(b)) (Kandidov et al., 2003a, 2004b; Kosareva et al., 2003).

3.2.6. Influence of the chirp of the input pulse

Golubtsov et al. (2003) have shown by means of numerical simulations that it is possible to control the filamentation length and the supercontinuum generation by modifying the temporal chirp of the input pulse. Fig. 32 shows the fluence patterns, the peak intensity and the energy content of the generated high frequency part of the spectrum along the propagation distance for infrared, 60 mJ, pulses in air. The minimum duration is 21 fs and decreasing input chirp from positive to negative values were used. Large positive or negative chirps yield long pulses with lower peak power than the transform limited pulse having the same energy; the filament obtained from the chirped pulses therefore starts at a larger distance from the laser output than the position of the collapse obtained for an unchirped pulse with the same energy. With large positive or negative chirps, the filament is found to be longer. The generation of short wavelengths
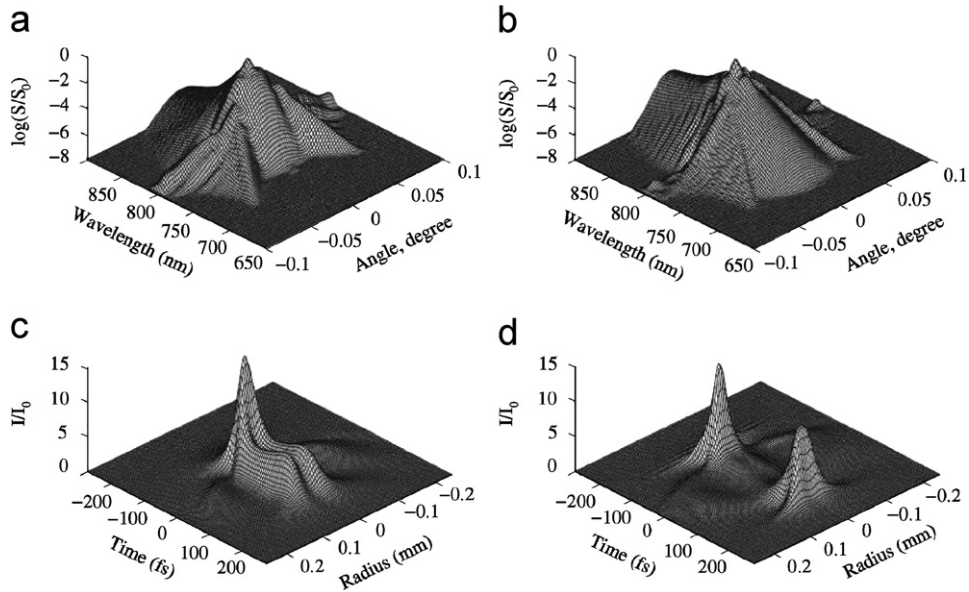
Fig. 31. Frequency angular spectrum (a, b) and spatio-temporal distribution (c, d) of the pulse at two propagation distances: (a, c) $z = 0.43L_d$; (b, d) $z = 0.6L_d$. In the simulations the pulse duration was $\tau_{FWHM} = 250$ fs, the input peak power was $6.3P_{cr}$ and the input beam radius $w_0 = 0.25$ mm. From Kandidov et al. (2003a).
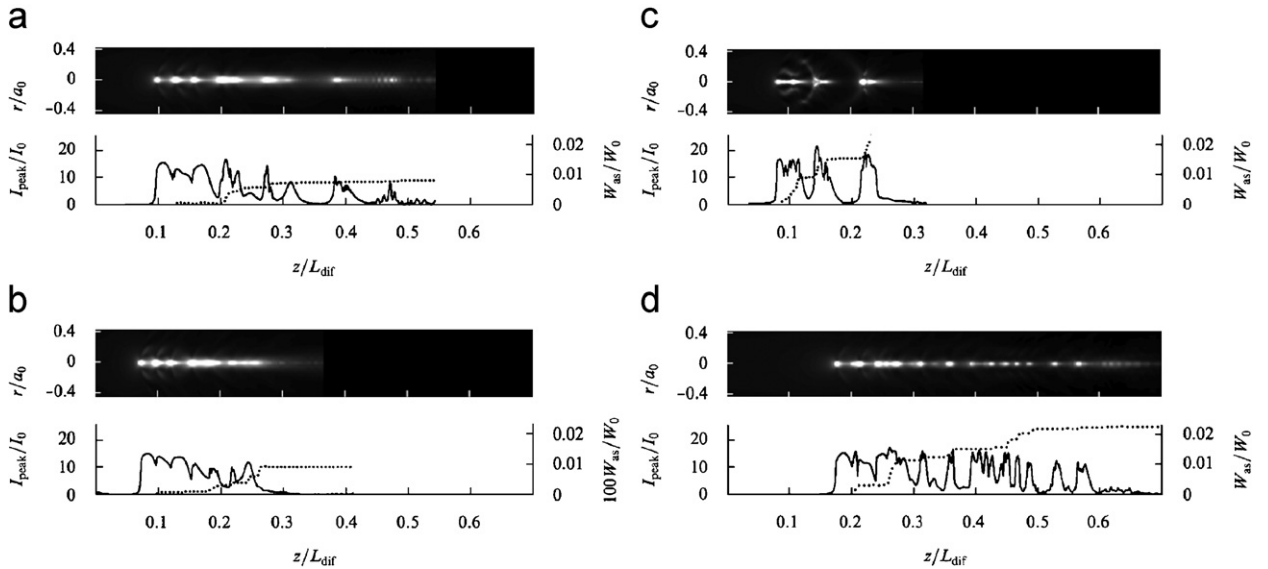
Fig. 32. Fluence distribution $F(r, z)$ (gray level images) and peak intensity (continuous curves) vs. propagation distance in air of a 800 nm, 60 mJ laser pulse undergoing filamentation. The dashed curves indicate the energy content of the short wavelengths in the supercontinuum. Input pulse durations: (a) $t_p = 100$ fs with positive chirp. (b) Transform limited with $t_p = 21$ fs. (c) $t_p = 150$ fs with negative chirp. (d) $t_p = 600$ fs with negative chirp. According to Golubtsov et al. (2003).

is more efficient for a negatively chirped pulse with a conversion efficiency larger than 10^{-2} (two orders of magnitude larger than with positive chirps), over a wide range of pulse durations from 100 to 800 fs. The dashed curves indicate that the energy conversion into the supercontinuum is determined by the formation of a large numbers of intensity peaks with large gradients of the phase modulated pulse along the filament.
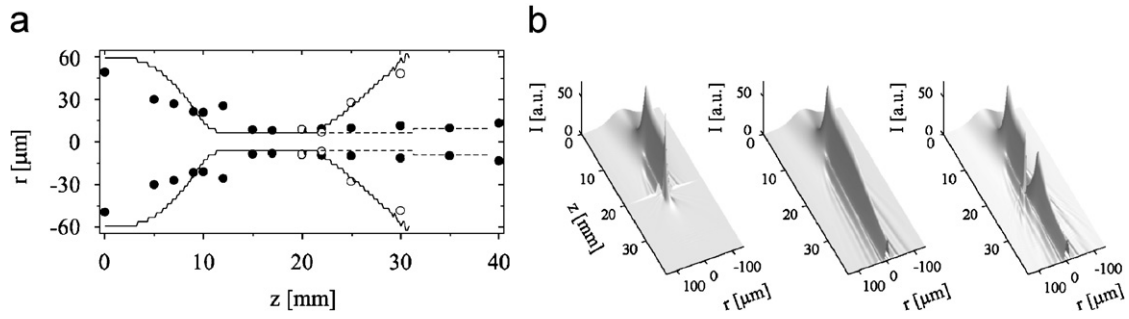
Fig. 33. (a) Beam radius (HWHM) vs. z: experiments (full circles) and simulation (dashed curve). Open circles and solid line: same results with a 55 μm pinhole transmitting the filament core only (b) transverse intensity profiles from simulations for the clipped (left) free (center) and stopped (right) filament for $P_{\mathrm{in}} = 15 P_{\mathrm{cr}}$. From Dubietis et al. (2004a).
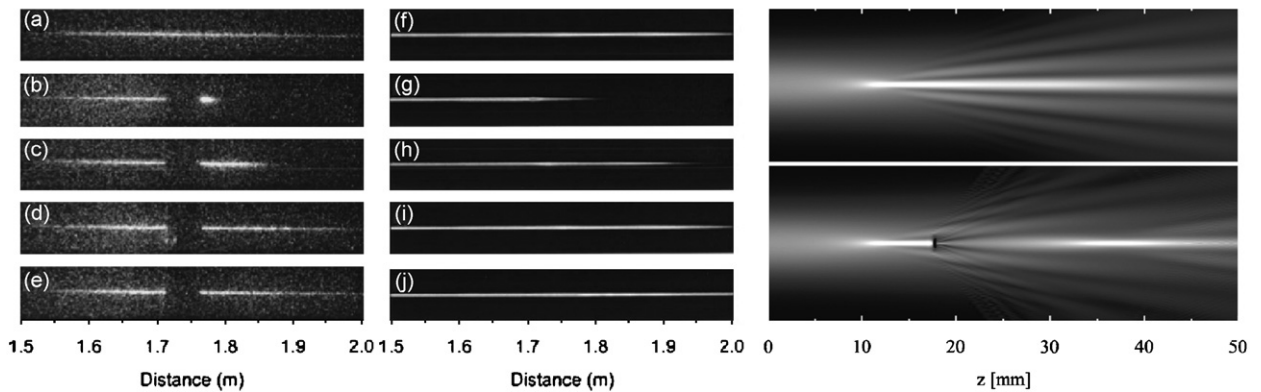
Fig. 34. Left column, images of the nitrogen fluorescence signal recorded by an intensified CCD camera. Middle column, electron density distribution from numerical simulations. (a), (f) Free propagation; (b), (g) pinhole diameter 220 μm; (c), (h) pinhole diameter 440 μm; (d), (i) pinhole diameter 1 mm; (e), (j) pinhole diameter 2 mm. From Liu et al. (2005f). Right column: Numerical results for (top) free and (bottom) blocked at $z = 18$ mm filament propagation in water. Transverse dimension, 400 μm. From Dubietis et al. (2004c).

3.2.7. Self-reconstruction of filaments

The proposition that the high intensity core of a filament is sustained over long distances owing to the extended low intensity part of the beam which constitute an energy reservoir refilling the hot core was first made by Mlejnek et al. (1999a). The redistribution of energy in the transverse diffraction plane during filamentation was shown to take place over a region greatly exceeding the volume of a filament core and even exceeding the initial beam diameter (Kandidov et al., 2003a, b). The scenario of the energy reservoir, however, was practically ignored until experiments demonstrating that filaments are unaffected by water droplets were performed (Courvoisier et al., 2003). These experiments triggered numerical simulations of filamentation in air in the presence of droplets, modeled by a small central stopper of appropriate size which annihilates the whole hot core (Kolesik and Moloney, 2004b). The authors showed that the robustness of the filament comes from the transverse low intensity pedestal that is able to rebuild the hot core after it encountered a droplet. The consequence of this property is the ability of the energy reservoir to regenerate the filament core when it is attenuated, even in the extreme case of a central stopper (Mlejnek et al., 1999a; Courvoisier et al., 2003; Kolesik and Moloney, 2004b; Liu et al., 2005e,f). The concept of the energy reservoir turned out to be a universal feature of filaments. It was found to be valid for filamentation in water (Dubietis et al., 2004a, b). Figs. 33 and 34 show the results of numerical simulations compared to measurements of diaphragmed or blocked filamentation in water. A clipped filament is clearly destroyed after the diaphragm whereas a central stopper extinguishes the filament only over a short distance beyond which the self-healing process rebuilds the filament. Interestingly, these simulations do not
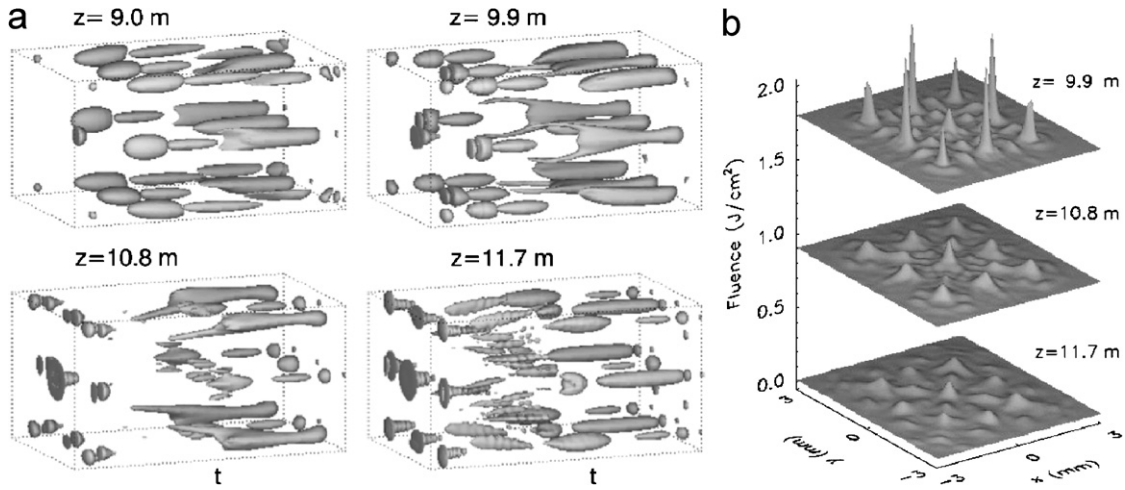
Fig. 35. Numerical simulations show the appearance of multiple filaments whose distribution changes with the propagation distance. (a) Iso-surface for the pulse intensity showing the space–time distribution of the filaments at the indicated propagation distances. The leading edge of the pulse is on the left side of the temporal axis. The filaments were found to be generated on the leading edge but to decay and recur on the trailing edge. (b) Time integrated intensity at the same distances. The input power was $P_{in} = 35 P_{cr}$. According to Mlejnek et al. (1999a).

take into account plasma generation, thus indicating that plasma defocusing is not necessary in the self-healing process. The main physical mechanisms in this process were shown to be self-focusing and multiphoton absorption. Dubietis et al. (2004a, b) outlined the key active role played by MPA in supporting the filament dynamics. In particular, MPA was proposed to be considered as a distributed loss channel in the nonlinear sample which leads to a self imaging effect similar to the that involved in the Arago spot experiment (Dubietis et al., 2004b; Gaižauskas et al., 2007). As proposed in a different context by Polyakov et al. (2001), this self-imaging effect relies on the interplay between nonlinear losses and self-focusing which generates a nonlinear phase modulation mediated by propagation. This phenomenon acts so as to drive the beam shape toward a nonsoliton-like structure (Dubietis et al., 2004a), identified later as a conical wave called *nonlinear unbalanced Bessel beam* (Porras et al., 2004).

3.2.8. Multifilamentation

Most situations described so far relate to a pulse having an incident power around P_{cr}, the threshold power for filamentation. If $P_{in} \gg P_{cr}$, multifilamentation occurs triggered by short range modulational instability as proposed originally by Bespalov and Talanov (1966). Irregularities and noise in the incident beam profile, even modest, are rapidly reinforced and lead to a break-up of the beam in several hot spots which act as nuclei for several filaments. This process supports a seemingly random nucleation of hot spots or filaments, which is not necessarily observed in experiments on multiple filamentation (Hao et al., 2006). If the noise is stochastic, the transverse distribution of filaments is expected to be random. Mlejnek et al. (1999a) performed the first realistic $(3 + 1)$-dimensional simulations about multiple filamentation and called *optical turbulence* this propagation regime, which describes rather well the self-guided propagation of an initially collimated beam over long distances (see Fig. 35). The picture proposed in the optically turbulent regime is that of a large collection of coexisting collapsing wavepackets sustained by the background energy reservoir and suffering dissipation at small spatial scales via a physical regularizing mechanism. It is similar to the strong turbulence scenario (Robinson, 1997), irrespective of the physical origin of the process.

Yet, modulational instability also leads to the selection of a specific transverse wavenumber $k_\perp^{opt}$ (see Section 1.2.13) and length scale $d_{fil} = 2\pi / k_\perp^{opt}$ which should appear as a main feature in the filamentation patterns. The question whether multiple filamentation is only featured by the random noise therefore led to different studies demonstrating that several possibilities exist to organize the multiple filamentation patterns, as shown in Section 3.2.11.

Using large negative initial chirps so as to delay the beginning of the filamentation process, it was shown numerically by means of $(3 + 1)$D simulations that the effect of azimuthal perturbations on input beam traversing
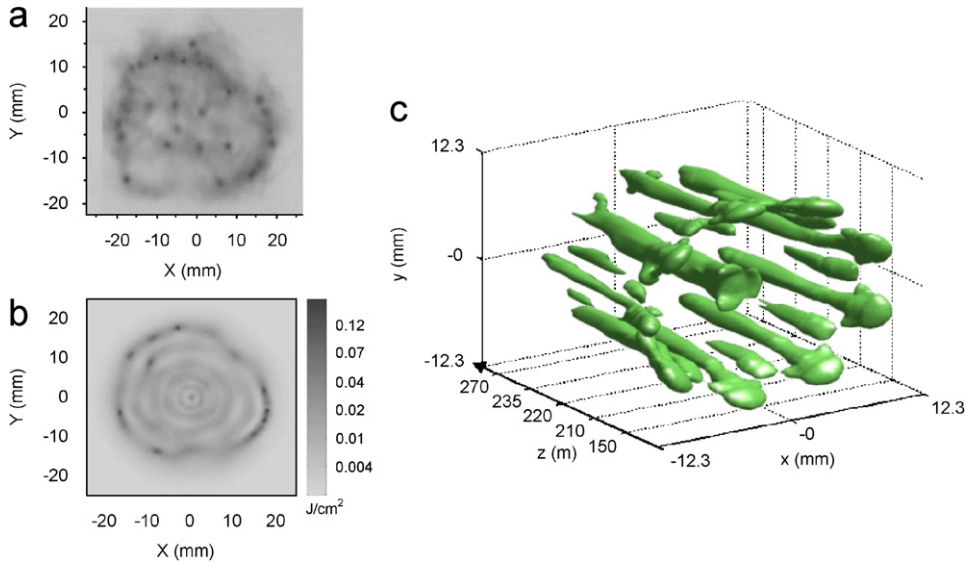
Fig. 36. (a) and (b): Comparison between the multiple filamentation patterns obtained in (a) experiments and (b) $(3+1)$D simulations after propagation over 68 m of a 190 mJ, 800 nm laser pulse stretched to 1.2 ps by a negative chirp. From Méchain et al. (2005a, 2004a). (c) Multiple filaments predicted by $(3 + 1)$D simulations. The iso-surfaces for the fluence distribution are shown for a 150 mJ, chirped 500 fs, 800 nm input pulse whose initial beam includes azimuthal perturbations of order 10. From Méchain et al. (2004a).

a circular diaphragm leads to long and intense light filaments that mutually interact via the background energy reservoir (see Fig. 36(c)). The pattern in Fig. 36(a) was obtained during an horizontal filamentation campaign (Méchain et al., 2005a, 2004a) which led to the observation of weakly ionizing filaments over distances exceeding 2 km, connected by a network of moderately intense energy, clearly visible in Fig. 36(a). Although this network itself forms in a quasi-linear propagation regime, it indicates the part of the beam where energy started to accumulate and which will therefore preferentially feed the filaments. Fig. 36(b) shows the pattern obtained numerically from $(3 + 1)$D simulations starting with the beam intensity measured at the output of the laser, which exhibits good agreement with the measurement in Fig. 36(a). The multifilamentation patterns posses many of the features shown in the regular patterns numerically obtained with prescribed azimuthal perturbations in the input beam (Fig. 36(c)), although with a symmetry breaking. This demonstrates that the features of the filamentation, i.e. the number and the location of the filaments, are governed by the properties of the input pulse rather than by the amplification of noise originating in shot to shot fluctuations or air turbulence. The energy exchange between the background energy reservoir and the filaments constitutes the process sustaining the propagation, extinction and nucleation of filaments over long distances (Méchain et al., 2005a, 2004a; Rodriguez et al., 2004).

The nucleation process from beam inhomogeneities and the interaction between filaments giving rise to new filaments fed from the energy reservoir were studied from $(3 + 1)$D simulations in several publications (Hosseini et al., 2004a, b; Liu et al., 2004; Kosareva et al., 2005b). It was shown that the filament competition consists of several stages: First, independent filaments form; their independence requires a sufficiently large separation between the beam inhomogeneities leading to the filaments. This separation was quantified analytically by Couairon et al. (2002). Second, the child filaments are nucleated from the interference of the ring structures of the initially developed filaments. Third, the total number of filaments decreases due to energy losses, defocusing and diffraction of the radiation, finally leading to the survival of one filament out of the group. The redistribution of energy in the form of rings around the core of each filament and the interferences between the rings were investigated by Chin et al. (2002a). The authors interpret the nucleation of filaments as due to the intensity peaks resulting from the interference between rings. On the other hand, the scenario of the amplification of modulationally unstable perturbations was investigated numerically from a different perspective (Skupin et al., 2002, 2003). From an analysis of the evolution of azimuthal perturbations growing on intense rotationally symmetric pulsed beams, the authors showed that the dipolar mode leading to a breakup into two filaments has the maximum growth, in agreement with experimental results by Tzortzakis et al. (2001a). The
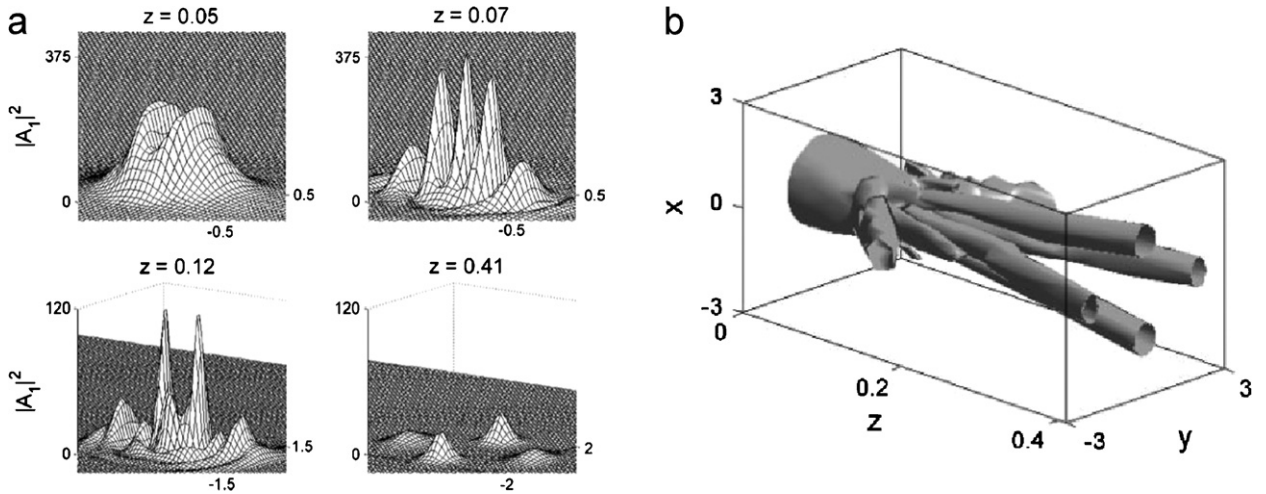
Fig. 37. Numerical simulation of vectorial and nonparaxial multiple filamentation for an input beam having $P_{\mathrm{in}} = 20 P_{\mathrm{cr}}$ and a nonparaxiality parameter of $\epsilon \equiv 1/kw_0 = 0.08$. (a) The normalized intensity is shown at different propagation distances, normalized to the Rayleigh length. (b) The iso-surface of the normalized intensity shows the multiple filaments. From Fibich and Ilan (2001b).

understanding of the different scenarios for the nucleation of child filaments and their competition for the available energy in the background reservoir should ultimately allow the prediction of possible control mechanisms.

It should be noted that for long propagation distances, it is necessary to take into account the effect of air turbulence, which was attempted by Peñano et al. (2004), Kandidov et al. (1999, 2005), Chin et al. (2002b) (see Section 3.2.10).

3.2.9. Beam break-up due to vectorial and nonparaxial effects

A standard explanation for the break-up of a beam into several hot-spots, due to Bespalov and Talanov (1966), states that the multifilamentation process is initiated by random noise or inhomogeneities in the input-beam profile. The inhomogeneities grow according to the modulational instability theory. A few years ago, an alternative theory was proposed: Fibich and Ilan (2001a, 2001b) showed that vectorial effects and nonparaxiality can lead to multiple filamentation when they are properly taken into account in the propagation equation, and might even prevail over the growth of modulationally unstable beam inhomogeneities in the process leading to multiple filamentation. Nonparaxial effects follow mainly from the small component of the electric field along the propagation axis that appears in tight focusing conditions. Vectorial effects arise when nontransverse components are accounted for in the nonlinear polarization (see Section 2.2.9). The nontransverse nature of the electric field then determines a polarization instability likely to be responsible for multiple filamentation. Fig. 37 shows the results of numerical simulations including the effect of vectorial and nonparaxial terms. The input beam with 20 P_{cr} is shown to break-up into multiple filaments whereas it would have kept its initial cylindrical symmetry in the absence of these additional terms. Interestingly, vectorial and nonparaxial effects were shown to prevail over noise in the process leading to multiple filamentation. Simulations with 10% noise added in the amplitude of a Gaussian input beam were shown to lead to a cylindrically symmetric collapse in the absence of vectorial or nonparaxial terms. The main reason of this apparent discrepancy with the Bespalov and Talanov theory lies in the fact that this theory deals with the instability of a plane wave assumed to remain unchanged during the growth of the perturbations, whereas the transverse dynamics of the localized beam precisely dominates the evolution of the noise during self-focusing. Further clarification was given by Fibich et al. (2005a) who determined the threshold power around 100 P_{cr} for the Bespalov and Talanov modulational instability.

3.2.10. Effect of air turbulence

Simulations of the effect of air turbulence on filamentation constitute a challenging problem that has been tackled very partially. The formation and wandering of filaments in the presence of air turbulence have been studied by Kandidov et al. (1999), Chin et al. (2002b) and Shlyonov and Kandidov (2004a, b). A stochastic model of phase screens located along the propagation distance was used to model refractive-index fluctuations in air. From the theory of Kolmogorov
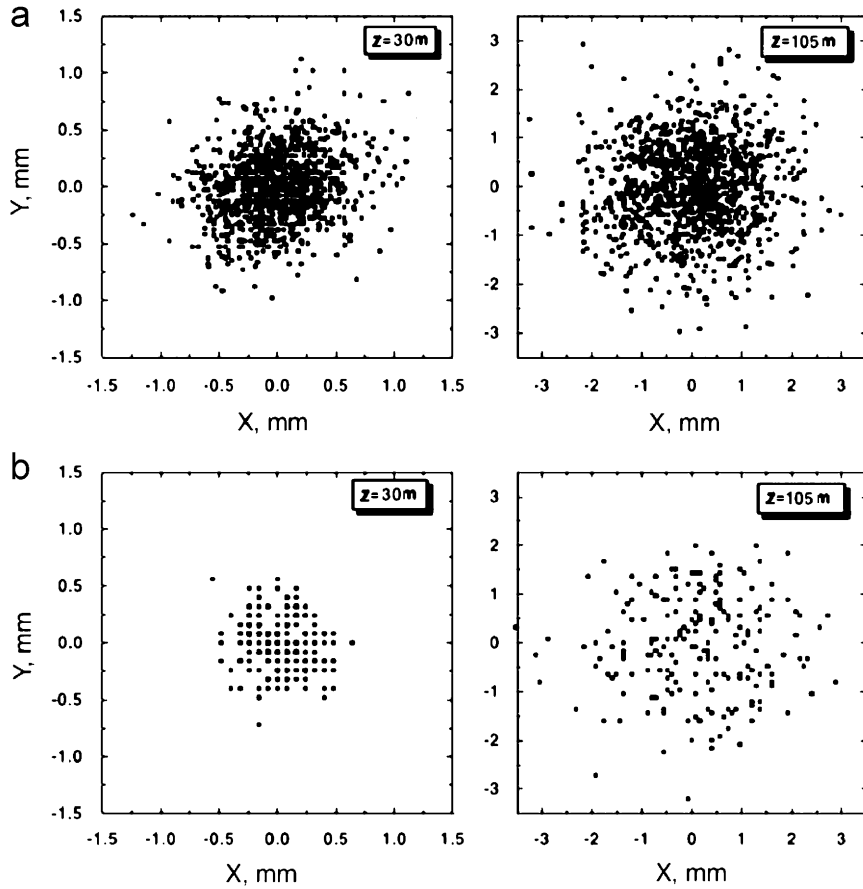
Fig. 38. Comparison between measured and calculated filament positions in the transverse diffraction plane at distances $z = 30$ and 105 m from the laser. (a) Experiments, 1100 shots. (b) Simulations 200 shots. From Chin et al. (2002b).

atmospheric turbulence, the von Karman spectrum Φ_n describes the power spectral density of the refractive index fluctuations

$$\Phi_n(\kappa) = 0.033C_n^2(\kappa^2 + \kappa_0^2)^{-11/6}\exp(-\kappa^2/\kappa_m^2), \tag{146}$$

where n denotes the refractive index, C_n^2 is a structure constant of atmospheric turbulence characterizing the intensity of the fluctuations, which typically lies in the range 5×10^{-13}–1.5×10^{-14} cm$^{-2/3}$, $\kappa_0 = 2\pi/L_0$, $\kappa_m = 5.92/l_0$, $L_0 = 1$ m and $l_0 = 1$ mm are the outer and the inner scales of turbulence.

A Monte-Carlo method was used to model the propagation of several hundreds of laser pulses during the first self-focusing stage. The refraction index fluctuations cause random formation and displacement of the filament (see Fig. 38). In the transverse diffraction plane, the displacement of the center R_c of the filament from the propagation axis follows a Rayleigh distribution law:

$$\Psi(R_c) = 1 - \exp(-R_c^2/w^2). \tag{147}$$

Fig. 39 shows the evaluation of the averaged displacement of the filament center by statistical data processing which is found to be about 0.3–0.5 mm at 30 m and 1.3–1.5 mm at 100 m. These results show the influence of air turbulence during the initial self-focusing stage. Kandidov et al. (2005) have shown that during this initial stage, a competition between the self-focusing hot spots leads to an increase of the distance at which filaments are generated.

The evolution in a turbulent atmosphere of the filaments themselves once formed is still an open question. If the filament core was a localized, soliton-like structure, it would be natural to expect a limited impact of air turbulence on
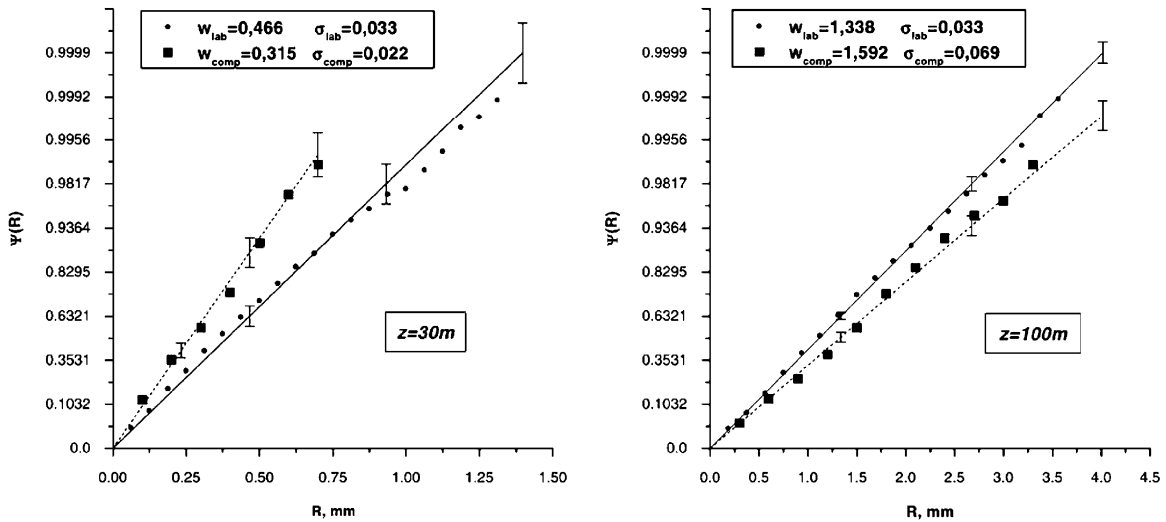
Fig. 39. Distribution function of the displacements of the filament center in the probability scale of the Rayleigh law. Solid curves: experiments. Dashed curves: simulations. The computed or measured averaged displacements are indicated for propagation distances of $z = 30$ and 105 m. From Chin et al. (2002b).

filaments. The core of the filaments would be insensitive to air turbulence due to their diameter much smaller than the inner scale of viscous dissipation. The energy reservoir, however, has centimetric scale and should see the refraction index fluctuations. It is established that filaments are continuously rebuilt from the energy reservoir. Their sensitivity to air turbulence is therefore expected to be correlated to that of the reservoir. It would be interesting to determine which part of the beam plays the dominant role in the location of the filament center over long distances.

In this spirit, Kandidov et al. (2005) have shown that once formed, the filaments interfere and produce intensity maxima on which secondary filaments rise. Fluctuations of the refractive index due to the turbulent atmosphere generate an irregular interference pattern and a stochastic decay of the beam into numerous filaments, the length of which depends on their dynamic competition for the available energy. Recent calculations by Zemlyanov and Geints (2006, 2005b) have shown that the presence of an aerosol layer on the path of the femtosecond laser pulse can drastically reduce the available energy and therefore the filament length when the aerosol layer is located beyond the location where filamentation start.

3.2.11. Multiple filamentation induced by specific features in the intensity or phase of the input beam

As was shown in Section 3.2.9, a novel scenario was proposed by Fibich and Ilan (2001a, b), who showed that vectorial or nonparaxial effects could prevail over the amplification of beam inhomogeneities in the process of multiple filamentation. This scenario requires an efficiency of these physical effects likely to be obtained only under tight focusing conditions. For this reason, it has not yet been corroborated by experiments, but other scenarios, more easily achievable experimentally, have been proposed to control the multiple filamentation process.

The term of *control* means here any external action that allows a modification of the distance necessary to produce multiple filaments or a change of their transverse distribution, without considering whether the control free multifilamentation pattern is deterministic or stochastic. Amplitude and phase distortions caused by defects in optical elements or boundary effects lead to beam inhomogeneities which are reproducible shot to shot. These factors seed a beam breakup which does not change from shot to shot. In contrast, shot to shot fluctuations induced by air turbulence, spatiotemporal quantum noise are factors which might seed a stochastic regime, in possible competition with deterministic effects (Salerno et al., 2004). The control scenarios are based on the idea that the growth of beam perturbations imposed externally can be faster than the growth of the modulationally unstable beam inhomogeneities, whatever the stochastic or deterministic nature of these inhomogeneities. Several control mechanism were found, leading to the demonstration that the nucleation and location of multiple filaments can be organized by acting either on the intensity or on the phase of the input field (Méchain et al., 2004b; Schroeder et al., 2004; Kandidov et al., 2004a). Concerning the action on the
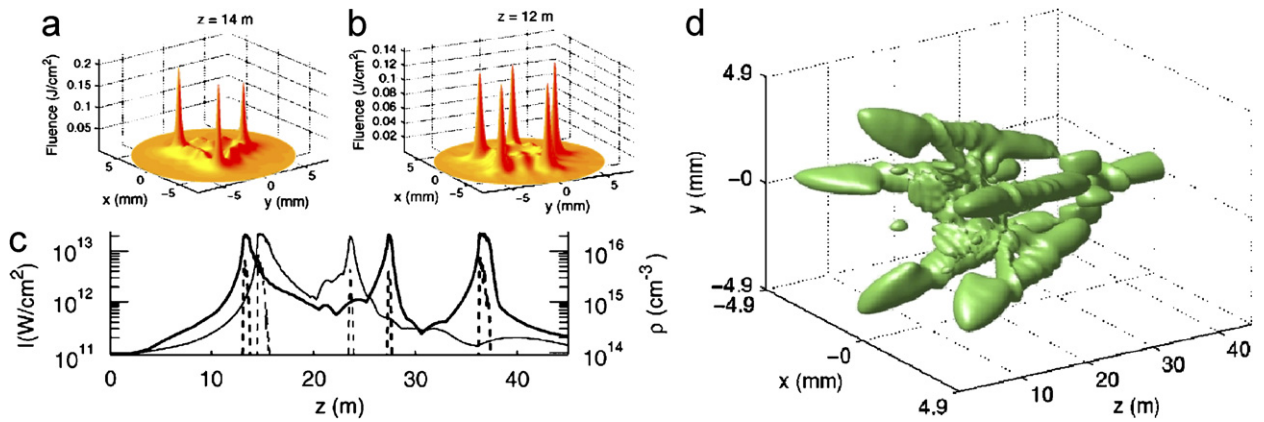
Fig. 40. Organization of multiple filamentation predicted by $(3 + 1)$D simulations. Numerically predicted fluence patterns obtained by sending a 10 mJ, 130 fs, 800 nm laser pulse beyond (a) a trefoil mask or (b) a five-foil mask. (c) Peak intensity (continuous curves, scale on the left axis) and electron density (dashed curves, scale on the right axis) in the most intense filament for the cases of the trefoil (fine curves) and the five-foil (thick curves) mask. (d) Iso-surfaces for the fluence distribution $(0.2 \, \mathrm{J/cm^2})$ are shown for the laser pulse whose beam is initially reshaped by a five-foil mask. From Méchain et al. (2004b).
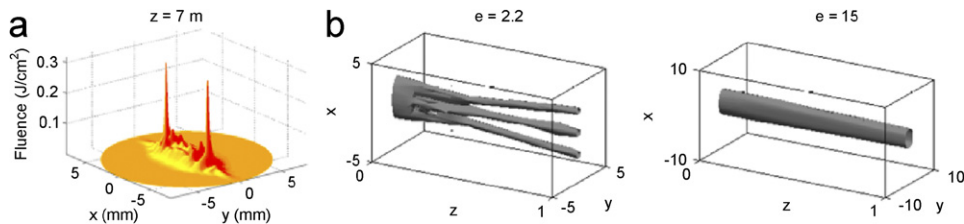
Fig. 41. (a) Organized multifilamentation pattern predicted numerically when astigmatism is introduced in the input beam (Méchain et al., 2004b). (b) Multiple filamentation is suppressed by increasing ellipticity of the input beam; according to Fibich et al. (2004).

intensity distribution, several works appeared where it was suggested that a small ellipticity of the input beam should lead to well determined multiple filamentation patterns (Dubietis et al., 2004c; Fibich et al., 2004).

Amplitude masks: Méchain et al. (2004b) have shown experimentally and numerically that multiple filamentation patterns could be produced either by using amplitude masks or by introducing phase distortions in the input beam. Non-circular diaphragm with a trefoil or a five-foil shape were shown to lead to beam break-up and multiple filaments regularly located on each foil, at the periphery of the input beam where the largest intensity gradients are found (see Fig. 40). The multiple filaments further coalesce into a single filament on axis, which constitute a very simple process to enlarge the propagation distance of a multifilamenting pulsed beam and the energy content of a single filament. This advocates for the possibility that the amplification of beam inhomogeneities present in the input beam can be overcome by adding external distortions to the laser beam or pulse. Since a filament which does not result from a coalescence process carries a limited amount of energy, the production of controlled multiple filaments is an issue for the transport of large laser energy over long distances.

Astigmatism: When the phase of the input beam is modified by tilting a focusing lens, astigmatism is introduced in the beam and should lead to specific multiple filamentation patterns. Méchain et al. (2004b) performed simulations of multiple filamentation by using as initial conditions the spatial phase profiles of an astigmatic beam measured with a Shack–Hartmann apparatus. The authors predicted a very stable pattern, shown in Fig. 41, propagating over several meters in air. Whatever the polarization direction of the laser, the filaments align along the direction perpendicular to the rotation axis of the lens and the whole pattern eventually undergoes a rotation of 90° from the sagittal to the tangential plane. Control of the multiple filamentation pattern by using a tilted lens was also achieved by Fibich et al. (2004).

Ellipticity: Fibich et al. (2004) have shown theoretically that an elliptically shaped laser beam should lead, under certain conditions, to the suppression of multiple filaments. For the same power, a beam with small ellipticity was
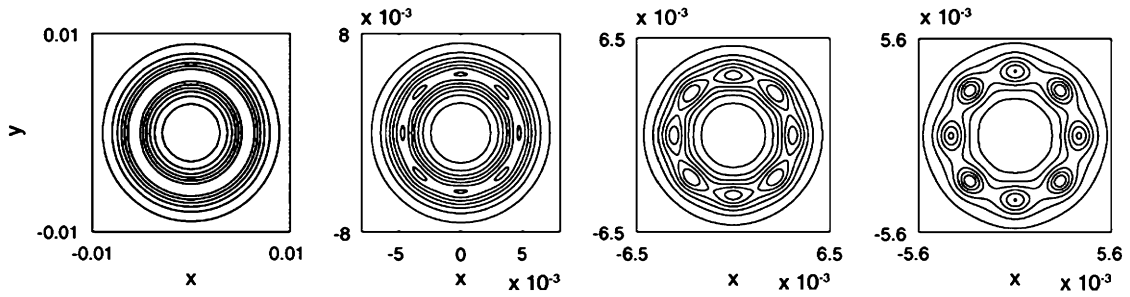
Fig. 42. Evolution of a slightly elliptic single ring profile. Iso contours for the amplitude show generation of multiple filaments located on the elliptic ring. From Fibich et al. (2005b).

predicted numerically to produce two filaments whereas a beam with large ellipticity was predicted to lead to a single, intense laser filament with a high pointing stability, as shown in Fig. 41(b,c). Fibich and Ilan (2000) as well as Kandidov and Fedorov (2004) have established that the critical power for self-focusing is larger for an elliptic beam than for a beam with cylindrical symmetry. For an initially elliptic beam in the form $\mathcal{E}(x, y) \propto \exp(-x^2/a^2 - y^2/b^2)$, the critical power for self-focusing reads:

$$P_{cr}^{elliptic} \simeq \left[0.4 \frac{(a^2 + b^2)}{2ab} + 0.6 \right] \frac{3.77 \lambda_0^2}{8 \pi n_0 n_2}. \tag{148}$$

Assuming that the maximum number of filaments is roughly given by the number of critical powers of a beam, elliptic beams having a given input power P_{in} are predicted to generate a smaller number of filaments when their ellipticity a/b is large because the ratio $P_{in}/P_{cr}^{elliptic}$ decreases when a/b increases (from $a/b = 1$). The result that ellipticity can suppress multiple filamentation is due to this increase of $P_{cr}^{elliptic}$, the critical power for self-focusing of elliptic beams, for increasing ellipticity.

The previous arguments are purely based on the notion of critical power for self-focusing. Whether this quantity is related to the notion of threshold for multiple filamentation is still unknown. In the case of elliptic beams (with power larger than $P_{cr}^{elliptic}$), Grow and Gaeta (2005) have shown from experiments and simulations that increasing the beam ellipticity may force multiple filamentation, in apparent contradiction with the results by Fibich et al. (2004). Multiple filaments appear along the major axis of the elliptic input beam. Their location is compatible with the predictions of the modulational instability theory, however, the patterns are independent of noise and of the polarization of the laser. Grow and Gaeta (2005) pointed out that the threshold for multiple filamentation decreases for an increasingly elliptic beam. There is, however, no contradiction with the results by Fibich et al. (2004) since the estimation of the number of filaments based on the ratio $P_{in}/P_{cr}^{elliptic}$ is a maximum number; the effective number of filaments which are generated indeed not only depends on the beam ellipticity but also on the beam inhomogeneities.

Ring break-up: An efficient way to generate organized multiple filamentation patterns using the beam ellipticity is to start from an elliptic super-Gaussian beam. The self-focusing of a super-Gaussian beam with cylindrical symmetry leads to a stable ring structure, as shown numerically in several publications (Chiron et al., 1999; Tzortzakis et al., 2001b; Couairon et al., 2002). When the revolution symmetry is broken during the propagation, multiple filaments grow on this ring (Grow et al., 2006). Simulations over long distances in air, using chirped infrared pulses, clearly showed this trend (Méchain et al., 2004a). Recently, the ring structure reached during the self-focusing of a super-Gaussian beam was identified analytically (Fibich et al., 2005b; Grow et al., 2006). As shown in Fig. 42, breaking the symmetry of this ring profile by making it slightly asymmetric leads to a very well organized multiple filamentation pattern. An open question is the ultimate coalescence of these filaments as in the organization process using amplitude masks for the input beam.

Multiple filaments controlled by a grid: Kandidov et al. (2004a) have shown from numerical simulations that chaotically distributed filaments, generated by high-power femtosecond laser pulses, can be spatially regularized by the introduction of regular light field perturbations induced by a mesh on the propagation path. A systematic arrangement of the filament was obtained for input fields with random additive perturbations having a variance below a certain

threshold. This spatial regularization in the bundle of filaments increases the filament density that would be obtained in the absence of a mesh.

Interaction of light filaments: Xi et al. (2006) have performed simulations of the interaction between well controlled filaments with specific relative phase shift and crossing angle. They have uncovered interesting features observed in the interaction of solitons (Stegeman and Segev, 1999; Tikhonenko et al., 1996) such as attraction, fusion, repulsion and spiral propagation of the filaments. In particular, two in phase filaments are found to fuse into a stable light channel. The simulation results by Xi et al. (2006) are in keeping with experimental and numerical results by Méchain et al. (2004b); Hosseini et al. (2004a); Centurion et al. (2005b). The fusion of filaments is driven by the constructive interference leading to an increase of the intensity in the overlapping region and to an enhancement of the Kerr refractive index, therefore attracting energy of the background reservoir toward the center. The mechanism is similar to the interaction of two laser beams in underdense plasmas (Dong et al., 2002; Wu et al., 2004), except that the Kerr effect plays the role of the relativistic mass and the ponderomotive force in the attraction between the filaments. The light channel becomes unstable when the crossing angle or the phase shift is increased.

Linear power partitioning: Roskey et al. (2006) have shown from numerical simulations that diffraction plays a crucial role in partitioning the power of laser beams carrying many critical powers for self-focusing. The organization of arrays of filaments is dominated by this linear power partitioning when apertured beams with steep edges or any strong phase aberrations are involved. High power pulses undergo quasilinear propagation featured by these aberrations. This stage partitions the power of the wide, moderately intense beam into subcritical or still supercritical domains. Multiple filaments or hot spots are potentially able to be formed in the supercritical domains whereas the locally subcritical regions remains in a quasi-linear regime. This analysis provided a useful insight in the physics of the organization of multiple filament arrays for the goal of energy transport in ultrashort laser pulses or long distance laser matter interaction (Roskey et al., 2006). All experiments or simulations based on mesh induced filaments rely on this scenario. In this respect, Kosareva et al. (2006a) and Kandidov et al. (2007) have shown that a control of the peak power flowing through a single mesh unit via the mesh size allows the simultaneous generation of periodically spaced filaments in a single shot pulse. Regular arrays of filaments in transparent solids can find applications in the fabrication of microoptics devices. As for the transport of energy over long distances, it was shown from the evolution of integral beam characteristics obtained via numerical simulations that in the absence of any organization process, the coefficient of energy transmission of femtosecond laser radiation generating filaments is lower than in the linear regime and decreases when the laser power increases (Zemlyanov and Geints, 2007, 2005c).

To summarize, multiple filamentation patterns arise for powers $P_{in} \gg P_{cr}$ and result from the growth of modulationally unstable perturbations in the beam. Their nucleation and coalescence are seemingly disordered, yet they can be organized by means of several control processes. They are sustained by the background energy reservoir which can refill a specific filament or reform another light string if it is destroyed by an obscurant on its path. This leads to their observation at considerable distances reaching several kilometers.

3.2.12. Filamentation at low pressures

Several applications of filamentation rely on the long distance propagation of filaments at high altitude in the sky. Filamentation in low pressure argon was predicted to occur (Mlejnek et al., 1998b) and observed (Nurhuda et al., 2002a; Hauri et al., 2004). The features of filaments at low air pressure have been studied numerically by Couairon et al. (2006b). The results show that femtosecond filamentation can occur in air at low pressures ($0.2 \leqslant p \leqslant 1$ atm), which corresponds to altitudes up to 11 km. The effect of lowering the pressure modifies mainly the self-focusing stage during the propagation of the ultra-short pulse. The length of the plasma string does not change significantly in the range of pressure from 0.2 to 1 atm. Below 0.2 atm, the length is strongly reduced but this reflects the fact that the critical power for self-focusing increases when the pressure decreases. Fig. 43 shows this feature. In addition, the comparison of results at different pressures shows that the diameter of the filament core is larger at low pressures, the clamping intensity is independent of the pressure, the generated electron density is proportional to the pressure but the radially integrated electron density which is the experimentally accessible quantity is nearly independent of the pressure. From analytical estimations and numerical simulations, Arévalo (2006) showed that even in gases such as air where the Raman Kerr effect is present, the intensity obtained at the beginning of the filament is independent of pressure. Couairon et al. (2006b) also studied the influence of various parameters. The length of the generated plasma channel significantly differs when the beam profile is changed (even if the peak power or pulse energy are kept constant). A negative chirp in the input pulse delays the beginning of the filamentation and modifies the continuity of the plasma
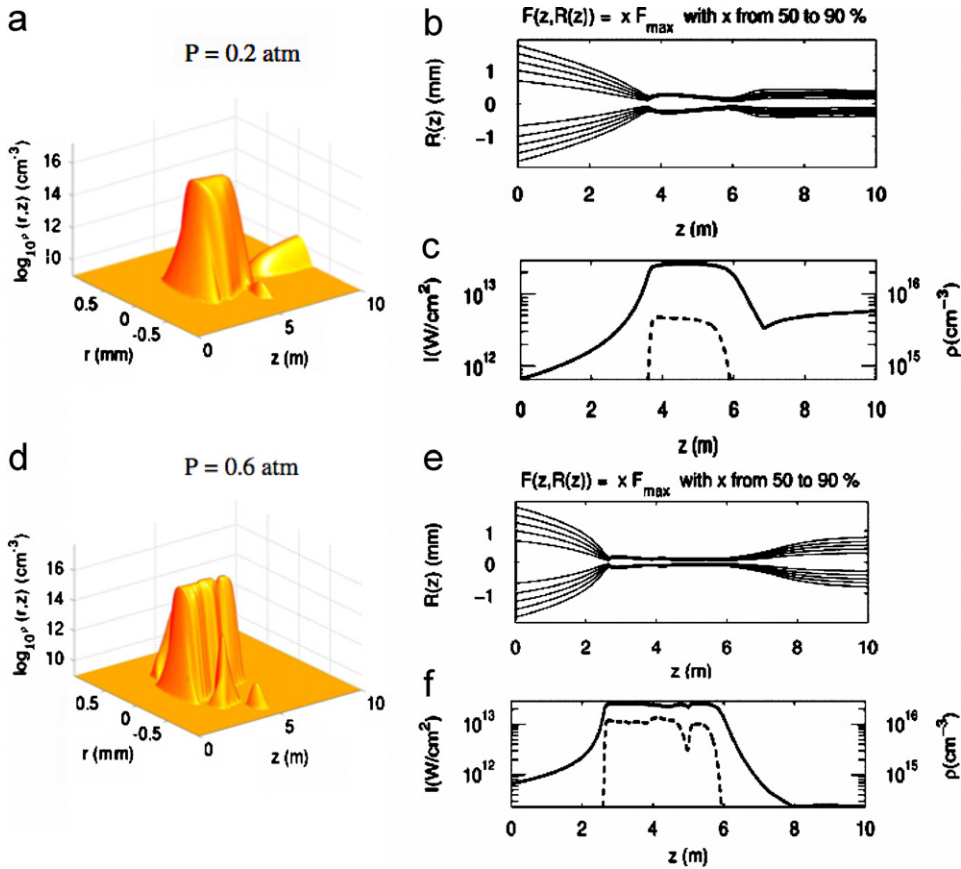
Fig. 43. Plasma channel generated in the wake of the ultrashort pulse for a Gaussian input beam with $w_0 = 3$ mm, $E_{in} = 6$ mJ, $f = 6$ m, $\tau_{FWHM} = 60$ fs. (a) $p = 0.2$ atm, (d) $p = 0.6$ atm. (b) Beam diameter as a function of the propagation distance z for $p = 0.2$ atm. (e) Same as in (b) for $p = 0.6$ atm. (c) Intensity (continuous line, left axis) and electron density (dashed line, right axis) vs. z for $p = 0.2$ atm. (f) Same as in (c) for $p = 0.6$ atm. From Couairon et al. (2006b).

channel, as shown by Kandidov et al. (2003a). However, calculations by Couairon et al. (2006b) show that the features of the plasma channel obtained in the regime of long distance filamentation at low pressures are more easily controlled by changing the shape of the input beam than by changing the chirp of the pulse to which they are rather insensitive. In particular the total length of the plasma bursts along the propagation distance was shown to be nearly the same for chirped and unchirped pulses having the same duration and peak power. Zemlyanov and Geints (2005a) performed numerical simulations of filamentation in the atmospheric pressure gradient which agree with the above results. They showed that the filamentation length is smaller for vertical than for horizontal propagation at constant pressure.

3.2.13. Filamentation with circularly polarized pulses

Most simulations are performed by assuming a linearly polarized electric field. However, it is interesting to know whether the polarization state is stable during the filamentation process. Schjødt-Eriksen et al. (2001) have investigated the stability of the polarization state of elliptically polarized intense femtosecond pulses after self-focusing and pulse splitting in normally dispersive Kerr media. Model (56) including only the self and cross phase modulation terms and GVD was therefore integrated starting from pulses with different polarization states. Schjødt-Eriksen et al. (2001) found that when the input power is distributed asymmetrically between the two linearly polarized modes, higher amplitudes are reached and the propagation distance needed for the occurrence of pulse splitting decreases (see Fig. 44). The results were interpreted by the authors as resulting from a polarization instability which tends to equalize the energy contained in each of the circularly polarized states. The linearly polarized mode was inferred to be unstable with respect to perturbations of the polarization state while at the opposite, the circularly polarized mode is stable. The parameters
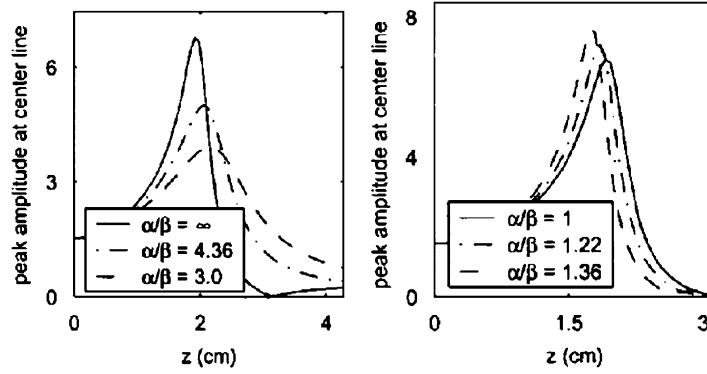
Fig. 44. Peak amplitude in the center of the pulse ($r = 0, t = 0$) for different amplitude ratio of the two input linearly polarized modes. According to Schjødt-Eriksen et al. (2001).
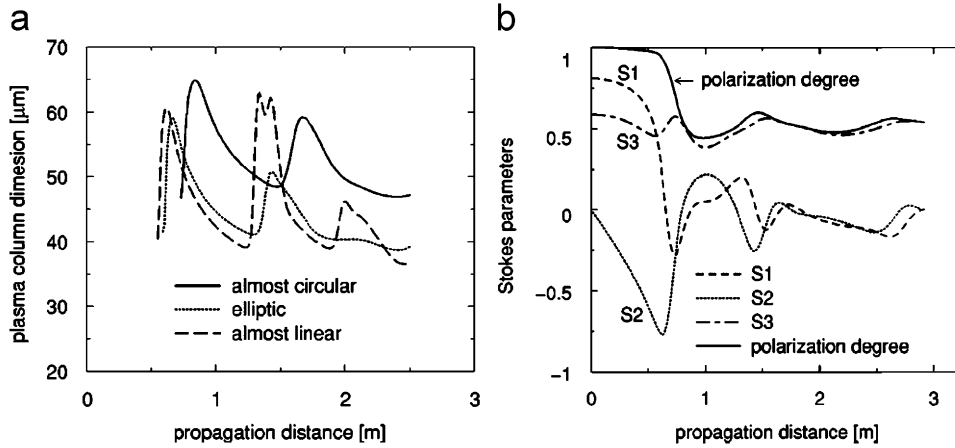
Fig. 45. (a) Characteristic transverse dimension of the generated plasma column for three different initial polarizations. (b) Stokes polarization parameters S_j as functions of the propagation distance for an elliptic initial polarization of the pulse. The Stokes parameters are defined as $S_0 = \mathcal{F}_{\pi/2} + \mathcal{F}_0$, $S_1 = (\mathcal{F}_{\pi/4} - \mathcal{F}_{-\pi/4})/S_0$, $S_2 = (\mathcal{F}_{\pi/2} - \mathcal{F}_0)/S_0$, $S_2 = (\mathcal{F}_{cr} - \mathcal{F}_{cl})/S_0$, where $\mathcal{F}_\beta$ denotes the total energy detected after passing the pulse through a polarizer of state β and cr,cl correspond to right and left polarization settings of a circular polarizer. The central part of the filament evolves into a predominantly circular polarization state after the second self-focusing collapse event. The rate of change of the polarization state correlates with the loci of maximal plasma production. According to Kolesik et al. (2001).

chosen in the simulations corresponded to fused silica; however, the results are general for all normally dispersive Kerr media where the input peak power is moderately above critical so as to make GVD sufficient to arrest collapse.

Building on this analysis, Kolesik et al. (2001) have studied numerically the effects of the polarization state on the plasma and supercontinuum generation during filamentation. Model (56) was solved including all effects except the shock terms. It was found that when the initial polarization state is changed from linear through elliptic to circular, the amount of the generated plasma decreases. The onset of filament formation is delayed for circularly polarized pulse because of a higher ($1.5\times$) critical power for self-focusing and the number of refocusing events can therefore be larger for a linearly polarized input pulse having the same power as a circularly polarized pulse. The transverse dimensions of the plasma channel, however, do not significantly depend on the polarization state although small variations between different initial polarizations exist (see Fig. 45(a)).

An elliptically polarized pulse is found to evolve toward a stable circularly polarized pulse, with changes of polarization state occurring at the collapse events (see Fig. 45(b)). Finally, a much stronger supercontinuum generation was obtained for a linearly polarized pulse with respect to a circularly polarized pulse with the same power (see Fig. 46). This is due to the larger critical power for self-focusing in the case of circular polarization.
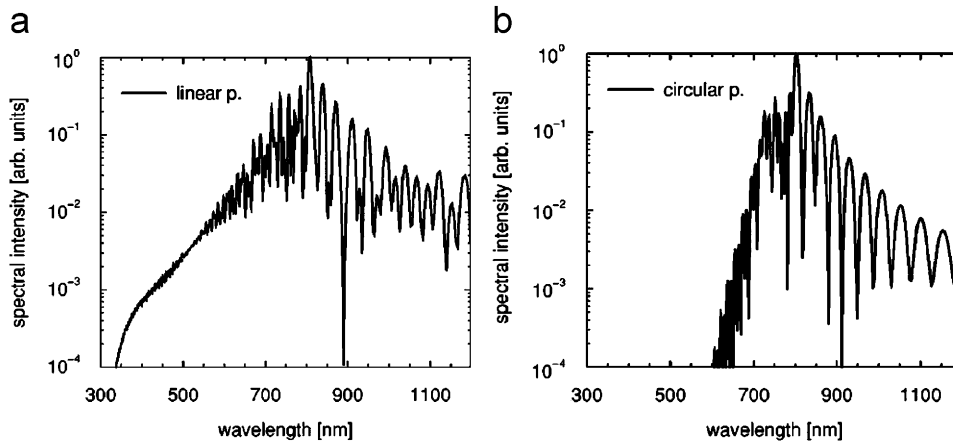
Fig. 46. Spectral broadening of two femtosecond pulses with different initial polarizations. The linearly polarized pulse (a) produces significantly more supercontinuum light than an equally intense circularly polarized pulse (b). From Kolesik et al. (2001).

Fibich and Ilan (2002, 2003) studied the multiple filamentation of circularly polarized input beams and found that multiple filamentation is suppressed even for a non perfect circular polarization as long as the beam is sufficiently clean, i.e., is not too noisy, or does not exhibit astigmatism. In contrast, a linearly polarized input beam has a smaller threshold for multiple filamentation whatever the origin of the process, i.e., in both cases of stochastic noise or deterministic effects such as the input polarization state or nonparaxial effects.

3.2.14. Filamentation in transparent solids

Henz and Herrmann (1999) have performed numerical simulations predicting self-channeling of femtosecond laser pulses in dispersive dielectric solids. They show that a significant pulse shortening with a compression factor of 5.5 should occur when the critical power is exceeded. Their numerical simulations show that in a restricted range of the parameter space, in particular for powers between 1 and 3 P_{cr}, an initially sufficiently narrow pulsed beam undergoes long lived intensity and beam width oscillations, typical of the dynamics obtained in a medium with a saturable nonlinear refraction index change. Nevertheless, the dynamics never reaches a spatial soliton characterized by a strictly constant beam width and intensity.

This self-channeling regime corresponds well to the filamentation regime which was shown to occur in transparent solids in a collimated beam geometry or under weak focusing conditions (Tzortzakis et al., 2001d). Numerical simulations have shown that the time integrated beam width, i.e., the FWHM of the fluence distribution lies between 10 and 20 μm while the pulse temporal profiles are generically split into two few-cycle substructures (Tzortzakis et al., 2001d). Multiphoton absorption and associated plasma generation and defocusing constitute in this case the splitting mechanism arresting the collapse. The competition of these effects with self-focusing leads to successive refocusing cycles as in gases (Wu, 2003). Sirutkaitis et al. (2003) showed that MPA alone, without considering plasma defocusing, is sufficient to arrest the collapse and induces a pulse splitting by a fast attenuation of the self-focused central time slices while the self-focusing of outer time slices with power close to P_{cr} needs a longer distance. After the nonlinear focus, it is clear that the peak intensity of the still self-focusing outer time slices become more intense than the intensity of the initial peak that underwent MPA. This filamentation regime is quite different from the propagation regime with powers close to P_{cr} in BK7 glasses, explored by several authors (Ranka et al., 1996; Diddams et al., 1998a, b; Zozulya et al., 1998, 1999; Zozulya and Diddams, 1999), where pulse splitting occurred without long-range channeling. In the latter case, GVD together with self-steepening and space–time focusing were concluded to provide the main mechanism in limiting the self-focusing of ultrashort pulses through the splitting process. Fig. 47 shows a comparison between measured [Fig. 47(a,c)] and computed [Fig. 47(b,d)] data which confirms this scenario for powers close to P_{cr}. Fig. 47(c,d) show the measured and the computed axial spectrum which exhibit a moderate supercontinuum generation.

By means of numerical simulations of the collapse of ultrashort laser pulses in sapphire, Gaeta (2000) predicted that supercontinuum generation, interpreted as a large pedestal on the blue side of the on-axis spectra, should occur because of the formation of a sharp trailing edge (an optical shock) in the pulse temporal profile, owing to self-steepening
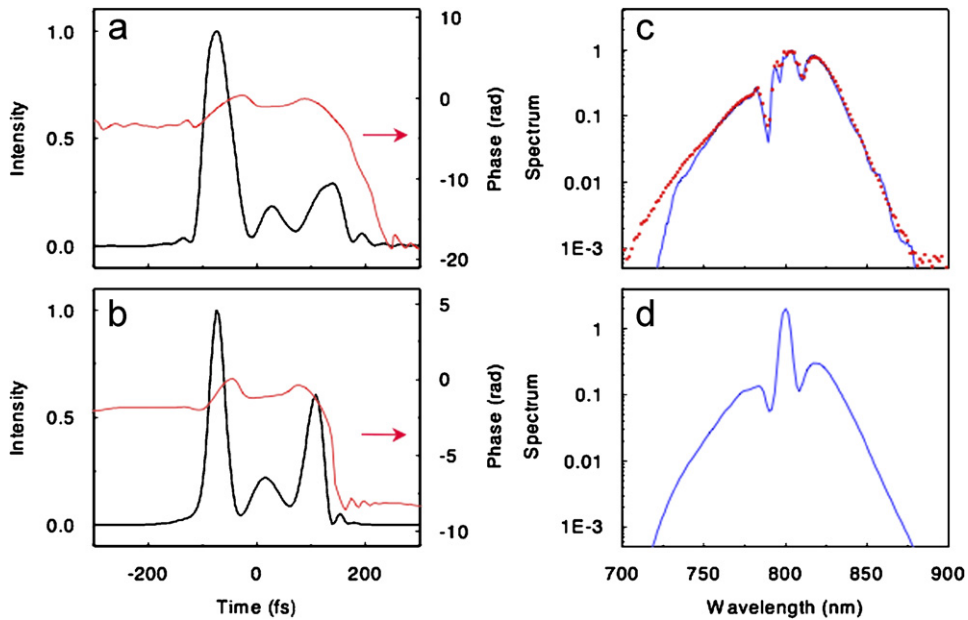
Fig. 47. (a) Axial intensity and phase measured with SHG-FROG. (b) Calculated axial intensity and phase. (c) Measured axial spectrum of field shown in (a). The curve is the square modulus of the Fourier transform of data in (a), while the points are measured with a spectrometer. (d) Calculated axial spectrum. From (Zozulya and Diddams, 1999).

effect. According to these results, multiphoton ionization which acts on the trail of the pulse pushes the peak intensity toward the leading part of the pulse. This occurs preferentially when shock terms are neglected and should lead to the generation of a redshifted pedestal, although the electron density front steepens the decreasing part of the pulse. Supercontinuum generation should therefore be obtained more efficiently when self-steepening occurs before MPA and MPI. A similar result was found in air (Aközbek et al., 2001).

Junnarkar (2001) performed a series of simulations of the propagation of ultrashort laser pulses in transparent bulk media for both soft and tight focusing conditions. For input peak powers above critical, the soft focusing conditions correspond to the regime of filamentation after a self-focusing stage, and lead to supercontinuum generation. In this case, Junnarkar (2001) calculated the efficiency of the supercontinuum generation in a number of experimental situations (Brodeur and Chin, 1999) and pointed out the importance of the accuracy of multiphoton ionization rates for realistic simulations of supercontinuum generation.

In the case of tight focusing conditions, damage of the material is usually obtained in the form of a hot plasma ablated from the surface or, if trapped inside the material, in the form of a void surrounded by densified materials due to the constrained shock wave. In both regimes (soft and tight focusing), multiphoton ionization plays a dominant role in the generation of the free electrons but these seed electrons can further generate an electron–ion plasma by avalanche ionization for tight focusing conditions. The damage threshold usually corresponds to a conduction electron density for which the energy density of these electrons equal to the lattice binding energy. For tight focusing conditions, Junnarkar (2001) determined optimal laser parameters which could lead to bulk damage and potential direct writing of buried waveguides. From the results shown in Fig. 48, an optimal pulse duration of more than 100 fs, with power below critical, was inferred for the generation of an electron plasma above $10^{19}\,\mathrm{cm}^{-3}$.

The regime of filamentation in fused silica, with pulse powers above critical and tight focusing conditions was further investigated numerically and experimentally (Couairon et al., 2005b; Sudrie et al., 2002; Wu et al., 2003). Simulations predict that a first damage zone around the focus should be followed by a narrow track with submicron width, indicating a filamentary propagation. The shape and size of the damage tracks correspond to the zone where the electron density created by optical field ionization and avalanche is close to $10^{20}\,\mathrm{cm}^3$. The plasma density produced in the wake of the pulse saturates around $2\text{–}4\,10^{20}\,\mathrm{cm}^3$.

Fig. 49(a) shows an image of this damage track from electron microscope. The comparison of the damage track with the results of numerical simulations shown in Fig. 49(b,c) and 50 have evidenced two types of damage: The head
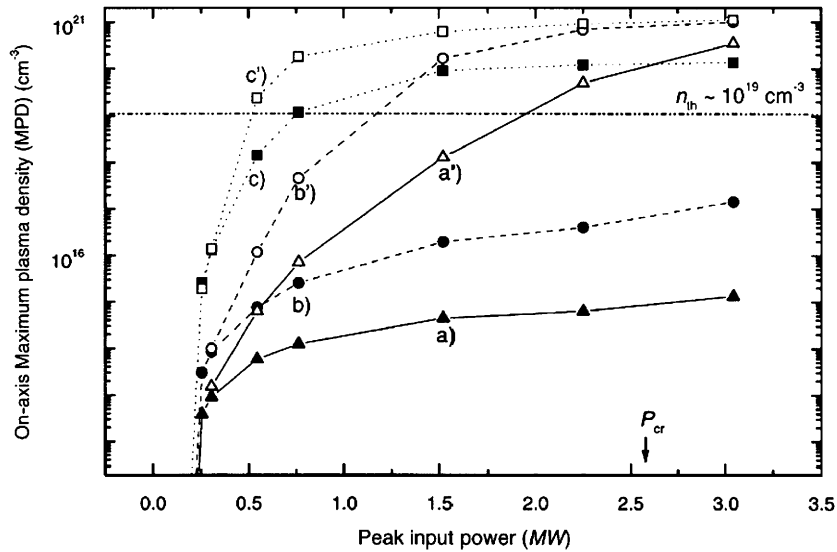
Fig. 48. Maximum plasma density at the physical focii in the bulk of a fused silica sample for: (a) 12 fs; (b) 36 fs; and (c) 120 fs pulses (filled symbols). The open symbols (a′), (b′), and (c′) are the corresponding results when the focii are at the surface of the sample. From Junnarkar (2001).
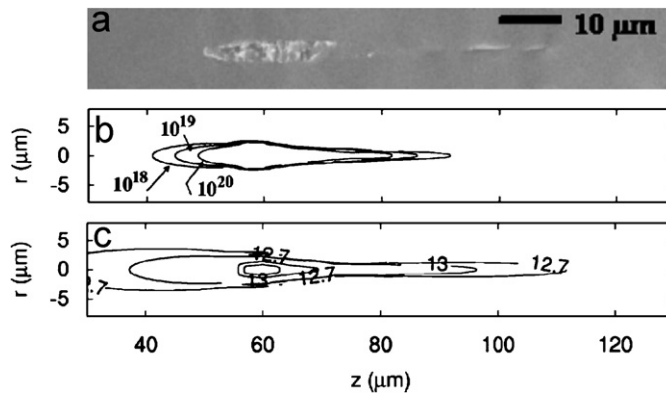
Fig. 49. Comparison between experiments and simulation. (a) Image from electron microscope of a damage track obtained by 800 nm, 160 fs, 1 μJ pulses tightly focused in fused silica. Objective 20× with NA = 0.5. (b) Numerical simulation: the curves bound regions where the electron density exceeds the level 10^{18}, 10^{19}, or $10^{20} e^-/cm^3$. (c) Computed intensity contourplots. The labels 12.7 and 13 in (c) indicate 5×10^{12} and 10^{13} W/cm^2. From Couairon et al. (2005b).

corresponds to the generation of an electron density above 10^{20} cm^3 while the long filamentary track corresponds to the region where the fluence exceeded 2–3 J/cm^2. Numerical simulations of femtosecond filamentation in water have shown similar trends (Liu et al., 2003b).

Finally, it is worth commenting the high-power regime explored numerically by Ishikawa et al. (2002). Their simulations in fused silica, with the constraint of cylindrical symmetry, show that for pulses with input peak powers from several tens to several hundreds times P_{cr}, the pulse splits many times both temporally and in the transverse diffraction plane, leading to a multiple cone structure. This structure is robustly formed in a large domain of the parameters space. The half-angle of the cones and their number increases when the input pulse energy is increased. The authors interpret the formation of these cones as an effect of the interplay between self-focusing and plasma defocusing. Plasma defocusing yields a low refractive index in the center of the beam and to the generation of a first cone (defocusing of the trailing part of the pulse). A local maximum of the refractive index necessarily lies outside this cone where there is no contribution from the plasma. Local self-focusing then generates a second cone around this maximum and the process
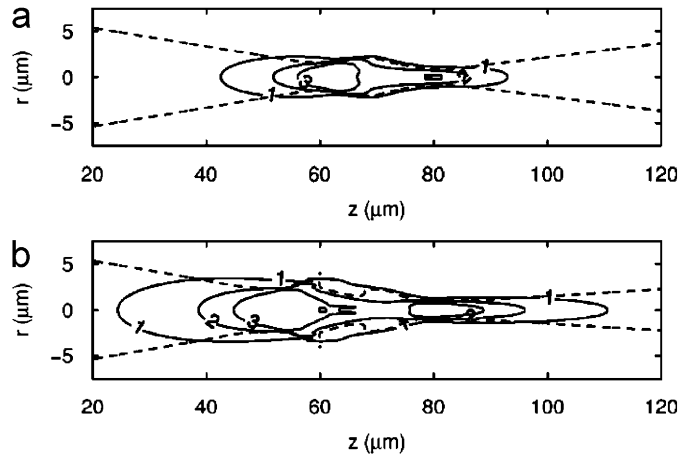
Fig. 50. Beam diameter in dashed curve (FWHM of the fluence at each propagation distance) and various levels of the fluence distribution (continuous contours for 1, 2, and $3\,\mathrm{J/cm^2}$ as a function of the propagation distance. Pulse: 800 nm, 160 fs. Focusing lens $20\times$ with NA $= 0.5$. (a) $0.45\,\mu\mathrm{J}$. (b) $1.1\,\mu\mathrm{J}$. From Couairon et al. (2005b).

repeat itself until the power remaining at the periphery of the external cone becomes smaller than P_{cr}. This is actually an effect similar to the modulational instability in a Kerr medium constrained by the cylindrical symmetry, with an additional contribution from the plasma which depends on the integrated intensity (Couairon and Bergé, 2000). In a way, the mechanism is similar to the spatiotemporal instability of intense laser pulses in gases proposed by Kandidov et al. (1997b). The multicone formation is solely due to the time dependence, related to the generated plasma, of the nonlinear response of the medium. In this respect, Ando and Fujimoto (2005) have predicted similar multiple cone formation in nitrogen from $(3+1)$D numerical simulations of the nonlinear Schrödinger equation with self-steepening and space–time focusing terms. Recently, Liu et al. (2006f) have shown from numerical simulations that tightly focused pulses in the bulk of a fused silica sample lead to similar spatio-temporal transformations in the form of multiple cone, even if the pulse powers are below P_{cr}. In this case, the role of plasma defocusing is prevailing (Fig. 51).

3.2.15. Filamentation in liquids

Simulations of femtosecond pulse propagation and filamentation in water have been performed by several authors (Kolesik et al., 2003a, b, 2004; Liu et al., 2003b; Matijošius et al., 2004a; Dubietis et al., 2004a; Kandidov et al., 2004b; Faccio et al., 2005b; Couairon et al., 2006c). Water (and more generally liquids) is used as a prototype of condensed medium for studying femtosecond filamentation. For experiments, it is indeed easier to enlarge the length of a water cell than the propagation distance in a crystal. The numerical simulations performed in water for modeling experiments therefore allowed the researchers to test and tune the models or to check the role of physical effects at the origin of different phenomena associated with filamentation such as supercontinuum generation, conical emission or optical breakdown. Liu et al. (2002b) have shown that the initial beam curvature and the pulse energy determine whether optical breakdown and supercontinuum generation coexist. For sufficiently short focal lengths, the energy threshold for optical breakdown is smaller than that for supercontinuum generation. For long focal lengths, both phenomena can coexist. Concerning SCG, Liu et al. (2002c) have explained the extent of the SC generated during filamentation in condensed media by the SPM effect and have proposed that the clamping of the peak intensity inside a filament limits the spectral broadening toward the blue frequencies. This analysis of SCG was extended by Kolesik et al. (2003a, b) so as to account for the presence of chromatic dispersion in numerical simulations. The authors found that the spectral extent of supercontinuum generation is not solely imposed by the SPM driven by Kerr self-focusing and plasma defocusing. The chromatic dispersion of the medium plays a major role in the physical factors limiting this extent. Fig. 52(a) shows the main features of the supercontinuum spectra with modest and symmetric spectral broadening for pulses below the self-focusing threshold while the spectra broaden to several hundreds of nanometers above threshold, with little changes when the pulse energy is further increased. A dynamic three wave mixing (TWM) process was proposed to explain the supercontinuum extent Kolesik et al. (2003a, b). This TWM process can be viewed as the scattering of the
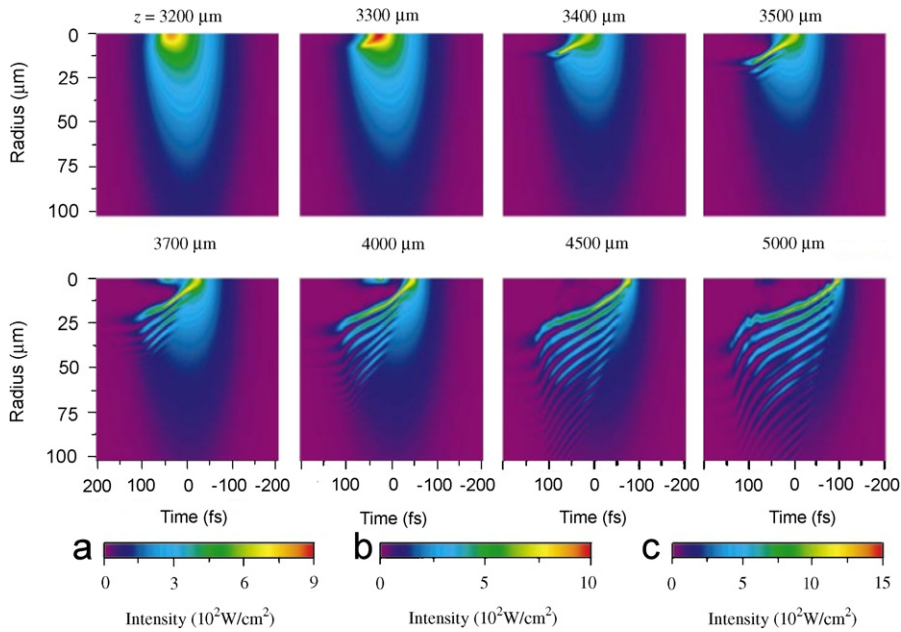
Fig. 51. Spatiotemporal intensity distribution of an initially Gaussian pulse with an energy of 135 μJ propagating in silica at eight different propagation distances z indicated above each image. The colormap (a) of intensity applies for $z = 3200$ m, (b) for $z = 3300$ m, and (c) for the other values of z. From Ishikawa et al. (2002).
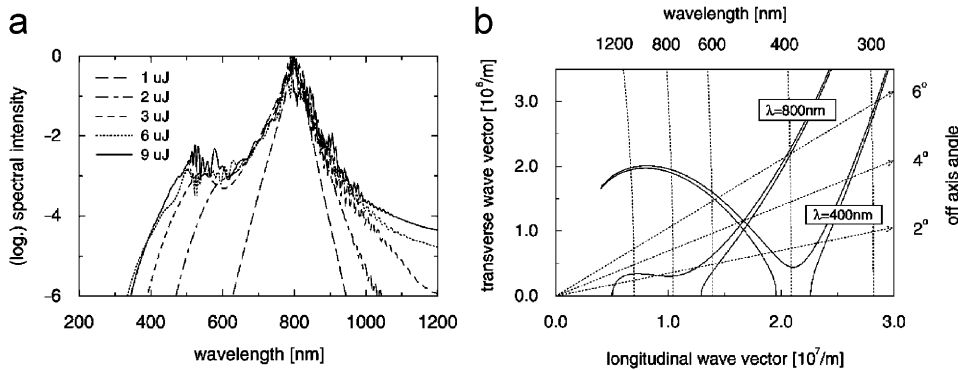
Fig. 52. (a) Simulated wide-angle integrated SC spectra at distance 8.03 cm in water for a range of input pulse energies. Except for small absorption in the far infrared region, the spectra do not further evolve with increasing propagation distance. (b) Contour of the phase matching boundaries determined for water. Two incident wave vector $2\pi/\lambda$ are considered, corresponding to the pulse central wavelength λ equal to 400 and 800 nm. Full lines: allowed scattered wave vectors satisfying a three wave mixing phase-matching condition Dotted lines show the wavelength and the propagation angle. From Kolesik et al. (2003a).

incident optical pulse from the material polarization, which produces a third optical wave. Fig. 52(b) shows the region of allowed scattered wave vectors as predicted by this model. In particular, the supercontinuum on-axis is predicted to be broader with an asymmetric angular dependence of the scattered waves for infrared wavelengths.

A similar conclusion was reached from a quite different argument by (Kandidov et al., 2004b), who investigated the supercontinuum sources from an analysis of the SPM of the laser pulse during filamentation. The frequency shift and the angular divergence of the spectral components were reconstructed from the phase of the filamenting pulse obtained by numerical simulations according to $\delta\omega(r, t) = \partial\phi(r, t)/\partial t$ and $\theta(r, t) = \arctan[-(1/k)\partial\phi/\partial r]$. Fig. 53 shows that the redshifted components are located close to the intensity rings nearest to the optical axis with their radiation directed toward the axis. In contrast, the blueshifted components are located near the periphery rings and their radiation is
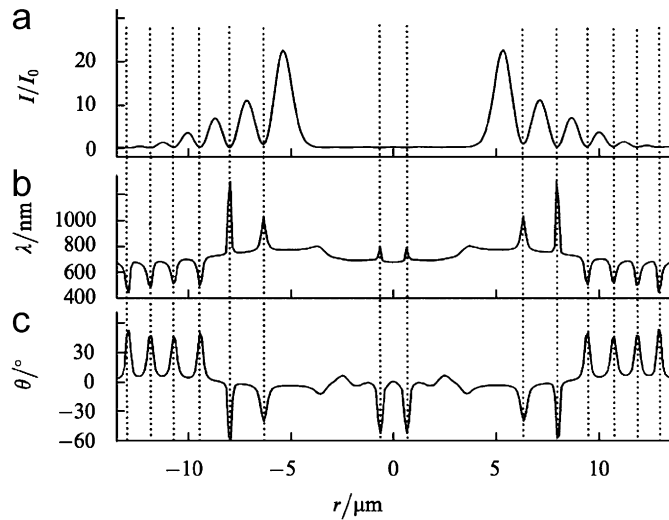
Fig. 53. (a) Transverse distribution of the beam intensity $I(r, t=0)$ at 40 μm in front of the focus of a 45 fs, 3 μJ infrared laser pulsed beam focused in a water cell. (b) Wavelength of the supercontinuum sources $\lambda(r, t=0) = 2\pi c/[\omega_0 + \Delta\omega(rt=0)]$. (c) Divergence angle of their radiation $\theta(r, t=0)$. The pulse intensity is normalized to $I_0 = 10^{12} \, \text{W/cm}^2$. From Liu et al. (2003a).

directed from the axis. The blueshifted components should therefore carry the angular divergence while the redshifted part of the spectrum predominantly propagates along the optical axis.

3.2.16. From the role of the energy reservoir to the spontaneous formation of X-waves

Liu et al. (2003a) have performed numerical simulations of femtosecond filamentation in a methanol + coumarine solution and have studied in particular the multiple refocusing process and the energy transfer from the energy reservoir to the core of the filament during the whole propagation. The fluorescence signal, simulated as the amount of energy absorbed due to three photon excitation of coumarine molecules, shows these multiple refocusing peaks in Fig. 54(e) associated with a step-like decrease of the total energy as a function of the propagation distance (Fig. 54(f)). The energy in the near-axis region oscillates with largest values at the fluorescence peaks (Fig. 54(b)). The surrounding ring-shaped region transfers energy to the near-axis region before these peaks. Immediately after the fluorescence peaks, the near-axis region restores part of its energy to the first ring region. The peripheral region refills the first ring region before each fluorescence peak (Fig. 54(c,d)). The average energy flow is directed outwards with a globally increasing energy of the peripheral region while the energy content of the first ring region slowly decreases.

From beam clipping experiments in water and associated simulations, Dubietis et al. (2004a) have shown that this compensation by external radiation of multiphoton absorption occurring in the center of the beam is structural to the existence of femtosecond filaments. Precisely, the energy flow directed toward the center of the beam induces the self-healing property of the filament shown in Fig. 33. In this interpretation, femtosecond filaments are viewed as quasi-stationary wavepackets undergoing nonlinear absorption. Multiphoton absorption was proposed not only to reshape the beam, but also to establish an energy flow from the external to the central part of the beam, with the constraint of maximum stationarity and minimum nonlinear losses. These constraints were predicted to result in a spontaneous transformation of the input Gaussian beam into a conical beam later identified as a nonlinear unbalanced Bessel beam (Porras et al., 2004). The application domain of this scenario extends beyond the mere case of liquids and solids for which it was proposed: this interpretation is in agreement with the results of numerical simulations of femtosecond filamentation in air exhibiting transverse ring formation (Chiron et al., 1999; Chin et al., 2001; Aközbek et al., 2002a; Couairon et al., 2002), a possible signature of the conical nature of the wavepacket during the filamentation process.

When strong coupling in space and time are involved as is the case in filamentation, it is still possible to identify nonlinear wavepacket distributions that ensure a quasi-stationary (z invariant) propagation. These wavepackets take the shape of conical waves. Notably, these waves possess a weakly localized intensity distribution which exhibits a central peak and extended tails. In normally dispersive media, the intersection of these wavepackets by a plane spanned by the
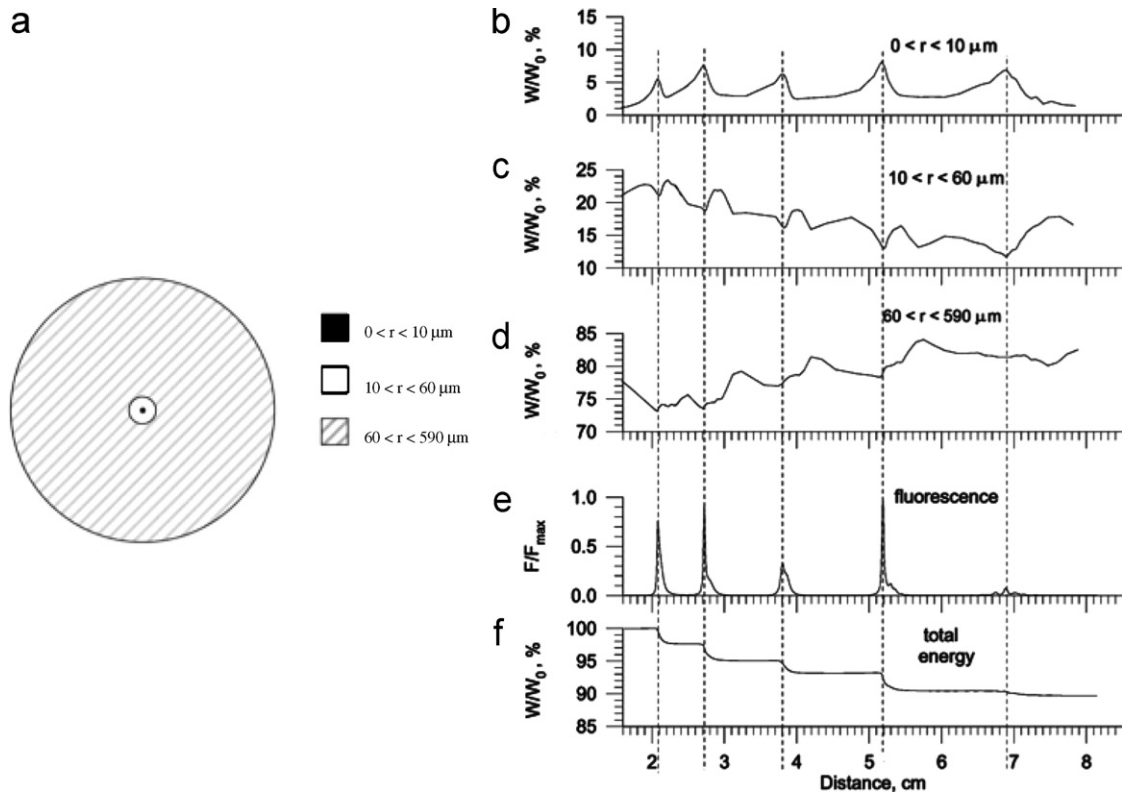
Fig. 54. Energy exchange between the near-axis region $0 < r < 10\,\mu$m, the first ring-shaped region $10 < r < 60\,\mu$m and the peripheral region $60 < r < 590\,\mu$m in the transverse beam section shown in (a). Input pulse energy is 1.6 μJ. (b,c,d) Fraction of energy as a function of the propagation distance for each region. Change of (e) the normalized fluorescence signal F and (f) the total pulse energy W as functions of the propagation distance. Vertical dashed lines indicate the positions of fluorescence peaks along the propagation direction. From (Liu et al., 2003a).

transverse r and longitudinal t directions forms a characteristic X-shape. Likewise, the space–time Fourier transform of these wavepackets exhibit the shape of an X in the space $(k_\perp, \omega)$ spanned by the transverse wavenumber and frequency. Such X-waves were first introduced in acoustics (Stepanishen and Sun, 1997; Salo et al., 1999), in linear optics (Salo et al., 2000; Reivelt and Saari, 2000), and have been recently identified in the field of nonlinear optics by means of experiments in $\chi^{(2)}$ media (Di Trapani et al., 2003; Jedrkiewicz et al., 2003; Trull et al., 2004). In Kerr media, nonlinear electromagnetic X-waves defined as stationary and weakly localized nonlinear solutions were identified theoretically as resulting from the competition of diffraction, group velocity dispersion and optical Kerr effect (Conti et al., 2003). Kolesik et al. (2004, 2005) have shown by means of numerical simulations of femtosecond filamentation in water that robust X-waves, called dynamic X-waves are formed in the far-field $(k_\perp, \omega)$ due to the interplay between nonlinearity and chromatic dispersion (see Fig. 55(a)). The term *dynamic* refers to the absence of a clearly identified z invariant and X-shaped wavepacket from the space–time intensity profiles obtained numerically. The authors indicate that the pulse temporal splitting arresting the collapse generates two daughter waves departing from each other and producing the interference structure shown in the far-field in Fig. 55.

Recent measurements and numerical simulations of filamentation in water have shown that the near-field of the wavepacket also undergoes a transformation from a Gaussian to an X-shaped structure emerging as the peak of a vaster and weaker underlying structure interpreted as resulting from the interference and interaction of multiple, overlapping X-forms born by multiple split-off pulses (Faccio et al., 2005b; Couairon et al., 2006c). Fig. 55(b) shows the far-field and the near-field intensity patterns computed from the filamentation of an infrared laser pulse in water. The pulse temporal splitting was found to lead not only to the interferences clearly visible in the far-field, but also to a double X structure where each X is split in two halves exhibiting a gap in frequency. The blue half-X is present in both Fig. 55(a) and (b) while the infrared half-X is not visible due to the asymmetry in the dispersive properties of the
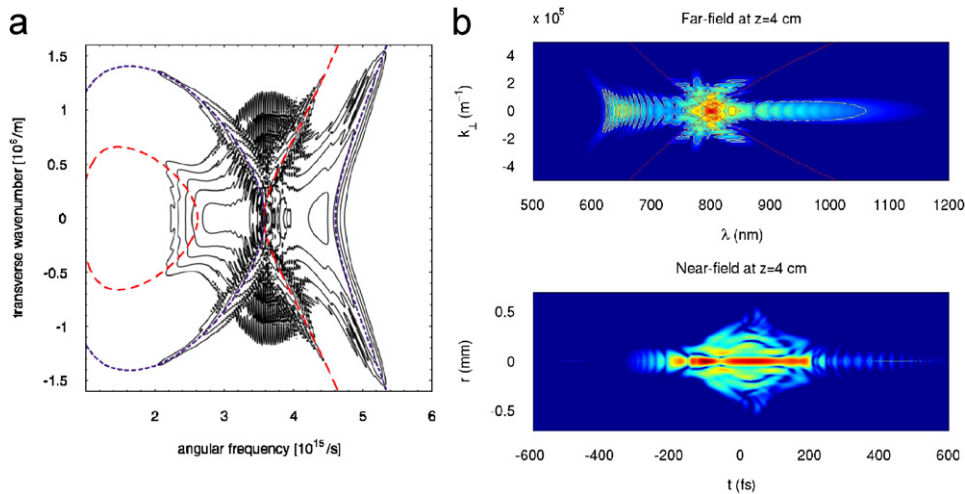
Fig. 55. (a) Contour plot of the logarithmic spectral intensity in (k, ω) space for $z = 1.7$ cm after the first pulse splitting. From Kolesik et al. (2004). (b) Far-field (top) and near field (bottom) at a propagation distance of 4 cm for a 3.3 µJ infrared laser pulse undergoing filamentation in water. From Couairon et al. (2006c).

medium. This double X structure was interpreted as a result of a four wave mixing interaction between two strongly localized pumps with two X-waves (Faccio et al., 2006b). The evolution from Gaussian to a conical wave for ultrashort laser pulses undergoing filamentation in water was also reported recently by Liu et al. (2005d).

3.2.17. Simulation of THz emission

Sprangle et al. (2004) predicted that an intense radiation peaked around 100 GHz should be emitted from the filament due to the action of the ponderomotive force. In this model, the ionization front has frequency components propagating at superluminal velocity, giving rise to a Cerenkov-like emission. Other authors have proposed another model, in which the ponderomotive force is not the main mechanism for THz emission (Cheng et al., 2001; Keskinen et al., 2004). In this model, radiation pressure separate axially electrons from ions after multiphoton ionization, inducing an oriented dipole moment aligned in the direction of the filaments (Proulx et al., 2000). The created plasma string vibrates longitudinally at its eigenfrequency determined by the plasma density. More recently, the same group has predicted incoherent THz generation due to electron–ion scattering (Hoyer et al., 2005), a process similar to intraband scattering of free carriers in solids.

4. Review of the experimental results on femtosecond filamentation

From the previous discussion, it is clear that a complete characterization of filaments is a difficult, ill-defined task. What is the filament size? The laser energy surrounding a filament core is an integral part of a filament, since it can feed energy to the filament core. The surrounding laser energy may have a complex pattern in space and time. The conical emission is often considered as a signature of filamentation. Thus, a complete characterization of a filament should include a measurement of the complete intensity maps $I(\mathbf{r}, t)$ as well as $I(\mathbf{k}, \omega)$ as a function of z. More strictly, it requires a three-dimensional determination of the field amplitude and phase. Most experiments in gases so far have obtained only partial information.

4.1. Measurements in gases—laboratory experiments

The filaments generated in air were studied mainly with femtosecond or picosecond lasers working at 1060 nm (La Fontaine et al., 1999b), 800 nm (Braun et al., 1995; Nibbering et al., 1996; Brodeur et al., 1997; Lange et al., 1998c; Yau et al., 2000; Tzortzakis et al., 2001a; Chin et al., 2001; Yang et al., 2002a; Fujimoto et al., 2002), 527 nm (Mikalauskas et al., 2002), 400 nm (Prade et al., 2006a) and 248 nm (Tzortzakis et al., 2000b, 2001b; Schwarz et al., 2000). Several
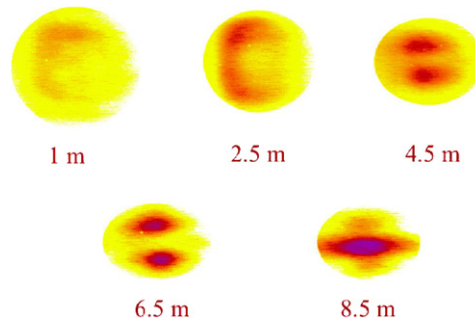
Fig. 56. Formation and fusion of twin filaments by an initially collimated laser beam (800 nm, 50 fs, 5 mJ). The transverse section of the beam is shown at various propagation distances. From Tzortzakis et al. (2001a).

groups observed the existence of plasma strings created by filaments over lengths ranging from a few tenth of meters to several hundreds of meters (Nibbering et al., 1996; La Fontaine et al., 1999b; Chin et al., 2002b; Yang et al., 2002a). It is convenient to consider separately the case $P_{in} \sim P_{cr}$ and $P_{in} \gg P_{cr}$ for air, since the former can be characterized in a small size laboratory while the latter requires a long unobstructed propagation path. When $P_{in} \gg P_{cr}$, a large number of ionizing filaments are initially formed (see Fig. 35).

At the present time, however, very few data about the characteristics of multiple filaments in air are available (intensity, pulse duration, density of the generated plasma, length of the multiple filaments). On the other hand, several measurements aiming at characterizing a single filament, formed from a beam with power close to the critical power, were carried out in details in several laboratories. For experimental convenience the majority of these measurements were made on short scales, with a beam focused by a lens of long focal length ($f > 1$ m). This allows a reduction of the distance necessary to the formation of the filament and a stabilization of its position in space. Khan et al. (2002) have reviewed the existing works a few years ago and published a table where some representative measured values for typical filament characteristics such as the diameter or the energy content have been collected from the literature.

4.1.1. Energy per filament, coupling

The coupling of the energy of the initial beam in a filament depends on the convergence, the diameter and the input power of the beam. The optimum coupling is obtained for a beam of small diameter ($d_0 < 3$ mm), having a weak convergence ($f/d_0 > 500$) and an initial power close to the critical value (Kosareva et al., 2006b). Between 10% and 40% of the initial energy of the pulse is channeled in the filament (Lange et al., 1998c; Brodeur et al., 1997; Mikalauskas et al., 2002). The losses partially correspond to the appearance of a conical emission in the forward direction (see Fig. 9), with an angle of the order of the mrad (Nibbering et al., 1996; Kosareva et al., 1997a). The energy in a filament in air was observed to remain limited to a value close to 1 mJ, independently of the initial energy of the beam (Braun et al., 1995; Nibbering et al., 1996; Mikalauskas et al., 2002). Above 10–30 critical powers, the laser beam breaks up into several filaments, each filament carrying an energy of the order of one mJ (Tzortzakis et al., 2001a; Day, 2001; Mikalauskas et al., 2002). For a collimated beam, beyond 25 P_{cr}, the initial beam divides initially in two closely spaced filaments, which fuse after a few meters (see Fig. 56 and Tzortzakis et al., 2001a). At 248 nm, the energy contained in a filament in air was reported to be slightly less (0.2 mJ) than in the infrared domain (Tzortzakis et al., 2000b, 2001b).

4.1.2. Transverse dimension of the filament core

A coarse estimate of the diameter of the filament core can be done by examining the size of the damage caused by the pulse in a blade of glass or the micro-burns on an exposed photographic paper. The attenuated image of the impact of the filament on a diffuser can also be recorded. All-optical methods such as ombroscopy, Schlieren and diffractometry allow a more precise reconstruction of the filament core profile (Centurion et al., 2004; Yang et al., 2002a; Gopal et al., 2007). The principle of time resolved optical diffractometry is shown in Fig. 57 (Tzortzakis et al., 2000a, 2001). The laser pulse is divided into a principal pulse, which is used to form a filament, and a much less intense pulse, which is used as a probe. The probe beam crosses the filament and sees a rectilinear phase object. The phase front of the probe pulse undergoes a deformation which is analyzed in the far field (right part in Fig. 57). A rectilinear phase object gives
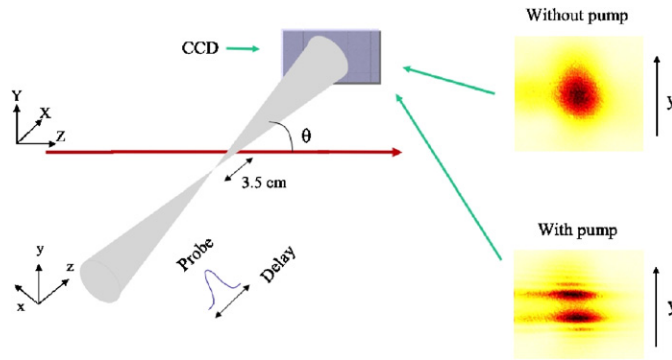
Fig. 57. Experimental diagram for time-resolved optical diffractometry, allowing the measurement of the filament size and the duration of the generated plasma. Note the fringes in the far field, when there is spatial and temporal overlap between the probe beam and the plasma column generated by the filament. From Tzortzakis et al. (2000a); Tzortzakis (2001).

rise to a system of fringes, whose variation depends on the changes in the refraction index. By moving the probe pulse perpendicularly to the propagation axis of the filament, the dimension of the object which modifies the refraction index (the plasma channel) is obtained, about 80 μm in the initial stage of the filamentation. Yang et al. (2002a) measured the phase contrast and obtained similar results. These measurements are in agreement with several reported values of the diameter of the filament core for infrared wavelengths (Braun et al., 1995; Nibbering et al., 1996; Brodeur et al., 1997; Kosareva et al., 1997a; Kasparian et al., 2000b; Rairoux et al., 2000; Schillinger and Sauerbrey, 1999; La Fontaine et al., 1999b) and with numerical results (Chiron et al., 1999; Lange et al., 1998c; Couairon et al., 2002). Recently, Deng et al. (2006) have shown by using a longitudinal diffraction method and a plasma fluorescence imaging technique that the diameter of an infrared filament increases from 20 to 80 μm when the peak power increases from 1.5 to 4 critical power for self-focusing. Above 4 P_{cr}, multiple filaments are obtained. Théberge et al. (2006b) have measured the diameter of the filament core for different focal lengths and have found that the increase of the filament diameter as a function of pulse power is steeper for short focal lengths (down to 50 cm). Filament diameters between 55 and 100 μm were obtained for focal lengths between 4 m and 50 cm.

Several groups announced the presence of filaments with a millimeter size after a propagation over several tens of meters (La Fontaine et al., 1999b; Chin et al., 2002b; Méchain et al., 2004a). In these filaments, the intensity of the pulse is lower than the ionization threshold, but the optical Kerr effect still plays its role. At 527 nm, a filament diameter of 120 μm was reported (Mikalauskas et al., 2002). At 248 nm, filaments in air have typically the same diameter as in the IR (150 μm from Tzortzakis et al. (2000b, 2001b) and 100 μm from (Schwarz et al., 2000)).

4.1.3. Filamentation length

What is meant by a filament length? In a broad definition, filamentation does not imply the presence of a continuous plasma channel. It relates to a narrow beam that does not obey the linear diffraction law, but propagates in a nonlinear regime keeping a power $P_{in} > P_{cr}$ such that beam collapse is expected at a later stage. According to this definition the distance of filamentation covers at least the distance between the first and last beam collapse. However, many experiments characterize filaments using a narrower definition, by referring to the length over which the pulse intensity is sufficiently high to ionize the material. In an even more restricted definition it only refers to the length over which the filament produces a continuous plasma channel. The most general definition is adopted here.

In air or other gases, the first and last self-focusing points may be found by a careful measurement of ionization as a function of distance. The measurement of the last focusing point is difficult because the corresponding plasma string can be very short. Furthermore, its location may vary from shot to shot due to laser intensity fluctuations or air turbulence. In condensed media, an imaging technique is necessary.

The filamentation length depends on the initial conditions of the laser beam (intensity, diameter and convergence of the beam). In a collimated geometry, there is initially a region of a few meters where the diameter of the filament can be constant but the beam diameter generally exhibits, oscillations with an amplitude of the order of the size of the filament, corresponding to several separated beam refocusing cycles (see Fig. 6).
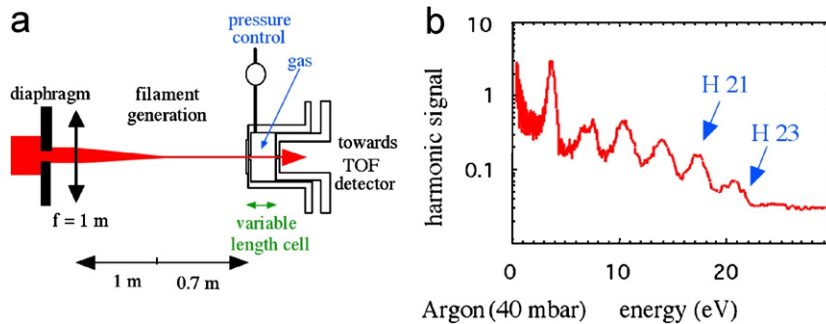
Fig. 58. (a) Principle for the measurement of the peak intensity in a filament. The odd harmonics generated in a cell filled with argon at low pressure are detected in a second cell filled with xenon. The energy of the free electrons in the xenon gas is measured by a detector of time of flight, which informs about the energy of VUV photons responsible for ionization. (b) The figure shows the odd harmonics ranging between the 11th and 23rd orders. From Lange (1998); Lange et al. (1998a).

The filamentation length was investigated by several teams using the intuitive idea that a filament disappears either because it spatially diverges and temporally disperses or because the feeding energy from the input laser pulse decreases during the propagation (Schwarz and Diels, 2001; Couairon, 2003b; Luo et al., 2005b). The idea is close to that of the energy reservoir. A laser pulse loses its energy owing to linear Rayleigh–Mie scattering; it is also either partially absorbed through MPI or scattered by the microsize plasma generated by filamentation. SPM further converts the energy initially contained in the fundamental bandwidth into a white-light supercontinuum. When the peak power of the input pulse at the fundamental wavelength becomes lower than the critical power for self-focusing, filamentation can no longer take place. However, filamentation can stop, even if the beam contains a power exceeding the critical power, when the curvature of its spatial phase induced by plasma defocusing and diffraction becomes too large to be counterbalanced by self-focusing at the remaining power (Liu et al., 2006d). Measurements by Fibich et al. (2006) also suggest this beam curvature effect. The authors reported that the filamentation length increases with the collapse distance owing to the change of the convergence angle at the onset of collapse.

Luo et al. (2005b) measured the effective attenuation coefficient of an intense femtosecond pulse undergoing filamentation in air by using a lidar remote-sensing technique, and assuming an exponential decay of the input pulse energy with the propagation distance. This coefficient of $0.0077 \pm 0.0012\,\mathrm{m}^{-1}$ yields an attenuation equivalent to that in a thick haze in the atmosphere for a linearly propagating beam. It was used to estimate an upper bound of 760 m for the total extent of the filament generated by a 51 mJ, 42 fs, 800 nm laser pulse. A much smaller total extent was estimated by Couairon (2003b); while both estimations assume a connected single plasma channel exhausting all the energy available in the laser pulse, the main difference lies in the attenuation coefficient which in one case is measured under experimental conditions that might generate multiple disconnected filaments, and in the other case is estimated from the MPA cross section computed from the Keldysh theory.

4.1.4. Peak intensity of a filament

Measurements of the peak intensity in a filament are far from being easy. Estimates based on the measurements of the energy and the dimensions of the filament give a set of dispersed values ranging between 10^{12} and $10^{14}\,\mathrm{W/cm}^2$. A more precise measurement was performed by Lange et al. (1998a). It consists in introducing a filament, after its propagation over a distance of 50 cm in air, inside a cell containing a noble gas, like argon (see Fig. 58). For intensities of about 10^{13}–$10^{14}\,\mathrm{W/cm}^2$, the atoms generate a great number of odd high-order harmonics (Salières et al., 1999). A simple and well established relation links the order of the highest harmonic to the intensity of the laser (Corkum, 1993; Kulander et al., 1993):

$$\hbar\omega = U_i + 3.2U_p, \tag{149}$$
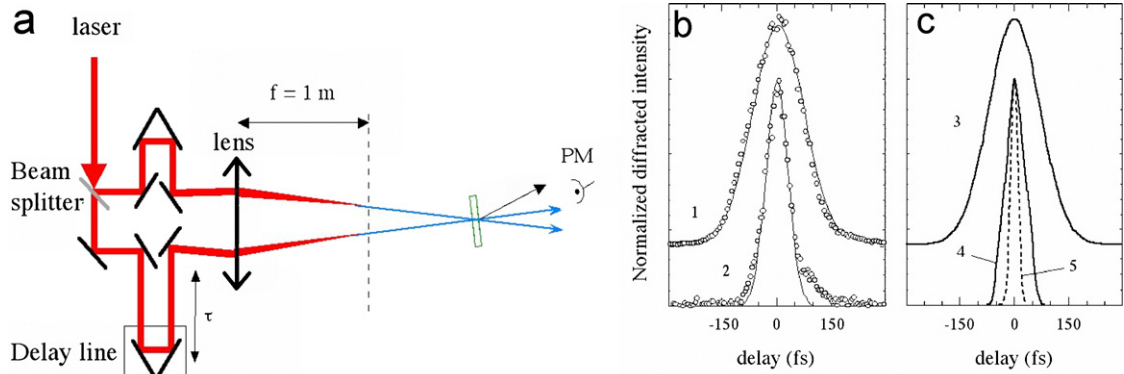
Fig. 59. Principle of the measurement of the duration of the self-guided (filamented) pulse in air. From Lange (1998). Two filaments are formed in air. They cross in a silica blade, which gives rise to a four wave mixing signal. (a) Experimental setup used to measure the duration of self-guided pulses. (b) The measurement of the signal as a function of the delay between the two filaments gives the cross correlation trace of the filaments. 1: trace of two nonfilamented pulses; 2: trace corresponding to two filaments. (c) Numerical results taking into account the temporal resolution of the detector (full curve).

where U_i is the ionization potential of the atom and U_p is the ponderomotive energy (the mean kinetic energy of the free electrons oscillating in the laser field), which is directly proportional to the peak intensity:

$$U_p = \frac{1}{2} m_e \langle v^2 \rangle = \frac{e^2 E^2}{4 m_e \omega^2} = 9.33 \times 10^{-14} I \lambda^2. \tag{150}$$

Here, I is expressed in W/cm^2, λ in μm and U_p is in eV. Once generated, the various harmonics are introduced into a second cell where a detector measures the energy of the UV photons produced by the filament. Fig. 58 shows that harmonics are generated up to the 23rd order in argon, which corresponds to a peak intensity in the filament of $5 \times 10^{13}\,W/cm^2$, in agreement with the evaluations obtained from numerical simulations.

Ting et al. (2005b) and Gordon et al. (2006) have used an helium gas interface in order to characterize filaments in air without perturbing the measurement by the introduction of an optical element. Because of its low Kerr index, the helium allows beam expansion before attenuation by reflection on the surface of a glass plate. Ting et al. (2005b) found a fluence between 0.23 and 0.67 J/cm^2 in a single filament and estimate a peak intensity between 0.45 and $1.3 \times 10^{13}\,W/cm^2$. However, the estimated intensity is based on the assumption that the pulse duration has not been changed during filamentation. As can be seen in Section 4.1.5, pulse self-compression occurs during filamentation so that a correction by a factor 4–10 is required, yielding peak intensities in agreement with the results of Lange et al. (1998a). Independently, Becker et al. (2001a) found slightly higher values for the peak intensity in a gas of nitrogen molecules from an analysis of the fluorescence signals.

4.1.5. Duration of the self-guided pulse and pulse self-compression

To measure the duration of the pulse in a filament, Lange et al. (1998b, d) used the method described in Fig. 59. Two filaments cross in a silica blade. The cross diffraction signal emitted in the direction $2\mathbf{k}_1 - \mathbf{k}_2$, (where $\mathbf{k}_1$ and $\mathbf{k}_2$ are the wavevectors of the two filaments) is measured according to the delay between the two filaments. The obtained cross-correlation trace indicates a reduction of the pulse duration in the filaments by a factor 4 (see Fig. 59(b,c)). The resolution of the correlator, about 20 fs, did not make it possible to resolve the substructures predicted by numerical simulations.

Since these measurements, pulse shortening was reported by several groups. Hatayama et al. (2003) have measured a compression ratio of more than two from filamentation of 70 fs Ti:sapphire laser pulses in argon. Mikalauskas et al. (2002) showed by a measurement of third order autocorrelation that a pulse at 527 nm, with an initial duration of 900 fs, was shortened by a factor 6 (from 900 to 160 fs) after a propagation in the form of a filament over 16 m in air. Tzortzakis et al. (2001b) have shown that ultraviolet picosecond pulses in the form of filaments are significantly shortened (see Fig. 60). By probing the spectrum evolution along a filament with a hollow fiber (diameter of 400 μm), Cao et al. (2006) have reported an optimal position in a filament generated by a 50 fs, 800 nm laser pulse where the
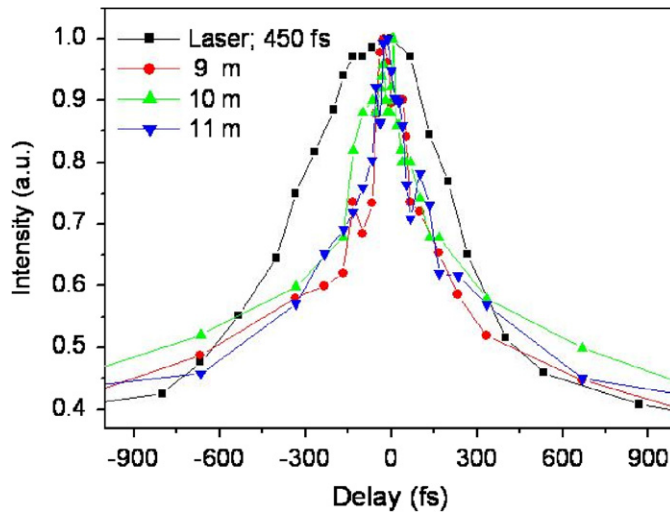
Fig. 60. Autocorrelation traces of an ultraviolet (248 nm) pulse (initial duration 450 fs) undergoing filamentation at various distances. From Tzortzakis et al. (2001b).
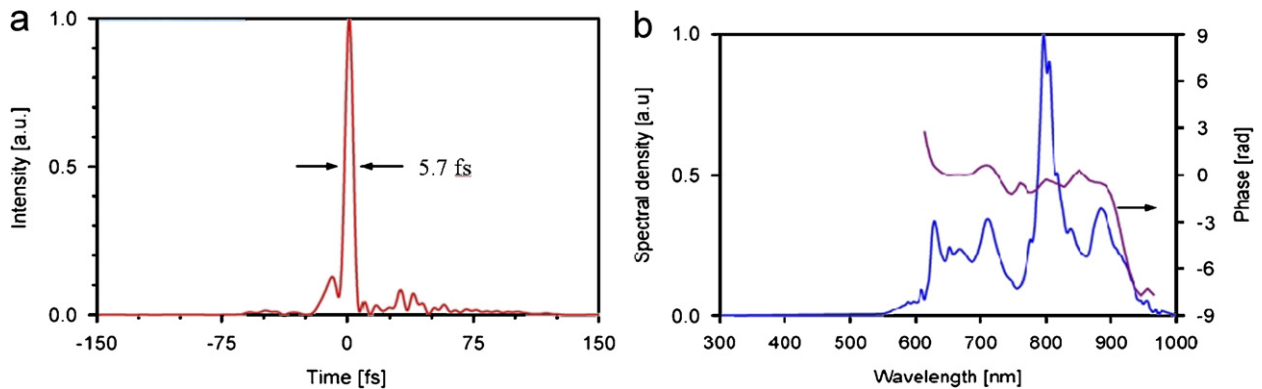
Fig. 61. Pulse self shortening by filamentation in argon gas cells. According to Hauri et al. (2004); Couairon et al. (2006a). (a) Temporal profile. (b) Spectral intensity (left axis) and phase (right axis).

spectrum broadening potentially supports 25 fs duration. By measuring cross-correlation traces between a pulse at the end of a filament and a non filamented pulse from the same laser ($\lambda = 800$ nm, duration 120 fs), Couairon et al. (2003) report a temporal compression ratio of 10 from (from 120 to 12 fs) for the self-guided pulse. Stibenz et al. (2006) have obtained self-compressed pulse emerging from an argon cell with a duration of about 8 fs and an energy of 3 mJ starting from an optical pulse of 45 fs duration with an energy of 5 mJ. Apparently, self-compression by filamentation can proceed down to nearly the ultimate limit of a single cycle pulse. Hauri et al. (2004) showed a pulse shortening down to nearly one optical cycle by filamentation of a 1 mJ, 42 fs, 800 nm laser pulse in two successive argon gas cells (see Fig. 61(a)). Chirped mirrors placed after each cell recompressed the chirp introduced by the windows at the exit of the cells. The pulse duration was measured by a single shot SPIDER technique (Kornelis et al., 2003) to be 5.7 fs. The resulting 5.7 fs pulse exhibited a nearly flat temporal phase as shown in Fig. 61(b). With better chirped mirrors, a 5.1 fs pulse was measured (Hauri et al., 2005; Guandalini et al., 2006). Chen et al. (2006a) and Liu et al. (2006b) have used chirped mirrors to recompress self-shortened pulses by filamentation in an argon gas cell, from 52 to 12 fs. Hauri et al. (2006) recently generated filaments about 65 cm long in argon from 40 fs, 800 nm, 4 mJ laser pulses. Astonishingly, the filaments were shown to carry a strong negative chirp of -500 fs^2 allowing an easy temporal compression down to 9.6 fs by propagation over a suited length of any dispersive medium. A control of the plasma induced dispersion within
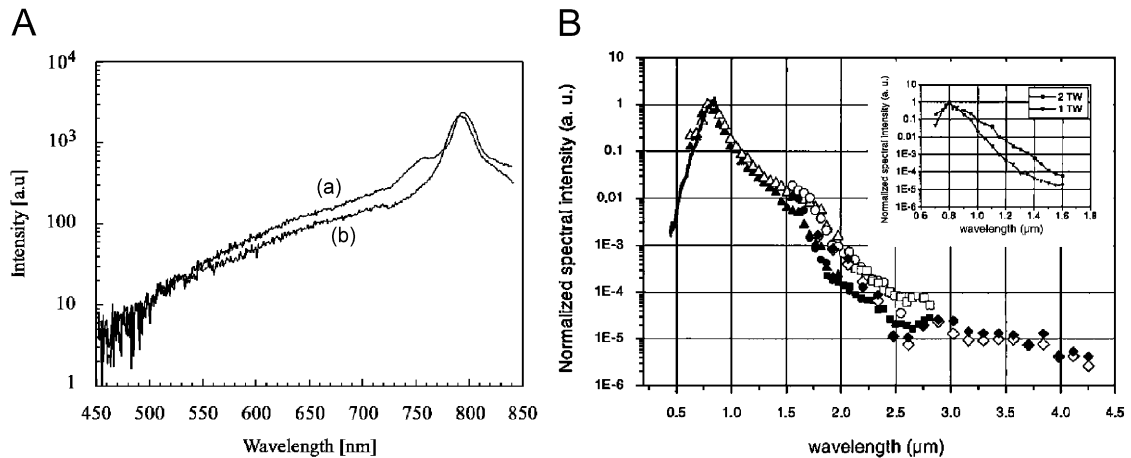
Fig. 62. (A) Spectra of the atmospheric white light continuum. The traces (a) and (b) depict spectra which were measured for two different pre-chirp settings of the fundamental laser emission. From Rairoux et al. (2000). (B) Measured spectrum of the white light continuum generated in the center of the beam by 2-TW laser pulses. Filled symbols: pulse duration of 35 fs without chirp. Open symbols: 55-fs initial pulse duration with negative chirp. Inset, spectrum of the white light continuum generated in the center of the beam by 100 fs pulses as a function of pulse power (200 and 100 mJ for 2 and 1 TW, respectively). From Kasparian et al. (2000b).

the filament would therefore allow a simplification of the set-up for pulse compression by filamentation. In keeping with this result, Liu et al. (2006a) have shown that negatively chirped laser pulses in normally dispersive Kerr media undergo successively spectral shortening and pulse self-compression, due to the combined action of GVD and SPM. Finally, It was shown that the locking of the carrier envelope offset is not destroyed by the filamentation process (Hauri et al., 2004, 2005). There are good hopes to up-scale the energy in the output pulse by generating the filament in a pressure gradient (Couairon et al., 2005a). In this respect, it should be noted that the hollow fiber compression technique (Nisoli et al., 1997), whose principle is based on the spectral broadening of femtosecond laser pulses and subsequent recompression by chirped mirrors, was recently shown numerically to be very efficient for enhancing the transmitted energy with addition of a pressure gradient in the hollow waveguide (Nurhuda et al., 2003). Compressed pulses of less than 10 fs duration and an energy as high as 5 mJ were obtained in this way (Suda et al., 2005). Improvement of this technique was shown to potentially lead to single-pulses with FWHM duration of 5.4 fs and an energy of 8.1 mJ (Nurhuda et al., 2005). Calculations by Couairon et al. (2005a) predict that filamentation in a gas with pressure gradient generates single cycle pulses with an energy of several hundreds of μJ.

4.1.6. Continuum generation in gases

Supercontinuum generation or white light continuum was first discovered by Alfano and Shapiro (1970) by focusing picosecond pulses into glass. The first report of a supercontinuum generation extending from the UV to the IR in high pressure N_2, CO_2 and H_2 gases was made by Corkum et al. (1986). Supercontinuum generation in high pressure gases from 248 nm laser pulses was reported by Gosnell et al. (1990). More recently, white light generation was reported to occur during the propagation of IR ultrashort laser pulses undergoing filamentation in condensed media as well as in gases. In air, the white continuum covers the entire visible domain (see Fig. 62(A)) and has a short drop around 360 nm. SPM considerably broadens the spectrum which takes the form of a plateau between 700 and 500 nm, followed by a weaker emission falling off abruptly around 350 nm (see Figs. 8 and 62; Rairoux et al., 2000; Wöste et al., 1997). The measurement of correlations within the continuum between pairs of symmetric frequencies with respect to the central wavelength of the laser was interpreted as the signature of four wave mixing processes (Béjot et al., 2006). Prade et al. (2006a) have investigated the continuum generated by a filament at 400 nm. They find that the continuum is in fact strongly structured as expected from SPM. Spectral phase fluctuations from shot to shot lead to a smoothing of the broadened spectrum when recorded in a multiple exposure.

An extension of the power spectrum in the UV was observed by Théberge et al. (2005b, c) and attributed to the presence of an intense third harmonic pulse copropagating with an infrared filament (see Section 4.1.12 and
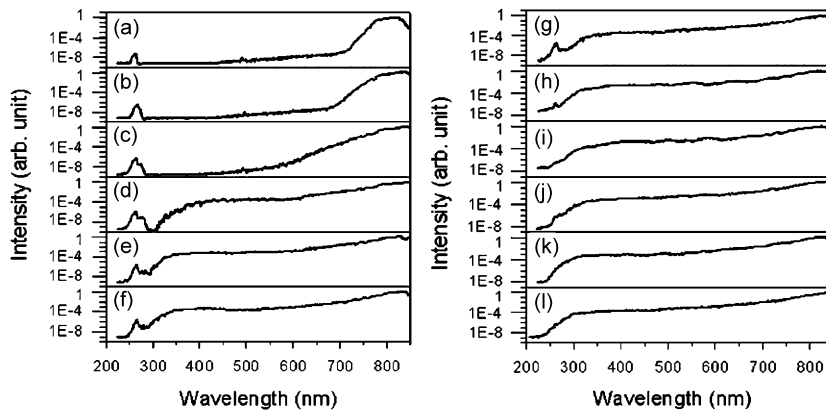
Fig. 63. Experimental spectrum of the third harmonic and fundamental continuum generated in atmospheric air at different pulse energies (a) 250 μJ, (b) 500 μJ, (c) 750 μJ, (d) 1.0 mJ, (e) 1.25 mJ, (f) 1.5 mJ, (g) 1.75 mJ, (h) 2.0 mJ, (i) 3.0 mJ, (j) 4.0 mJ, (k) 5.0 mJ and (l) 10.0 mJ using a lens of 380 cm focal length. From Théberge et al. (2005b, c).

Fig. 63). Trushin et al. (2005) have measured a supercontinuum reaching 150 nm from 10 fs, 805 nm pulses with powers moderately above critical, loosely focused ($f = 5$ m) in argon.

The infrared extension of the continuum generated in air was investigated by Kasparian et al. (2000b). A continuum reaching 4 μm has been detected but with an intensity reduced by 4 orders of magnitude from the center wavelength (see Fig. 62(B)).

Yang et al. (2005) have observed that the supercontinuum emission generated from filaments produced by intense femtosecond laser pulses propagating through air over a long distance is polarization dependent. The conversion efficiency from the 800-nm fundamental to white light was found to be higher for circular polarization than for linear polarization when the laser intensity exceeds the threshold of the breakdown of air. The authors explain this result, apparently in contradiction with numerical predictions by Kolesik et al. (2001), by the fact that a higher intensity was reached at the focus of the circularly polarized beams thus leading to an enhanced plasma induced self-phase modulation.

The angular distribution of the continuum generation has been measured by Yu et al. (2001). A pronounced peak was measured in the backward direction. To date, the physical mechanism at the origin of this backward emission has not been discovered.

4.1.7. Evidence for ionization of air molecules during filamentation

The presence of plasma generated by filamentation was highlighted using several techniques: measurements of the electric conductivity of air (Tzortzakis et al., 2000a, 1999; Ladouceur et al., 2001; Schillinger and Sauerbrey, 1999), spectral interferometry (La Fontaine et al., 1999a; Tzortzakis et al., 2000a; Chien et al., 2000; Rambo et al., 2001b; Yang et al., 2002a; Liu et al., 2005a), measurement of the sub-THz pulse emitted by the plasma column (Cheng et al., 2001; Tzortzakis et al., 2002), observation of a luminescence characteristic of excited ionized nitrogen molecules (Talebpour et al., 1999a). A sonographic technique was also proposed, based on the detection of the pressure wave induced by the expansion of the column of air heated by Joule effect (Yu et al., 2003). A linear antenna or a circular antenna around the filament was used to detect the electromagnetic pulse (EMP) radiated from the filament and compared with good agreement to the measurements of the backscattered fluorescence (Hosseini et al., 2003a). The latter method can detect the dynamics of plasma generation but is useless over long propagation distances.

4.1.8. Evolution in time of the plasma density and determination of the plasma lifetime

Several experiments have characterized the time evolution of the density of free electrons generated in the wake of filaments. The plasma decay is obtained from time-resolved diffraction measurements (Tzortzakis et al., 2000a) and from electric measurements of the plasma conductivity (Tzortzakis et al., 1999; Ladouceur et al., 2001; Schillinger and Sauerbrey, 1999). The first method makes it possible to obtain the initial density and its evolution on a picosecond scale. The second gives the variation of the density on a time scale larger than the nanosecond. The principle of diffraction
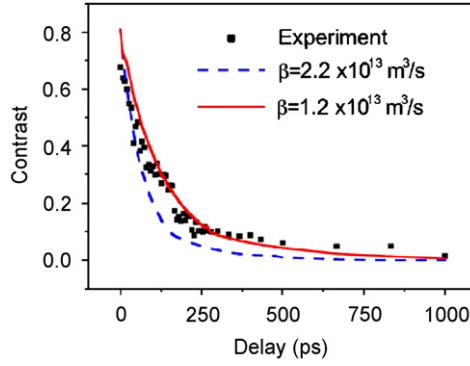
Fig. 64. Contrast of the probe wave front central fringe as a function of the delay between probe and self-guided pulse. The curves are obtained from the analytic formula (154). From Tzortzakis et al. (2000a).

measurements is indicated in Fig. 57. The contrast of the fringes observed in far-field is measured as a function of the delay between the probe pulse and the self-guided pulse. The evolution equations for the electron density (ρ_e) and the densities of positive (p) or negative (n) ions (ρ_p, ρ_n) generated instantaneously by the pump pulse at $t = 0$ read:

$$d\rho_e/dt = v\rho_e - \eta\rho_e - \beta_{ep}\rho_e\rho_p, \tag{151}$$
$$d\rho_p/dt = v\rho_e - \beta_{ep}\rho_e\rho_p - \beta_{np}\rho_n\rho_p, \tag{152}$$
$$d\rho_n/dt = -\eta\rho_e - \beta_{np}\rho_n\rho_p. \tag{153}$$

The coefficient v corresponds to the multiplication of electrons by avalanche in the presence of an electric field (either the laser field, or an external applied field). The quantity $\eta = 2.45 \times 10^7 \text{ s}^{-1}$ is the coefficient of electron attachment to the neutral oxygen molecules. The coefficients β_{ep} and β_{np} corresponds to electron–ion and ion–ion recombination processes. The solution to these equations reads

$$\rho_e(t) = \frac{\rho_e(0)\exp[-(\eta - v)t]}{1 - \rho_e(0)\beta_{ep}(\exp[-(\eta - v)t] - 1)/(\eta - v)}. \tag{154}$$

When $\eta \ll v$, the electron density varies according to the law:

$$\rho_e(t) = \frac{\rho_e(0)\exp[-\eta t]}{1 + bt}. \tag{155}$$

The decay of the electron density is initially dominated by the rate $b = \rho_e(0)\beta_{ep}$.

Experiments indeed show a fast initial decrease, in the form $\rho_e(t) = \rho_e(0)/(1+bt)$, with a coefficient $b = 4.7 \times 10^8 \text{ s}^{-1}$ close to the value found in the literature (Fig. 64; Tzortzakis et al., 2000a). This nonexponential decrease indicates that the capture of electrons on the parents ions dominates the initial evolution of the plasma during the first nanoseconds. The latter evolution, when $\rho_e < 10^{15} \text{ cm}^{-3}$, is due to the attachment of electrons on the oxygen molecules. The electron density decreases exponentially with a characteristic time $\tau = 1/\eta \sim 130 \text{ ns}$ (Ladouceur et al., 2001). These results were corroborated by Rambo et al. (2001b) who proposed a Mach–Zender based interferometric technique to measure the time derivative of the index of refraction in a single shot that can be used to temporally resolve the evolution of an electron plasma with two-dimensional spatial information. The temporal resolution is limited by the probe pulse duration while the spatial resolution depends upon the ratio of pump to probe intensity and the pixel size of the CCD.

4.1.9. Plasma density

The values published for the mean plasma density in a filament vary over several orders of magnitude between 10^{14} and 10^{18} cm^{-3} (Tzortzakis et al., 1999; Schillinger and Sauerbrey, 1999; Chien et al., 2000; Yang et al., 2002a, b; Ting et al., 2005a). Besides the fact that different measurement methods were used, this great dispersion is partly explained by the fact that some measurements were performed in the multifilamentation regime. In this case, the average value integrated on the whole section of the beam is obtained, whereas the measurements performed in a single filament give

the density inside a filament, which is usually larger since it does not take into account the plasma free energy reservoir. From the measurement of the conductivity of a filament generated by 120 fs, 800 nm laser pulse, the plasma density corresponding to only one plasma channel was found by Tzortzakis et al. (1999) to lie between 10^{16} and 10^{17} cm^{-3}. Precise measurements of the evolution of the plasma density, using an all optical method of time resolved diffraction allows one to infer with precision the initial density $\rho_e(0)$ from Eq. (155), which reaches 10^{17} cm^{-3} in the vicinity of the focus. Measurements of the electric conduction give $\rho_e(0) \sim 10^{16}$ cm^{-3} (Tzortzakis et al., 1999; Ladouceur et al., 2001; Ting et al., 2005a). From measurements by means of an interferometric method, Yang et al. (2002a, b) inferred an electron density as high as 2.7×10^{18} cm^{-3} for 45 mJ, 25 fs, 800 nm laser pulses focused with various lenses ($f = 40$ cm, 2 and 4 m). For an 800 fs, ultraviolet laser pulse at 248 nm, Rambo et al. (2001b) obtained an electron density of 10^{16} cm^{-3} 400 ps after the ionizing pulse, with an interferometric method. From an evaluation of the recombination and refraction effects that occurred during this delay, Rambo et al. (2001b) estimated that air was fully ionized by the 800 fs UV pulse. According to Eq. (21), the electron density should slightly depend on the pulse duration in the regime of intensity clamping. There is, however, not enough data to conclude about the accuracy of Eq. (21) to fit the measurements.

The electron density and decay dynamics of a plasma channel generated by a 2 cm long filament in air was recently investigated by employing pump–probe back longitudinal diffractometry (Liu et al., 2005a). From an analytical reconstruction method of electron density which is sensitive to the phase shift and channel size, the electron density in the weak plasma channel generated by 800 nm, 50 fs laser pulses, was extracted to be about 4×10^{16} cm^{-3} and the diameters of the plasma channel and light filament were estimated about 50 and 150 μm, respectively. Théberge et al. (2006b) have shown that the plasma density in a filament, characterized by side imaging fluorescence and longitudinal diffraction techniques, is highly dependent on the focal length of the lens and slightly dependent on the pulse power. The density was found to increase from 10^{15} to 2×10^{18} cm^{-3} when the focal length decreased from 4 m to 10 cm.

4.1.10. Length of the plasma column

The maximum length of the plasma string that can be generated by filamentation can be roughly evaluated by the ratio of the pulse energy to the energy losses per length unit. This approach is not equivalent to that based on the energy reservoir; it also assumes a continuous plasma channel and an effective use of all the energy available in the reservoir to generate a plasma. Estimations of the length of a plasma column from this simple model have been performed for UV pulses by Schwarz et al. (2000) and for IR pulses by Couairon (2003b). Fig. 65A shows that for a given pulse energy, the largest filamentation length L_{fil}, i.e., the largest plasma column, is obtained for a specific pulse duration. The maximal values and corresponding pulse durations are reported in Fig. 65B as functions of the pulse energy. Fig. 65C shows the associated peak intensity and electron density.

Several techniques have been developed to measure the length of the plasma column generated by filamentation (see Fig. 65D). Measurements of the conductivity (Schillinger and Sauerbrey, 1999; Tzortzakis et al., 2000a) by moving the detector along the axis of the filament give direct access to the length and density of the plasma channel (Fig. 65D(a)): For a strongly convergent IR beam ($f \leqslant 1$ m) a peak density is observed in the vicinity of the focus, which indicates the presence of a hot plasma, followed by a plateau of constant density over 1–2 m. Similar values have been obtained by displacing a THz detector (Fig. 65D(b)) or monitoring the luminescence (Fig. 65D(c)) in a direction perpendicular to the filament axis. From interferometric measurements, Yang et al. (2002a) observed plasma channels generated by femtosecond laser pulses over 5 m in air. In a converging geometry, the length of the filament associated to an uninterrupted ionization of the medium, which is formed in the vicinity of the focus, varies between 1 and 2 m. With a collimated beam, this distance can reach several tens of meters (Nibbering et al., 1996; Mikalauskas et al., 2002). A confirmation of this point is, however, difficult to obtain in the presence of fluctuations in the position where a filament starts, which can be due to shot to shot fluctuations or to the effect of external parameters such as air turbulence. With a beam having $P_{in} > P_{cr}$, a 10 m long plasma column was obtained (Ladouceur et al., 2001).

Electrons generated by MPI are ejected from molecules with an initial kinetic energy of a few electron volts, which corresponds to an initial free-electron temperature in the order of 10^4–10^5 K. An energy transfer occurs between the free electrons and the background gas ions and neutral molecules owing to elastic and inelastic collisions. The gas in the filament is then heated to a high temperature when thermal equilibrium is reached in the filament. The heated gas expands, leading to a shock wave emission. The energy transfers from electrons to nuclei in a time of the order of 1–10 ns in air. A final equilibrium temperature of approximately 400 K is reached in a filament in air a few ns after the exciting laser pulse (Tzortzakis et al., 2001c). The acoustic wave emitted from a long plasma channel associated
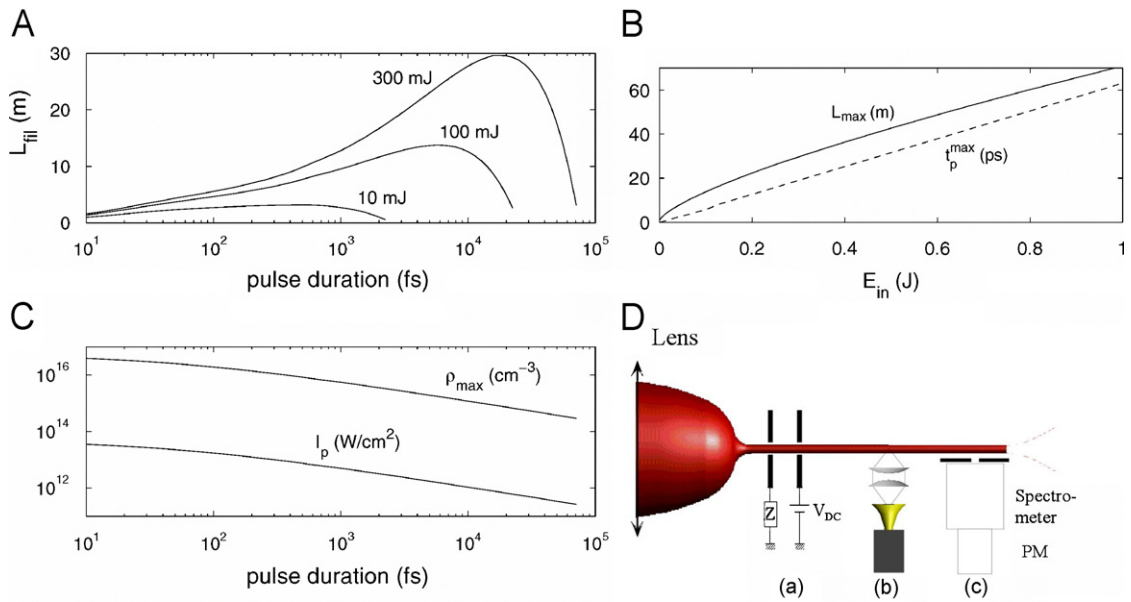
Fig. 65. (A) Length of the plasma channel generated by a filament in air as a function of the initial duration of the laser pulse ($\lambda_0 = 800$ nm), for three values of pulse energy: 10, 100 and 300 mJ. (B) Maximum length of the plasma column in meters and optimal duration of the pulse in ps (values on the same axis) as a function of the initial pulse energy. (C) Maximum intensity in the filament and electron density as a function of the duration of the pulse. From Couairon (2003b). (D) The plasma channel can be detected by three methods: (a) electric conductivity. (b) Heterodyne detection of sub-THz radiation. (c) Luminescence detection of excited nitrogen atoms. From Méchain (2005).

to a filament was detected with a microphone with high sensitivity, low noise, and high spatial resolution (Yu et al., 2003). A similar technique has been used by Matvienko et al. (2005). This method enables the authors to reconstruct the energy characteristics of the femtosecond filament laser radiation, the filament geometric size and the transmission of aerosol layer.

4.1.11. Plasma resistivity

Up to now, the characteristics of the plasma were mainly measured in the laboratory. The principle of the measurements of electric conductivity of air is shown in Fig. 66. The filament connects two electrodes to which a dc voltage is applied. In the absence of filament, the electric circuit is open, no current is detected. After the passage of the pulse, air becomes conducting and closes the circuit; A pulse of current is collected at the boundaries of an external resistance. From the measured charge, the initial density is estimated about 10^{16} cm^{-3}, in agreement with the predictions of the numerical simulations (Chiron et al., 1999; Tzortzakis et al., 2001a; Couairon et al., 2002).

Ladouceur et al. (2001) measured an average resistance varying in time between $3.6 \times 10^5 \, \Omega/$m (initially) and $6.4 \times 10^7 \, \Omega/$m after 150 ns. The resistance is directly proportional to the length of the plasma column in the filament up to 6 m. The evolution of the resistance as a function of time is explained by the capture of the electrons on the oxygen molecules. Tzortzakis et al. (1999) found $2 \times 10^6 \, \Omega/$m during the first ns, at an inter-electrode distance ranging between 2 and 10 cm. In these two cases, the diameter of the filament was about 80 μm, which leads to a value of the resistivity (resistance per conducting unit of area) about $1 \, \Omega$ cm. These values are in agreement with a plasma density of 10^{16} cm^{-3}. A resistivity of less than $1 \, \Omega$ cm was also reported by Yang et al. (2002a, b) for a filament diameter of 120 μm.

4.1.12. Third harmonic generation inside filaments

Aközbek et al. (2002b) have shown from laboratory experiments and simulations that an infrared filament (800 nm) in air generates a pulse at the frequency $3\omega_0$ which propagates at the same group velocity as the fundamental pulse. Moreover, pulses at ω_0 and $3\omega_0$ preserve a constant intensity ratio over a distance longer than the coherence length
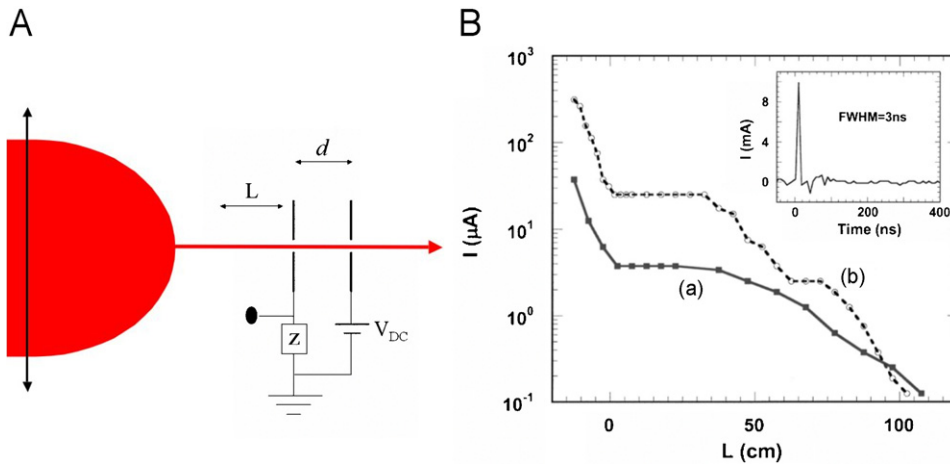
Fig. 66. (A) Principle of the measurement of the plasma density generated by a filament in air. The plasma column formed in the wake of the laser pulse closes an electric circuit. (B) Single shot measurements of the current as a function of the propagation distance L showing a plateau in the conductivity over several tens of cm, in agreement with calculations. From the charge collected at the boundaries of the electrodes, the density of free carriers can be estimated: $\rho \sim 3 \times 10^{16}$ cm^{-3} for a 800 nm, 120 fs, 14 mJ laser pulse focused by a lens $f = 2$ m. The applied voltage is 1000 V dc across the electrodes with spacing (a) $d = 11.5$ cm and (b) $d = 3$ cm. The external resistance is $Z = 8.2$ kΩ. The origin of L corresponds to the geometric focus of the lens. The inset shows the shape of the transient voltage, measured across a 100-Ω resistance, with an applied voltage of 1500 V. From Tzortzakis et al. (1999).
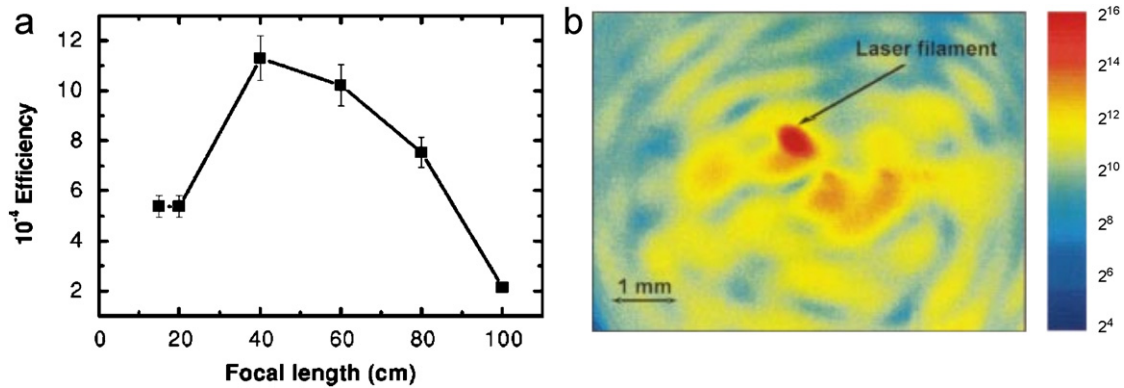
Fig. 67. (a) Conversion efficiency of the filamented pulse into its third harmonic, according to the propagation distance in the form of a filament. From Yang et al. (2003). (b) Typical transverse image of the UV light taken with a 12 bit CCD camera after 7 m of propagation in air (intensity scale is log2). From Alexeev et al. (2005).

$L_c = \pi/|\Delta k|$, where $|\Delta k| = |3k_{\omega_0} - k_{3\omega_0}|$ thus resulting in a two-colored filament. The ratio of the intensities between $3\omega_0$ and ω_0 frequencies is about 10^{-3}. The authors explain this effect by cross-phase modulation, which locks the phases and the amplitudes of the waves at the fundamental frequency and its third harmonic. These results were confirmed by Yang et al. (2003) (see Fig. 67). Locking of the amplitudes of the waves is tantamount to a high-order saturation mechanism for the optical Kerr effect at ω_0 fully equivalent to the cascading limit studied in the context of second harmonic-generation in a crystal with no inversion symmetry (Stegeman et al., 1996; Buryak et al., 2002). This interpretation, however, was recently revisited by Kolesik et al. (2006). From numerical simulations, the authors have interpreted the third harmonic and supercontinuum components of the spectrum as generated by scattering of the fundamental carrier off the local perturbations of the medium susceptibility. The axial component was compared to a forced oscillator driven by the pump at a frequency far from resonance, which provides an alternative explanation for the fact that the fundamental and the third harmonic copropagate with a fixed phase shift of π.

Images of the UV component of a filament after 7 m of propagation were recorder by Alexeev et al. (2005) (see Fig. 67(b)). A distinct UV filament core was observed, giving another direct support to the concept of two-colored filamentation.

Naudeau et al. (2006) have recorded a 0.2% conversion efficiency into THG in air from a 100 GW, 1.54 μm laser source, comparable to that obtained at 800 nm.

Third and fifth harmonics created by an ultraviolet (248 nm) fundamental pulse undergoing filamentation in an argon cell were measured by Kortsalioudakis et al. (2005). The energy-conversion efficiencies for the harmonics were found to be at least two orders of magnitude higher than those previously reported in the literature for similar gas pressures. The enhancement was attributed to the quasi-phase matching of the harmonics due to the self-guiding of the driving pulse (Aközbek et al., 2002b).

The spatial profile of THG in air by high power near-infrared femtosecond laser pulses was further investigated by Théberge et al. (2005a). A third harmonic conical emission appeared at pump power around the critical power for self-focusing where off-axis phase-matching conditions have been generated at the beginning of the filament. By increasing the pump energy, it was shown that the TH rings energy increased rapidly with strong conversion efficiency and then saturated for higher pump energy. Most of the TH energy generated by filamentation in air was attributed to conical emission (Fig. 68). Kolesik et al. (2006) showed from numerical simulations that the appartition of third harmonic rings requires phase matching conditions to be fulfilled, corresponding to a three wave mixing process between an incident photon, a scattered photon and a nonlinear susceptibility wave. This process is enhanced under tight focusing conditions which emphasize narrow structures in the nonlinear susceptibility.

In tight focusing conditions, Ganeev et al. (2005) have shown that THG becomes stable and less influenced by spatiotemporal variations of the fundamental beam than in the filamentation regime. The authors pointed out that THG in tight focusing conditions can be applied as a stable source of coherent ultraviolet radiation at relatively high conversion efficiencies up to 10^{-3}.

4.1.13. Enhancement of continuum in the UV from third harmonic generation

Théberge et al. (2005b) have investigated the energy dependent evolution of supercontinuum and third harmonic generation by intense femtosecond laser pulses propagating in air. They found that the third harmonic continuum can extend over several tens of nm and can even overlap with the fundamental continuum. The locking phenomenon due to cross-phase modulation leads to broad and efficient continuum generation of the third harmonic pulse itself. Consequently, the effective spectral content of the supercontinuum is extended into the UV and, hence, into an important wavelength regime for the detection of pollutants and bio-aerosols. The importance of this extended supercontinuum for atmospheric applications was shown by Théberge et al. (2005a–c) who measured the backscattered third harmonic signal originated from the self-induced remote plasma filaments using a Lidar technique.

4.1.14. THz emission from the plasma

It has been recently observed that plasma filaments formed by ultrashort laser pulses propagating in gases emit a broadband EMP of radiation in the direction transverse to the propagation axis of the filament (Tzortzakis et al., 2002). One interesting aspect of THz emission in the context of filamentation studies is that it provides a new, non invasive technique to detect air ionization. The measurement principle used by Tzortzakis et al. (2002) is shown in Fig. 69. The sub-THz emission is detected by a heterodyne receiver using a local oscillator functioning at 94 or 118 GHz. A signal is detected at these two frequencies, in the form of a narrow cone of emission, perpendicular to the propagation axis z of the filament. The intensity of the sub-THz emission from the filament is constant over a distance z of about one meter, in good agreement with the length of the plasma channel, as detected independently by direct electric conductivity of air. These measurements were confirmed by calorimetric measurements, using a cooled bolometer (Méchain et al., 2003). Up to now, however, the power of the THz emission has not been precisely measured due to the lack of suitable calibration. Finally, the emission from two closely spaced filaments was found to exhibit interference, showing that the THz emission has a spatial coherence. Its longitudinal coherence has also been determined by interference between the THz radial emission from the same section of the filament in opposite directions. A mirror allows overlap of the two signals. Interference fringes with a high contrast are observed showing a high degree of longitudinal coherence (D'Amico et al., 2006a, 2007a).

Two models have been proposed to explain the THz emission. According to Cheng et al. (2001), a longitudinal charge separation is initially induced in the plasma channel by the radiation pressure due to the pulse. Electrons then
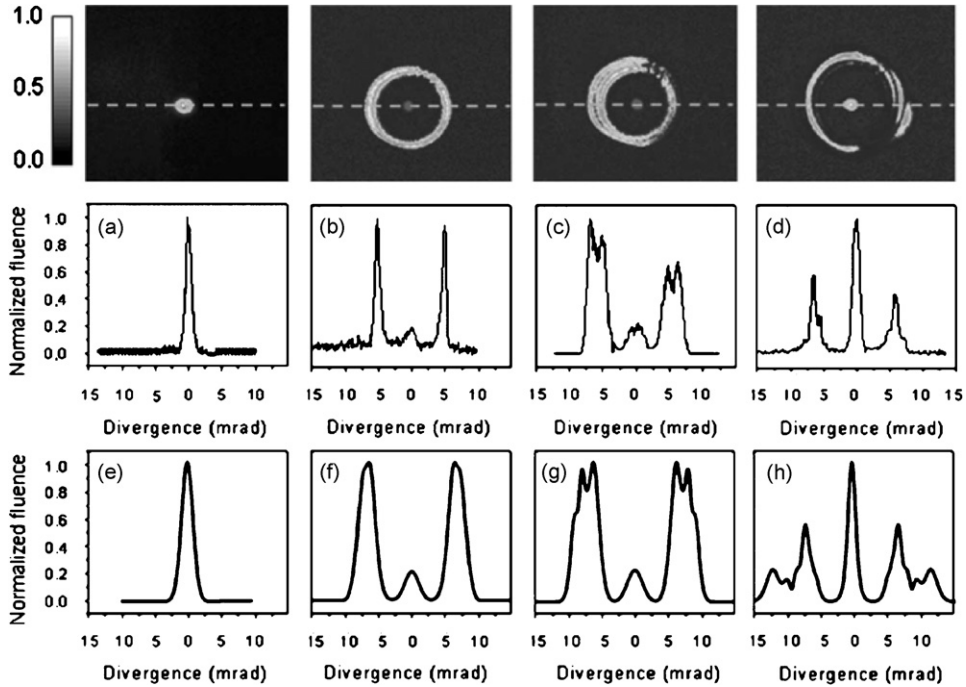
Fig. 68. TH pictures and profiles taken by ICCD camera at different pump energy (a) 100 μJ, (b) 400 μJ, (c) 500 μJ and (d) 1.3 mJ using 100 cm focal length lens. Simulated spatial profile of the TH at different pump energy (e) 85 μJ, (f) 340 μJ, (g) 510 μJ and (h) 1.278 mJ. From Théberge et al. (2005a).
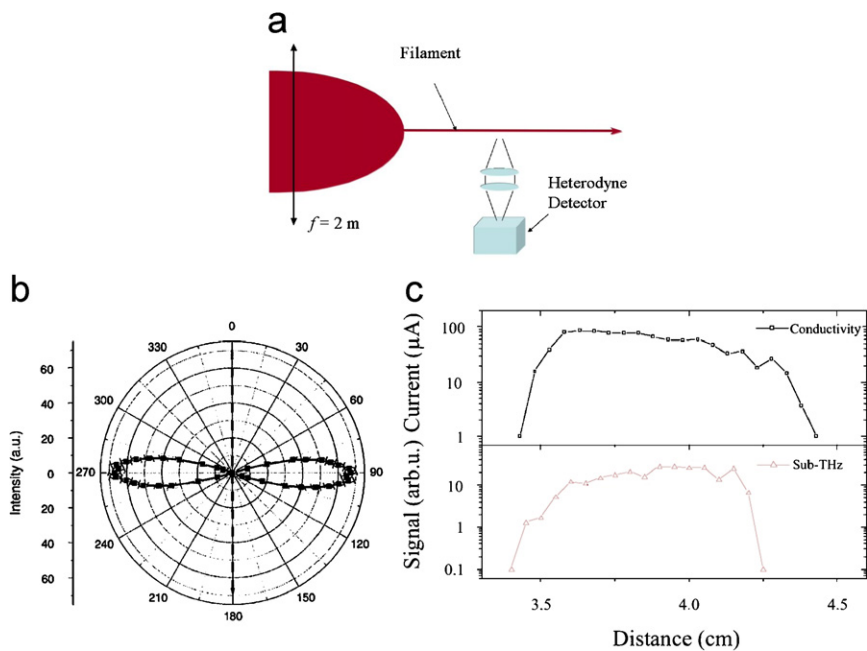
Fig. 69. (a) General diagram for the detection of the sub-THz radiation from a plasma channel generated by a filament. (b) The radiation diagram shows two lobes with an intensity maximum. The lobes are perpendicular to the axis of the filament (Tzortzakis et al., 2002). (c) Comparison of filamentation lengths measured by conductivity and by sub-THz detection.
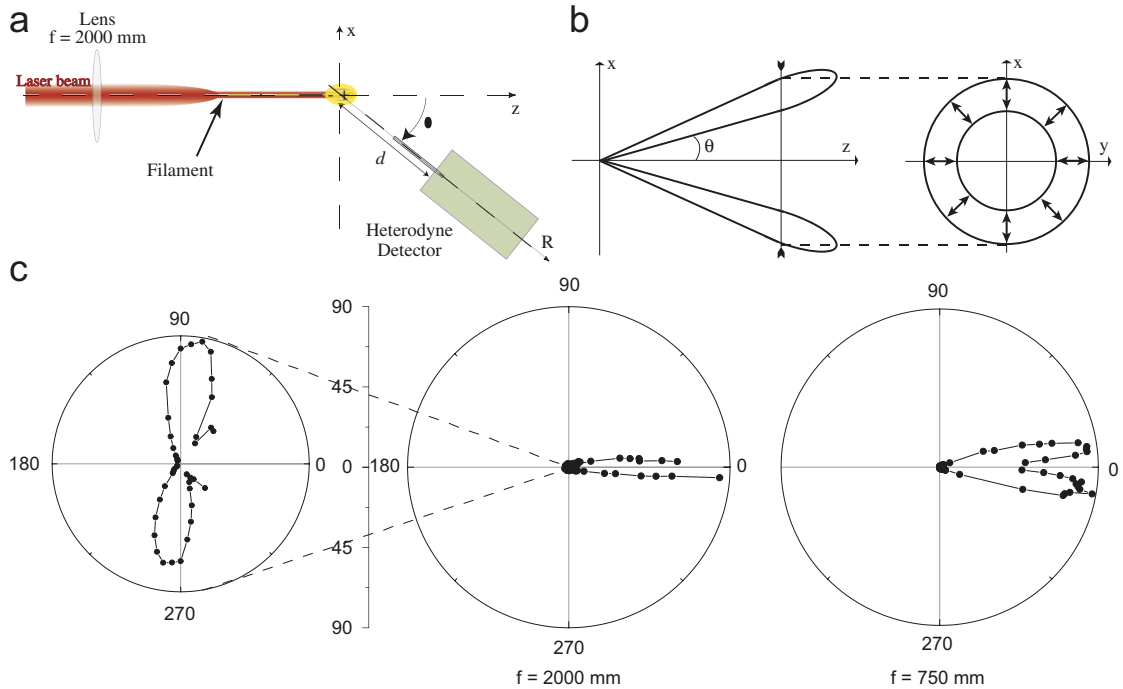
Fig. 70. (a) Experimental set-up for the measurement of THz emission. (b) Direction of the THz wave polarization in the emission cone. (c) Comparison between radial and forward THz emission from a filament. The polar diagram for the THz emission intensity as a function of the cone angle defined in (b) is shown for two different focal lengths $f = 2$ m (middle) and $f = 75$ cm (right). The radial emission (left) is magnified by a factor 100. From D'Amico et al. (2007b).

oscillate at the plasma frequency $\omega_p^2 = \rho_e e^2 / \epsilon_0 m$, and generate the plasma current which constitute the sources for the EMP. For an electron density of 10^{16} cm^{-3} in the plasma channel, the frequency of this sub-THz EMP is expected to be around 100 GHz and should be emitted in a narrow cone perpendicular to the plasma axis. Tzortzakis et al. (2002) have measured a sub-THz EMP with these features. However, the interpretation of this effect proposed by Cheng et al. (2001) has been disputed (Shvets et al., 2002; Tikhonchuk, 2002; Cheng et al., 2002). Sprangle et al. (2004) show that the source of the radiative EMP is the ponderomotive force. The ionization front has superluminal Fourier components leading to a mechanism similar to the Čerenkov radiation.

Forward emission: Recently, experimental evidence of a new THz emission occurring in the forward direction during filamentation of femtosecond laser pulses in air has been reported by Houard et al. (2007a) and D'Amico et al. (2007b). In contrast to a previously reported radial THz emission from filaments (Tzortzakis et al., 2002; Méchain et al., 2003), this new emission is confined to a very narrow cone in the forward direction (see Fig. 70).

The polarization of the THz signal is independent of the laser polarization. It lies in the plane defined by the laser axis z and the detector axis R (see Fig. 70(a)). The intensity of the forward emission exceeds by orders of magnitude the radial emission, as shown in Fig. 70(c).

In view of its polarization properties, the emission cannot be attributed to a mechanism involving the oscillation of the free electron cloud driven by the electric field, since one would expect it to be aligned along the electric field vector of the laser pulse. Houard et al. (2007a) attribute it to a Čerenkov emission due to the ionization front, which moves at a velocity higher than the speed of light in the medium. Evidence of superluminal motion of the ionization wave front in filaments has been discussed in Section 1.3.9 (Tzortzakis et al., 2003). In contrast to the usual Čerenkov emission due to a charge moving at a speed exceeding the velocity of light in the medium, we consider a dipolar charge distribution oriented along the propagation axis.
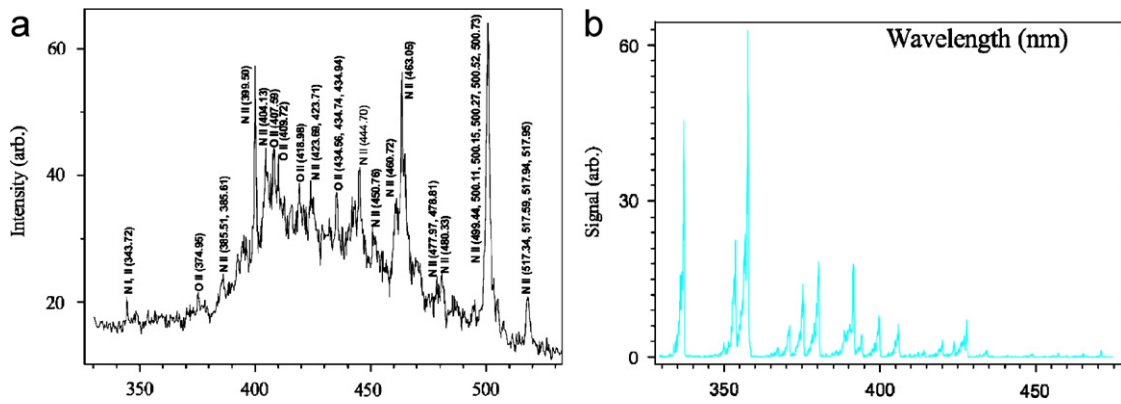
Fig. 71. (a) Nitrogen spectrum for a hot plasma with continuum and atomic lines. (b) Fluorescence spectrum of air interacting with Ti:sapphire laser pulses. According to Talebpour et al. (1999a).
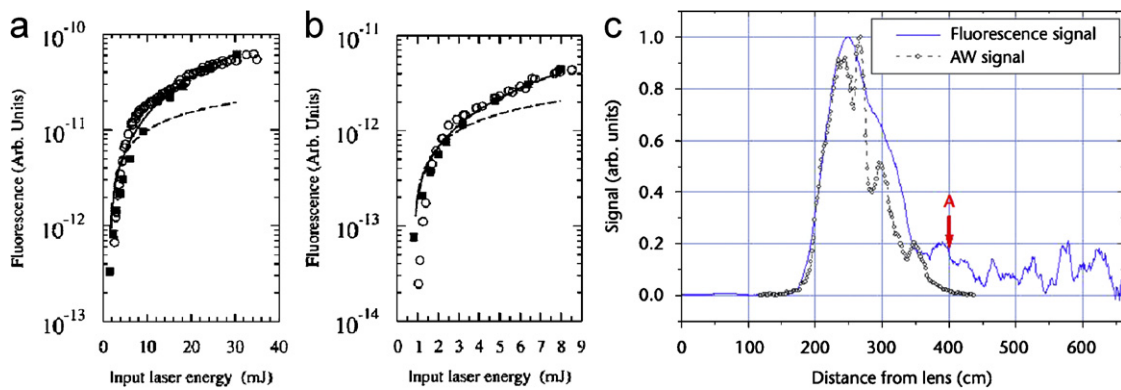
Fig. 72. Comparison of the experimental data of the fluorescence signal of the first negative band in nitrogen molecular ion (open circles), and the numerical predictions for the total number of ions in the second excited state (full squares) at (a) 400 Torr and (b) 760 Torr as a function the laser energy. The experimental data given in arbitrary units have been scaled vertically to match the numerical predictions. Also shown are the qualitative estimations from a variational approach (solid lines), and those assuming that the focal volume has cylindrical symmetry (dashed lines). According to Arevalo and Becker (2005a). (c) Typical waveform of fluorescence signal detected by a photomultiplier tube (solid line) and acoustic wave signal intensity measured along the filament (dotted line). From Luo et al. (2004).

4.1.15. Fluorescence measurement

Another measurement technique of air ionization relies on the detection of the luminescence of the nitrogen molecules excited by multiphoton ionization. A general diagram showing the detection of a plasma by luminescence is shown in Fig. 65. The interest of this method is to provide fluorescence spectra of molecules at high (~ 1 atm) pressure that are much cleaner than those obtained with a laser pulse of longer duration, as shown in Fig. 71, due to the absence of emission from atomic lines and of a broad component due to a hot plasma (Talebpour et al., 1999a, 2001; Becker et al., 2001a).

The observation of the fluorescence of excited nitrogen molecules in filaments has been assigned by Luo et al. (2003, 2004) to the first negative band of ($B^2\Sigma_u^+ \rightarrow X^2\Sigma_g^+$) of N_2^+ and the second positive band ($C^3\Pi_u \rightarrow B^3\Pi_g$) of N_2. The first negative band corresponds to the radiative decay of an excited ion by ejection of inner valence electron at 357 nm. The second positive band corresponds to the emission at 391 nm after electron–ion recombination. The lifetime of the nitrogen fluorescence is around 1–2 ns (Iwasaki et al., 2003). The measurement of the fluorescence signal by a photomultiplier was compared with good agreement to the acoustic wave that arises from the sudden expansion of the hot gas column caused by the heating of the fine column of air after recombination of the plasma inside the filament (see Fig. 72(c)).

Luo et al. (2005a) measured the back-scattered fluorescence signal from nitrogen molecules in filaments generated by intense femtosecond laser pulses in air. A higher fluorescence signal was obtained when filamentation was induced by small beam diameters. This was attributed to the reduction in the fluctuations induced by the competition between multiple filaments for the available energy. Reducing initial beams by an inverse telescope forces the beam inhomogeneities to be closer and leads to interferences between the filaments growing from these inhomogeneities, resulting in a larger number of filaments and plasma channels and giving rise to a higher fluorescence signal. The fluctuations in the fluorescence signal were shown to constitute a signature of the interaction between filaments, in particular their nucleation or their fusion (Hosseini et al., 2004a). The scenario of a more efficient use of the background energy reservoir for small beams (resulting in this higher fluorescence signal) was confirmed by numerical simulations including the modeling of shot to shot fluctuations (Kosareva et al., 2006b).

Arevalo and Becker (Arevalo and Becker, 2005a) have analyzed the role of self-focusing, geometrical focusing and plasma defocusing in the formation of the fluorescence signal during the filamentation of ultrashort laser pulses in nitrogen molecular gas. They have shown that the fluorescence signal is proportional to the focal volume, defined as the volume of the high-intensity core in the filament where the clamping phenomenon maintains a maximum intensity. Estimations of the focal volume V_{foc} following a variational approach to evaluate the beam width along the propagation distance resulted in the following expression:

$$
\begin{aligned}
V_{\text{foc}} = \frac{\pi}{64 K_2} & \frac{(1 + K_0)^2 (L_{\text{DF}}/L_{\text{SF}})^{K_0}}{2^{1+K_0} g_0 L_{\text{DF}}/L_{\text{PL}}} \\
& \times \left[9 \left(\frac{1}{L_{c,f}} - \frac{1}{f} \right) + \left(32 + \frac{9}{f^2} \right) (f - L_{c,f}) - \frac{18}{f} \log \left(\frac{f}{L_{c,f}} \right) \right],
\end{aligned}
\tag{156}
$$

where K_0 and K_2 denote the effective orders of the ionization processes for N_2 in the ground state: $K_0 = 6.78$, $\sigma_{K_0} = 4.45 \times 10^{-84} \, (\text{cm}^2/\text{W})^{K_0}$ (Aközbek et al., 2000), and in the second excited state: $K_2 = 8.32$ (Becker et al., 2001b; Arevalo and Becker, 2005a). The quantity $L_{c,f}$ is the location where the filament starts, estimated by $L_{c,f}^{-1} = \sqrt{\frac{32}{9} \left(\frac{P_{\text{in}}}{P_{\text{cr}}} - 1 \right)} + \frac{1}{f}$ and $g_0 \propto t_p \sigma_{K_0} I_0^{K_0}/2$ (Arevalo and Becker, 2005b).

This estimation is in good agreement with the number of excited nitrogen atom to which the fluorescence signal is proportional, as obtained by full numerical simulations (see Fig. 72).

Finally, Théberge et al. (2006c) have shown that fluorescence measurements give information on the spatial distribution of the chirp, pulse duration and fluence for ultrashort laser pulses which do not undergo strong spatio-temporal coupling. Théberge et al. (2006c) used a dispersive medium containing two-photon absorbing dye molecules acting as the spectator of the local pulse intensity and an imaging system to measure the emitted fluorescence, from which a fitting procedure allows the authors to infer the spatio-temporal distribution of the pulse.

4.1.16. Rebirth of filaments in the presence of an obstacle

Courvoisier et al. (2003) have measured the propagation of a filament beyond a droplet in the laboratory. A droplet of $50 \, \mu\text{m}$ placed in the path of the filament does not affect its further propagation. Similar results have been obtained with a single droplet of $95 \, \mu\text{m}$. Surprisingly, even an absorbing ink droplet does not give an appreciable difference. They attribute this effect to the rebirth of the filament from the energy reservoir surrounding the filament which quickly generates a new filament beyond the droplet. Kolesik and Moloney (2004b) have confirmed this hypothesis by numerical simulations. Courvoisier et al. (2003) have also analyzed the transmission through 35 cm long cloud chamber with a concentration of $4 \times 10^5 \, \text{drops/cm}^3$. The authors deduce that for a concentration up to $1.2 \times 10^5 \, \text{drops/cm}^3$, the filament is fully transmitted and further propagates almost unaffected; the filamentation length is close to the one in clean air. Multifilament propagation under rainy conditions is discussed in Section 5.2.4.

An interpretation of the rebirth of filaments was given by Dubietis et al. (2004a) who showed that filaments in water were recreated after a stopper placed either in the nonlinear medium (e.g. inside the water cell), or in air beyond the water cell. The experiments highlight the active role of the stopper in re-focusing the radiation, by means of diffraction. The robustness of filaments against multiphoton absorption follows from the interpretation of nonlinear losses as a distributed stopper along the optical axis. According to this model, the filament is then continuously replenished by an energy flow toward the core resulting from a nonlinear phase shift induced by nonlinear losses and mediated by
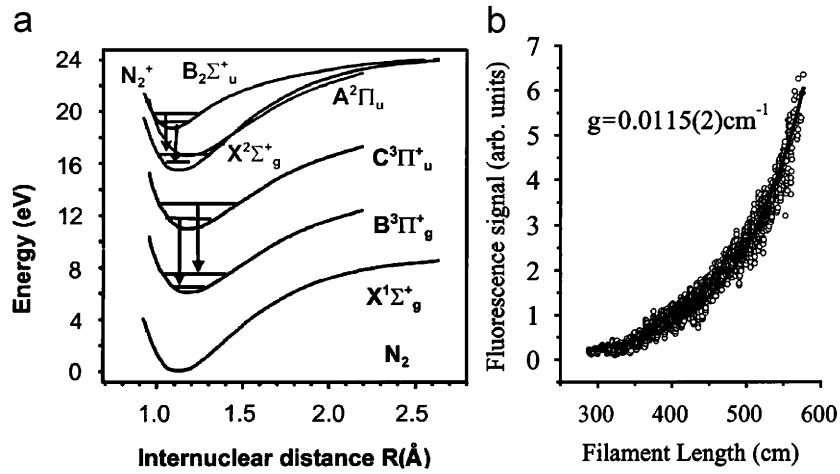
Fig. 73. (a) Schematic potential energy diagram for N_2 and N_2^+. (b) Intensity of the fluorescence below 400 nm from nitrogen versus the filament length for an initially collimated laser beam. The solid line is the gain curve given by (157). From Luo et al. (2003, 2004).

propagation and diffraction. This active role of nonlinear losses leads to the apparent stationarity of the core of the filament (see Gaižauskas et al., 2007, for a review).

4.1.17. Lasing action in the sky

The long track geometry of the plasma channel gives a favorable geometry for optical gain on the transitions shown in Fig. 73(a). Since the excitation involves first the removal of a deep valence electron followed by a recapture on peripheral orbits, a transient inversion of population occurs. One expects therefore the spontaneous emission to be amplified along the column according to the law

$$I \propto \frac{P_s}{g}[\exp(gL) - 1], \tag{157}$$

where P_s is the spontaneous emission power per unit length, g is the optimal gain coefficient and L is the filament length. Luo et al. (2003, 2004) have indeed observed optical gain as shown in Fig. 73(b). The nitrogen fluorescence can be distinguished from an increase of continuum by spatially resolved measurements (Théberge et al., 2005c).

4.1.18. Ultraviolet filamentation in air (248 nm)

The filamentation of UV laser pulses at 248 nm, is particularly interesting for the conducting properties of the plasma column generated in the wake of the pulse. Qualitatively, the ionization rate is indeed much more significant in the UV domain because it requires the simultaneous absorption of 3–4 photons to ionize an oxygen molecule, instead of 8–10 photons at 800 nm. In addition, the critical power for self-focusing P_{cr} at 248 nm is 120 MW instead of 3.2 GW at 800 nm. The defocusing of the beam by the plasma intervenes more quickly in the Kerr stage, which involves a lower intensity and a larger diameter in the filament, but a higher number of electrons. Better conducting properties are thus expected. Measurements were performed with a laser emitting pulses with a duration of either 4 ps, or 400 fs at 248 nm (Tzortzakis et al., 2000b, 2001b). The pulse resulted from a dye laser, initially doubled in frequency then amplified by an excimer laser. The beam was focused using a quartz lens with a focal length of 10 m. At the focus 40% of the input energy was lost. Ten percent of the energy was found in the filament, the remainder was found in a conical emission surrounding the filament. Fig. 27 shows the formation of an ultraviolet filament. The determination of the intensity in UV filaments is indirect: it was obtained from the measurement of the energy in the filament, its diameter and its duration. The pulse duration was obtained from autocorrelation measurements (see Fig. 60) (Tzortzakis et al., 2001b). A clamping intensity value of about 10^{11} W/cm^2 was found, which is two orders of magnitude below the intensity found at 800 nm. A spectral broadening was also observed but it is less significant than for IR filaments. On the other hand, the total number of free electrons generated is higher by a factor 25. A 6 m long plasma column was observed from electrical measurement in air for an input pulse of 2 mJ, i.e., the length is about ten times larger than that obtained
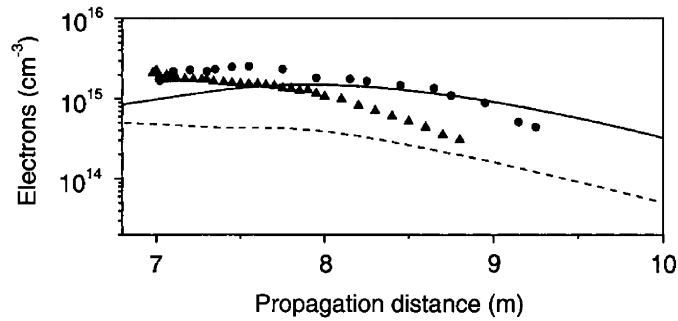
Fig. 74. Calculated and measured electron densities for a 2 mJ pulse with duration of 450 fs, (dashed line and triangles respectively), and for a 2 mJ pulse with duration of 5 ps, (solid line and circles respectively). From Tzortzakis et al. (2001b).

with a pulse at 800 nm with the same energy (see Fig. 74).The density of electrons in the plasma column was estimated around $10^{16}\,\mathrm{cm}^{-3}$, for a diameter of 150 μm (Tzortzakis et al., 2000b; Schwarz et al., 2000). As will be discussed in Section 5.1.7, the plasma absorption cross-section is proportional to the factor $I\lambda^2$ where I is the laser intensity and λ, the wavelength. Shorter wavelengths therefore minimize the losses, which make ultraviolet filaments interesting for their potential in lightning protection (Zhao et al., 1995a; Zhao and Diels, 1995) (see Sections 4.2.14 and 5.2.5 for more details). A high voltage discharge could be triggered by a UV ultrashort laser pulse (Rambo et al., 2001a).

4.1.19. Filamentation in the visible domain with picosecond laser

Mikalauskas et al. (2002) reported the observation of light filaments produced by picosecond laser pulses in the visible domain (527 nm, at the second harmonic of a Nd:glass laser). The energy content of the filament was found to be about 0.9 mJ, independently of the energy of the input pulse. From the FWHM diameter of 120 μm and the critical power of $P_{cr} = 1.4\,\mathrm{GW}$, an intensity of $6 \times 10^{12}\,\mathrm{W/cm}^2$ was estimated. The authors report apparent pulse shortening, measured by autocorrelation traces of the filament. They also observed clear signatures of four-wave mixing between the spectral components within the filament, in the form of fishbone structures in the angularly resolved spectra. The blue-shifted spectral components of the filaments were shown to posses a larger angular spread than the red-shifted components with opposite frequency shift with respect to the pump, a trend opposite to diffraction but similar to conical emission.

4.1.20. Effect of pressure

A study of filamentation at low pressure is important in the context of applications because it answers the question of the possibility of filament formation at high altitude. Filamentation in air at low pressure was investigated over laboratory scales (Couairon et al., 2006b; Méchain et al., 2006). Using a 2 m cell filled with air at pressure between 0.2 and 1 atm, the authors found that the length of the plasma column does not change significantly between 0.2 and 1 atm confirming the theoretical calculation which predicts that filamentation should be possible at altitudes of 10 km and more (Fig. 75). The authors found that the spatially integrated electron density is independent of pressure although the electron density is proportional to the pressure. This is due to the larger diameter of filaments at low pressure.

Measurements have also been performed outdoors at an altitude of 3200 m where the pressure is 0.7 bar using the teramobile laser (Méchain et al., 2005b). Multiple filaments are observed over a distance of several hundreds of meters with no significant changes with respect to see level conditions.

4.1.21. Control of filaments

Motivated by the potential of applications of filaments, recent research has aimed to control the multiple filamentation process and their distribution. Méchain et al. (2004b) achieved a degree of control by introducing field gradients and phase changes on the input beam in air. Schroeder et al. (2004) performed similar investigations for controlling filaments in water. Other methods for filament control have utilized the effects of beam astigmatism and ellipticity (Dubietis et al., 2004c; Fibich et al., 2004). Cook et al. (2005) have demonstrated that Fresnel diffraction from a hard-edge aperture can be used to control filament formation, thus avoiding the use of any focusing lens. Their experiment demonstrates
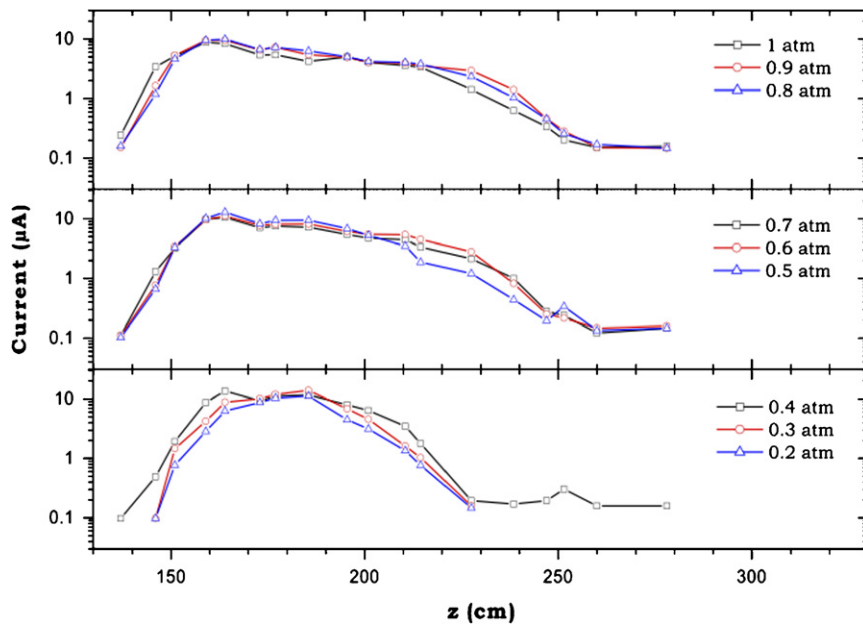
Fig. 75. Evolution of the conductivity of the filament along the optical axis with an energy equal to 3.7 mJ/pulse. z is the distance from the focusing lens. The presented signal corresponds to the current in the load resistance. The measurements have been performed for different pressures varying from 0.2 to 1 atm. From Méchain et al. (2006) and Méchain (2005).

that filaments are formed at distances from the aperture that coincide with local intensity maxima in the near field diffraction pattern. Below, we show a few examples of processes designed to control multiple filaments.

Masks: Fig. 76 shows the organized filamentation pattern formed by introducing amplitude masks in the laser beam before filamentation (Méchain et al., 2004b). A trefoil mask leads to three filaments, the position of which depends on the orientation of the trefoil. An excellent agreement with the results of numerical simulations was found (see Section 3.2.11).

Astigmatism: A control of the filament pattern can also be achieved by introducing changes in the spatial phase of the input beam. This method has the advantage that no energy loss is introduced because there is no beam-clipping. By tilting a lens, Méchain et al. (2004b) have introduced an astigmatism which gives a controlled phase distortion. Fig. 77 shows the emerging double filament, the orientation of which can be modified at will. Again the results are in agreement with numerical simulations shown in Fig. 77 and with results by Fibich et al. (2004).

Ellipticity: Experimental evidence that multiple filamentation of ultrashort laser pulses can be induced by input beam ellipticity was first reported by Dubietis et al. (2004c). Unlike noise-induced multiple filamentation, which results in complete beam breakup, the filaments induced by small input beam ellipticity appeared in the form of predictable and reproducible multiple filamentation patterns with the filaments mainly located along the principal axes of the elliptic input beam, in addition to a robust central filament. Fig. 78 shows that the filaments appear by pairs located symmetrically along the major and (or) minor axis and (or) quadruples located symmetrically along the bisectors of the major and minor axes. It was shown that the input beam ellipticity can dominate the effect of noise (transverse modulational instability). In contrast with polarization induced multiple filaments, the orientation of the multifilamentation pattern is independent of the direction of the linear polarization of the laser.

Grids and slits: Multiple filamentation can be controlled by any mechanism producing a specific diffraction pattern with local intensity maxima, such as a grid or a slit. The filaments superimpose to the diffraction pattern in the form of an array or a line. Anticipating on the next section, the examples here concern filamentation in condensed media. Centurion et al. (2005a) have shown the emergence of a self-organized line of filaments in CS_2 that is finally destroyed by the fusion and repulsion of in-phase or out of phase neighboring filaments, the phase difference being accumulated along the propagation path with linear and nonlinear contributions. Schroeder et al. (2004) have used a grid so as to impose a diffraction pattern overcoming the inherent beam irregularities which naturally give rise to random small-scale
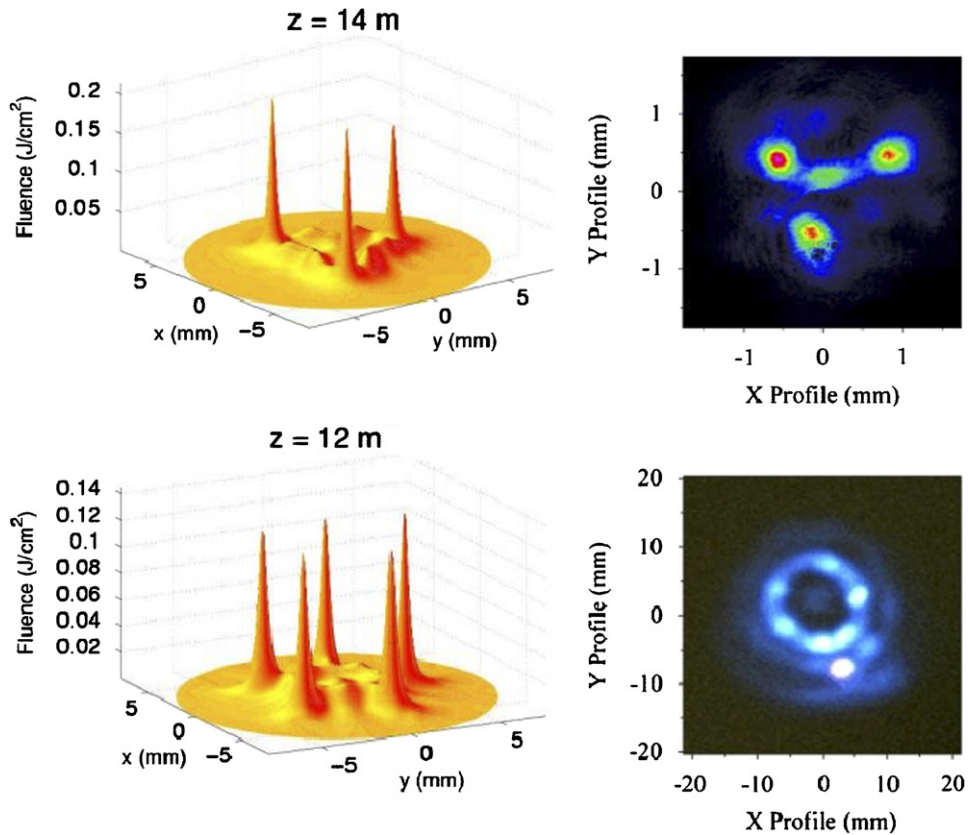
Fig. 76. Comparison of measured and simulated organized multiple filamentation patterns. A trefoil mask was used for the first line while a five-foil mask was used for the second (Méchain et al., 2004b).
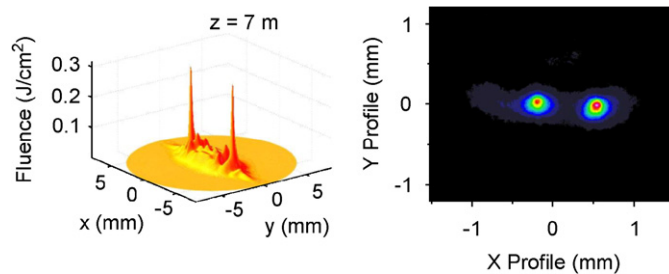
Fig. 77. Comparison of measured and simulated organized multiple filamentation patterns for an input beam with astigmatism (Méchain et al., 2004b).

multiple filamentation. Fig. 79 shows mesh-generated arrays of filaments at various propagation distances in water. Liu et al. (2005c) have achieved ultrafast control of mesh-induced multiple filamentation patterns in an ethanol cell by using a BK7 plate before the ethanol cell as an interaction medium between a second femtosecond laser pulse and the diffraction pattern produced by the mesh. By controlling the local overlap both in space and time of the two laser pulses, Liu et al. (2005c) have shown that the white light patterns can be switched on and off on a femtosecond time scale, opening up potential applications in optical communications.

   Control of the spectral phase: Heck et al. (2006) have achieved an independent control of filament starting position and extent through the manipulation of the spectral phase of a 50 fs, 800 nm laser pulse propagating in water. They used a closed feedback loop employing a spatial light modulator and a genetic algorithm to manipulate the spectral phase.
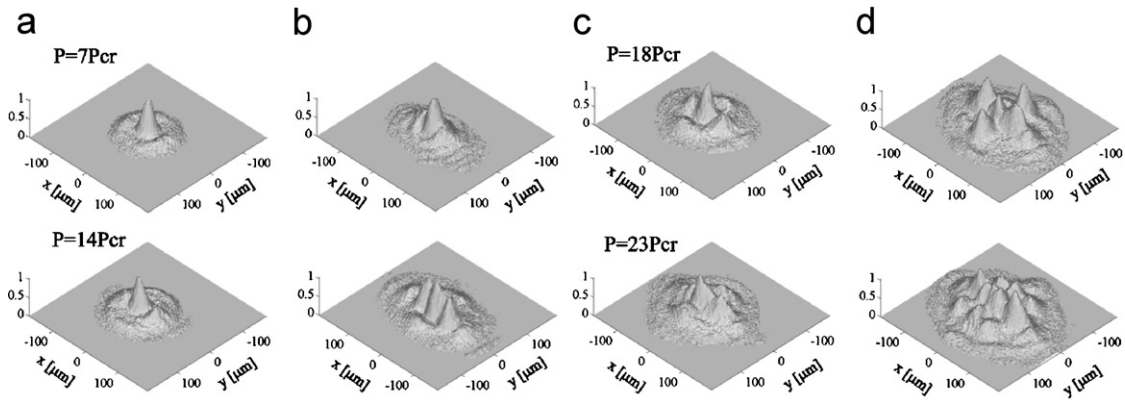
Fig. 78. Normalized three-dimensional views of filamentation patterns at $z = 31$ mm recorded with (a,c) a nearly circular incident beam (ellipticity $e = 1.09$) and (b,d) an elliptical incident beam ($e = 2.2$). The major axis of the ellipse lies along the x-axis of each plot. $P_{cr} = 1.15$ MW in water, with 527 nm, 170 fs laser pulses. From Dubietis et al. (2004c).
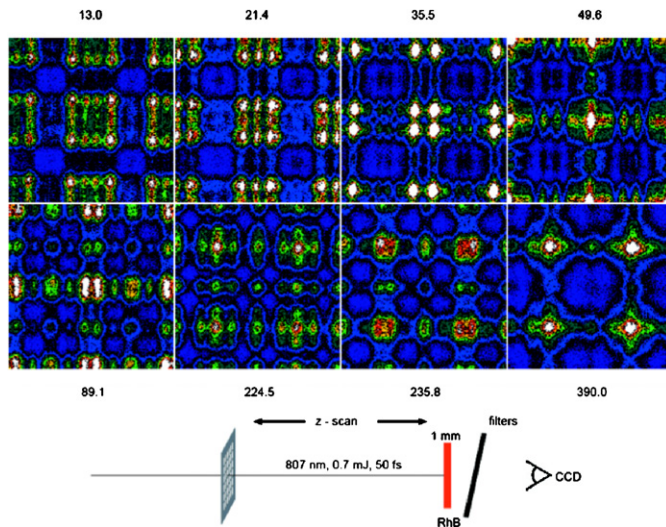
Fig. 79. Creation of space-controlled 2-D arrays of filaments by launching the beam through a wire mesh (11×11 meshes, mesh 497 μm, wire diameter 54 μm). The characteristic diffraction patterns are shown for various distances. The shown image sections (1 mm × 1 mm) contain the center mesh and half of its neighbors (Schroeder et al., 2004).

This adaptative control constitutes an alternative to that achieved by changing energy or chirp of the pulse. Another alternative was proposed by Pfeifer et al. (2006) who have used a circular phase mask to stabilize the pointing of the filament output and to optimize the spectral bandwidth of the supercontinuum.

4.1.22. Concatenation

In order to increase the overall length of the continuous plasma column, it is possible to connect conducting plasma channels generated by filaments by using two suitably delayed colinear pulses. This effect was shown in the laboratory (see Fig. 80) (Tzortzakis et al., 2003). In this diagram, each pulse generates its own filament, the beginning of the filament formed by the first pulse being located near the end of that formed by the second pulse. The linear polarizations of the two pulses are orthogonal. For a specific delay between the two pulses, only one continuous plasma column is formed, with an overall length larger than the sum of the two separate plasma columns. The concatenation is due to the cross-phase modulation between the fields of the two pulses, enhancing ionization in the gap between the individual
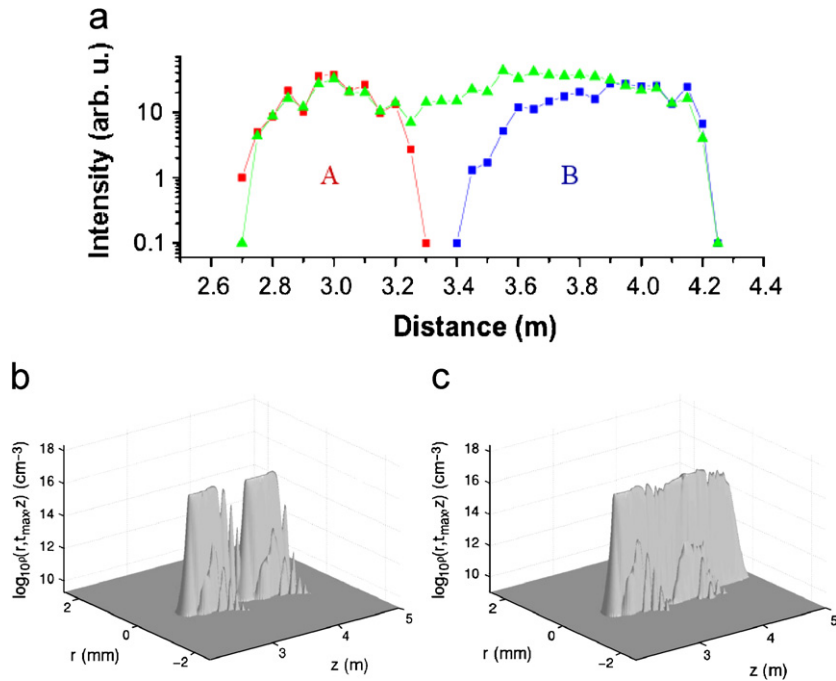
Fig. 80. Two filaments A and B are generated on the propagation axis by using two beams with different convergence. For a well suited delay between pulses A and B, it is possible to connect the filaments in order to give rise to only one plasma channel of constant density. (a) Measurements of the sub-THz emission characterizing a plasma. From Tzortzakis et al. (2003); Couairon et al. (2003). (b) Computed electron density in the plasma channels generated by the independent propagation of pulses A and B. (c) Computed electron density in the plasma channel obtained from the propagation of the twin pulses, with a delay of 100 fs. The simulations have been done for conditions corresponding to the experiments (Couairon et al., 2003).

filaments. It is also important to take into account the propagation velocity of the pulse in the form of a filament in order to adjust the adequate delay for a good concatenation. These results were well reproduced by numerical simulations (Couairon et al., 2003).

4.2. Measurements in solids and liquids

Femtosecond filamentation was also observed in condensed media including transparent solids such as fused silica or sapphire and liquids such as water and methanol (Tzortzakis et al., 2001d; Liu et al., 2003b; Dubietis et al., 2003; Philip et al., 2005). In these cases, the filamentation threshold is about a few MW, corresponding to an energy of the order of the μJ for a pulse of 100 fs duration.

4.2.1. Filamentation in transparent solids

Reports of filamentary damage or fluorescence tracks in transparent solids or in liquids can be found in numerous publications before the advent of femtosecond lasers (Lallemand and Bloembergen, 1965; Garmire et al., 1966). Although several phenomena associated with filamentation, such as conical emission or supercontinuum generation, were reported to occur when femtosecond laser pulses propagate in transparent solids, evidence of a long range propagation of an ultrashort laser pulse in the form of a filament in a fused silica sample was obtained only a few years ago (Tzortzakis et al., 2001d). Fig. 81 shows a photograph of a filament generated in fused silica by focusing a 2 μJ, 800 nm, 160 fs laser pulse on the entrance face of the sample. This regime of femtosecond filamentation in transparent solids is characterized as in air by a near constant beam waist over many Rayleigh lengths. Simulations showed that very high intensities in excess of 10^{13} W/cm^2 are reached in the filament but the pulse duration is too short to initiate avalanche. The filament was shown to be accompanied by supercontinuum generation, pulse splitting and time compression (Tzortzakis et al., 2001d). Dharmadhikari et al. (2006b) have obtained similar conclusions by investigating
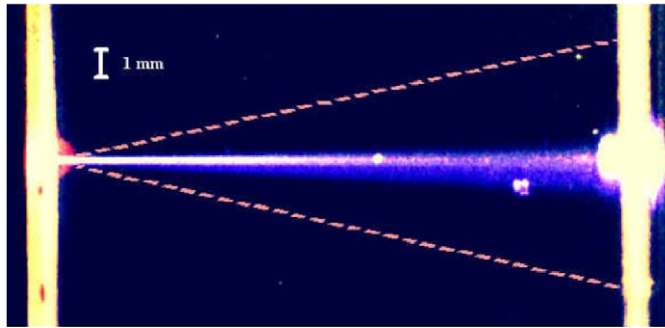
Fig. 81. Transverse photograph a 2 cm long filament generated in fused silica by focusing a 2 μJ, 800 nm, 160 fs laser pulse on the entrance face of the sample. From Tzortzakis et al. (2001d).

filaments in BaF_2 and have interpreted the white light spectral distribution as resulting from plasma induced self-phase modulation. Chen et al. (2006b, 2005) and Li et al. (2006) have shown experimentally that high-power femtosecond pulses undergoing filamentation in a piece of BK7 glass lead to a self-compression from 50 to 20 fs, with a compression factor of about 2.5. However, the output pulse was observed to be split into two peaks when the input intensity is high enough to generate supercontinuum and conical emission as shown by Tzortzakis et al. (2001d).

No permanent damage is observed in the bulk of the sample. This situation where the material seems to withstand the generation of damage corresponds to the case of weak focusing. The phenomenon is quite universal as it was also recently observed for ultraviolet (248 nm, 450 fs) laser pulses with an energy up to 4 mJ, forming filaments over a few centimeters in fused silica without any apparent bulk damage (Tzortzakis et al., 2006b). In contrast, when an ultrashort laser pulse is tightly focused in the bulk of a transparent solid, avalanche ionization can induce extensive damage, still in the form of filamentary tracks (Sudrie et al., 2002; Saliminia et al., 2004). As shown in Fig. 49, a first damage zone around the focus is followed by a narrow filamentary track with submicron width. The shape and size of the damage tracks were shown to correspond to the zone where the electron density created by optical field ionization and avalanche exceeds 10^{20} cm^3 whereas the plasma density produced in the wake of the pulse saturates around 2–4×10^{20} cm^3 (Sudrie et al., 2002; Couairon et al., 2005b).

These results indicate that there is obviously a competition between optical breakdown and laser pulse filamentation determined by external focusing conditions. This competition was investigated by Nguyen et al. (2003) who determined for 45 fs, 810 nm laser pulses propagating in fused silica the thresholds for optical breakdown, detected by plasma emission and scattered laser spectra, and filamentation, signaled by the appearance of a supercontinuum reaching 400 nm. A similar investigation was performed in air (Liu et al., 2003c). As shown in Fig. 82, the energy threshold for optical breakdown in fused silica is lower than the filamentation (supercontinuum) threshold for short focal lengths while filamentation can occur below the threshold for optical breakdown for long focal lengths. From the threshold map of pulse energy as a function of the focal length for optical breakdown, single and multiple filamentation, Nguyen et al. (2006) have shown that waveguides can be written in fused silica at 800 nm in the filamentation and optical breakdown regimes. The authors interpreted the smooth index change as a densification of the material by using Raman spectroscopy and stress birefringence measurements (Saliminia et al., 2006).

4.2.2. Permanent index modification and damage

A large number of experimental and theoretical studies have been conducted to understand the mechanisms of permanent index modification and laser damage (see Stuart et al., 1995, 1996; Schaffer et al., 2001b, and references therein). The reason why there is a change in the index of refraction is still a subject of debate, since there are noticeable differences in the mechanisms for producing damage with ultrashort or with longer laser pulses (see Mao et al., 2004, for a review of laser matter interaction with solids). For picosecond or longer pulses, bulk damage inside defect-free dielectrics involves the heating and multiplication of spurious electrons by the incident laser beam and transfer of this energy to the lattice. Damage occurring via this conventional heat deposition results in the melting and boiling of an extensive volume of the dielectric material. The situation is quite different for femtosecond pulses which are shorter than the time scale for electron energy transfer to the lattice (Stuart et al., 1995; Li et al., 1999). Damage caused by
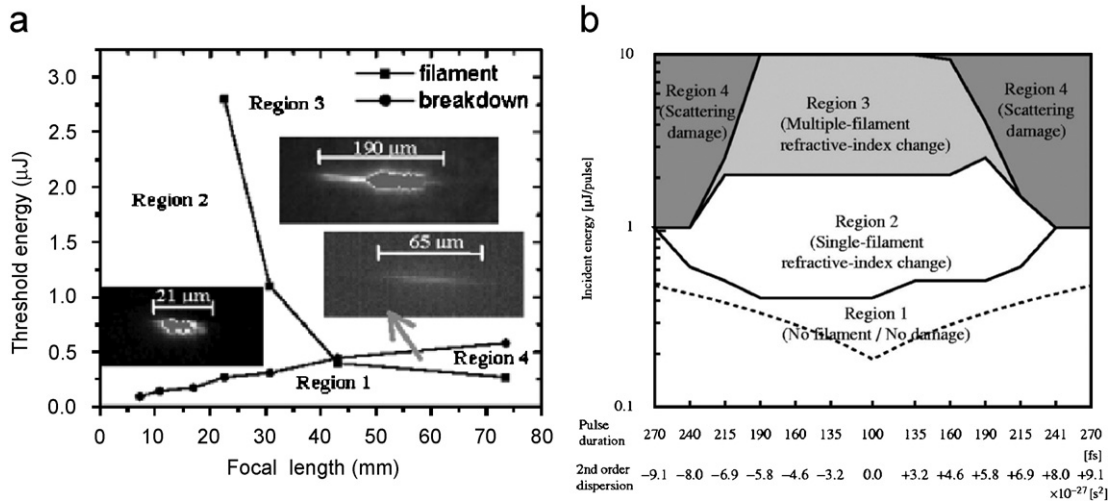
Fig. 82. (a) Threshold energies for optical breakdown and filamentation in fused silica as a function of focal length. The insets show typical optical breakdown and filamentation plasma images corresponding to each region according to Nguyen et al. (2003). (b) Energy thresholds for filamentary tracks of single-filament refractive-index changes, multiple-filament refractive-index changes, and scattering damage by varying the pulse duration and the incident energy. The dashed line denotes the critical energy for self-focusing. From Onda et al. (2005).

these pulses is produced with smaller statistical uncertainty and is controllable on a microscopic scale (Joglekar et al., 2003). It is characterized by a minimum of collateral damage. In transparent solids with low damage threshold, the permanent damage tracks provide an indirect diagnostic from which spatial features of the filamentation pattern can be extracted.

The damage tracks induced by tightly focused infrared femtosecond laser pulses in the bulk of a fused silica sample were investigated experimentally and numerically (Sudrie et al., 2001, 2002; Couairon et al., 2005b). Two types of irreversible damage were observed. The first type of damage corresponds to a permanent local isotropic change of the refractive index without structural modifications. It appears for input pulse energies beyond $0.1\,\mu J$. It takes the form of a narrow track extending over more than $100\,\mu m$ at higher input powers. It was attributed to a change of the polarizability of the medium, following a filamentary propagation which generated an electron–hole plasma through optical field ionization. A second type of damage occurs for input pulse energies beyond $0.3\,\mu J$ and corresponds to a local permanent induced birefringence (Poumellec et al., 2003). It takes the form of a pear-shaped structural damage associated with an electron–ion plasma triggered by avalanche. These different types of structural damage were also reported to be induced by 450 fs ultraviolet (248 nm) laser pulses in fused silica (Papazoglou et al., 2005). The temporal evolution of plasma absorption was studied by pump–probe experiments in fused silica (Sudrie, 2002; Couairon et al., 2005b). For type I damage, a fast electron–hole recombination was observed. Type II damage is linked with a longer absorption. A similar analysis was performed in MgO by Xu et al. (2006c) who analyzed the respective roles of MPI and avalanche in femtosecond laser induced breakdown and reported that avalanche ionization plays the dominant role.

Onda et al. (2005) have investigated the filamentary tracks in synthesized silica glass induced by varying both the duration and energy of chirped laser pulses under smooth focusing conditions. Short-duration pulses induced filamentary refractive-index change (type I damage) that can be annealed out by heating the material at $900\,^{\circ}C$, whereas longer pulses produced birefringent scattering (type II) damage in filamentary tracks that persisted when the material was heated at $900\,^{\circ}C$. Increasing the energy of the laser pulses led to multiple filamentary tracks, a regime also shown to be promoted by the beam ellipticity (Kudriašov et al., 2005). These regimes are classified in Fig. 82(b).

The transmission of ultrashort laser pulses in transparent solids was investigated by several teams (Couairon et al., 2005b; Wu et al., 2005; Beyer et al., 2005a, b). Fig. 83(a) shows a comparison between measured and computed transmission for pulses of 50 fs focused in fused silica by an objective of microscope ($20\times$) with NA$=0.5$. The calculated onset of absorption was satisfactorily compared with the onset of type I damage at $0.1\,\mu J$. The absorption was correctly reproduced up to values of the order of $1\,\mu J$ for the energy of the input pulse. A change of slope in the transmission signaling the onset of an additional mechanism occurs around $0.4\,\mu J$, close to the type II damage threshold (appearance
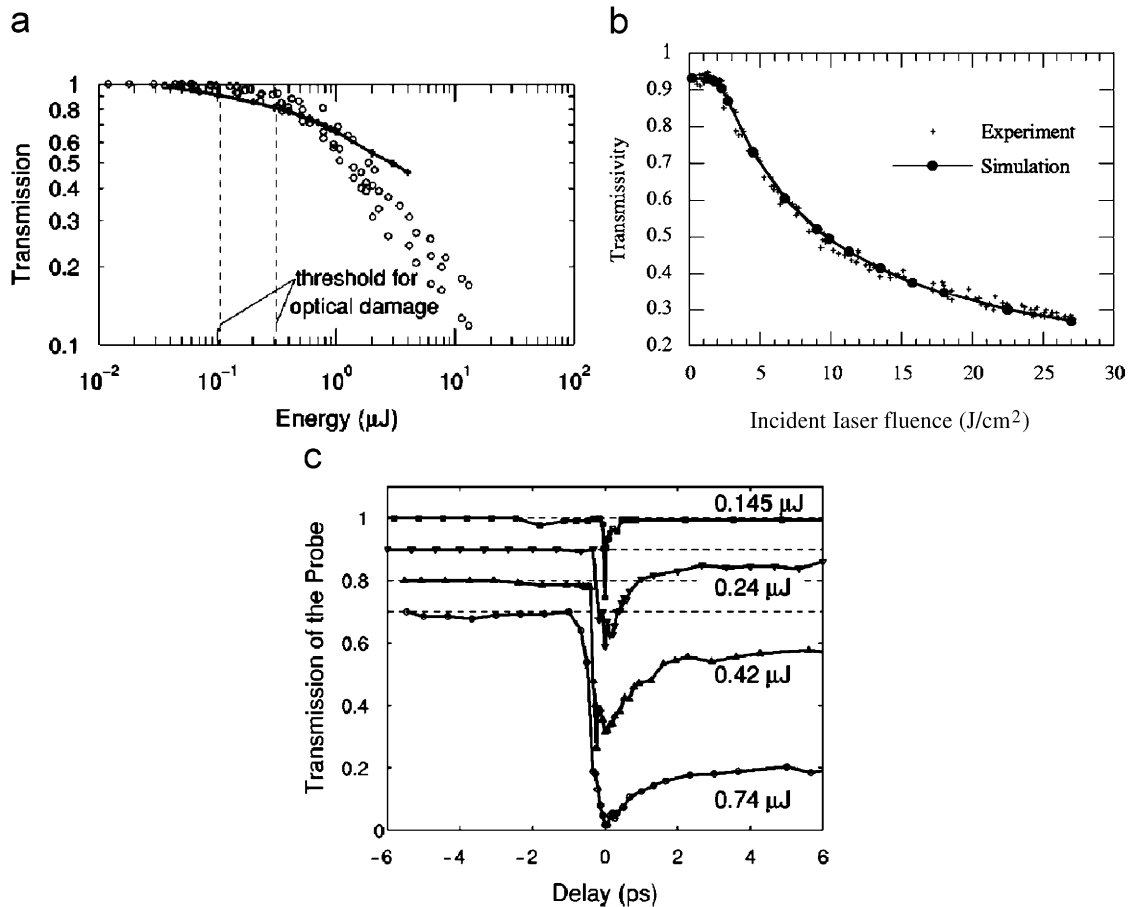
Fig. 83. (a) Transmission as a function of the pulse energy. The central wavelength was 800 nm. The pulse duration and repetition rate were 50 fs, 1 kHz. The beam was focused in fused silica with a focusing lens 20× with NA = 0.5. The curve marked with crosses indicates the results of numerical simulations. The dashed lines indicate the thresholds for type I and type II optical damage. From Couairon et al. (2005b). (b) Comparison between measured and computed laser fluence dependence of single pulse transmissivity in fused silica. From Wu et al. (2005). (c) Results of pump–probe experiments in fused silica. Focusing lens 20× with NA = 0.5. Probe pulse: 800 nm, 0.025 μJ, 50 fs, 1 kHz with modulation. Pump pulse: 800 nm, 50 fs, 1 kHz. The pump energies are 0.145 μJ (squares), 0.24 μJ (triangles down), 0.42 μJ (triangles up), and 0.74 μJ (circles). The three curves with largest energies have been shifted for clarity. The dashed lines indicate the shifts. From Couairon et al. (2005b), Sudrie (2002).

of irreversible damage). With higher energy, simulations significantly overestimate the transmission obtained in the experiments. Wu et al. (2005, 2006) performed measurements and simulations of single pulse transmissivity and reflectivity for fused silica irradiated by 90 fs laser pulses at a center wavelength of 800 nm. Good agreement between their measurements and numerical simulations indicated that avalanche ionization contributed little to the generation of free electrons (see Fig. 83(b)).

Pump–probe experiments were performed so as to study the absorption of the probe as a function of the delay between pump and probe (Couairon et al., 2005b). Fig. 83(c) shows that a direct multiphoton absorption process involving pump and probe photons leads to a pronounced short-duration transmission dip, whereas the probe absorption by pump-excited charge carriers results in a long-duration plateau. Beyer et al. (2005a, b) have found similar results by investigating two photon absorption processes in Lithium niobates crystals within the blue green spectral range. They have shown that initially, an instantaneous generation of free carriers takes place owing to direct two-photon processes with a corresponding high nonlinear absorption coefficient, so that the pump pulse experiences a strong attenuation even in relatively thin samples. When a weak probe pulse is overlapping in time and space with a strong pump pulse, an additional instantaneous probe absorption, involving pump and probe photons, takes place. This nonlinear absorption causes a pronounced dip in the dependence of the probe transmission on the delay time between pump and probe pulses.
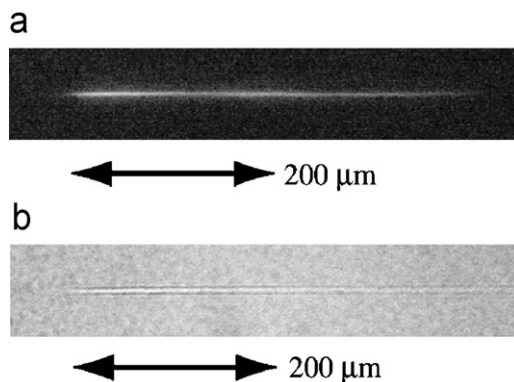
Fig. 84. Relationship between a filament and the region of refractive-index change: optical images of (a) the filament and (b) the region of refractive-index change. From Yamada et al. (2001).

The relevant nonlinear absorption coefficient is also relatively high. The pump-excited carriers are responsible for the plateau section of the probe transmission; they do not experience recombination to the levels where they originate from at least on the time scale of tens of picoseconds. Instead, they occupy shallow levels near the conduction band which are attributed to the structural defects of $LiNbO_3$ (small polarons). Recombination of such excited localized electrons occurs on the time scale 10^{-8}–10^{-5} s.

By means of numerical simulations that solve the time-dependent electromagnetic wave equation and include multiphoton ionization, electron attachment, Ohmic heating of free electrons, and temperature-dependent collisional ionization, Peñano et al. (2005) have modeled self-consistently the transmission, reflection, and absorption of laser pulses of 10–100 fs duration and peak intensities of 10^{12}–10^{14} W/cm^2, by a thin, highly collisional plasma layer. These laser pulses interacting with fused silica were shown to produce above-critical plasma densities and electron energy densities sufficient to attain experimentally measured damage thresholds. Significant transmission of laser energy is observed even in cases where the peak plasma density is above the critical density for reflection. The damage fluence based on absorbed laser energy was calculated for various pulse durations and was found to be consistent with recent experimental results.

4.2.3. Damage tracks in solids

A subject of great interest for its applications in buried guiding structures is the role of filamentation during the writing of permanent index changes of glasses. Damage of dielectrics caused by ultrashort laser pulses can be exploited to produce laser devices such as waveguides and gratings in the bulk of the material. In recent years, damage or refractive index changes produced in transparent materials by ultrashort laser pulses have been used for micromachining various optical elements (Liu et al., 1997; Schaffer et al., 2001a; Davis et al., 1996; Glezer et al., 1996; Homoelle et al., 1999; Kondo et al., 1999). The fabrication of buried optical elements necessitates a pulse with well controlled intensity and beam size at a specific tunable depth. Such characteristics are provided by self-guided pulses through the filamentation process. The most interesting buried structures are obtained when the index of the medium is permanently modified (increased usually) without the occurrence of permanent structural damage. Davis et al. (1996) discovered that damage produced by fs laser pulses can write waveguides in fused silica. It has been shown by Sudrie et al. (1999) that this occurs during filamentation with a weakly focused infrared laser beam. Yamada et al. (2001) have achieved efficient waveguides via filamentation resulting in a buried change of refractive index, the diameter of which is about 1.5 μm. The length of the permanent refractive index change coincides with that of the filament produced in the same medium (see Fig. 84). The permanent buried waveguides are able to trap light.

Chin et al. (2005) showed that the writing of good waveguides results from a combination of filamentation in weak focusing conditions, and melting that results from local heating of the glass material. The local melted material inside the filament zone cools down and results in a uniform higher index of refraction. A remarkable resistance of the glass against breakdown and physical damage at 1.5 μm even allowed Saliminia et al. (2005b) to realize efficient small-size core optical waveguides in silica based on the pure filamentation process within a broader range of writing parameters
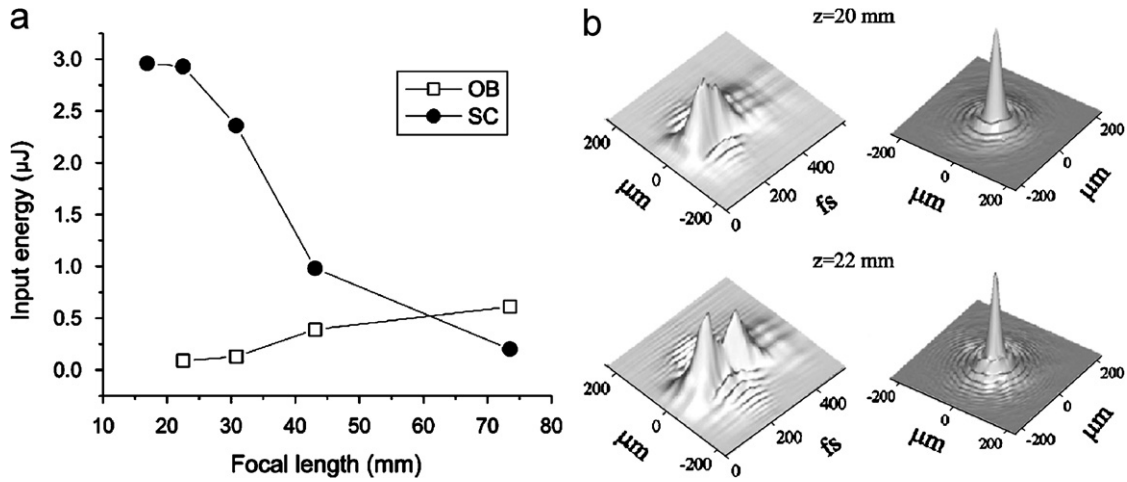
Fig. 85. (a) Threshold energies for supercontinuum generation (SC, filled circles) and optical breakdown (OB, open squares). From Liu et al. (2003b). (b) Measured space–time intensity profiles (left) and (time-integrated) normalized fluence profiles (right) for different propagation distances of a 150 fs, 527 nm laser pulse undergoing filamentation. From Matijošius et al. (2004b).

as compared to the 800 nm case. In contrast, strong focusing conditions lead to the generation of an avalanche plasma though still not dense enough to give a total breakdown. Nevertheless, a local small explosion can occur and result in void formation (Gamaly et al., 2006; Juodkazis et al., 2006). Such voids would not favor the formation of good wave guides (Saliminia et al., 2005b), yet they allow the formation of three-dimensional optical memories in the bulk of transparent solids (Glezer et al., 1996; Juodkazis et al., 2003).

4.2.4. Filamentation in liquids

Liquids have been used for decades as a prototype of condensed media for the white light continuum generation. However, except for preliminary indications of filamentation in water (Brodeur et al., 1996; Brodeur and Chin, 1999), no apparent filamentation in liquids has been reported until recently due to the tight focusing geometry used in these experiments, leading to avalanche ionization and optical breakdown. The competition between optical breakdown and laser pulse filamentation in water was studied by Liu et al. (2002b, 2003b), still under tight focusing conditions. Fig. 85 shows the threshold for optical breakdown and supercontinuum generation as a function of the focal length. Light filaments induced by 170 fs, 527 nm pulses propagation in water were reported by Dubietis et al. (2003). The filament had a 60 μm diameter (at the $1/e^2$ level) and persisted over a distance of 2 cm. The filamentary mode was shown to be sustained over a wide range of input powers, the energy in excess of the constant energy contained in the filament core being converted into conical emission. In the time domain, the pulse trapped in this filamentary mode was shown to experience pulse splitting in time as demonstrated by measurements of the full space–time intensity distribution (Matijošius et al., 2004b). Despite the important role of GVD in the dynamics (see Section 4.2.7), only the core of the beam was shown to split in time but the power profile does not split, in contrast with the splitting process due to the arrest of collapse by GVD (Rothenberg, 1992a).

4.2.5. Determination of model coefficients

The models presented in Section 2.2 need several coefficients which are not always well known. When the agreement between numerical simulations and experiments is not perfect, the question of the accuracy of the physical parameters, and that of the sensitivity of the models to the parameters can be raised. On the basis of systematic confrontation of numerical with real experiments, several works were performed with the specific goal of determining the values of specific physical parameters, in the filamentation regime, to be introduced in the models. Among these works, Pitts et al. (2004) favorably compared theoretical predictions of spectral, temporal, and transverse spatial widths, obtained by model (47)–(51) of Section 2.2.5 with dispersion limited to third order, with measurements in air for several propagation distances over a range of energies up to 2 mJ for pulse duration of 200 fs. By use of these data, a simple fit of the nonlinear

refractive index and delayed Raman contribution fraction yielded values of $n_2 = 2.8 \times 10^{-19}\,\mathrm{cm^2/W}$ and $\alpha = 0.58$, respectively. This value of α is in good agreement with measurements by Ripoche et al. (1997). In the same paper (Pitts et al., 2004), simulation results obtained by using the nonlinear index for fused silica $n_2 = 2.5 \times 10^{-16}\,\mathrm{cm^2/W}$ and $\omega_R = 84 \times 10^{12}\,\mathrm{rad/s}$, $\Gamma = 20 \times 10^{12}\,\mathrm{rad/s}$, $\alpha = 0.15$ were compared favorably with single-shot spectral experimental data.

Couairon et al. (2005b) inferred a slightly larger value for the nonlinear index of fused silica ($n_2 = 3.5 \times 10^{-16}\,\mathrm{cm^2/W}$ at 800 nm) by comparison of measured and numerically obtained positions for the nonlinear focus were filamentation starts. This approach was used to directly determine the critical power of femtosecond Ti:sapphire laser pulses in air (Liu and Chin, 2005). The principle rely on the fact that under geometrical focusing condition, the focal position shifts towards the focusing lens if the laser power is higher than the critical power. The movement of the focus was studied by observing the nitrogen fluorescence distribution in air. The critical power in air was reported to change from 10 to 5 GW when the pulse duration increases from 42 to 200 fs (chirped). For longer pulse durations, the critical power is almost constant (5 GW). The physical reason is that with shorter pulse length, only instantaneous electronic response of the media is responsible for self-focusing while with longer pulse length, the delayed nuclear response also contributes to the nonlinearity, in agreement with measurements by Ripoche et al. (1997). In principle, GVD also impact the critical power for self-focusing (Luther et al., 1994a). However, the effect is relevant mainly in condensed media for which the chromatic dispersion is much larger than in gases, or for pulses with large chirps propagating over long distances.

Using systematic comparison of the measured and simulated transmission of pulse energy undergoing filamentation in water, a value $\beta_K = 1 \times 10^{-25}\,\mathrm{cm^3/W^2}$ for the nonlinear absorption coefficient at 527 nm could be inferred (Dubietis et al., 2006a).

4.2.6. Measurements and interpretations of the continuum generation

There is a very large literature on supercontinuum generation (SCG) in liquids and solids. The broadband SCG has been widely exploited in ultrafast spectroscopy. For a review of supercontinuum, see for instance (Alfano, 1989). There are however a few reports clearly connecting broadband SCG to filamentation. The supercontinuum generated by using femtosecond pulses differs from that obtained with longer (picosecond) pulses. In the former, the anti-Stokes frequency components temporally lag the Stokes components, and the supercontinuum exhibits a smaller divergence; in both cases, the spectral width depends on the medium in which the supercontinuum is generated (Alfano, 1989; Fork et al., 1983; Corkum et al., 1986; Brodeur et al., 1996). The femtosecond continuum beam appears as a white disk surrounded by a distinct, concentric, rainbow-like conical emission. The term white-light continuum is usually reserved for the low-divergence, central part of the beam and excludes the conical emission.

Among the mechanisms that have been proposed to explain the white light continuum generation, there are self-phase modulation (SPM) (Fork et al., 1983; Yang and Shen, 1984), ionization-enhanced SPM (Fork et al., 1983; Corkum et al., 1986), with additional contributions from the interplay of diffraction and instantaneous electronic Kerr nonlinearity (Manassah et al., 1988), stimulated Raman scattering, temporal self-steepening, and four-wave parametric processes (Penzkofer et al., 1975; Yang and Shen, 1984; Corkum and Rolland, 1989; Chin et al., 1999a, b; Brodeur and Chin, 1999; Gaeta, 2000, 2002; Aközbek et al., 2001; Fang and Kobayashi, 2003). However, a definitive understanding of the rich physics involved in SCG is still missing (Schumacher, 2002). Experiments have shown that the power threshold for SCG coincides with the calculated critical power for self-focusing, in line with the proposal made by Bloembergen (1973) to explain the picosecond continuum. Self-focusing is therefore known to play an important role in the white light continuum generation (Corkum et al., 1986; Smith et al., 1977; Ilkov et al., 1993; Ranka et al., 1996). For the femtosecond continuum in condensed media, experiments by Brodeur and Chin (1998, 1999) confirmed that SCG is triggered by self-focusing. The dependence of the spectral broadening of the white light on material band-gap has been also reported (Brodeur and Chin, 1998). Below a band gap threshold of 4.7 eV, the medium does not generate a SC. Above this threshold, the spectral width of the continuum increases with band gap. The enhancement of SPM by the plasma generated by MPI has been proposed as the primary mechanism of SCG (Brodeur and Chin, 1998, 1999). MPI first reduces the incident energy of the collapsing field and then produces a plasma that absorbs, defocuses, and spectrally blue-shifts the intense laser field. The competition between the Kerr effect and plasma defocusing which leads to a clamping of the maximum intensity was interpreted as one of the dominant factors that determine the spectral extent of SC generation (Brodeur and Chin, 1999). More recently, chromatic dispersion (Kolesik et al., 2003a) was also shown to contribute to limiting the spectral extent of SCG (in addition to the band gap dependence) in gases as well as condensed media. From numerical simulations, self-steepening was shown to significantly enhance the spectral extent

of SCG (Aközbek et al., 2001). The combined effects of self-steepening and group velocity dispersion on SCG was clearly evidenced recently by measurements in water (Bragheri et al., 2007, 2005).

The efficiency of white light generation has been quantified and optimized by Dharmadhikari et al. (2004) who demonstrated that highly efficient ($\sim 40\%$) white light generation is achieved in a 10 cm long barium fluoride crystal irradiated by 45 fs, 800 nm laser pulses with incident energy up to 1 mJ, owing to the large band gap and low dispersion of BaF_2. Their experiments confirmed that multiphoton excitation occurs during SCG and showed that, at low incident intensity, the white light continuum is spatially coherent. By using a mesh so as to generate multiple filaments acting as supercontinuum sources Dharmadhikari et al. (2005b) have measured a conversion efficiency into conical emission varying from 16% to 87% for different condensed media. From a systematic study in different media (BaF_2, acrylic, water, BK-7), the authors have determined the influence of the pulse duration, focal position and laser polarization on white light generation (Dharmadhikari et al., 2005a). They have shown that flat white light spectra with high conversion efficiency are obtained for 45 fs, linearly polarized pulses when the beam is focused inside the media. The results obtained by Dharmadhikari et al. (2004) confirmed that of Cook et al. (2003) who have studied the white light supercontinuum interference of self-focused filaments in water. Using cylindrical lenses, they have generated a very stable one-dimensional array of filaments producing interference effects between neighboring filaments. The stable interference pattern created by a filament pair was found to be similar to that due to a pair of Young's slits, in agreement with predictions based on the assumption that the filaments are a pair of spatially coherent sources of white light. This implies a constant phase relationship between the white light continuum generated by each filament. Similar results were obtained by Corsi et al. (2004) who generated a linear array of phase coherent supercontinuum sources by producing an interference pattern between two laser beams in quartz and glass plates, thus forming filaments preserving their mutual phase coherence.

Chin et al. (1999a) have investigated SCG in the regime of large peak powers. For peak powers sufficiently higher than the critical power, the beam cross section breaks up into randomly distributed small-scale filaments acting as sources of the white light. Each spectral component of the white light was shown to act as a coherent source (Chin et al., 1999b). The white light supercontinuum was therefore proposed to essentially result from the spatial and spectral transformation of the initial pulse during its nonlinear propagation inside the medium (Chin et al., 1999a). The extinction ratio $I_\perp / I_\parallel$ of white light is defined as the ratio of intensity transmitted when an analyser is perpendicular to the polarization of the laser to the intensity when the analyser is parallel to the polarization. In order to investigate the white light polarization, Dharmadhikari et al. (2006a) have measured the extinction ratio of white light generated upon irradiation of BK7 glass by 36 fs laser pulses with incident power 1000 times larger than the critical power for self-focusing. The measurements suggest that the generation of an electron plasma by multiphoton ionization depolarizes the supercontinuum whereas the white light generated at lower intensity keeps the same polarization as the laser. In keeping with this result, a self-induced polarization change of the white-light continuum in LiF and CaF_2 was observed (Midorikawa et al., 2002; Nagura et al., 2002). Since both LiF and CaF_2 are isotropic media with a cubic crystal structure, the authors have attributed this effect to the nonlinear birefringence caused by the polarization and intensity dependent cross phase modulation.

In the domain of anomalous dispersion, Saliminia et al. (2005a) demonstrated broadband white light supercontinuum generation with a high efficiency upon focusing femtosecond pulses from an optical parametric amplifier at 1.5 μm inside silica glass. Stable interference fringes resulting from the superposition of two spatially coherent fields emanating from a pair of filaments were observed for individual spectral components. For the case of focusing very near the input glass surface in air, the interference fringes were observed by excitation at both 800 nm and 1.5 μm, whereas such fringes were not observed with 800 nm irradiation when focusing inside the glass. This feature was attributed to significantly reduced destructive influence of femtosecond breakdown and structural damage on filamentation of pulses at 1.5 μm.

A close connection exists between conical emission (CE) and supercontinuum generation (SCG). Eqs. (10) and (23) follows from a tentative interpretation of this connection as an effect of ionization enhanced SPM. The continuum generation and conical emission obtained from the propagation of green and red ultrashort laser pulses in CS_2 and in water were measured by Liu et al. (2005b). The authors followed the evolution of white light production by using one- and two-photon fluorescence and by recording the energy losses caused by MPA and CE from a *z*-scan technique. CE was observed to be much stronger for CS_2 than for water which has a larger bandgap of 7.5 eV and was interpreted to be mainly caused by SPM and dispersion whereas MPI as well as MPA were found to play a negligible role for input pulse powers up to 8 critical powers for self-focusing. A definitive link between CE and SCG was
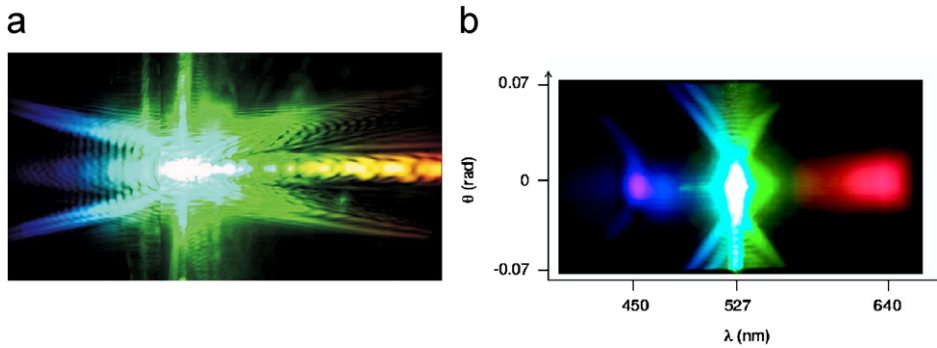
Fig. 86. (a) Typical angular spectrum recorded after filamentation of an ultrashort laser pulse over a few centimeters in lithium triborate (Day, 2004; Faccio et al., 2005a). (b) Double X θ–λ spectrum of a 527 nm, 3 µJ laser pulse undergoing filamentation in water. Each X-pattern exhibits a gap in frequency characterizing the velocity of each split pulse. The reduced visibility of the red tail was attributed to the increased absorption at these wavelengths (Faccio et al., 2006b).

established from measurements performed in water which showed that pulse-splitting, SCG and CE are manifestation of a single phase matching process between the two split pumps and two X-waves (see Sections 4.2.8 and 4.2.7, Faccio et al., 2006b).

4.2.7. Measurements of frequency resolved angular spectra and X-waves formed by filamentation

Many of the measurement techniques used to characterize filaments rely on the assumption that the physical phenomena involved in filamentation keep a clear separation between spatial and temporal effects. Filament are therefore often characterized in terms of pulse duration, beam diameter, peak intensity, and averaged quantities such as the fluence (time integrated intensity) or the power. When strong coupling between space and time occurs as in the generation of filaments, many of these concepts, however, lose their meaning. Recently, evidence of strong space–time coupling was revealed by use of an imaging spectrometer allowing a map of the far-field angular spectra of 200-fs optical pulses that have undergone beam collapse and filamentation in a Kerr solid or liquid (Faccio et al., 2005a). The far-fields exhibit an X-shape and a strong modulated on-axis emission (see Fig. 86). This fringe pattern was observed by studying the evolution of the spectra with increasing input powers, revealing the complexity of the space time coupled phenomena from angular-spectral characterization. He et al. (1993) characterized the conical emission in Kerr and non-Kerr liquids pumped with ultrashort laser pulses and observed X-shaped angular spectra. These X-shaped angular spectra were reinterpreted only recently as a manifestation of the spontaneous dynamics of ultrashort laser pulses undergoing filamentation, which tends to generate a stationary conical wave (Day, 2004; Faccio et al., 2005a, b). An analysis of the role of nonlinear losses in the filament dynamics was made in the framework of a monochromatic approach, where the role of chromatic dispersion was neglected (Dubietis et al., 2004a). In this case, a theoretical analysis confirmed the existence of weakly localized conical stationary solutions to the nonlinear Schrödinger equation in the presence of multiphoton absorption (Porras et al., 2004). In contrast, nonlinear X waves represent conical stationary solutions to the nonlinear Schrödinger equation in the presence of chromatic dispersion but when nonlinear losses are neglected; nonlinear X-waves are expected to be robust against nonlinear losses and the corresponding solutions to an extended nonlinear Schrödinger model fully accounting for nonlinear losses and chromatic dispersion should play the role of attractors for the dynamics of filamentation.

4.2.8. Measurement of the complete 3D mapping of the filament intensity pattern

Two major problems concern the experimental characterization of the wave-packet dynamics during filamentation. The first problem is that the high intensity within a filament usually prevents direct measurement of pulse properties without introducing additional nonlinear interactions. A comprehensive single-shot data set of the temporal, spectral, and spatial properties of a Gaussian, self-focusing beam has shown that by increasing the energy of a 130 fs, 800 nm input pulse, the temporal profiles modulate and generate spiky features with durations of ~ 25 fs, attributed to vibrational
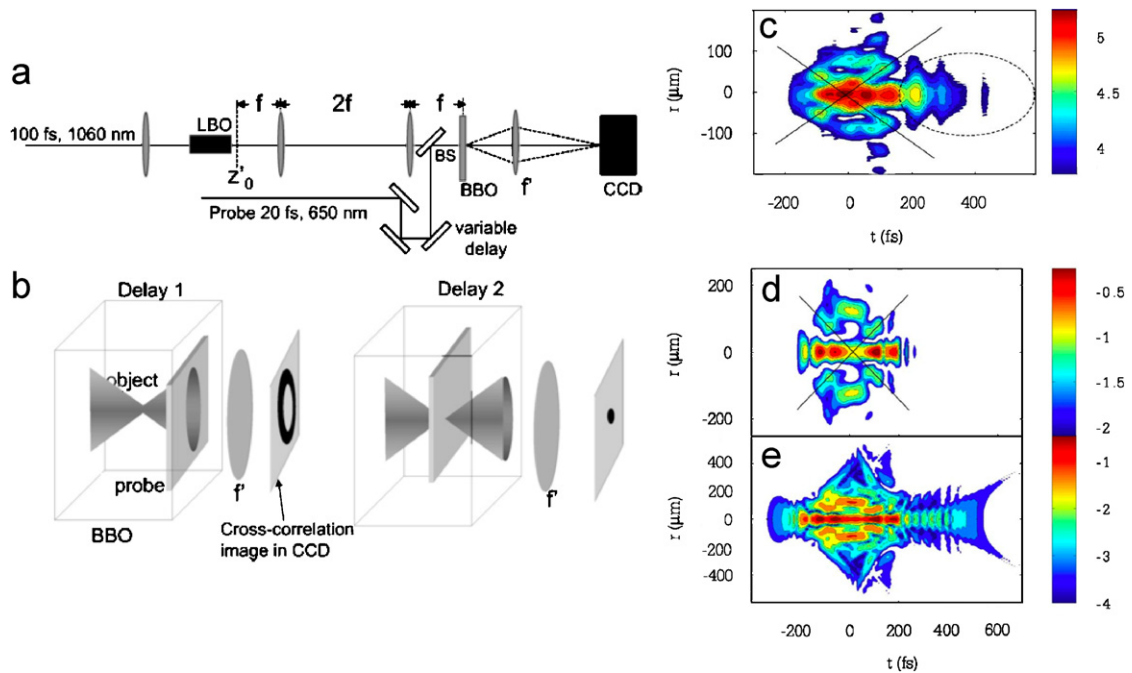
Fig. 87. (a) Experimental setup and (b) schematic representation of the cross-correlation nonlinear gating technique. From Trull et al. (2004). (c) Experimentally measured space–time (r, t) profiles of a pulse in a Kerr medium (water) for a propagation distance of 3 cm in logarithmic scale (the shaded bar indicates the intensity-level decade). Input pulse duration: 160 fs, diameter: 80 μm, energy: 3 μJ. (d) Numerical simulations in water at 800 nm showing the normalized space–time (r, t) intensity profile in logarithmic scale (two decades), in the same conditions as in (c). (e) Same as in (d) but with intensity profile plotted over four decades. From Faccio et al. (2005b).

Raman contribution to the Kerr effect (Bernstein et al., 2003, 2002). These measurements, however, were performed for pulses that did not have the intensity required to produce either filaments or multiphoton ionization.

The second problem is that most of the measurements of filament properties have been limited either to the pure temporal domain, by an on-axis autocorrelation or cross-correlation technique, or to the pure spatial domain, by time-integrated CCD-based detection. An attempt of space–time experimental characterization was reported by Kumagai et al. (2003). The technique used, based on optical polarigraphy, showed poor resolution and did not allow the fine details of the spatio-temporal structure to be recovered. A very powerful high spatio-temporal resolution three-dimensional mapping technique, based on the use of an ultrafast $\chi^{(2)}$ (sum-frequency) gate was proposed (Di Trapani et al., 2003; Trull et al., 2004; Matijošius et al., 2004a; Potenza et al., 2004). The approach resembles the cross-correlation measurement to some extent, but instead of recording the space-integrated (or simply on-axis) signal, here the entire space-resolved sum-frequency profile is captured. The whole wave packet is then reconstructed from the assembly of time slices recorded at different delay times (see Fig. 87). Thus, the space–time intensity distribution is mapped via a nonlinear second harmonic generation cross-correlation scheme. Fig. 85(b) shows an example 3D distribution of the space–time intensity of a 527 nm pulse undergoing filamentation in water, measured by this technique (Matijošius et al., 2004b). From this method, it was shown that filaments generated by infrared laser pulses in water generate an intensity distribution in the form of an X-wave (see Fig. 87(c)), which confirmed the property of these stationary wavepackets: the near field as well as the far-field are X-shaped. Numerical simulations shown in Fig. 87(d,e) were favorably compared with these measurements. A larger dynamical range achievable in the simulations indicated, however, that the pulse splitting phenomenon led not to a single but to a double X-wave, each of which is associated with an intensity peak in the near-field (see Fig. 87(e) and Faccio et al., 2005b). It was recently recognized that a double X structure also appears in the far-field as shown in Fig. 86(b) (Faccio et al., 2006b). The splitting process was interpreted as a four wave mixing process between two intense, highly localized pumps (split pulse) traveling with opposite velocities, and two X-waves. In the far field, each X-wave exhibits a frequency gap that depends on the velocity of the associated pump, thus leading
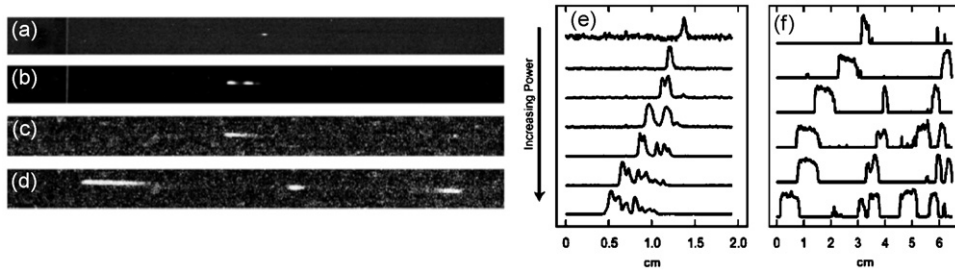
Fig. 88. Experimental results of multiple-collapse behavior as a function of input power. In the normal-GVD regime [(a) and (b)], collapse is localized, whereas extended filaments are observed in the anomalous-GVD regime [(c) and (d)]. The distance between the collapse events is also much larger in the anomalous-GVD regime. A more comprehensive series of lineouts depicting the collapse behavior is presented for the (e) normal- and (f) anomalous-GVD regimes. Note that different scales are used in (e) and (f). The light is propagating from left to right. From Moll and Gaeta (2004).

to a central X-pattern with a red (blue) tail belonging to the blue (red) pump, respectively (Kolesik et al., 2004; Faccio et al., 2006b).

4.2.9. Frequency conversion to Raman-excited modes by filaments

Filamentation in Kerr media with strong Raman gain such as ethanol was recently shown to lead to the generation of X-waves at the Raman shifted wavelength, called Raman-X waves (Faccio et al., 2007), whose group velocity matches that of the filament pump pulse. From a 1 ps, 527 nm laser pulse undergoing filamentation in ethanol, both seeded and spontaneous (starting from quantum noise) stimulated Raman scattering induced the formation of Raman X-waves. The large group velocity mismatch and short (50 fs) durations of the split pump pulses were expected to lead to a severe reduction of the conversion efficiency. In spite of this, a conversion efficiency of 75% to the Raman wavelength was measured for a 5 cm long ethanol cell. By using a delayed seed at the Raman shifted wavelength, Faccio et al. (2007) showed that the temporal overlap of the seed with one of the split pulses from the pump leads to the preferential excitation of a single set of X-tails of the Raman X pulse, i.e., a half Raman-X on the blue or on the red side of the Stokes wavelength. This suggests that the Raman X-wave, as for the pump, is formed by two half-X waves which are the red (or blue) legs of a blueshifted (or redshifted) X-wave with a frequency gap. The gap is featured by the velocity of the split pulses. Generating Raman X-waves may be a possible way of creating high intensity, single peaked, ultrashort X-waves with tailorable characteristics.

In this respect, Théberge et al. (2006a) have demonstrated that powerful and tunable ultrashort laser pulses are generated in the visible spectrum through four-wave mixing during filamentation of near infrared femtosecond laser pulses in air or in argon seeded by an infrared femtosecond laser pulse. Pulse durations of 12 fs in the visible range were obtained in air. Conversion efficiencies up to 25% in air and 40% in argon have been measured. Very low energy fluctuations and an excellent mode quality have been obtained (see Section 1.3.8).

4.2.10. Filamentation in the anomalous dispersion regime

Most studies on femtosecond filamentation have been performed in the regime of normal group velocity dispersion ($k'' > 0$) while much less attention has been paid to ultrashort pulse filamentation in media with anomalous GVD ($k'' < 0$). Theoretically, Kerr self-focusing with anomalous GVD might lead to fully localized light bullets (Silberberg, 1990). In a pure Kerr medium, spatio-temporal self-focusing and light bullets were shown to be supported in a planar waveguide, but not in all spatial dimensions (Eisenberg et al., 2001; Fibich and Ilan, 2004). In contrast with this result, simulations of filamentation in fused silica at 1.6 μm predict the generation of 6 fs light bullets (Liu et al., 2006c) when plasma generation, plasma defocusing and plasma absorption are accounted for. Light filamentation in the anomalous regime has been shown to result in long filament paths exceeding up to ten times the distances reached with normal dispersion (Fig. 88; Moll and Gaeta, 2004; Liu et al., 2006c). The anomalous regime also promotes ultra broadband continuum generation extending far into the visible wavelength region (Saliminia et al., 2005a; Kolesik et al., 2005). A new type of CE, characterized by decreasing emission angles with increasing frequency shifts, has been predicted in connection with the elliptical structure of the governing propagation equation (the hyperbolic structure in the regime of normal GVD leads to CE with bluer rings outside). This prediction is linked to the existence of nonlinear O-waves

which are the counterpart of nonlinear X-waves for the anomalous regime, i.e., stationary, weakly localized, nonlinear, dispersion and diffraction free wavepackets undergoing multiphoton absorption in their core and refilled by the energy contained in their wings (Porras et al., 2005b). Existence of this new type of CE associated with filamentation in the anomalous dispersion regime has been corroborated only recently with experiments in water at 1050 nm (Porras et al., 2005a) and in fused silica at wavelengths between 1400 and 1700 nm (Porras et al., 2007). Experiments and simulations have also shown that in the presence of strong high-order dispersion, which typically occurs at the frontier of the anomalous frequency range, the spatiotemporal spectral broadening of an intense pump pulse in a Kerr medium leads to asymmetric profiles(Faccio et al., 2006a). In contrast with the modulational instability gain of plane and monochromatic nonlinear eigenmodes, which remains symmetric in the wavenumber-frequency $(k_\perp, \omega)$ domain even with odd high order dispersive terms (Wen and Fan, 2002), the asymmetry of the measured angularly resolved spectra was interpreted in terms of spontaneously generated broadband linear stationary modes supported by the system. In the $(k_\perp, \omega)$ domain, these linear modes are fishlike linear conical waves, i.e., they follow the chromatic dispersion of the medium which, for large frequency detuning, is not dominated by second order dispersion as for X- or O-waves, but generically leads to long tails on the side of the normal dispersion frequency range and to a cut-off on the anomalous side (Faccio et al., 2006a; Kolesik et al., 2005).

4.2.11. Filamentation with Bessel beams

Since the works of Durnin et al. (1987), it has been recognized that Bessel beams possess specific reconstruction properties that enable new effects to be observed that are not seen with conventional Gaussian beams. Quasi-Bessel beams, which can be viewed as apertured Bessel beams carrying a large but finite energy, can be produced in the laboratory by various methods including axicons, holographic techniques, or placing an annular slit in the back focal plane of a convex lens. Spatial coherence of the source is not even a required condition although it enhances the contrast (Fischer et al., 2005). The central core of a quasi-Bessel beam remains remarkably resistant to diffraction compared to a Gaussian beam of similar spot size. Bessel beams have therefore been proposed for several applications from optical trapping of particles to efficient phase matching for second harmonic generation (see McGloin and Dholakia, 2005, for a review).

The question whether in the ultrashort pulse regime, Bessel beams can or not advantageously replace Gaussian beams to generate diffraction and dispersion free filaments, or wavepackets, is still open. However, preliminary experimental and numerical results have shown that high localization, focal depth and contrast can be achieved by generating a filament from a high power Bessel beams (Polesana et al., 2005). For instance, Polesana et al. (2006) have investigated the reshaping of ultrashort pulsed Bessel beams undergoing filamentation in Kerr media. The reshaping is featured by a spontaneous transformation into a pulsed nonlinear unbalanced Bessel beam, i.e., a stationary conical solution to the propagation equation in the presence of Kerr self-focusing and nonlinear losses (Porras et al., 2004). By exciting 3-photon absorption in a linearly transparent material (Coumarine 120 in Methanol) with pulsed Bessel beams, Polesana et al. (2005) found the induced nonlinear polarization much more suitable for applications than that obtained both from linearly propagated pulsed Bessel beams and from conventional Gaussian beams. Linear pulsed Bessel beams have a slowly decaying intensity profile whereas the nonlinear propagation of the Bessel beam maintains a high contrast along the long focal depth of the nondiffracting central Bessel spot. Arbitrary long focal depth maintaining the same desired resolution and contrast are achievable by generating filaments with pulsed Bessel beams, which can lead to new applications in various field such as multiphoton microscopy, photolithography, micromachining and channel wave guide writing with longitudinal illumination. In this respect, Kosareva et al. (2005a) have investigated the formation of extended plasma channels in a condensed medium by focusing a femtosecond laser pulse upon an axicon. Gaižauskas et al. (2006) have shown that filaments generated by pulsed Bessel beams form discrete equidistant damage spots in borosilicate glass with potential applications in microstructuring transparent optical materials.

4.2.12. Multiple filamentation in condensed media

Schroeder and Chin (2004) have taken advantage of the possibility of filament generation in liquids to provide a nonlinear fluorescence technique allowing the visualization of multiple filaments in methanol. Using different diluted dyes, the filamentation dynamics was visualized through two-photon fluorescence. Several processes visible on Fig. 89(A) were identified. (a) Filament extinction with a bright fluorescence zone which diverges into a larger diameter. (b) Extinction of filament. (c) Refocusing after a bright fluorescence. (d) Breakup of filament. (e) Fusion of filaments.
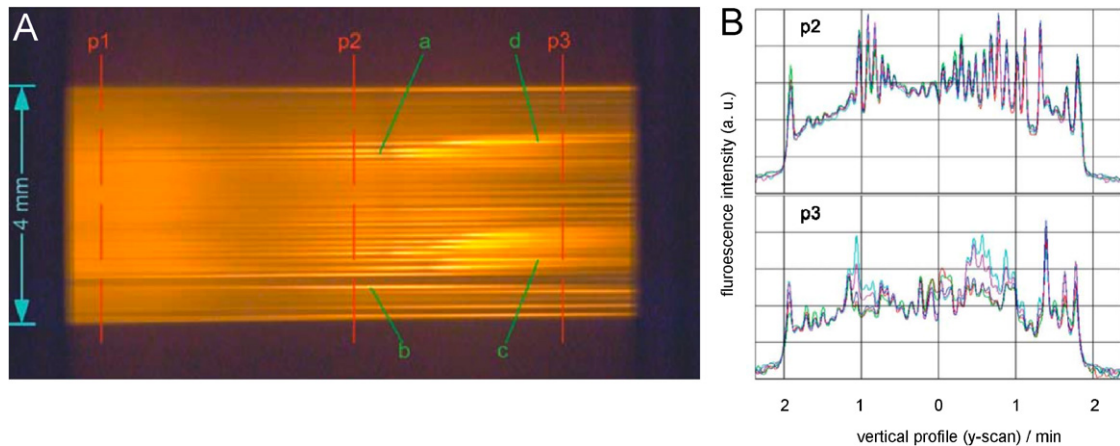
Fig. 89. (A) Development of a one-dimensional filament array in methanol behind a slit from a 23 μJ (200 P_{cr}), 46 fs, 810 nm laser pulse. The yellow color is the two-photon fluorescence from Rhodamine B which was added to monitor the local intensity of the propagation of the initially collimated, transform limited femtosecond Ti–sapphire laser beam. (B) Five profile scans in the same day were taken at positions p2 and p3. From Schroeder and Chin (2004).

Fig. 90. Side view photograph of a filament generated in an unpumped Ti:sapphire crystal with a pulse duration of 50 fs, a focusing lens of 20 cm, and an incident energy of 3.7 mJ. The converging laser beam is incident on the left side. A filament with 10 μm diameter is formed over the crystal length, displaying several secondary intensity maxima. From Philip et al. (2005).

Centurion et al. (2005b) have monitored the formation of a large number of filaments by launching femtosecond laser pulses with powers much higher than the critical power for self-focusing in carbon disulfide. They have observed three stages for the filament formation: (i) the beam breaks up into a constellation, (ii) filaments form on the constellation. (iii) filaments release a fraction of their energy through conical emission. In agreement with the scenario obtained for organizing multiple filaments, the interaction of conical emissions with the constellation generates additional filaments leading to a phase transition to a faster filamentation rate. By means of a holographic technique (Centurion et al., 2004) were able to capture laser induced plasma formation with 150 fs time resolution and to recover amplitude and phase information with 4 μm spatial resolution, Centurion et al. (2006) have shown that in carbon disulfide, a beam break-up into multiple filament occurs before the ionization intensity threshold is reached, in contrast with water and air where a fully ionized electron plasma was detected.

4.2.13. Amplification of filaments

Recently, Philip et al. (2005) have shown amplification of filaments. This is not just a process where an already formed filament is amplified by crossing a medium with a broadband gain, but a combined process where the medium can both produce and amplify the filament. The proof of principle has been performed in sapphire dopped with Ti^{3+}. This system provides a broadband gain. It was shown that filamentation can occur over a distance of the order of 1 cm for an unpumped crystal, provided the input power exceeds a few MW (Fig. 90). In Fig. 91(a) and (b), the spot at the exit surface of the crystal is shown. If the input power is further increased above several tens of MW, multifilamentation occurs (Fig. 91(c)). On the other hand, propagation of the infrared pulse in the inverted crystal shows (i) a decrease of the critical power, (ii) an increase of the filament length, (iii) an increase of the fluence above the value for irreversible damage. Inspection of the damage spot near the exit surface (Fig. 91(f)) revealed that no break-up into multifilaments occurred even if the fluence was larger than in the case of Fig. 91(c). This result shows that it is possible to increase the energy contained in a single filament while avoiding multifilamentation. D'Amico et al. (2006b) have obtained similar results in methanol with a dye. They could show that the increase of the fluence of a single filament is accompanied by
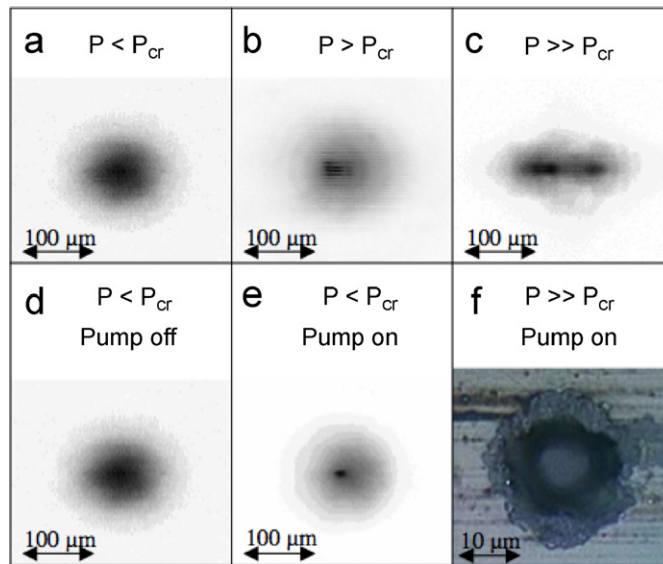
Fig. 91. Beam profile measured at the exit face of the crystal for several conditions. (a) $P_{in} < P_{cr}$, unpumped crystal; (b) $E_{in} = 12\,\mu J$, unpumped crystal; (c) $E_{in} = 47\,\mu J$, unpumped crystal; (d) same as (a); (e) $E_{in} = 3.6\,\mu J$, pumped crystal; (f) image of the damage seen through a microscope (note the change of scale). In all cases, the pulse duration was 80 fs and the focus length of the lens was 8 cm. From Philip et al. (2005).

a growth of the filament diameter and they could obtain significantly higher energies up to 80 μJ inside a single mode. For many applications, amplification of a filament would be interesting in a gas. This might be possible at infrared wavelengths in gases at high pressure where the gain becomes large enough to accommodate a short pulse.

4.2.14. Triggering of guided electric discharges in the laboratory

A natural lightning discharge is based on the propagation of a precursor called leader, which is a channel with high conductivity, larger than about $1\,\Omega^{-1}/m$ (Uman, 1987). In the head of the leader, defined by its large conductivity gradient, the air has been heated through Joule effect and its temperature is high enough (typically around 2000 K) to allow the detachment of electrons from the negative oxygen ions. In front of the leader channel, a multitude of cold, ionized channels termed streamers form a leader corona. Streamers are waves of ionization that can develop because the electric field is enhanced locally by the tip of the leader, over a finite region. In return these streamers, each carrying a small current, coalesce into a single stem and heat the volume in the leader head, leading to an extension of the leader and allowing its propagation. As the lightning leader propagates toward the ground, it reaches a point where its corona extends all the way to the ground and makes electrical contact with it. This is the beginning of the phase termed final jump. During this phase, the leader propagation is accelerated. This is due in part to the stronger electric field felt by the leader as the space charge produced by its corona is neutralized due to the connection to the ground (Pépin et al., 2001).

The generation of a plasma column in the wake of the self-guided pulses was proposed to be an efficient mechanism to accelerate the leader growth and lead to the triggering and the guiding of electric discharges (Zhao et al., 1995a; Zhao and Diels, 1995). Fig. 92 shows the photo of an experiment by Tzortzakis et al. (2001c) and the characteristic times to trigger the discharge, after the passage of the laser pulse, in the case of a discharge induced by a filament in the laboratory (Fig. 92(a)) and in the traditional case of a discharge triggered by a femtosecond laser pulse (Fig. 92(b)). A tension of 30 kV is applied in both cases at the boundaries of the two electrodes separated by 2 cm. In the traditional case, where a hot plasma of high density is generated in the middle of the electrodes, the discharge is not rectilinear and results from a complex process. The delay is on the average of about one microsecond, with strong shot to shot fluctuations (Desparois et al., 2000). In the case of a discharge induced by filamentation, the plasma density being quasi-uniform on-axis, the passage of the filament closes the circuit between the two electrodes with a resistance of low value. A rectilinear discharge is obtained, guided by the filament, with a constant delay of 80 ns after the passage of the filamenting laser pulse. The triggering of the guided discharge occurs for an applied voltage equal to 70% of that necessary to trigger the spontaneous discharge (Tzortzakis et al., 2001c).
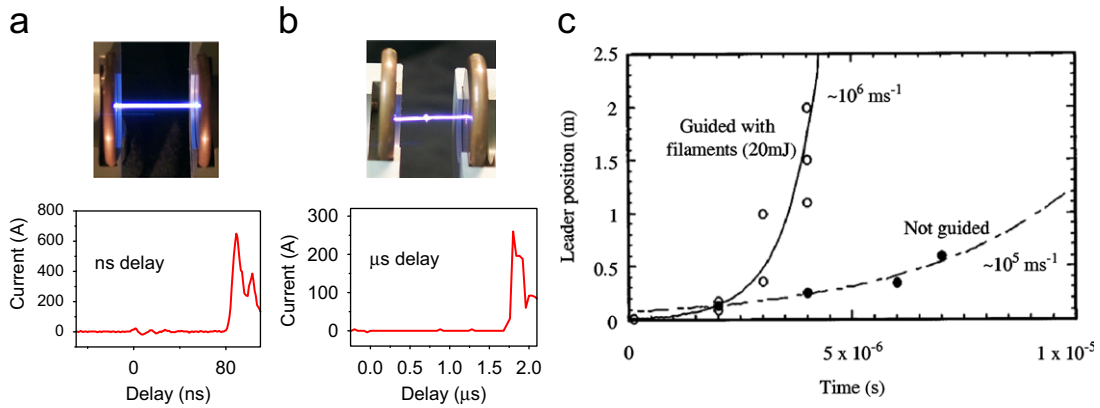
Fig. 92. (a) Discharge induced by a filament generated by an IR fs laser. A reproducible delay of 80 ns separates the laser pulse from the discharge. (b) Discharge induced by a plasma of high density generated by the same laser strongly focused between the two electrodes. The delay between the laser pulse and the discharge is about one μs, with strong shot to shot fluctuations. According to Tzortzakis et al. (2001c). (c) Evolution of the position of the leader tip inside the gap. The propagation of the leader is measured from time-resolved images. The laser-guided leader has a velocity (10^6 m/s) that is about ten times that of the natural leader (10^5 m/s). From La Fontaine et al. (2000).
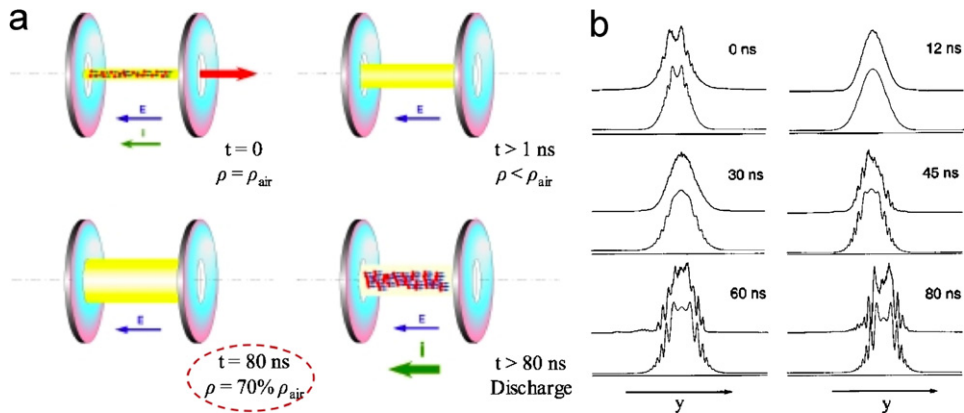
Fig. 93. (a) Hydrodynamic model describing the triggering of an electric discharge by a filament. The filament leaves in its wake a plasma of short life time, insufficient by itself to cause a sustained discharge. By Joule effect, this plasma induces during its life time a heating of a fine column of air, which extends then laterally. After 80 ns, the central depression in air, about 30%, fulfills the condition for a sustained discharge. According to Tzortzakis et al. (2001c). (b) Experimental results (upper curves) from time-resolved diffractometry and comparison with numerical simulations (lower curves) for different delays between pulse and probe. The best fit is obtained with an initial heating of the column of air corresponding to a temperature $\Delta T = 100$ K.

Tzortzakis et al. (2001c) developed a hydrodynamic model describing in a quantitative way the kinetics of the discharge in this case. Fig. 93 gives a cartoon of the physics in the model. It is mainly a thermal phenomenon. The heating of a fine column of air produced by Joule effect during the lifetime of the plasma leads to a depression in the center, which ultimately fulfills the conditions required for a discharge along the axis of the filament. By means of time resolved diffractometry measurements, the evolution of the density of air was followed before the triggering of the discharge. The plasma generated by the filament is not able in itself to trigger and guide the discharge as it recombines in a shorter time than the measured delay between the laser pulse and the discharge. The decrease of the pressure in the heated fine column of air leads to a decrease of the breakdown voltage, which induces the discharge after a delay typical of the gas expansion. An excellent agreement with the hydrodynamic model was found (Tzortzakis et al., 2001c).

Bogatov et al. (2005) have confirmed the thermally induced breakdown model by measuring the breakdown threshold as a function of laser energy. Tamošauskas et al. (2005) have shown that the electric breakdown voltage of air is significantly reduced (from 34 down to 10.4 kV/cm) in the presence of an ionizing light filament generated between
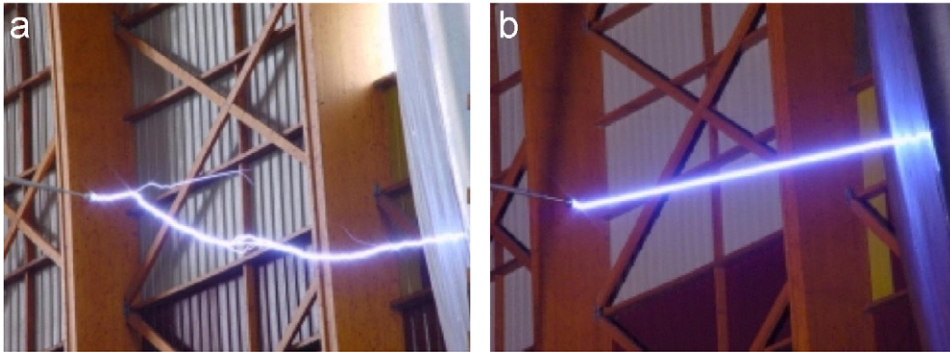
Fig. 94. Electric discharge between two electrodes separated by 4 m, with an applied difference of potential of 2 MV (a) and 1.7 MV (b). The rectilinear discharge is triggered by a filament connecting the two electrodes (Ackermann et al., 2005).

the electrodes. Measurements of the delay between the laser pulse and the discharge have revealed an exponential dependence on the electrode gap accurately fitted by the empirical expression

$$\Delta t = 2.48 \exp\left(\frac{\Delta l + \Delta}{0.22U}\right), \tag{158}$$

where Δl is the electrode gap expressed in mm, Δ is an additional distance set by the discharge geometry, U is the applied voltage in kV, and Δt is expressed in ns.

Recently several experiments were led to greater scales (Comtois et al., 2000; La Fontaine et al., 1999a, 2000; Pépin et al., 2001; Ting et al., 2005a). La Fontaine et al. (2000) have recorded images of the early stages of the discharge of a uniform 2 m air gap. The laser-produced ionized filaments were shown not to initiate the discharge process but to act rather as preferred channels where the leader growth is accelerated. In these experiments with 20 mJ laser pulses and a 2 m air gap, the natural breakdown voltage was not observed to be changed by the presence of filaments, but acceleration of the growth of the leader was corroborated by the delay between the laser pulse and the discharge, about half the expected duration of 2 μs for the streamer to bridge the 2 m gap (see Fig. 92(c)). With larger laser energies of 200 mJ, the generated plasma channel allowed the lowering of the leader inception voltage by 50% and the guiding of the leader propagation on a distance of up to 2.3 m, with a tenfold increase of its speed (Comtois et al., 2000). This led to an effective 40% reduction of the breakdown voltage. From these experiments and numerical modeling (Vidal et al., 2000), the laser energy per unit length required to guide a leader was inferred to be between 60 and 100 mJ/m. With laser energies of 400 mJ, the triggering and guiding of leaders could be extended over distances up to 3 m (Pépin et al., 2001).

Observations from recent measurements within the framework of the teramobile project (see Section 5.1.1) include the reduction of the breakdown threshold, the reduction of the delay between the laser pulse and the triggering and the guiding of the electric discharge. Laser-guided straight discharges have been observed for gaps of 3.8 m at a high voltage reduced to 68% of the natural breakdown voltage (Rodriguez et al., 2002). More recently, guided discharges were observed at distances going up to 4 m (see Fig. 94) (Ackermann et al., 2005).

5. Long range propagation and applications of femtosecond filamentation

Depending on which application one has in mind, different features of filaments may be promoted: it is interesting either to generate a filament at a predetermined distance, for example in the vicinity of a remote target, or to maximize the length of the conducting plasma column. Obviously, for light detection and ranging (LIDAR) applications, the desirable effect is the largest possible conversion into the white continuum, whereas the laser intensity is not of concern. For other applications as, e.g., laser induced breakdown spectroscopy (LIBS), the transfer of high intensity over large distances is the most important feature. In still other applications as, e.g., the formation of virtual antennas, the main required feature is the longest ionization track. We start this section on applications by briefly reviewing the results on long propagation distances in air. We proceed by reviewing the possible control parameters which can be tuned in theory to fulfill these objectives. Finally, we review the possible applications of filamentation.
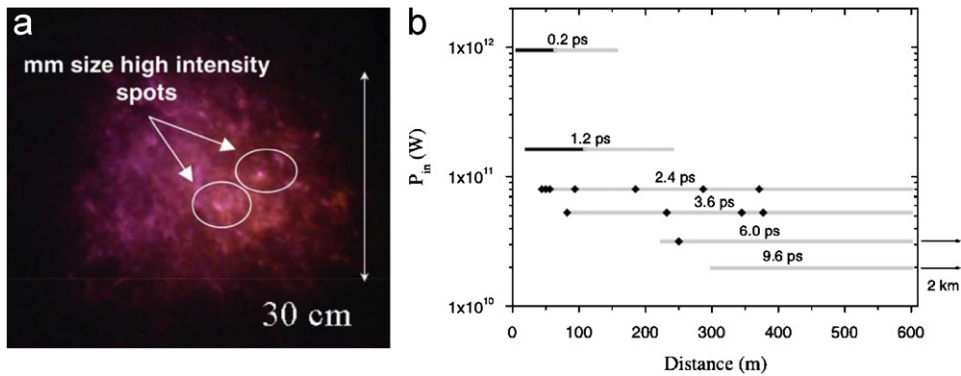
Fig. 95. (a) Beam cross section intercepted by a white screen at a propagation distance of 2350 m. The initial negative chirp corresponded to a duration of 9.6 ps. (b) Filamentation length as a function of the chirp of the input laser pulse. The duration of the non-chirped pulse is 100 fs. Black points and lines refer to locations where air ionization could be detected, gray lines to distances where bright light channels were observed. According to Méchain et al. (2005a, 2004a).

5.1. Outdoor propagation and filamentation over long distances

5.1.1. Teramobile

Several experimental works discussed in this review were performed with the Teramobile laser, which is the first mobile femtosecond-terawatt laser system (Wille et al., 2002). It is based on the chirped pulse amplification technique. This facility is shared by four laboratories located in Jena, Berlin (Germany), Lyon and Palaiseau (France). The Teramobile was funded jointly by the German Deutsche Forschungsgemeinschaft (DFG) and the French Centre National de la Recherche Scientifique (CNRS). It was developed in cooperation with Thales Laser. Its main characteristics are the following: Pulse energy: 350 mJ, pulse duration: 70 fs, peak power 5 TW, repetition rate 10 Hz, Beam diameter 5 cm, chirped pulse duration 70 fs to 10 ps. It is supplemented by a mobile standalone laboratory, including all the sending and receiving optics as well as diagnostics and detection systems. The system as a whole was designed as a versatile tool intended for atmospheric applied research.

This infrastructure is suited for km-range propagation experiments, since the mobile system can be installed on long horizontal spots such as the runway of an airfield, permitting to study the beam continuously along its propagation path with the characterization unit. Mobility of the laser has also the advantage to allow further evaluation of the potential of fs-TW pulses for specific applications or experiments, without permanently installing an expensive and complex system at the place of interest.

5.1.2. Detection of filaments at long distances

If the filamentation in laboratory ($P_{in} \sim P_{cr}$) is now well documented, the propagation at long distance with multi-terawatt beams ($P_{in} \gg P_{cr}$) is still largely unexplored. Several groups gave persistent reports on multifilamentary structures propagating over several hundreds of meters (Nibbering et al., 1996; La Fontaine et al., 1999b; Yang et al., 2002a; Chin et al., 2002b). The formation of filaments at kilometer-range distances in the sky was also reported from the detection of the supercontinuum by a telescope (Wöste et al., 1997; Rodriguez et al., 2004). During an horizontal propagation campaign led with the Teramobile laser (see Section 5.1.1 and Méchain et al., 2005a, 2004a), the presence of multiple filaments up to 600 m was clearly demonstrated. Step by step measurements of the plasma density were performed by using three different techniques (conductivity measurements, detection of the luminescence and detection of the sub-THz electromagnetic radiation emitted from the filament). As shown on Fig. 95, the domain where multiple filaments were observed with intensities sufficient to ionize air molecules extends on more than 450 m. The intensity of the filaments were found to lie between 10^{10} and 10^{13} W/cm^2. The presence of light channels of millimetric size was demonstrated up to 2.2 km. At these distances, their intensity was not sufficient to generate a measurable electron plasma, as corroborated by $(3 + 1)$D numerical simulations (Méchain et al., 2004a). These experiments on long range multiple filamentation gave clear indications that the competition of the filaments for the available energy keeps the beam intensity at the verge of the ionization threshold. Following this result, it was suggested from the results of
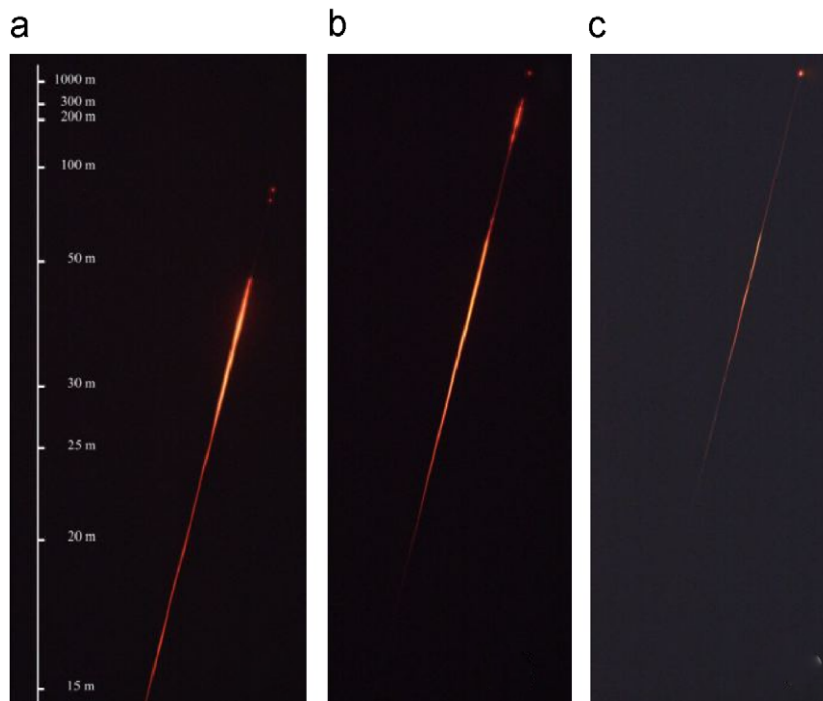
Fig. 96. Evolution of the white light continuum generation as a function of the propagation distance for different durations of the laser pulse: (a) 100 fs; (b) 1 ps; (c) 2 ps. From Méchain (2005).

a ray tracing method that filamentation might be possible without ionization (Kasparian et al., 2004). From laboratory experiments in air, Ruiz et al. (2005) reported a long distance propagation in the form of a quasi-Townes mode for pulse powers below the threshold for collapse, i.e., for conditions ruling out a possible role of ionization; this situation seemingly represents that of each filament in the bundle of the long range propagating multiple filaments.

5.1.3. Measurements of the plasma length

There exists very few reliable measurements with a very intense collimated beam. In this case, the measurements of the backscattered fluorescence induced by multiphoton ionization of excited nitrogen molecules constitute a non-intrusive method to detect the plasma channel. In contrast with the other detection methods, the luminescence can be detected remotely with a telescope. This method is therefore useful to detect long propagation distances in the atmosphere but does not give access to the dynamics of plasma generation or the plasma density in the filament. Using this technique associated with a lidar technique (Iwasaki et al., 2003), plasma channels covering about 200 m were detected from 40 mJ laser pulses (Hosseini et al., 2003b). This method was shown by Luo et al. (2005a) to be very sensitive to shot to shot fluctuations. Small beam diameters lead in particular to more intense and stable filaments. For an 8 mm beam diameter and 60 mJ energy, a filament length of about 600 m was extrapolated from measurements of the backscattered fluorescence signal, whereas a maximum length of 200 m was obtained with a beam diameter of 25 mm (Luo et al., 2005a; Hosseini et al., 2004a). By reducing the initial beam diameter, the authors observed a more stable fluorescence on a shot to shot basis.

5.1.4. Optimization of the white light supercontinuum and measurements of multiple filamentation over long distances

The long propagation of IR multi-terawatt laser pulses is shown on Fig. 96 as a function of the initial laser chirp of the laser pulse. Over long distances, the duration of a non-chirped pulse is expected to increase because of group velocity dispersion of air (see Section 5.1.5). This detrimental effect was precompensated by imparting a negative initial chirp. Initial chirped laser pulse has another effect. By increasing the pulse duration at constant pulse energy, it decreases its peak power. This is expected to increase the distance necessary for the onset of filamentation and also to reduce the
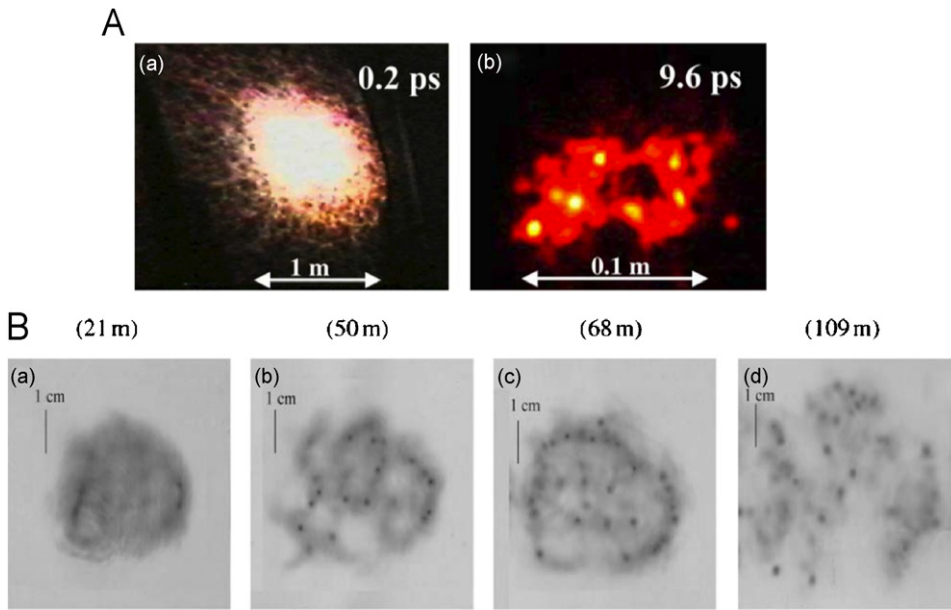
Fig. 97. (A) Comparison between two beam cross-sections at 1000 m. (a) minimum negative chirp: 0.2 ps, (b) maximum negative chirp: 9.6 ps. (B) Measured beam profile at various distances with a initial pulse duration stretched to 1.2 ps. From Méchain et al. (2005a).

number of generated filaments. These effects are clearly visible on Fig. 96 where the white light continuum generation starts at a larger distance for long pulses (large negative chirps). The conditions for optimal continuum generation at long distance $D > 600$ m were also investigated from the long propagation of multi-terawatt laser pulses on a horizontal path, carefully measured as a function of the initial chirp of the laser pulse by Méchain et al. (2005a, 2004a). Fig. 97A shows the beam cross-section intercepted by a white screen and photographed with a digital camera. Comparison of the beam cross section at 1000 m for two values of the chirp (durations enlarged from 100 fs to 0.2 and 9.6 ps) shows a bright continuum generation for the smallest duration, without discernible hot spots, with a beam divergence of 1 mrad. For the longest duration, the whole beam profile is slightly compressed, and bright channels (which persists beyond 2350 m) were clearly observable. By means of closed loop optimizations relying on a genetic algorithm and a liquid crystal spatial light modulator, Ackermann et al. (2006b) recently reshaped spectral pulse components of the same terawatt laser and showed enhancement of the supercontinuum signal by a factor of 2 at a distance of 36 m.

Measurements of the length over which ionized plasma channels are formed have indicated no reliable evidence of ionization in the case of large negative chirps corresponding to an initial pulse duration of 9.6 ps (Méchain et al., 2005a). Multifilamentary structures were recorded step by step along the propagation path using well calibrated photographic paper. One series of photographic exposures recorded at four distances, 21, 50, 68, and 109 m is shown in Fig. 97 for a negative initial pulse duration of 1.2 ps. One can clearly observe in Fig. 97(a)–(c) the appearance of a number of high intensity channels that tend to appear on a ring at the periphery of the beam. This highly uneven intensity distribution of the beam intensity profile persists after a hundred meters of propagation (Fig. 4(d)). High intensity channels are also linked by an energy web organization. The ring like multi-filamentary structure was understood as an organized pattern rising on the ring profile resulting from the self-focusing of the diaphragmed beam (Méchain et al., 2004a).

Since only the bright channels giving rise to ionization generate continuum, these results showed that a small negative chirp is better suited for applications where the continuum emission must be maximized.

5.1.5. Control parameters for delivering high intensities at long distances

In order to obtain a filamentation starting at a specific distance for a given laser with initial peak power $P_{in} > P_{cr}$, several parameters can be modified: the initial diameter of the beam, its initial convergence (spatial phase) and its temporal phase.

Diameter and beam focusing. The filament is generated at the distance where the collapse of the beam should have occurred if no saturation mechanism prevented the growth of intensity. This location, L_c is given by formula (5) for a collimated beam. For a convergent beam, the lens transformation (6)—which is a property of the cubic nonlinear Schrödinger equation (Marburger, 1975)—can be used to determine the position $L_{c,f}$ of the collapse where filamentation starts. It is thus possible theoretically to place the beginning of the filamentation at several km, either by using a slightly divergent laser beam (with initial peak power above critical), or by using a large diameter beam. However, this simple model does not take into account group velocity dispersion, or the noninstantaneous Kerr effect. Due to GVD, for distances higher than a few hundred of meters, this model can give only a coarse estimate. The contribution of the delayed Raman–Kerr effect in the position of the collapse can be estimated by using a Marburger-like formula (Couairon, 2003c), which reads for a collimated beam:

$$L_c^{(\mathrm{RK})} = \frac{0.367 L_{\mathrm{DF}}}{\sqrt{[(\max_t (\tilde{P}_{\mathrm{in}}(t)/P_{\mathrm{cr}}))^{1/2} - 0.852]^2 - 0.0219}}, \tag{159}$$

where

$$\tilde{P}_{\mathrm{in}}(t) = P_{\mathrm{in}} \left[(1 - \alpha) \mathrm{e}^{-2t^2/t_p^2} + \alpha \int_{-\infty}^{t} \mathcal{R}(t - \tau) \mathrm{e}^{-2\tau^2/t_p^2} \, \mathrm{d}\tau \right] \tag{160}$$

and $\mathcal{R}(t)$ is the molecular response function (45).

A control of the beginning of filamentation induced by femtosecond laser pulses has been achieved in experiments by Jin et al. (2005) who showed that a change of both the laser energy and the beam divergence angle (via a deformable mirror) leads to a precise control of the beginning of filamentation. Liu et al. (2006e) used a telescope so as to enlarge both the input beam diameter and the size of the beam inhomogeneities. In this way, the authors have shown that it is possible to overcome the early self-focusing of the unavoidable hot spots present in a terawatt laser pulse. A simple formula predicting the location of the nonlinear focus when a telescope is used was derived by Fibich et al. (2006) and validated by experiments.

Temporal phase. The majority of ultrashort intense lasers rely on the chirped pulse amplification (CPA) technique, well-known in the radar field. In a CPA laser, the ultrashort pulse from the oscillator is initially stretched temporally by a factor 10^4 by means of two gratings which delay the blue spectral components of the laser compared to the red components. The pulse is then amplified, before being recompressed by a compressor made up again of a grating pair. This device, by decreasing the intensity peak of the pulse at the time of its passage in the amplifying stages, makes it possible to remain below the threshold for irreversible damage of the materials. By increasing the distance between the two gratings of the compressor (from a distance corresponding to an optimal compression), a negative frequency shift (chirp) can be added to the pulse, so that the blue frequencies of the laser spectrum are in the front part of the pulse and the red frequencies in the trailing part. During the subsequent propagation of the pulse, the group velocity dispersion of air delays the blue components compared to the faster red components, so that the pulse shortens and increases its intensity during the propagation as sketched in Fig. 98(a). Fig. 98(b) shows the validity of this concept. Measurements by Méchain et al. (2005a) have shown that the beginning of the filament could be adjusted between 10 m (compressed pulse with energy of 150 mJ) and 100 m (significant negative chirp).

It should be noted that the Kerr effect dominates dispersion for high powers. Typical values for the dispersive length in air $L_{\mathrm{GVD}} = t_p^2/2k''$, where t_p denotes the duration of the pulse, are $L_{\mathrm{GVD}} = 250$ m with $k'' = 0.2 \, \mathrm{fs}^2/\mathrm{cm}$ at 800 nm and $L_{\mathrm{GVD}} = 50$ m with $k'' = 1 \, \mathrm{fs}^2/\mathrm{cm}$ at 248 nm, both for $t_p = 100$ fs. Eqs. (159) for estimating the beginning of filamentation is therefore valid for any pulse with peak power leading to a collapse distance smaller than L_{GVD}.

Space–time compression. It is possible to merge the two preceding techniques. The diameter of the beam and its divergence are adjusted to obtain the collapse by self-focusing at the required distance. At the same time, a frequency chirp is added to the pulse, so that it compresses the pulse during its propagation to the expected collapse point. Since the self-focusing distance depends on the peak power which is increasing along the propagation distance due to temporal compression, the two compression phenomena in space and time are coupled. It is therefore necessary to evaluate the location of the collapse iteratively and to resort to a nonlinear propagation code in order to find the correct initial conditions, the only available theoretical estimation for the collapse position of a chirped pulsed beam in a dispersive self-focusing medium being valid for anomalous dispersion uniquely (Cao et al., 1994). In principle, It is also necessary
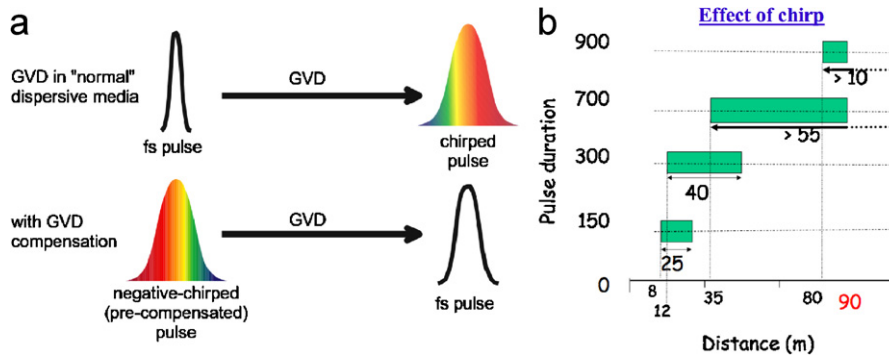
Fig. 98. (a) Principle of the GVD compensation. (b) Filamentation distance as a function of the duration of the laser pulse. The lengthening of the laser pulse is obtained by adding a negative chirp to the pulse. The optical Kerr effects dominates dispersion at high powers. From Méchain et al. (2005a).

to take into account the effects of atmospheric turbulence, and for vertical propagation, the variation of the atmospheric pressure with altitude. Lastly, the paramount importance of the quality of the input beam should be stressed.

5.1.6. Effect of air turbulence

A significant parameter for several applications is the precision of pointing of the filament. It is linked to the shot to shot reproducibility of the conditions for formation of multifilaments on the one hand, and to the effects of atmospheric turbulence on the other hand. Chin et al. (2002b) have reported fluctuations in the positions of the filaments of the order of the mm at a distance of 105 m. The dispersion of the impact points was attributed to air turbulence. Rigorously, it would be necessary to dissociate the effects of shot to shot fluctuations of the beam from the effects of air turbulence. It is also significant to distinguish the effects of air turbulence before and after filamentation. If a filament was a propagating soliton-like object, the reduced size of the filaments would make them rather insensitive to air turbulence because the scale of viscous dissipation (small scale in the Kolmogorov spectrum) is large compared to the transverse dimension of the filaments. Since the filament is continuously rebuilt by the reservoir, a phase distortion in the reservoir could impact the filament at any propagation distance, i.e. not only in its early stage but also when the filament is already formed. In the latter case, these distortions may stop the energy flow which is feeding the filament and expectedly cause a jump of the filament position within the beam. A good precision in the pointing of the filament can however be expected provided the filament is formed in a well controlled atmosphere, safe from air turbulence, before it is launched in free air. Recent experiment by Ackermann et al. (2006a) tend to confirm this point. They have shown that the generation of a filament from an ultrashort laser pulse is possible even if the beam propagates through strongly turbulent regions, with structure parameters C_n^2 exceeding by five orders of magnitude those corresponding to standard atmospheric conditions. The position of filaments within the beam is largely insensitive to the interaction with a turbulent region, Kerr-induced refraction index gradients prevailing over the turbulence-induced refractive-index gradients by 2 orders of magnitude.

5.1.7. Optimization of the length of the plasma channel

If an uninterrupted column of plasma is required over a large distance, it is useful to consider the type of laser pulses to be used.

Duration of the laser pulse. A first question concerns the optimal duration of the input laser pulse, for a given pulse energy. A long pulse causes losses by inverse Bremsstrahlung (absorption of the beam energy by the generated plasma). This leads to an exponential increase in the plasma density. When the plasma density approaches the critical density $\rho_c = 1.7 \times 10^{21}$ cm^{-3} at 800 nm, the trailing part of the pulse is strongly absorbed and reflected. This effect is well-known since the advent of powerful lasers; it is at the origin of damage in solids and dielectric breakdown of air. With very short pulses, the pulse dynamics in the filament yields higher intensities, which increase the losses per unit of length due to multiphoton absorption. Thus, an optimal duration exists between these two extreme cases. Fig. 65 illustrates this optimum with numerical results obtained from a semi-analytical model by Couairon (2003b), for pulses at 800 nm. The largest length L_{fil} of an uninterrupted plasma channel that a filament can generate by using

all the available energy in the laser pulse is shown for three values of the pulse energy [Fig. 65(A)]. The maximum length $L_{\max}$ and the corresponding optimal pulse duration are reported in Fig. 65(B). It is seen that with a multiterawatt femtosecond laser, it is advantageous to lengthen the duration of the laser pulse up to a few tens of picoseconds, for example by adding a strong frequency chirp to the pulse. The price to be paid is the reduction in the density of free carriers [Fig. 65(C)].

Beam convergence. By using a telescope, Fibich et al. (2006) have shown that the filamentation length increased with the collapse distance. This suggests that the convergence angle at the onset of collapse is worth to be considered as a control mechanism for the filamentation length. Since a telescope also modifies the beam width, this method may be combined with a mechanism for controlling the collapse distance so as to simultaneously control the distances where the plasma channel starts and ends.

Laser wavelength. The wavelength of the beam is another significant parameter to maximize the length of the conducting filament. For long pulses, the losses are determined by inverse Bremsstrahlung (energy acquired by the free electrons in the presence of the laser field). These losses are expressed in the form (Raizer, 1965, 1966):

$$\frac{\mathrm{d}E}{\mathrm{d}t} = -\frac{e^2 \nu_{ei}}{2\pi^2 \epsilon_0 m_e c^3} I \lambda^2, \tag{161}$$

where $\nu_{ei} = \tau_c^{-1}$ is the collision frequency between electrons and ions. It is thus interesting, because of the factor $I\lambda^2$ to decrease the wavelength of the laser in order to decrease the losses by plasma absorption. The formation of filaments in air was shown to occur at 248 nm (Tzortzakis et al., 2000b, 2001b; Schwarz et al., 2000). The higher limit of the pulse duration, for which the losses by inverse Bremsstrahlung remains negligible was estimated by Schwarz and Diels at 60 ns for an ultraviolet pulse at 248 nm, with an intensity in the filament of 5×10^{11} W/cm^2, which would lead to a length of about 1 km for the plasma column (Schwarz and Diels, 2001). It is necessary to remain careful on these estimates because they rely on a simplified semi-empirical model combined with a variational method as presented in Section 2.4.3, which assumes a prescribed beam shape along the propagation and does not take into account possible temporal breakup that was predicted to occur from numerical simulations with such long pulses in the presence of noise (see Niday et al., 2005, and Section 3.2.2 for details). It seems nevertheless advantageous to use UV laser pulses in order to generate a long conducting plasma column.

5.1.8. Optimization of the electric conductivity of the plasma

The conductivity of the plasma generated by ultrashort IR laser pulses at long distances (> 100 m) may be poor, for at least two reasons. On the one hand, the density of the plasma decreases, initially by fast recombination of the electrons on the parent ion, then exponentially by capture of the residual free electrons on oxygen molecules, with a decay constant of about 130 ns. Taking into account the propagation velocity of light (30 cm/ns), the decrease of the plasma density limits the length of plasma channels to a few tens of meters, at best, if a short pulse is used (with duration smaller than a ns). In addition, the studies carried out up to now with a collimated beam when $P_{\mathrm{in}} \gg P_{\mathrm{cr}}$, indicate the formation of a great number of filaments, probably disconnected along the propagation axis, separated transversally and longitudinally by domains of nonconducting air, which gives place to a high electric resistance.

In order to improve the conductivity of the plasma channel, several approaches can be investigated. The first approach consists in using very intense UV pulses and lengthening the duration of the pulse. The results obtained up to now in the laboratory indicate that UV filamention gives rise to a longer and more conducting plasma column than that obtained with an IR laser (Tzortzakis et al., 2000b, 2001b; Schwarz et al., 2000). A second approach consists in reducing the capture of the electrons by the oxygen molecules. This can be done by simultaneously propagating an intense laser beam, which detaches the electrons of the negative oxygen O_2^- ions. According to Zhao et al. (1995a), a laser intensity of 7×10^5 W/cm^2 at the wavelength of 532 nm (second harmonic of a Nd:YAG laser) with a pulse duration of 50 µs is sufficient to balance the rates of attachment of free electrons in air and detachment by laser (see also Lu et al., 2004). By using this idea, Méjean et al. (2006) have recently shown that a visible nanosecond laser propagating with a fs pulse reduces by 5% the breakdown voltage for triggering and guiding a megavolt discharge over laboratory scales. Another possibility would consist in propagating an intense electromagnetic field of low frequency. A micro wave field of 3×10^4 W/cm^2 would be sufficient to improve the conductivity of the plasma generated by the filament. This evaluation is based on the breakdown threshold of nitrogen at 700 Torr, about 10^3–10^4 V/cm at a frequency of 2.8 GHz (Raizer, 1997). Experiments in a static electric field show that the threshold to trigger a guided electric discharge by
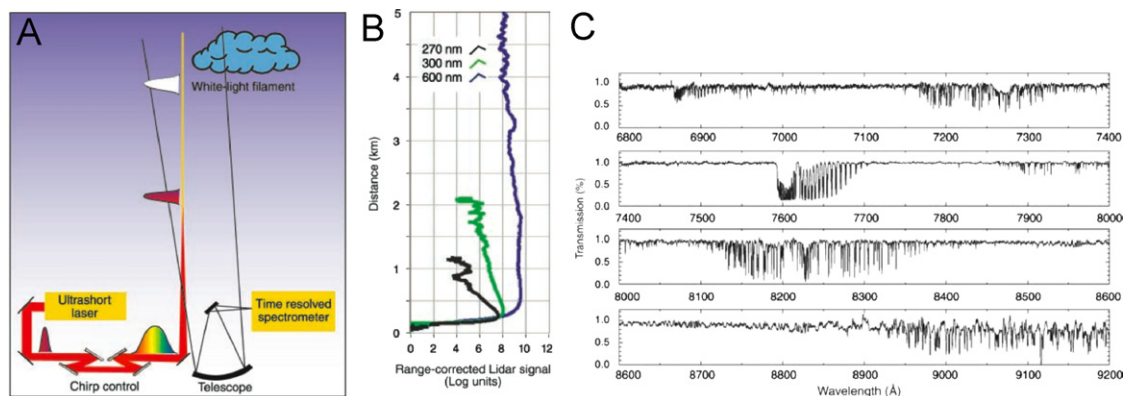
Fig. 99. White light LIDAR. (A) Schematic of the LIDAR experimental setup. Before launch into the atmosphere, the pulse is given a chirp, which counteracts GVD during its propagation in air. Hence, the pulse recombines temporally at a predetermined altitude, where white light continuum is produced, and then is backscattered and detected by LIDAR. (B) Vertical white light LIDAR profile at three wavelengths: 270 (third harmonic), 300, and 600 nm. (C) High-resolution atmospheric absorption spectrum from an altitude of 4.5 km measured in a LIDAR configuration. From Kasparian et al. (2003).

a multifilamentary beam is reduced by a factor of 30% compared to the threshold of spontaneous triggering. A sustained discharge can thus be expected, which could persist between two laser pulses. At the present time relatively compact microwave generators delivering powers in the MW range are available.

5.2. Applications of femtosecond filamentation

5.2.1. White light continuum light detection and ranging techniques (LIDAR)

The strong white light continuum generated by a filament in air can be exploited for remote atmospheric diagnostics (Rairoux et al., 2000; Matvienko et al., 2003; Kasparian et al., 2003). Among the most attractive features of this promising method for analyzing air pollution, one should note its capability of providing 3D-range resolved measurements of concentrations of gaseous and solid particles in a single shot (Frejafon et al., 1998). Filament based LIDAR techniques are advantageous with respect to conventional LIDAR techniques since the entire spectrum can be acquired in one shot, while by conventional LIDAR, a tunable source must be used so as to scan the wavelength.

The principle of a LIDAR technique based on the white light continuum is shown in Fig. 99A. The long-range colli-mated white light filaments have several favorable characteristics. The broad spectrum covers most of the visible and part of the IR wavelengths. The retro-diffused track of the white continuum can be detected at distances exceeding 10 km (Wöste et al., 1997). Méjean et al. (2003) reported a 10-fold enhancement of the infrared signal backscattered from the atmosphere compared with that expected using conventional LIDAR, which suggests a more efficient frequency conversion into the infrared (7% into the 1–1.5 μm band) under long-distance propagation conditions. This backscat-tered signal can be spectrally and time resolved, allowing a single shot multi-species analysis at different altitudes. Fig. 99B shows an example of the strong backward signal detected at three wavelengths as a function of altitude. The measurements exhibit a rich spectrum (see Fig. 99C) where the absorption lines represent rotovibrational progressions of highly forbidden transitions of O_2. All these lines can be very well fitted with a HITRAN code. Since the magnitude of the vapor lines depends on the local humidity and the width of the oxygen lines on the temperature, these measurements offer a meteorological diagnostics (Bourayou et al., 2005). White light LIDAR might also simultaneously yield wind profiles through the measurement of Doppler shifts. The experimental data also revealed lines that are not tabulated in the database, highlighting the high resolution of this technique.

Filament based LIDAR should allow the detection of pollutants in the atmosphere. A special class of pollutants is aerosols, particularly because they can carry bio-agents. By using a multispectral LIDAR technique, interesting preliminary results on the remote identification of bio-simulants were obtained (Méjean et al., 2004; Kasparian et al., 2003). The high peak power of the fs pulses offers the possibility of retrieving the abundance, particle size, refractive index, and composition of aerosols by generating nonlinear effects directly inside the aerosol particles and recording the backscattered multiphoton-excited fluorescence signal. Remote identification at a distance of 50 m of

clean and contaminated water particles was demonstrated by producing a controlled distribution of water droplets of about 1.5 μm diameter in an open cloud chamber. The droplets were doped with the biosimulant riboflavin, which exhibits a characteristic fluorescence emission around 540 nm. When the cloud was illuminated with adequate peak power (250 GW), a two-photon excited fluorescence signal emerged from the riboflavin-containing droplets, allowing unambiguous identification of the signature of the biosimulant. This result demonstrated the ability of white light continuum nonlinear LIDAR (Faye et al., 2001) to distinguish bio-aerosols from natural background aerosols of the same size.

5.2.2. Atmospheric applications

Plasma channels generated by filamentation provide the opportunity to detect supersaturation of the atmosphere directly. Supersaturation refers to an atmosphere in which water vapor has not condensed to form clouds, despite favorable thermodynamic conditions (humidity, temperature, and pressure) that imply condensation at equilibrium. Condensation requires sufficient natural or artificial nucleation germs, for example heavy molecules such as AgI. Charges induced by laser filaments can serve as nucleation germs instead of the natural ionizing radiation from a radioactive source. Experiments by Kasparian et al. (2003) have shown that supersaturated water vapor nucleates and condensates around the charges generated by fs laser pulses sent into a fog chamber. Strong droplet formation was observed inside the chamber after each laser shot. This result demonstrates the possibility of creating laser-induced nucleation germs at distances that can be controlled by the laser chirp. The ability to determine by remote probing whether the atmosphere is supersaturated is of great importance for the prediction of rain, hail, or snow.

The lidar technique using the supercontinuum generated by the filamentation of femtosecond pulses during their vertical propagation in the atmosphere was recently used to analyze both the clouds (droplet size distribution and number density) and the thermodynamical properties of the atmosphere in their vicinity, such as the temperature and relative humidity (Bourayou et al., 2005). Both of these measurements can be performed in a simultaneous operation since they use the same laser source equipped with suitable diagnostics for imaging and spectral analysis. These results open the way to a multiparameter analysis of the cloud microphysics by combined white-light differential absorption and multi-field of view lidar. Routinely obtaining data about the cloud microphysics would be of high relevance for atmospheric modeling, especially considering the two-dimensional and three-dimensional mapping capability of lidar.

Femtosecond laser-induced nonlinear molecular spectroscopy was applied for sensing atmospheric greenhouse gas methane (Xu et al., 2006a). Inside the filaments, the pollutants are dissociated into small fragments, which emit characteristic fluorescence. The analysis of the pollutant concentration was performed from direct measurements of the characteristic spectral lines. Relying on the possible generation of filaments at kilometric distances, this technique may find future applications in the remote analysis of hazardous or unreachable spots, such as deep mine wells, or chemical leakages (Xu et al., 2006a, b). The feasibility of this technique was also shown by recording the nonlinear fluorescence spectra of ethanol molecules induced by ultra-fast fs laser pulses, used as a fingerprint for their detection in air (Luo et al., 2006).

5.2.3. Virtual antenna

It is interesting to see if the plasma columns generated by filamentation are able to act as virtual emitting antennas. Such antennas would be furtive and easily deployable. They are expected to radiate electromagnetic pulses over a broad frequency band. The electromagnetic emission from a plasma column was investigated by using a reception antenna active in the region 10 kHz–30 MHz (Méchain et al., 2005c). The plasma was generated by a CPA laser system emitting pulses at a repetition rate of 10 Hz. Each pulse had duration of 100 fs and energy of 200 mJ for a beam diameter of 5 cm. The power of 2 TW exceeds the critical power for filamentation by a factor 400. Under such conditions, a large number of filaments are generated in air. In order to group these filaments into a single conducting channel, the beam was focused with a reflective telescope to a distance of 30 m. About 20–30 grouped filaments were then observed, starting at a distance of 20 m from the focusing mirror. The length of 10–15 m for the conductive air region was measured by the electric technique described in Section 4.1.11.

A difference of potential of 12 kV was then applied to a portion of the plasma column. This was performed with two charged metal electrodes with circular holes to let the beam pass through, as shown in Fig. 100(a). The first electrode was placed a few meters after the beginning of the plasma, the second electrode 81 cm further away. The reception antenna was placed to a distance between 1 and 8 m in a direction perpendicular to the filament axis and was directly coupled to an oscilloscope with a 50 Ωm resistance. Results are shown in Fig. 100(b). The signal corresponds to the
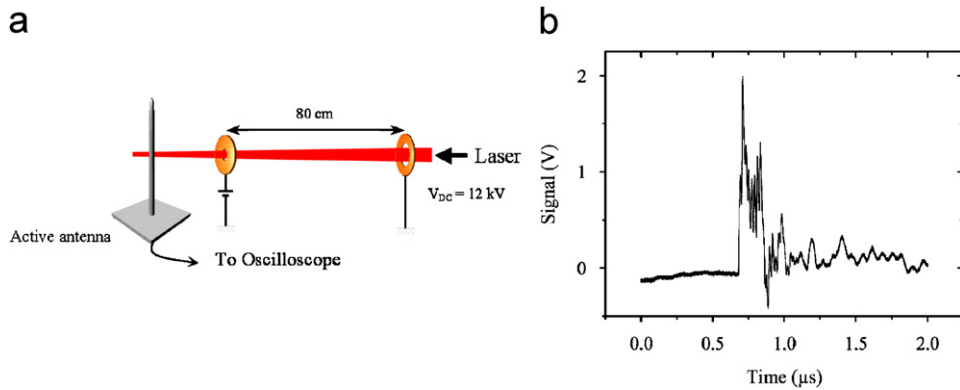
Fig. 100. (a) Experimental set up to measure the radiation at long wavelength from a plasma column in air (see text for details). (b) Signal detected by an antenna active between 10 kHz and 30 MHz. The signal corresponds to the average of 8 successive recordings. From Méchain et al. (2005c).
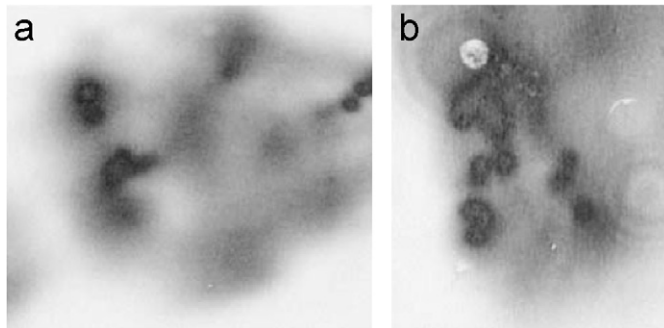
Fig. 101. Single-shot beam impacts on photosensitive papers after 75 m propagation in (a) dry air and (b) rain. The air pressure is 0.67 atm (altitude 3230 m). Filaments are clearly visible in both cases. The ring patterns on the profile in rain are due to the diffraction of the beam on the rain droplets.

average of 8 successive shots. The signal starts with a set of high frequency oscillations, with a periodicity on the order of 140 ns. This corresponds to a frequency above the receiving bandwidth of the antenna. It is followed by a set of 9 oscillations at lower frequency with a periodicity comprised between 1 and 2 µs, corresponding to a frequency around 14 MHz. Note that the tuning frequency is 92 MHz for a 81 cm long $\lambda/4$ antenna, and around 10 MHz for a 10 m long antenna. These results show that the plasma column can indeed emit EM pulses of relatively long wavelengths, of the order of a few tens of meters.

5.2.4. Propagation in adverse conditions

Méchain et al. (2005b) have studied the propagation of filaments under rainy conditions. At altitude of 3200 m, the rain was composed of drops with a diameter less than 0.5 mm, and a concentration of $1.7 \times 10^4 \, \mathrm{m}^{-3}$. This gives a linear extinction of $\alpha = 6.6 \, \mathrm{km}^{-1}$ which corresponds to a transmission of 37% after 150 m propagation. With a beam diameter of 3 cm, the beam encounters a drop every 3 cm. As can be seen in Fig. 101, no significant change is visible between filamentation in dry air or in rain. Multifilaments have been observed up to 150 m, the maximum available horizontal distance of propagation.

This phenomenon is explained by the regeneration process as described in Sections 3.2.7 and 4.1.16. Filaments are easily reborn provided the energy reservoir has a corresponding power above critical. Kandidov and Militsin (2006) have shown from numerical simulations that coherent scattering on water particles initiates filament generation.

5.2.5. Lightning protection

The generation of a laser lightning rod was proposed in the seventies and considerable effort has been devoted to achieve this spectacular goal. Schemes that rely on high energy, long laser pulses, such as those produced by large CO_2 or Nd:glass laser systems, have been studied for a number of years now (Wang et al., 1995; Shindo et al., 1993;
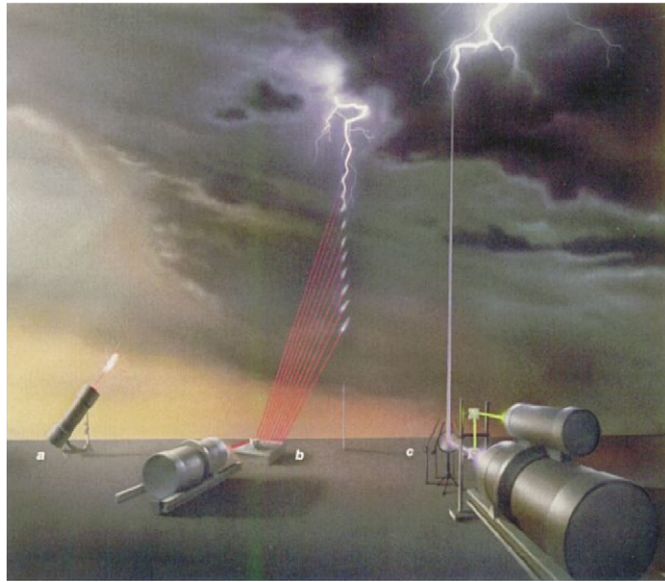
Fig. 102. Artistic view of possible scheme to trigger and guide lightning with a laser. (a) powerful long laser pulse induce a plasma ball at a finite propagation distance. (b) Dashed lightning rod made up of a collection of plasma balls generated by successive long laser pulses. (c) Potential straight lightning rod from earth to cloud generated by a filamenting ultrashort laser pulse. From Diels et al. (1997).

Miki et al., 1993, 1996). Although significant progress was achieved using such long laser pulses, or even ultraviolet lasers (Miki and Wada, 1996), the propagation of these laser beams over a long distance is problematic because electron avalanches have time to develop during the pulse and discrete plasma balls are formed. As a consequence, the air becomes opaque to laser light and the propagation of the laser beam is significantly perturbed (Fig. 102(a,b)).

The results described in Section 4.2.14 where filaments are shown to trigger and guide electric discharges in the laboratory and the potential long distance propagation of filamenting ultrashort laser pulses suggest an interesting alternative to realize a lightning rod (Zhao et al., 1995a; Zhao and Diels, 1995; Diels et al., 1997; Chin and Miyazaki, 1999). The hope is to use the plasma column to divert and guide a leader in the atmosphere and to bring it to a conventional rod (Fig. 102(c)). However, a scheme which would rely solely on the electric conductivity of the plasma column would be hopeless. Indeed, the plasma lifetime is a few ns (see Section 4.1.8) allowing for an effective electric path of a few meters only. On the other hand, the thermal induced triggering shown to be effective in the laboratory gives more hope (Tzortzakis et al., 2001c; Comtois et al., 2000). The thermal induced depression is expected to last for several hundreds of ns and therefore can give a preferential path for an electric discharge of several hundreds of meters. To date, no experimental evidence has been obtained for the feasibility of earth–cloud filament based lightning protection, the largest electrode gap in the laboratory being 4 m (Comtois et al., 2000; Pépin et al., 2001; Rodriguez et al., 2002; Ackermann et al., 2005). Recent experiments have shown that filaments generated by ultrashort laser pulses are transmitted through a dense water cloud filling an electrode gap of 1.2 m, and ionize a continuous plasma channel. The cloud typically reduces the discharge probability (by 30%, for given experimental conditions) but has almost no influence on the threshold required to trigger single discharge events, both in electrical field and laser energy (Ackermann et al., 2004).

It was speculated that in order to achieve a lightning rod with a laser filament, the attachment of free electrons in air must be counterbalanced by the detachment of the electrons of negative oxygen O_2^- ions obtained by copropagating an intense and longer laser pulse with the filamenting ultrashort pulse (Zhao et al., 1995a). A 50 µs, 532 nm laser pulse with an intensity of $7 \times 10^5 \, W/cm^2$ should make this scenario feasible.

5.2.6. Generation of single cycle pulses and high order harmonics

In recent years, considerable progress have been made in the production of ultrashort coherent optical pulses below the fs limit. Attosecond pulses are important tools for studying and controlling the motion of electrons inside atoms and molecules. Well controlled extreme ultraviolet pulses with a duration as short as 120 as have been reported

(Sansone et al., 2006). The key to accessing the attosecond domain is high-harmonic generation in a noble gas jet starting with an intense infrared fs pulse. The high-order harmonic spectrum has a very characteristic and universal shape: it falls off for the first few harmonics, then exhibits a plateau where all the harmonics have the same strength, and ends up with a sharp cut-off (Krause et al., 1992). One can understand the high-order nonlinear response of an atom by considering the following three steps (Corkum, 1993; Kulander et al., 1993): ionization, acceleration and recombination. The successful generation of isolated attosecond pulses is an important step towards attosecond physics since single attosecond pulses are more promising for applications in time resolved spectroscopy. Obtaining single pulses remains an important problem.

In order to produce isolated reproducible attosecond pulses, the primary IR pulse must have some specific charac-teristics. The linearly polarized fundamental pulse must have a few optical cycles (duration shorter than 7 fs) such that the emission of the cut-off harmonics (i.e., the highest harmonics which can only be emitted at the peak intensity) is naturally confined to a fraction of the laser oscillation period at the peak of the pulse. The peak intensity must be of the order of 10^{15} W/cm^2. Finally, the phase of the carrier must be locked to the maximum of the pulse envelope (Brabec and Krausz, 2000). The HHG pumped by an ultrashort (7 fs) laser pulse has led to an isolated 650 attosecond pulse (Hentschel et al., 2001). Up to now, few cycle IR pulses with the requested properties have been obtained by sending a 30 fs pulse in a long hollow fiber filled with a noble gas. The pulse was then recompressed, further amplified and CEO locked (Nisoli et al., 1997). Only very few laboratories are able to master this elaborate technology. Filamentation offers a considerable simplification. As shown in Sections 3.2.4 and 4.1.5, self-compression induced by filamentation allows obtaining pulses of a few fs duration without the need of a precise alignment in long hollow fibers. Hauri et al. (2004) have shown that in addition to a short pulse, filamentation yields a beam of excellent mode quality and surprisingly, preserve an initial CEO locking. Several groups report that more than 60% of the incident energy is contained in the pulse emerging from the filament (Hauri et al., 2004, 2005; Stibenz et al., 2006). However, simulations predict that only a fraction of this energy should be contained in the single cycle pulse with 100 μm diameter, 3 fs duration and an intensity clamped to a maximum value of a few 10^{14} W/cm^2 (Couairon et al., 2006a, 2005a). The question of the influence of the spatial wings and temporal pedestals is therefore still open.

Besides this fundamental aspect whose understanding should lead to energy upscaling of the single cycle pulses produced by filamentation, the generation of high harmonics in noble gases from a filament has been demonstrated from experiments and simulations (Tamaki et al., 1999, 2000; Tosa et al., 2003; Takahashi et al., 2003). In a 30 Torr Neon gas, it was shown that a phase-matched propagation of harmonics over 7 mm magnifies the conversion efficiency around the 49th harmonic (in the cutoff region) by 40 times and by more than 100 times in the cutoff region corresponding to a few nJ per high-harmonic pulse in the 76 eV region (Tamaki et al., 1999). In argon, the efficiency and spatial quality of high-order harmonics could be simultaneously optimized by controlling the interaction length and the gas density. A Gaussian profile with beam divergence of 4.5 mrad full width at $1/e^2$ maximum was produced at the 29th harmonic, without any surrounding spatial structures, by phase-matched propagation in 20 Torr, 10 mm thick argon gas (Tamaki et al., 2000). In Xenon, a filament was generated for experimental conditions ensuring the formation of a leaky waveguide with a prevailing influence of ionization in forming the guiding structure (Tosa et al., 2003). In turn, the self-guided beam ensured phase matched high harmonics generation over several typical characteristic absorption lengths, which allowed enhancement of the harmonic yield. These results keep open the possibility of increasing the output energy in the sub-fs pulse by using larger input energies. According to Shon et al. (2001), the generation and propagation of high-order harmonics by intense, ultrashort laser pulses in argon gas cells can be used for generation of a train of subfemtosecond pulses. Shon et al. (2001) have also shown that HHG obtained in bulk media, even by a short 5-fs laser driver, is not favorable for single attosecond-pulse generation, in contrast with HHG produced in a gas-filled hollow waveguide which exhibit a quasi-continuous spectrum. Recently, the generation of isolated attosecond pulses from self-compressed filaments via recombination of a selected range of high harmonics was predicted by Chakraborty et al. (2006).

Another way to generate harmonics was explored from a pulse whose polarization changes with time (Corkum et al., 1994; Ivanov et al., 1995; Antoine et al., 1996). HHG efficiency is the highest for linearly polarized pump pulse and rapidly decreases with increasing pump pulse ellipticity (Budil et al., 1993; Dietrich et al., 1994). Temporal modulation of pump pulse ellipticity confines the xuv emission to a temporal gate where the polarization is very close to linear (Altucci et al., 1998). In this scheme, single attosecond pulses and xuv supercontinuum are produced in the high-order harmonic plateau. The reader is referred to Huo et al. (2005, and references therein) for the generation of ellipticity time-gate.
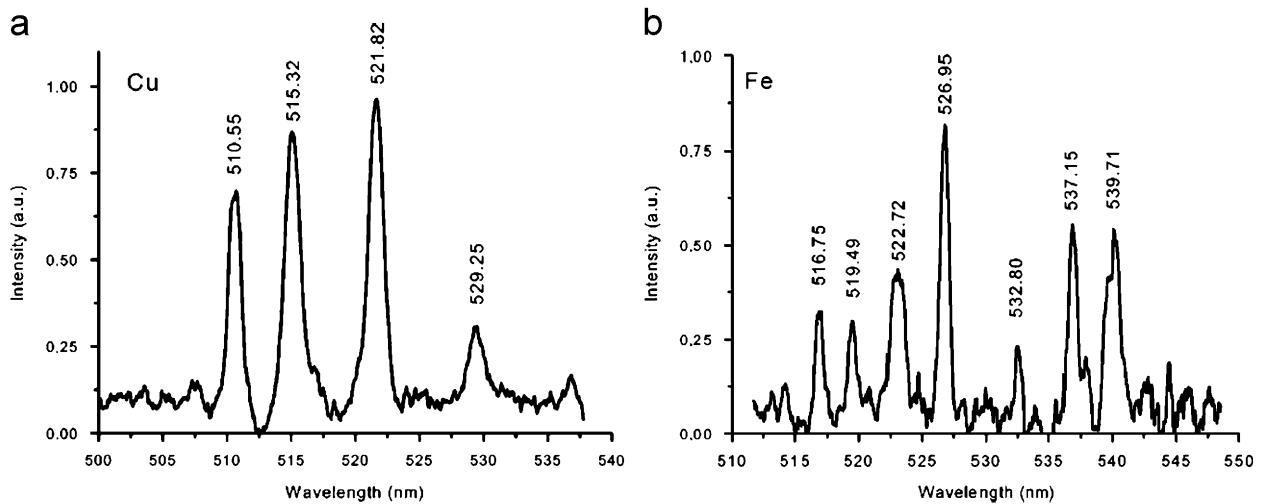
Fig. 103. LIBS spectra of copper (a) and steel (b), measured at 90 m distance (Stelmaszczyk et al., 2004).

5.2.7. Laser induced breakdown spectroscopy (LIBS)

The ability of filaments to achieve very high light intensities over long distances can be used for the analysis of remote solid targets using the laser induced breakdown spectroscopy (LIBS) technique. A plasma plume is produced by the absorption of the intense laser pulse on the vicinity of the surface. The ablated material consists of ions, atoms and molecules in an excited state. An analysis of the luminescence of the plasma gives information on the composition of the target. Stelmaszczyk et al. (2004) and Rohwetter et al. (2004, 2005) have demonstrated this technique by recording atomic lines of copper and steel at a distance of 90 m (see Fig. 103).

Tzortzakis et al. (2006a) have recently demonstrated that remote LIBS using ultrashort UV laser filaments in air has considerable potential in the remote monitoring of cultural-heritage-related items. Intensity clamping inside filaments provides ideal conditions for rapidly mapping large monuments. The small radial dimensions of filaments together with the limited plasma plume created on the surface of the target guarantee minimal invasion. This technique could find other applications, such as surveying contaminated industrial wasteland or the characterization of industrial scrap material.

5.2.8. Applications in solids

A subject of great interest for its applications in buried guiding structures is the role of filamentation during the writing of permanent index changes of glasses. Damage of dielectrics caused by ultrashort laser pulses can be exploited to produce laser devices such as waveguides (Davis et al., 1996) and gratings in the bulk of the material, arrays of damage dots for all optical memories with high data storage density (Glezer et al., 1996), longitudinal grooves forming waveguides (Homoelle et al., 1999; Schaffer et al., 2001a), or arrays of parallel grooves to form transmission gratings (Kondo et al., 1999; Sudrie et al., 1999). Understanding in detail the mechanisms of laser–solid interaction leading to damage in the bulk of dielectrics therefore became an essential issue. The fabrication of buried optical elements necessitates a pulse with well controlled intensity and beam size at a specific tunable depth. Such characteristics are provided by self-guided pulses through the filamentation process. The most interesting buried structures are obtained when the index of the medium is permanently modified (increased usually) without the occurrence of permanent structural damage. Several groups have reported that filamentation is responsible for the writing of good waveguides in fused silica. Sudrie et al. (1999) have shown that permanent index changes without damage occur during filamentation with a weakly focused infrared laser beam. Yamada et al. (2001) have achieved efficient waveguides via filamentation. By translating the sample, a permanent waveguide over a length of 2 mm could be written with excellent quality. The permanent buried waveguides are able to trap light (see Fig. 104). By preparing a set of adjacent buried waveguides, it is possible to make a transmission grating buried in the bulk of a transparent material. Such buried waveguides can show interesting properties (Sudrie et al., 1999).
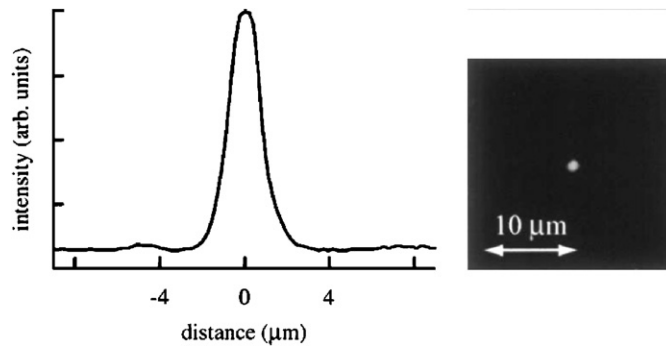
Fig. 104. Waveguide output profile at 633 nm. A near-field image is shown on the right-hand side. From Yamada et al. (2001).

5.2.9. Power supply for high speed electric vehicles

During filamentation of intense femtosecond laser pulses in air, a long low density plasma column is created. It has been demonstrated that this plasma column is able to trigger and guide high voltage electric discharges over a distance of several meters in air (see Section 4.2.14). This effect is attractive for potential applications such as the contactless conduction of current in high-speed vehicles. It is well known that the mechanical friction between the pantograph and the voltage line becomes a major obstacle at reaching still higher speed. A crucial requirement for such applications is the resistivity of the produced plasma, which must remain low in order to minimize unwanted power dissipation. Other important questions concern the amount of current such a discharge is able to carry, and the plasma lifetime, which ideally should be long enough so that the plasma column is sustained between successive laser shots even at a low repetition rate. In order to address these questions, experiments have been performed using the teramobile laser in conjunction with electric power facilities designed to supply the motors of high-speed trains (TGV) (Houard et al., 2007b).

The laser beam of the teramobile (200 mJ, 100 fs, 10 Hz) was focused in air with a telescope of 15 m focal length. This led to the formation of a bundle of about 40 plasma filaments over a distance of ~ 10 m. Two electrodes consisting of cylindrical copper blocks of 5 cm diameter were placed 5 m beyond the beginning of the filaments. At this point the diameter of the filament bundle was ~ 5 mm. It crossed through a 5 mm diameter hole pierced in the first electrode and impinged on the second electrode. The distance between the two electrodes could be varied between 3 and 60 mm. In some experiments, both electrodes were pierced, letting the filament bundle through, with no significant change in the results. The electric voltage applied across the electrodes was either DC voltage up to 6 kV or AC up to 20 kV. In all measurements, we checked that no spontaneous discharge occurred in the absence of a laser pulse. The current flowing through the plasma when triggered by the laser generated filaments was measured with a Hall probe.

In the case of a 4 kV DC voltage, the results are shown in Fig. 105. One notices a sudden drop (within the detection resolution) of the voltage across the electrodes while simultaneously the current reaches 250 A, the maximum value allowed by the power supply. The total ohmic resistivity of the plasma was found lower than $0.01\,\Omega/cm$. This value is much lower than the resistivity obtained when spontaneous arcing is produced between the electrodes. This high conductivity can last for several seconds, even when triggered by a single laser shot, but sometimes led to a partial melting of the electrodes.

Experiments were also successful with AC voltage. Fig. 105(b) shows the current flowing through the electrodes with a peak voltage of 20 kV. The 50 Hz alternative peak current was again limited by the power supply. The high conducting discharge could be obtained over a distance of 4 cm, with a peak current again limited by the power supply.

The plasma generated by femtosecond laser filaments has therefore a low resistivity, and it is able to carry a large current, either DC or AC over a long time > 1 s. These features are very promising for applications such as the contactless capture of current.

5.2.10. Propulsion

Filamentation was recently demonstrated to be able to continuously propel a paper airplane without complicated focusing optics (Zheng et al., 2005). The maximum coupling coefficient generated by the plasma channel was found to
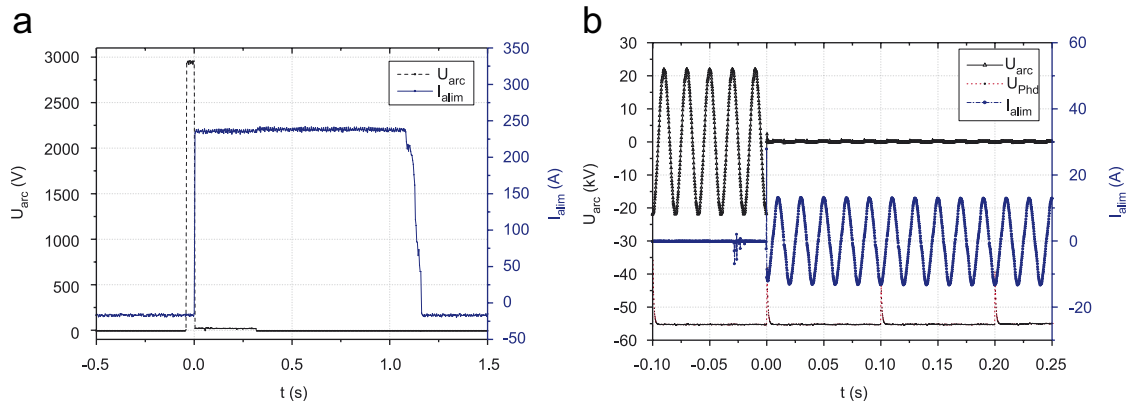
Fig. 105. (a) Voltage (dotted line) and current flowing (continuous line) between the two electrodes. The voltage is applied at $t = 5.5$ s during 1 s. The current discharge is triggered by the filaments.(b) Applied AC voltage (in kV units) and current flowing between the electrodes. The photodiode signal (U_{PhD}) also gives the arrival time of the laser pulse on the electrode (at 1.05, 1.15 and 1.25 s).

be more than 8.5 dyne/W. In contrast with longer (ns) pulses which can be used to achieve propulsion by ablating the target material, filament base propulsion relies on the generation of a detonation wave associated with ionization of air, which acts as a propulsive source. Plasma channels generated by femtosecond filaments are promising to realize a long propulsion in the atmosphere where a very long distance propulsion with high coupling coefficient could be expected.

6. Conclusion

Most aspects of the physics of femtosecond filamentation in the laboratory are well understood and can be well modeled in many cases. The universality of the phenomenon of filamentation, occurring in gases, transparent solids and in liquids has led to numerous experimental and theoretical works in various conditions. While the agreement between simulations and experiments is often very satisfactory, a complete and coherent interpretation of all phenomena associated with filamentation of ultrashort laser pulses (conical emission, pulse splitting, generation of THz radiation…) is still under construction.

Concerning outdoor filamentation, the formation of filaments was announced at a distance of the order of the kilometer. It is however useful to insist on the fact that up to now, no serious characterization of these filaments over long distances has been carried out except by Méchain et al. (2004a, 2005a). In particular, the intensity or even the remaining energy in the beam at these distances still constitute lacking data. Moreover, at the present time there are very few realistic numerical simulations for filamentation over long propagation distances. This field remains thus largely to be investigated.

Finally, we would like to mention a few review papers on filamentation which are complementary to ours (Couairon and Mysyrowicz, 2007, 2006; Chin et al., 2005; Aközbek et al., 2005; Sprangle et al., 2002).

Acknowledgements

References

Abramowitz, M., Stegun, I.A., 1972. Handbook of Mathematical Functions. Dover, New York.

Ackerhalt, J.R., Milonni, P., 1986. Solitons and four wave mixing. Phys. Rev. A 33 (5), 3185–3198.

Ackermann, R., Méchain, G., Méjean, G., Bourayou, R., Rodriguez, M., Stelmaszczyk, K., Kasparian, J., Yu, J., Salmon, E., Tzortzakis, S., André, Y.-B., Bourrillon, J.-F., Tamin, L., Cascelli, J.-P., Campo, C., Davoise, C., Mysyrowicz, A., Sauerbrey, R., Wöste, L., Wolf, J.-P., 2005. Influence of negative leader propagation on the triggering and guiding of high voltage discharges by laser filaments. Appl. Phys. B 82 (4), 561–566.

Ackermann, R., Méjean, G., Kasparian, J., Yu, J., Salmon, E., Wolf, J.-P., 2006a. Laser filaments generated and transmitted in highly turbulent air. Opt. Lett. 31 (1), 86.

Ackermann, R., Salmon, E., Lascoux, N., Kasparian, J., Rohwetter, P., Stelmaszczyk, K., Li, S., Lindinger, A., Wöste, L., Béjot, P., Bonacina, L., Wolf, J.-P., 2006b. Optimal control of filamentation in air. Appl. Phys. Lett. 89, 171117.

Ackermann, R., Stelmaszczyk, K., Rohwetter, P., Méjean, G., Salmon, E., Yu, J., Kasparian, J., Méchain, G., Bergmann, V., Schaper, S., Weise, B., Kumm, T., Rethmeier, K., Kalkner, W., Wöste, L., Wolf, J.-P., 2004. Triggering and guiding of megavolt discharges by laser-induced filaments under rain conditions. Appl. Phys. Lett. 85 (23), 5781–5783.

Aközbek, N., Becker, A., Chin, S.L., 2005. Propagation and filamentation of femtosecond laser pulses in optical media. Laser Phys. 15, 607.

Aközbek, N., Bowden, C.M., Chin, S.L., 2002a. Propagation dynamics of ultra-short high-power laser pulses in air: supercontinuum generation and transverse ring formation. J. Mod. Opt. 49 (3–4), 475–486.

Aközbek, N., Bowden, C.M., Talebpour, A., Chin, S.L., 2000. Femtosecond pulse propagation in air: variational analysis. Phys. Rev. E 61 (4), 4540–4549.

Aközbek, N., Iwasaki, A., Becker, A., Scalora, M., Chin, S.L., Bowden, C.M., 2002b. Third-harmonic generation and self-channeling in air using high-power femtosecond laser pulses. Phys. Rev. Lett. 89 (14), 143901.

Aközbek, N., Scalora, M., Bowden, C.M., Chin, S.L., 2001. White light continuum generation and filamentation during the propagation of ultra-sort laser pulses in air. Opt. Commun. 191, 353.

Alexeev, I., Ting, A.C., Gordon, D.F., Briscoe, E., Hafizi, B., Sprangle, P., 2005. Characterization of the third-harmonic radiation generated by intense laser self-formed filaments propagating in air. Opt. Lett. 30 (12), 1503.

Alfano, R.R. (Ed.), 1989. The supercontinuum laser source. Springer, New York.

Alfano, R.R., Shapiro, S.L., 1970. Observation of self-phase modulation and small-scale filaments in crystals and glasses. Phys. Rev. Lett. 24, 584–587.

Altucci, C., Delfin, C., Roos, L., Gaarde, M.B., L'Huillier, A., Mercer, I., Starczewski, T., Wahlström, C.-G., 1998. Frequency-resolved time-gated high-order harmonics. Phys. Rev. A 58, 3934–3941.

Ammosov, M.V., Delone, N.B., Krainov, V.P., 1986. Tunnel ionization of complex atoms and of atomic ions in an alternating electromagnetic field. Sov. Phys. JETP 64 (6), 1191–1194.

Anderson, D., Bonnedal, M., 1979. Variational approach to nonlinear self-focusing of Gaussian laser beams. Phys. Fluids 22 (1), 105–109.

Anderson, D., Lisak, M., Bernston, A., 2001. A variational approach to nonlinear evolution equations in optics. Pramana—J. Phys. 57 (5–6), 917–936.

Ando, T., Fujimoto, M., 2005. Femtosecond pulse propagation in nitrogen: numerical study of $(3 + 1)$-dimensional extended nonlinear schrödinger equation with shock-term correction. Phys. Rev. E 72, 026706.

Antoine, P., Piraux, B., Milosevic, D.B., Gajda, M., 1996. Generation of ultrashort pulses of harmonics. Phys. Rev. A 54, R1761–R1764.

Arévalo, E., 2006. Self-focusing arrest of femtosecond laser pulses in air at different pressures. Phys. Rev. E 74, 016602.

Arevalo, E., Becker, A., 2005a. Theoretical analysis of fluorescence signals in filamentation of femtosecond laser pulses in nitrogen molecular gas. Phys. Rev. A 72, 043807.

Arevalo, E., Becker, A., 2005b. Variational analysis of self-focusing of intense ultrashort pulses in gases. Phys. Rev. E 72, 026605.

Askar'yan, G.A., 1962. Effects of the gradient of a strong electromagnetic beam on electrons and atoms. Sov. Phys. JETP 15, 1088–1090.

Augst, S., Meyerhofer, D.D., Strickland, D., Chin, S.L., 1991. Laser ionization of noble gases by Coulomb-barrier suppression. J. Opt. Soc. Am. B 8 (4), 858–867.

Aumiler, D., Ban, T., Pichler, G., 2005. Femtosecond laser-induced cone emission in dense cesium vapor. Phys. Rev. A 71, 063803.

Azarenkov, A.N., Altshuler, G.B., Belashenkov, N.R., Kozlov, S.A., 1993. Fast nonlinearity of the refractive index of solid-state dielectric active media. Quantum Electron. 23 (8), 633–655.

Azarenkov, A.N., Altshuler, G.B., Kozlov, S.A., 1991. Nonresonance nonlinear polarization response of matter in a field of ultrashort light pulses. Opt. Spectrosc. 71, 195.

Bang, O., Krolikowsky, W., Wyller, J., Rasmussen, J.J., 2002. Collapse arrest and soliton stabilization in nonlocal nonlinear media. Phys. Rev. E 66, 045519 1–5.

Becker, A., Aközbek, N., Vijayalakshmi, K., Oral, E., Bowden, C.M., Chin, S.L., 2001a. Intensity clamping and re-focusing of intense femtosecond laser pulses in nitrogen molecular gas. Appl. Phys. B 73, 287–290.

Becker, A., Bandrauk, A.D., Chin, S.L., 2001b. S-matrix analysis of non-resonant multiphoton ionisation of inner-valence electrons of the nitrogen molecule. Chem. Phys. Lett. 343, 345–350.

Béjot, P., Kasparian, J., Salmon, E., Ackermann, R., Gisin, N., Wolf, J.-P., 2006. Laser noise reduction in air. Appl. Phys. Lett. 88, 251112.

Bergé, L., Couairon, A., 2000. Nonlinear propagation of self-guided ultra-short pulses in ionized gases. Phys. Plasmas 7 (1), 210–230.

Bergé, L., Couairon, A., 2001a. Gas induced solitons. Phys. Rev. Lett. 86, 1003–1006.

Bergé, L., Couairon, A., 2001b. A variational method for extended nonlinear schrödinger systems. Physica D 152–153, 752–762.

Bernstein, A.C., Diels, J.-C., Luk, T.S., Nelson, T.R., McPherson, A., Cameron, S.M., 2003. Time-resolved measurements of self-focusing pulses in air. Opt. Lett. 28 (23), 2354–2356.

Bernstein, A.C., Luk, T.S., Nelson, T.R., McPherson, A., Diels, J.-C., Cameron, S.M., 2002. Asymmetric ultra-short pulse-splitting measured in air using frog. Appl. Phys. B 75 (1), 119–122.

Bespalov, V.G., Kozlov, S.A., Shpolyanskiy, Y.A., Walmsley, I.A., 2002. Simplified field wave equations for the nonlinear propagation of extremely short light pulses. Phys. Rev. A 66, 013811.

Bespalov, V.I., Talanov, V.I., 1966. Filamentary structure of light beams in nonlinear liquids. Zh. Eksper. Teor. Fiz. Pis'ma 3, 471–476 [JETP Lett. 3 (1966) 307–310].

Beyer, O., Maxein, D., Buse, K., Sturman, B., Hsieh, H.T., Psaltis, D., 2005a. Femtosecond time-resolved absorption processes in lithium niobate crystals. Opt. Lett. 30 (11), 1366–1368.

Beyer, O., Maxein, D., Buse, K., Sturman, B., Hsieh, H.T., Psaltis, D., 2005b. Investigation of nonlinear absorption processes with femtosecond light pulses in lithium niobate crystals. Phys. Rev. E 71, 056603.

Bian, Z., T.M. Antonsen, J., 2001. Ionization instabilities of an electromagnetic wave propagating in a tenuous gas. Phys. Plasmas 8, 3183.

Bloembergen, N., 1973. The influence of electron plasma formation on superbroadening in light filaments. Opt. Commun. 8, 285–288.

Bogatov, N., Kartashov, D., Stepanov, A., 2005. Controlling of a dc discharge by a plasma filament produced by intense femtosecond laser pulse. In: Technical Digest of the ICONO/LAT 2005 Conference. vol. St. Petersburg, Russia. p. IWF4.

Bourayou, R., Méjean, G., Kasparian, J., Rodriguez, M., Salmon, E., Yu, J., Lehmann, H., Stecklum, B., Laux, U., Eislöffel, J., Scholz, A., Hatzes, A.P., Sauerbrey, R., Wöste, L., Wolf, J.-P., 2005. White-light filaments for multiparameter analysis of cloud microphysics. J. Opt. Soc. Am. B 22 (2), 369–377.

Brabec, T., Krausz, F., 1997. Nonlinear optical pulse propagation in the single-cycle regime. Phys. Rev. Lett. 78, 3282–3285.

Brabec, T., Krausz, F., 2000. Intense few-cycle laser fields: Frontiers of nonlinear optics. Rev. Mod. Phys. 72 (2), 545–591.

Bragheri, F., Faccio, D., Couairon, A., Matijosius, A., Tamošauskas, G., Varanavičius, A., Degiorgio, V., Di Trapani, P., 2007. Conical emission and shock front dynamics in fs laser pulse filamentation. Phys. Rev. Lett.

Bragheri, F., Liberale, C., Degiorgio, V., Faccio, D., Matijosius, A., Tamošauskas, G., Varanavičius, A., Di Trapani, P., 2005. Time-gated spectral characterization of ultrashort laser pulses. Opt. Commun. 256, 166–170.

Braun, A., Korn, G., Liu, X., Du, D., Squier, J., Mourou, G., 1995. Self-channeling of high-peak-power femtosecond laser pulses in air. Opt. Lett. 20 (1), 73–75.

Brodeur, A., Chien, C.Y., Ilkov, F.A., Chin, S.L., Kosareva, O.G., Kandidov, V.P., 1997. Moving focus in the propagation of ultrashort laser pulses in air. Opt. Lett. 22 (5), 304–306.

Brodeur, A., Chin, S.L., 1998. Band-gap dependence of the ultrafast white-light continuum. Phys. Rev. Lett. 80 (20), 4406–4409.

Brodeur, A., Chin, S.L., 1999. Ultrafast white-light continuum generation and self-focusing in transparent condensed media. J. Opt. Soc. Am. B 16 (4), 637–650.

Brodeur, A., Ilkov, F.A., Chin, S.L., 1996. Beam filamentation and the white light continuum divergence. Optics Commun. 129, 193–198.

Budil, K.S., Salières, P., Perry, M.D., L'Huillier, A., 1993. Influence of ellipticity on harmonic generation. Phys. Rev. A 48, R3437–R3440.

Buryak, A.V., Di Trapani, P., Skryabin, D.V., Trillo, S., 2002. Optical solitons due to quadratic nonlinearities: from basic physics to futuristic applications. Phys. Rep. 370, 63–235.

Campillo, A.J., Shapiro, S.L., Suydam, B.R., 1973. Periodic breakup of optical beams due to self-focusing. Appl. Phys. Lett. 23 (11), 628–630.

Campillo, A.J., Shapiro, S.L., Suydam, B.R., 1974. Relationship of self-focusing to spatial instability modes. Appl. Phys. Lett. 24 (4), 178–180.

Canuto, C., Hussaini, Y.M., Quarteroni, A., Zang, T.A., 1988. Spectral Methods in Fluid Dynamics. Springer, New York.

Cao, S., Wang, Y., Huang, W., Chai, L., Wang, C., Yang, J., Zhu, X., Zhang, Z., 2006. Experimental observation on spectrum evolution of femtosecond pulses in filamentation. Opt. Express 14 (12), 5492.

Cao, X.D., Agrawal, G.P., McKinstrie, C.J., 1994. Self-focusing of chirped optical pulses in nonlinear dispersive media. Phys. Rev. A 49 (5), 4085–4092.

Centurion, M., Pu, Y., Liu, Z., Psaltis, D., Hänsch, T.W., 2004. Holographic recording of laser-induced plasma. Opt. Lett. 29 (7), 772–774.

Centurion, M., Pu, Y., Psaltis, D., 2005a. Self-organization of spatial solitons. Opt. Express 13 (16), 6202–6211.

Centurion, M., Pu, Y., Tsang, M., Psaltis, D., 2005b. Dynamics of filament formation in a kerr medium. Phys. Rev. A 71, 063811.

Centurion, M., Pu, Y., Psaltis, D., 2006. Holographic capture of femtosecond pulse propagation. J. Appl. Phys. 100, 063104.

Chakraborty, H.S., Gaarde, M.B., Couairon, A., 2006. Single attosecond pulses from high harmonics driven by self-compressed filaments. Opt. Lett. 31, 3662.

Chegotov, M.V., 2002a. Ionisation refraction as the cause of space-time modulation of a short intense laser pulse. Quantum Electron. 32 (1), 19–26.

Chegotov, M.V., 2002b. Ionization modulation of a short intensive laser pulse. J. Phys. D: Appl. Phys. 35 (7), 647–657.

Chen, X., Jiang, Y., Leng, Y., Liu, J., Ge, X., Li, R., Xu, Z., 2006a. Pulse compression by filamentation in argon with an acoustic optical programmable dispersive filter for predispersion compensation. Chin. Phys. Lett. 23 (5), 1198–1200.

Chen, X., Leng, Y., Liu, J., Zhu, Y., Li, R., Xu, Z., 2006b. Pulse self-compression in normally dispersive bulk media. Opt. Commun. 259 (1), 331–335.

Chen, X.W., Zhu, Y., Liu, J., Leng, Y.X., Ge, X.C., Li, R., Xu, Z., 2005. Self-compression of femtosecond laser pulses in normally dispersive solid material. Acta Physica Sinica 54 (11), 5178–5183.

Chen, Y.-F., Beckwitt, K., Wise, F.W., Malomed, B.A., 2004. Criteria for the observation of multidimensional optical solitons in saturable media. Phys. Rev. E 70, 046610.

Cheng, C.-C., Wright, E.M., Moloney, J.V., 2001. Generation of electromagnetic pulses from plasma channels induced by femtosecond light strings. Phys. Rev. Lett. 87, 213001.

Cheng, C.-C., Wright, E.M., Moloney, J.V., 2002. Cheng, Wright, and Moloney reply. Phys. Rev. Lett. 89, 139302.

Chernev, P., Petrov, V., 1992. Self-focusing of light pulses in the presence of normal group-velocity dispersion. Opt. Lett. 17 (3), 172–174.

Chiao, R.Y., Garmire, E., Townes, C.H., 1964. Self-trapping of optical beams. Phys. Rev. Lett. 13 (15), 479–482.

Chiao, R.Y., Kelley, P.L., Garmire, E., 1966. Stimulated four-photon interaction and its influence on stimulated rayleigh-wing scattering. Phys. Rev. Lett. 17 (22), 1158–1161.

Chien, C.Y., Fontaine, B.L., Desparois, A., Jiang, Z., Johnston, T.W., Kieffer, J.-C., Pépin, H., Vidal, F., 2000. Single-shot chirped-pulse spectral interferometry used to measure the femtosecond ionization dynamics of air. Opt. Lett. 25, 578–580.

Chin, S.L., 2004. The physics and the challenge of the propagation of powerful femtosecond laser pulses in optical media. Phys. Can. 60, 273–281.

Chin, S.L., Aközbek, N., Proulx, A., Petit, S., Bowden, C.M., 2001. Transverse ring formation of a focused femtosecond laser pulse propagating in air. Opt. Commun. 188 (1–4), 181–186.

Chin, S.L., Brodeur, A., Petit, S., Kosareva, O.G., Kandidov, V.P., 1999a. Filamentation and supercontinuum generation during the propagation of powerful ultrashort laser pulses in optical media (white light laser). J. Nonlinear Opt. Phys. Mater. 8, 121–146.

Chin, S.L., Petit, S., Borne, F., Miyazaki, K., 1999b. The white light supercontinuum is indeed an ultrafast white light laser. Jpn. J. Appl. Phys. 38, L126–L128.

Chin, S.L., Hosseini, S.A., Liu, W., Luo, Q., Théberge, F., Aközbek, N., Becker, A., Kandidov, V., Kosareva, O., Schröder, H., 2005. The propagation of powerful femtosecond laser pulses in optical media: physics, applications and new challenges. Can. J. Phys. 83, 863–905.

Chin, S.L., Miyazaki, K., 1999. A comment on lightning control using a femtosecond laser. Jpn. J. Appl. Phys. 38, 2011–2012.

Chin, S.L., Petit, S., Liu, W., Iwasaki, A., Nadeau, M.-C., Kandidov, V.P., Kosareva, O.G., Andrianov, K.Y., 2002a. Interference of transverse rings in multifilamentation of powerful femtosecond laser pulses in air. Opt. Commun. 210, 329–341.

Chin, S.L., Talebpour, A., Yang, J., Petit, S., Kandidov, V.P., Kosareva, O.G., Tamarov, M.P., 2002b. Filamentation of femtosecond laser pulses in turbulent air. Appl. Phys. B 74, 67–76.

Chin, S.L., Théberge, F., Liu, W., 2007. Filamentation nonlinear optics. Appl. Phys. B 86, 477–483.

Chiron, A., Lamouroux, B., Lange, R., Ripoche, J.-F., Franco, M., Prade, B., Bonnaud, G., Riazuelo, G., Mysyrowicz, A., 1999. Numerical simulations of the nonlinear propagation of femtosecond optical pulses in gases. Eur. Phys. J. D 6, 383–396.

Comtois, D., Chien, C.Y., Desparois, A., Génin, F., Jarry, G., Johnston, T.W., Kieffer, J.-C., La Fontaine, B., Martin, F., Mawassi, R., Pépin, H., Rizk, F.A.M., Vidal, F., Couture, P., Mercure, H.P., Potvin, C., Bondiou-Clergerie, A., Gallimberti, I., 2000. Triggering and guiding leader discharges using a plasma channel created by an ultrashort laser pulse. J. Appl. Phys. 76 (7), 819–821.

Conti, C., Di Trapani, P., Trillo, S., 2007. X Waves in Self-focusing of Ultra-short Pulses. In: Boyd, R.W., Lukishova, S.G., Shen, Y.R. (Eds.), Self-focusing: Past and Present, Fundamentals and Prospects, Springer Topics in Applied Physics, Springer, Berlin (Chapter 19), in print.

Conti, C., Trillo, S., Di Trapani, P., Valiulis, G., Piskarskas, A., Jedrkiewicz, O., Trull, J., 2003. Nonlinear electromagnetic X-waves. Phys. Rev. Lett. 90 (17), 170,406.

Cook, K., Kar, A.K., Lamb, R.A., 2003. White-light supercontinuum interference of self-focused filaments in water. Appl. Phys. Lett. 83 (19), 3861–3863.

Cook, K., Kar, A.K., Lamb, R.A., 2005. White-light filaments induced by diffraction effects. Opt. Express 33 (6), 2025.

Corkum, P.B., 1993. Plasma perspective on strong field multiphoton ionization. Phys. Rev. Lett. 71, 1994–1997.

Corkum, P.B., Burnett, N.H., Ivanov, M.Y., 1994. Subfemtosecond pulses. Opt. Lett. 19, 1870–1872.

Corkum, P.B., Rolland, C., 1989. Femtosecond continua produced in gases. IEEE J. Quant. Electron. QE-25, 2634–2639.

Corkum, P.B., Rolland, C., Srinivasan-Rao, T., 1986. Supercontinuum generation in gases. Phys. Rev. Lett. 57 (18), 2268.

Corsi, C., Tortora, A., Bellini, M., 2004. Generation of a variable linear array of phase-coherent supercontinuum sources. Appl. Phys. B 78, 299–304.

Couairon, A., 2003a. Dynamics of femtosecond filamentation from saturation of self-focusing laser pulses. Phys. Rev. A 68, 015,801.

Couairon, A., 2003b. Filamentation length of powerful laser pulses. Appl. Phys. B 76, 789–792.

Couairon, A., 2003c. Light bullets from femtosecond filamentation. Eur. Phys. J. D 27, 159–167.

Couairon, A., Bergé, L., 2000. Modeling the filamentation of ultra-short pulses in ionizing media. Phys. Plasmas 7 (1), 193–209.

Couairon, A., Bergé, L., 2002. Light filaments in air for ultraviolet and infrared wavelengths. Phys. Rev. Lett. 88 (13), 135003.

Couairon, A., Biegert, J., Hauri, C.P., Kornelis, W., Helbing, F.W., Keller, U., Mysyrowicz, A., 2006a. Self-compression of ultrashort laser pulses down to one optical cycle by filamentation. J. Mod. Opt. 53 (1–2), 75–85.

Couairon, A., Franco, M., Méchain, G., Olivier, T., Prade, B., Mysyrowicz, A., 2006b. Femtosecond filamentation in air at low pressures: Part I: Theory and numerical simulations. Opt. Commun. 259, 265–273.

Couairon, A., Gaižauskas, E., Faccio, D., Dubietis, A., Di Trapani, P., 2006c. Nonlinear X-wave formation by femtosecond filamentation in Kerr media. Phys. Rev. E 73, 016608.

Couairon, A., Franco, M., Mysyrowicz, A., Biegert, J., Keller, U., 2005a. Pulse-compression to the single cycle limit by filamentation in a gaz with a pressure gradient. Opt. Lett. 30 (19), 2657–2659.

Couairon, A., Sudrie, L., Franco, M., Prade, B., Mysyrowicz, A., 2005b. Filamentation and damage in fused silica induced by tightly focused femtosecond laser pulses. Phys. Rev. B 71, 125,435.

Couairon, A., Méchain, G., Tzortzakis, S., Franco, M., Lamouroux, B., Prade, B., Mysyrowicz, A., 2003. Propagation of twin laser pulses in air and concatenation of plasma strings produced by femtosecond infrared filaments. Opt. Commun. 225, 177–192.

Couairon, A., Mysyrowicz, A., 2006. Femtosecond filamentation in air. In: Yamanouchi, K., Chin, S.L., Agostini, P., Ferrante, G. (Eds.), Progress in Ultrafast Intense Laser Science I, vol. 84. Springer, Berlin, pp. 235–258 (Chapter 13).

Couairon, A., Mysyrowicz, A., 2007. Self-focusing and Filamentation of Femtosecond Pulses in Air and Condensed Matter: Simulations and Experiments. In: Boyd, R.W., Lukishova, S.G., Shen, Y.R. (Eds.), Self-focusing: Past and Present, Fundamentals and Prospects, Springer, Berlin. (Chapter 14), p. in print.

Couairon, A., Tzortzakis, S., Bergé, L., Franco, M., Prade, B., Mysyrowicz, A., 2002. Infrared light filaments: simulations and experiments. J. Opt. Soc. Am. B 19 (13), 1117–1131.

Courvoisier, F., Boutou, V., Kasparian, J., Salmon, E., Méjean, G., Yu, J., Wolf, J.-P., 2003. Ultraintense light filaments transmitted through clouds. Appl. Phys. Lett. 83 (2), 213–215.

Dalgarno, Kingston, 1966. The refractive indices and verdet constants of the inert gases. Proc. Roy. Soc. London Ser. A 259, 424–429.

D'Amico, C., Houard, A., Franco, M., Prade, B., Pellet, M., Mysyrowicz, A., 2006a. Coherent sub-THz radiation emission from femtosecond filaments in air. In: Technical Digest of the European Optical Society Annual Meeting. European Optical Society.

D'Amico, C., Prade, B., Franco, M., Mysyrowicz, A., 2006b. Femtosecond filament amplification in liquids. Appl. Phys. B 85 (1), 49–53.

D'Amico, C., Houard, A., Franco, M., Prade, B., Mysyrowicz, A., 2007a. Coherent and incoherent radial THz emission from femtosecond filaments in air. Opt. Commun., in print.

D'Amico, C., Houard, A., Franco, M., Prade, B., Mysyrowicz, A., Couairon, A., Tikhonchuk, V.T., 2007b. Phys. Rev. Lett., submitted.

Davis, K.M., Miura, K., Sugimoto, N., Hirao, K., 1996. Writing waveguides in glass with a femtosecond laser. Opt. Lett. 21 (21), 1729.

Dawes, E.L., Marburger, J.H., 1969. Computer studies in self-focusing. Phys. Rev. 179 (3), 862–868.

Day, C., 2001. Experiments detail how powerful ultrashort laser pulses propagate through air. Phys. Today 54 (8), 17–19.

Day, C., 2004. Intense X-shaped pulses of light propagate without spreading in water and other dispersive media. Phys. Today 57 (10), 25–26.

DeMartini, F., Townes, C.H., Gustafson, T.K., Kelley, P.L., 1967. Self-steepening of light pulses. Phys. Rev. 164, 312–323.

Deng, Y.P., Zhu, J.B., Ji, Z.G., Liu, J.S., Shuai, B., Li, R.X., Xu, Z.Z., 2006. Transverse evolution of a plasma channel in air induced by a femtosecond laser. Opt. Lett. 31 (4), 546.

Desparois, A., Fontaine, B.L., Bondiou-Clergerie, A., Chien, C.-Y., Comtois, D., Johnston, T.W., Kieffer, J.-C., Mercure, H.P., Pépin, H., Rizk, F.A.M., Vidal, F., 2000. Study of laser-induced breakdown in a 30-cm air gap under a uniform field. IEEE Trans. Plasma Sci. 28 (5), 1755.

Dharmadhikari, A.K., Rajgara, F.A., Mathur, D., 2005a. Systematic study of highly efficient white light generation in transparent materials using intense femtosecond laser pulses. Appl. Phys. B 80 (1), 61–66.

Dharmadhikari, A.K., Rajgara, F.A., Mathur, D., Schroeder, H., Liu, J., 2005b. Efficient broadband emission from condensed media irradiated by low-intensity, unfocused, ultrashort laser light. Opt. Express 13 (21), 8555.

Dharmadhikari, A.K., Rajgara, F.A., Mathur, D., 2006a. Depolarization of white light generated by ultrashort laser pulses in optical media. Opt. Lett. 31 (14), 2184.

Dharmadhikari, A.K., Rajgara, F.A., Mathur, D., 2006b. Plasma effects and the modulation of white light spectra in the propagation of ultrashort, high-power laser pulses in barium fluoride. Appl. Phys. B 82, 575–583.

Dharmadhikari, A.K., Rajgara, F.A., Reddy, N.C.S., Sandhu, A.S., Mathur, D., 2004. Highly efficient white light generation from barium fluoride. Opt. Express 12 (4), 695.

Di Trapani, P., Valiulis, G., Piskarskas, A., Jedrkiewicz, O., Trull, J., Conti, C., Trillo, S., 2003. Spontaneously generated X-shaped light bullets. Phys. Rev. Lett. 91 (9), 093904.

Diddams, S.A., Eaton, H.K., Zozulya, A.A., Clement, T.S., 1998a. Amplitude and phase measurements of femtosecond pulse splitting in nonlinear dispersive media. Opt. Lett. 23 (5), 379–381.

Diddams, S.A., Eaton, H.K., Zozulya, A.A., Clement, T.S., 1998b. Characterizing the nonlinear propagation of femtosecond pulses in bulk media. IEEE J. Selected Topics Quantum Electron. 4 (2), 306–316.

Diels, J.-C., Bernstein, R., Stahlkopf, K.E., Zhao, X.M., 1997. Lightning control with lasers. Scientific American 277 (2), 50–55.

Dietrich, P., Burnett, N.H., Ivanov, M., Corkum, P.B., 1994. High-harmonic generation and correlated two-electron multiphoton ionization with elliptically polarized light. Phys. Rev. A 50, R3585–R3588.

Dong, Q.-L., Sheng, Z.-M., Zhang, J., 2002. Self-focusing and merging of two copropagating laser beams in underdense plasma. Phys. Rev. E 66 (2), 027402.

Dubietis, A., Couairon, A., Kučinskas, E., Tamošauskas, G., Gaižauskas, E., Faccio, D., Di Trapani, P., 2006a. Measurement and calculation of nonlinear absorption associated with femtosecond filaments in water. Appl. Phys. B 84, 439,446.

Dubietis, A., Valiulis, G., Varanavičius, A., 2006b. Nonlinear localization of light. Lithuanian J. Phys. 46 (1), 7–18.

Dubietis, A., Gaižauskas, E., Tamošauskas, G., Di Trapani, P., 2004a. Light filaments without self-channeling. Phys. Rev. Lett. 92 (25), 253903.

Dubietis, A., Kučinskas, E., Tamošauskas, G., Gaižauskas, E., Porras, M.A., Di Trapani, P., 2004b. Self-reconstruction of light filaments. Opt. Lett. 29, 2893–2895.

Dubietis, A., Tamošauskas, G., Fibich, G., Ilan, B., 2004c. Multiple filamentation induced by input-beam ellipticity. Opt. Lett. 29 (10), 1126.

Dubietis, A., Tamošauskas, G., Diomin, I., Varanavičius, A., 2003. Self-guided propagation of femtosecond light pulses in water. Opt. Lett. 28 (14), 1269–1271.

Durnin, J., Miceli Jr J.J., Eberly, J.H., 1987. Diffraction-free beams. Phys. Rev. Lett. 58 (15), 1499.

Dyachenko, S., Newell, A.C., Pushkarev, A., Zakharov, V.E., 1992. Optical turbulence: weak turbulence, condensates and collapsing filaments in the nonlinear Schrödinger equation. Physica D 57, 96.

Eisenberg, H.S., Morandotti, R., Silberberg, Y., Bar-Ad, S., Ross, D., Aitchison, J.S., 2001. Kerr spatiotemporal self-focusing in a planar glass waveguide. Phys. Rev. Lett. 87, 043902.

Faccio, D., Averchi, A., Couairon, A., Dubietis, A., Piskarskas, R., Matijosius, A., Bragheri, F., Porras, M.A., Piskarskas, A., Di Trapani, P., 2006a. Competition between phase-matching and stationarity in Kerr-driven optical pulse filamentation. Phys. Rev. E 74, 047603.

Faccio, D., Porras, M., Dubietis, A., Bragheri, F., Couairon, A., Di Trapani, P., 2006b. Conical emission, pulse splitting and X-wave parametric amplification in nonlinear dynamics of ultrashort light pulses. Phys. Rev. Lett. 96, 193,901.

Faccio, D., Porras, M.A., Dubietis, A., Tamošauskas, G., Kučinskas, E., Couairon, A., Di Trapani, P., 2006c. Angular and chromatic dispersion in Kerr-driven conical emission. Opt. Commun. 265, 672677.

Faccio, D., Averchi, A., Dubietis, A., Polesana, P., Piskarskas, A., Di Trapani, P., Couairon, A., 2007. Stimulated-raman X-waves in ultrashort optical pulse filamentation. Opt. Lett. 32 (2), 184.

Faccio, D., Di Trapani, P., Minardi, S., Bramati, A., Bragheri, F., Liberale, C., Degiorgio, V., Dubietis, A., Matijosius, A., 2005a. Far-field spectral characterization of conical emission and filamentation in Kerr media. J. Opt. Soc. Am. B 22 (4), 862–869.

Faccio, D., Matijosius, A., Dubietis, A., Piskarskas, R., Varanavičius, A., Gaižauskas, E., Piskarskas, A., Couairon, A., Di Trapani, P., 2005b. Near- and far-field evolution of laser pulse filaments in Kerr media. Phys. Rev. E 72, 037601.

Fan, C.H., Sun, J., Longtin, J.P., 2002. Breakdown threshold and localized electron density in water induced by ultrashort laser pulses. J. Appl. Phys. 91 (4), 2530–2536.

Fang, X.-J., Kobayashi, T., 2003. Evolution of a super-broadened spectrum in a filament generated by an ultrashort intense laser pulse in fused silica. Appl. Phys. B 77, 167–170.

Faye, G., Kasparian, J., Sauerbrey, R., 2001. Modifications to the lidar equations due to nonlinear propagation in air. Appl. Phys. B 73 (2), 157–163.

Feit, M.D., Fleck, J.A., 1974. Effect of refraction on spot-size dependence of laser-induced breakdown. Appl. Phys. Lett. 24 (4), 169–172.

Feng, Q., Moloney, J.V., Newell, A.C., Wright, E.M., 1995. Laser-induced breakdown versus self-focusing for focused picosecond pulses in water. Opt. Lett. 20 (19), 1958–1960.

Feng, Q., Moloney, J.V., Newell, A.C., Wright, E.M., Cook, K., Kennedy, P.K., Hammer, D.X., Rockwell, B.A., Thompson, C.R., 1997. Theory and simulation on the threshold of water breakdown induced by focused ultrashort laser pulses. IEEE J. Quant. Electron. 33 (2), 127–137.

Fibich, G., 1996. Adiabatic law for self-focusing of optical beams. Opt. Lett. 21 (21), 1735–1737.

Fibich, G., Eisenmann, S., Ilan, B., Erlich, Y., Fraenkel, M., Henis, Z., Gaeta, A.L., Zigler, A., 2005a. Self-focusing distance of very high power laser pulses. Opt. Express 13 (15), 5897.

Fibich, G., Gavish, N., Wang, X.-P., 2005b. New singular solutions of the nonlinear Schrödinger equation. Physica D 211 (3–4), 193–220.

Fibich, G., Eisenmann, S., Ilan, B., Zigler, A., 2004. Control of multiple filamentation in air. Opt. Lett. 29 (15), 1772.

Fibich, G., Gaeta, A.L., 2000. Critical power for self-focusing in bulk media and in hollow waveguides. Opt. Lett. 25 (5), 335–337.

Fibich, G., Ilan, B., 2000. Self-focusing of elliptic beams: an example of the failure of the aberrationless approximation. J. Opt. Soc. Am. B 17 (10), 1749–1758.

Fibich, G., Ilan, B., 2001a. Deterministic vectorial effects lead to multiple filamentation. Opt. Lett. 26 (11), 840–842.

Fibich, G., Ilan, B., 2001b. Vectorial and random effects in self-focusing and in multiple filamentation. Physica D 157, 112.

Fibich, G., Ilan, B., 2002. Multiple filamentation of circularly polarized beams. Phys. Rev. Lett. 89 (1), 013901 1–4.

Fibich, G., Ilan, B., 2003. Self-focusing of circularly polarized beams. Phys. Rev. E 67 (3), 036622 1–15.

Fibich, G., Ilan, B., 2004. Optical light bullets in a pure Kerr medium. Opt. Lett. 29 (8), 887.

Fibich, G., Malkin, V.M., Papanicolaou, G.C., 1995. Beam self-focusing in the presence of small normal time-dispersion. Phys. Rev. A 52, 4218–4228.

Fibich, G., Papanicolaou, G., 1999. Self-focusing in the perturbed and unperturbed nonlinear Schrödinger equation in critical dimension. SIAM J. Appl. Math. 60 (1), 183–240.

Fibich, G., Papanicolaou, G.C., 1997. Self-focusing in the presence of small time dispersion and nonparaxiality. Opt. Lett. 22 (18), 1379–1381.

Fibich, G., Ren, W., Wang, X.P., 2003. Numerical simulations of self-focusing of ultrafast laser pulses. Phys. Rev. E 67, 056603.

Fibich, G., Sivan, Y., Ehrlich, Y., Louzon, E., Fraenkel, M., Eisenmann, S., Katzir, Y., Zigler, A., 2006. Control of the collapse distance in atmospheric propagation. Opt. Express 14 (12), 4946.

Fischer, P., Brown, C.T.A., Morris, J.E., López-Mariscal, C., Sibbett, E.M.W.W., Dholakia, K., 2005. White light propagation invariant beams. Opt. Express 13 (17), 6657.

Fischetti, M.V., D.J. Di Maria, S.D.B., Theis, T.N., Kirtley, J.R., 1985. Theory of high-field electron transport in silicon dioxide. Phys. Rev. B 31, 8124.

Fork, R.L., Shank, C.V., Hirlimann, C., Yen, R., Tomlinson, W.J., 1983. Femtosecond white-light continuum pulses. Opt. Lett. 8, 1–3.

Frejafon, E., Kasparian, J., Rambaldi, P., Vezin, B., Boutou, V., Yu, J., Ulbricht, M., Weidauer, D., Ottobrini, B., de Saeger, E., Krämer, B., Leisner, T., Rairoux, P., Wöste, L., Wolf, J.-P., 1998. Laser applications for atmospheric pollution monitoring. Eur. Phys. J. D 4, 231.

Fujimoto, M., Aoshima, S., Tsuchiya, Y., 2002. Multiframe observation of an intense femtosecond optical pulse propagating in air. Opt. Lett. 27 (5), 309–311.

Gaeta, A.L., 2000. Catastrophic collapse of ultrashort pulses. Phys. Rev. Lett. 84, 3582.

Gaeta, A.L., 2002. Nonlinear propagation and continuum generation in microstructured optical fibers. Opt. Lett. 27, 924–926.

Gaeta, A.L., Wise, F., 2001. Comment on "self-compression of high-intensity femtosecond optical pulses and spatiotemporal soliton generation". Phys. Rev. Lett. 87 (22), 229,401.

Gaižauskas, E., Dubietis, A., Kudriašov, V., Sirutkaitis, V., Couairon, A., Faccio, D., Di Trapani, P., 2007. On the Role of Conical Waves in Self-focusing and Filamentation of Femtosecond Pulses. Springer, Berlin, (Chapter 20).

Gaižauskas, E., Vanagas, E., Jarutis, V., Juodkazis, S., Mizeikis, V., Misawa, H., 2006. Discrete damage traces from filamentation of Gauss–Bessel pulses. Opt. Lett. 31, 80.

Galkin, Y.S., Tatevian, R.A., 1997. The problem of obtaining formulae for the refractive index of air for high-precision edm. Journal of Geodesy 71, 483–485.

Gamaly, E.G., Juodkazis, S., Nishimura, K., Misawa, H., Luther-Davies, B., Hallo, L., Nicolai, P., Tikhonchuk, V.T., 2006. Laser–matter interaction in a bulk of a transparent solid: confined micro-explosion and void formation. Phys. Rev. B 73, 214,101.

Ganeev, R.A., Suzuki, M., Baba, M., Kuroda, H., Kulagin, I.A., 2005. Third-harmonic generation in air by use of femtosecond radiation in tight-focusing conditions. Appl. Opt. 45 (4), 748.

Garmire, E., Chiao, R.Y., Townes, C.H., 1966. Dynamics and characteristics of the self-trapping of intense light beams. Phys. Rev. Lett. 16, 347–349.

Giuliano, C.R., Marburger, J.H., 1971. Observations of moving self-foci in sapphire. Phys. Rev. Lett. 25, 905–908.

Glezer, E.N., Milosavljevic, M., Huang, L., Finlay, R.J., Her, T.-H., Callan, J.P., Mazur, E., 1996. Three-dimensional optical storage inside transparent materials. Opt. Lett. 21 (24), 2023.

Golub, I., 1990. Optical characteristics of supercontinuum generation. Opt. Lett. 15 (6), 305.

Golubtsov, I.S., Kandidov, V.P., Kosareva, O.G., 2001. Conical emission of high-power femtosecond laser pulse in the atmosphere. Atmos. Oceanic Opt. 14, 303–315.

Golubtsov, I.S., Kandidov, V.P., Kosareva, O.G., 2003. Initial phase modulation of a high-power femtosecond laser pulse as a tool for controlling its filamentation and generation of a supercontinuum in air. Quant. Electronics 33 (6), 525–530.

Golubtsov, I.S., Kosareva, O.G., 2002. Influence of various physical factors on the generation of conical emission in the propagation of high-power femtosecond laser pulses in air. J. Opt. Technol. 69, 462.

Golubtsov, I.S., Kosareva, O.G., Mozhaev, E.I., 2000. Nonlinear optical spectral transformation of the powerful femtosecond laser pulse in air. Phys. Vibr. 8 (2), 73–78.

Gopal, A., Minardi, S., Tatarakis, M., 2007. Quantitative two-dimensional shadowgraphic set-up for high-sensitivity measurement of low-density laser-plasmas. Opt. Lett., in print.

Gordon, D.F., Ting, A.C., Alexeev, I., Fischer, R.P., Sprangle, P., 2006. Direct measurements of the dynamics of self-guided femtosecond laser filaments in air. IEEE Trans. Plasma Sci. 34 (2), 249–253.

Gori, F., 1994. Flattened gaussian beams. Optics Commun. 107 (5–6), 335–341.

Gosnell, T.R., Taylor, A.J., Greene, D.P., 1990. Supercontinuum generation at 248 nm using high-pressure gases. Opt. Lett. 15 (2), 130–132.

Grow, T.D., Gaeta, A.L., 2005. Dependence of multiple filamentation on beam ellipticity. Opt. Express 13 (12), 4594.

Grow, T.D., Ishaaya, A.A., Vuong, L.T., Gaeta, A.L., Gavish, N., Fibich, G., 2006. Collapse dynamics of super-Gaussian beams. Opt. Express 14 (12), 5468.

Gruzdev, V.E., 2004. Analysis of the transparent-crystal ionization model developed by l. v. Keldysh. J. Opt. Technol. 71 (8), 504–508.

Guandalini, A., Eckle, P., Anscombe, M., Schlup, P., Biegert, J., Keller, U., 2006. 5.1 fs pulses generated by filamentation and carrier envelope phase stability analysis. J. Phys. B: At. Mol. Opt. Phys. 39, S257–S264.

Guo, Q., Luo, B., Chi, S., 2006. Optical beams in sub-strongly non-local nonlinear media: a variational solution. Opt. Commun. 259, 336341.

Gupta, D.N., Sharma, A.K., 2003. Propagation of high power short pulse laser in a tunnel ionizing inhomogeneous gas. Physica Scripta 67, 246–249.

Gustafson, T.K., Taran, J.P., Haus, H.A., Lifsitz, J.R., Kelley, P.L., 1969. Self-modulation, self-steepening, and spectral development of light in small-scale trapped filaments. Phys. Rev. 177, 306–313.

Hao, Z.-Q., Zhang, J., Lu, X., Xi, T.-T., Li, Y.-T., Yuan, X.-H., Zheng, Z.-Y., Wang, Z.-H., Ling, W.-J., Wei, Z.-Y., 2006. Spatial evolution of multiple filaments in air induced by femtosecond laser pulses. Opt. Express 14 (2), 773.

Hatayama, M., Suda, A., Nurhuda, M., Nagasaka, K., Midorikawa, K., 2003. Spatiotemporal dynamics of high-intensity femtosecond laser pulses propagating in argon. J. Opt. Soc. Am. B 20 (3), 603–608.

Hauri, C.P., Guandalini, A., Eckle, P., Kornelis, W., Biegert, J., Keller, U., 2005. Generation of intense few-cycle laser pulses through filamentation—parameter dependence. Opt. Express 13 (19), 7541.

Hauri, C.P., Kornelis, W., Helbing, F.W., Heinrich, A., Couairon, A., Mysyrowicz, A., Biegert, J., Keller, U., 2004. Generation of intense, carrier-envelope phase-locked few-cycle laser pulses through filamentation. Appl. Phys. B 79, 673–677.

Hauri, C.P., Trisorio, A., Merano, M., Rey, G., Lopez-Martens, R.B., Mourou, G., 2006. Generation of high-fidelity, down-chirped sub-10 fs mJ pulses through filamentation for driving relativistic laser-matter interactions at 1 kHz. Appl. Phys. Lett. 89, 151125.

He, G.-S., Xu, G.C., Cui, Y., Prasad, P.N., 1993. Difference of spectral superbroadening behavior in Kerr-type and non-Kerr-type liquids pumped with ultrashort laser pulses. Appl. Opt. 32 (24), 4507.

Heck, G., Sloss, J., Levis, R.J., 2006. Adaptive control of the spatial position of white light filaments in an aqueous solution. Opt. Commun. 259, 216–222.

Hentschel, M., Kienberger, R., Spielmann, C., Reider, G.A., Milosevic, N., Brabec, T., Corkum, P., Heinzmann, U., Drescher, M., Krausz, F., 2001. Attosecond metrology. Nature (London) 414, 509–513.

Henz, S., Herrmann, J., 1996. Two-dimensional spatial solitons in bulk Kerr media stabilized by self-induced multiphoton ionization: variational approach. Phys. Rev. E 53 (4), 4092–4097.

Henz, S., Herrmann, J., 1999. Self-channeling and pulse shortening of femtosecond pulses in multiphoton-ionized dispersive dielectric solids. Phys. Rev. A 59 (3), 2528–2531.

Hercher, M., 1964. Laser-induced damage in transparent media. J. Opt. Soc. Am. 54, 563.

Hermann, J.A., 2003. Optimisation approach to modelling nonlinear optical absorption in thick media. Opt. Commun. 217, 421–429.

Hickman, A.P., Bischel, W.K., 1988. Theory of Stokes and anti-Stokes generation by Raman frequency conversion. Phys. Rev. A 37 (7), 2516–2523.

Homoelle, D., Wielandy, S., Gaeta, A.L., Borrelli, N.F., Smith, C., 1999. Infrared photosensitivity in silica glasses exposed to femtosecond laser pulses. Opt. Lett. 24 (18), 1311.

Hosseini, S.A., Ferland, B., Chin, S.L., 2003a. Measurement of filament length generated by an intense femtosecond laser pulse using electromagnetic radiation detection. Appl. Phys. B 76, 583–586.

Hosseini, S.A., Luo, Q., Ferland, B., Liu, W., Aközbek, N., Roy, G., Chin, S.L., 2003b. Effective length of filaments measurement using backscattered fluorescence from nitrogen molecules. Appl. Phys. B 77 (6–7), 697–702.

Hosseini, S.A., Luo, Q., Ferland, B., Liu, W., Chin, S.L., Kosareva, O.G., Panov, N.A., Aközbek, N., Kandidov, V.P., 2004a. Competition of multiple filaments during the propagation of intense femtosecond laser pulses. Phys. Rev. A 70, 033802.

Hosseini, S.A., Yu, J., Luo, Q., Chin, S.L., 2004b. Multi-parameter characterization of the longitudinal plasma profile of a filament: a comparative study. Appl. Phys. B 79 (6–7), 519–523.

Houard, A., D'Amico, C., Franco, M., Prade, B., Mysyrowicz, A., Couairon, A., Tikhonchuk, V., 2007a. Cerenkov thz emission from femtosecond filamentation in air. In: Technical Digest of the CLEO/QELS Conference. Optical Society of America, Baltimore, p. in print.

Houard, A., D'Amico, C., Liu, Y., André, Y.-B., Franco, M., Prade, B., Salmon, E., Pierlot, P., Cleon, L.-M., Mysyrowicz, A., 2007b. High current permanent discharges in air induced by femtosecond laser filamentation. In: Technical Digest of the CLEO/QELS Conference. Optical Society of America, Baltimore, p. in print.

Hoyer, W., Knorr, A., Moloney, J.V., Wright, E.M., Kira, M., Koch, S., 2005. Photoluminescence and terahertz emission from femtosecond laser-induced plasma channels. Phys. Rev. Lett. 94, 115004.

Hua, Z., 2005. The propagation dynamics of ultraviolet light filaments with rayleigh scattering in air. Chinese Phys. 10, 2019.

Huo, Y., Zeng, Z., Li, R., Xu, Z., 2005. Single attosecond pulse generation using two-color polarized time-gating technique. Opt. Express 13 (24), 9897.

Ilkov, F.A., Decker, J.E., Chin, S.L., 1992. Ionization of atoms in the tunnelling regime with experimental evidence using Hg atoms. J. Phys. B: At. Mol. Opt. Phys. 25, 4005–4020.

Ilkov, F.A., Ilkova, L.S., Chin, S.L., 1993. Supercontinuum generation versus optical breakdown in CO_2 gas. Opt. Lett. 18, 681–683.

Ishikawa, K., Kumagai, H., Midorikawa, K., 2002. High-power regime of femtosecond-laser pulse propagation in silica: multiple cone formation. Phys. Rev. E 66, 056608.

Ivanov, M., Corkum, P.B., Zuo, T., Bandrauk, A., 1995. Routes to control of intense-field atomic polarizability. Phys. Rev. Lett. 74, 2933–2936.

Iwasaki, A., Aközbek, N., Ferland, B., Luo, Q., Roy, G., Bowden, C.M., Chin, S.L., 2003. A lidar technique to measure the filament length generated by a high-peak power femtosecond laser pulse in air. Appl. Phys. B 76 (3), 231–236.

Javan, A., Kelley, P.L., 1966. Possibility of self-focusing due to intensity dependent anomalous dispersion. IEEE J. Quant. Electron. 2 (9), 470–473.

Jedrkiewicz, O., Trull, J., Valiulis, G., Piskarskas, A., Conti, C., Trillo, S., Di Trapani, P., 2003. Nonlinear X-waves in second-harmonic generation: experimental results. Phys. Rev. E 68, 026610.

Jin, Z., Zhang, J., Xu, M.H., Lu, X., Li, Y.T., Wang, Z.H., Wei, Z.Y., Yuan, X.H., Yu, W., 2005. Control of filamentation induced by femtosecond laser pulses propagating in air. Opt. Express 13 (25), 10424.

Jisha, C.P., Kuriakose, V.C., Porsezian, K., 2005. Variational approach to spatial optical solitons in bulk cubic-quintic media stabilized by self-induced multiphoton ionization. Phys. Rev. E 71, 056611.

Joglekar, A.P., Liu, H., Spooner, G.J., Meyhöfer, E., Mourou, G., Huni, A.J., 2003. A study of the deterministic character of optical damage by femtosecond laser pulses and applications to nanomachining. Appl. Phys. B 77, 25–30.

Junnarkar, M.R., 2001. Short pulse propagation in tight focusing conditions. Opt. Commun. 195, 273.

Juodkazis, S., Misawa, H., Hashimoto, T., Gamaly, E.G., Luther-Davies, B., 2006. Laser-induced microexplosion confined in a bulk of silica: formation of nanovoids. Appl. Phys. Lett. 88, 201909.

Juodkazis, S., Rode, A.V., Gamaly, E.G., Matsuo, S., Misawa, H., 2003. Recording and reading of three-dimensional optical memory in glasses. Appl. Phys. B 77, 361–368.

Kandidov, V., Kosareva, O.G., Golubtsov, I.S., Liu, W., Becker, A., Aközbek, N., Bowden, C.M., Chin, S.L., 2003a. Self-transformation of a powerful femtosecond laser pulse into a white-light laser pulse in bulk optical media or supercontinuum generation. Appl. Phys. B 77 (2-3), 149–165.

Kandidov, V.P., Kosareva, O.G., Koltun, A.A., 2003b. Nonlinear-optical transformation of a high-power femtosecond laser pulse in air. Quant. Electron. 33 (1), 69–75.

Kandidov, V.P., Aközbek, N., Scalora, M., Kosareva, O.G., Nyakk, A.V., Luo, Q., Hosseini, S.A., Chin, S.L., 2004a. A method for spatial regularisation of a bunch of filaments in a femtosecond laser pulse. Quant. Electron. 34 (10), 879–880.

Kandidov, V.P., Golubtsov, I.S., Kosareva, O.G., 2004b. Supercontinuum sources in a high-power femtosecond laser pulse propagating in liquids and gases. Quant. Electron. 34 (4), 348–354.

Kandidov, V.P., Dormidonov, A.E., Kosareva, O.G., Aközbek, N., Scalora, M., Chin, S.L., 2007. Optimum small-scale management of random beam perturbations in a femtosecond laser pulse. Appl. Phys. B, DOI: 10.1007/S00340-006-2555-9.

Kandidov, V.P., Fedorov, V.Y., 2004. Specific features of elliptic beam self-focusing. Quant. Electron. 34 (12), 1163–1168.

Kandidov, V.P., Kosareva, O.G., Brodeur, A., Chin, S.L., 1997a. State of the art of investigations into the filamentation of high-power subpicosecond laser pulses in gases. Atmos. Oceanic Opt. 10 (12), 966.

Kandidov, V.P., Kosareva, O.G., Shlenov, S.A., 1997b. Spatiotemporal instability of an intense subpicosecond laser pulse in gases. Quant. Electron. 27 (5), 443–446.

Kandidov, V.P., Kosareva, O.G., Mozhaev, E.I., Tamarov, M.P., 2000. Femtosecond nonlinear optics in the atmosphere. Atmos. Oceanic Opt. 13 (5), 394–401.

Kandidov, V.P., Kosareva, O.G., Shlenov, S.A., 1994. Influence of transient self-defocusing on the propagation of high-power femtosecond laser pulses in gases under ionisation conditions. Quant. Electron. 24 (10), 905–911.

Kandidov, V.P., Kosareva, O.G., Shlenov, S.A., Panov, N.A., Fedorov, V.Y., Dormidonov, A.E., 2005. Dynamic small-scale self-focusing of a femtosecond laser pulse. Quant. Electron. 35 (1), 59–64.

Kandidov, V.P., Kosareva, O.G., Shlyonov, S.A., 1993. Effect of the cubic nonlinearity and multiphoton ionization on spatiotemporal behavior of a subpicosecond laser pulse in air. Atmos. Oceanic Opt. 6 (1), 48.

Kandidov, V.P., Kosareva, O.G., Tamarov, M.P., Brodeur, A., Chin, S.L., 1999. Nucleation and random movement of filaments in the propagation of high-power laser radiation in a turbulent atmosphere. Quant. Electron. 29 (10), 911–915.

Kandidov, V.P., Militsin, V.O., 2006. Computer simulation of laser pulse filament generation in rain. Appl. Phys. B 83, 171–174.

Kasparian, J., Rodriguez, M., Méjean, G., Yu, J., Salmon, E., Wille, H., Bourayou, R., Frey, S., André, Y.-B., Mysyrowicz, A., Sauerbrey, R., Wolf, J.-P., Wöste, L., 2003. White light filaments for atmospheric analysis. Science 301, 61.

Kasparian, J., Sauerbrey, R., Chin, S.L., 2000a. The critical laser intensity of self-guided light filaments in air. Appl. Phys. B 71, 877.

Kasparian, J., Sauerbrey, R., Mondelain, D., Niedermeier, S., Yu, J., Wolf, J.-P., André, Y.-B., Franco, M., Prade, B., Tzortzakis, S., Mysyrowicz, A., Rodriguez, M., Wille, H., Wöste, L., 2000b. Infrared extension of the supercontinuum generated by femtosecond terawatt laser pulses propagating in the atmosphere. Opt. Lett. 25 (18), 1397–1399.

Kasparian, J., Solle, J., Richard, M., Wolf, J.-P., 2004. Ray-tracing simulation of ionization-free filamentation. Appl. Phys. B 79 (8), 947–951.

Keldysh, L.V., 1965. Ionization in the field of a strong electromagnetic wave. Sov. Phys. JETP 20 (5), 1307–1314.

Kelley, P.L., 1965. Self-focusing of optical beams. Phys. Rev. Lett. 15 (26), 1005–1008.

Kennedy, P.K., 1995. A first-order model for computation of laser-induced breakdown thresholds in ocular and aqueous media: Part I- theory. IEEE J. Quant. Electron. 31 (12), 2241–2249.

Keskinen, M.J., Fernsler, R., Ladouceur, H.D., Baronavski, A.P., Grounds, P.W., 2004. Generation of transient electric field structures in femtosecond high intensity ionizing laser pulses. Opt. Commun. 238, 341–344.

Khan, N., Mariun, N., Aris, I., Yeak, J., 2002. Laser-triggered lightning discharge. N. J. Phys. 4 (61), 61.1–20.

Khashan, M.A., Nassif, A.Y., 2000. Accurate measurement of the refractive indices of solids and liquids by the double-layer interferometer. Appl. Opt. 39 (32), 5991.

Kim, A.V., Lirin, S.F., Sergeev, A.M., Vanin, E.V., Stenflo, L., 1990. Compression and frequency up-conversion of an ultrashort ionizing pulse in a plasma. Phys. Rev. A 42, 2493.

Kinsler, P., Radnor, S.B.P., New, G.H.C., 2005. Theory of directional pulse propagation. Phys. Rev. A 72, 063807.

Kolesik, M., Katona, G., Moloney, J.V., Wright, E.M., 2003a. Physical factors limiting the spectral extent and band gap dependence of supercontinuum generation. Phys. Rev. Lett. 91 (1–4), 043905.

Kolesik, M., Moloney, J.V., Katona, G., Wright, E.M., 2003b. Theory and simulation of supercontinuum generation in transparent bulk media. Appl. Phys. B 77, 185–195.

Kolesik, M., Moloney, J.V., 2004a. Nonlinear optical pulse propagation simulation: from maxwell's to unidirectional equations. Phys. Rev. E 70 (3), 036604.

Kolesik, M., Moloney, J.V., 2004b. Self-healing femtosecond light filaments. Opt. Lett. 29 (6), 590–592.

Kolesik, M., Moloney, J.V., Mlejnek, M., 2002. Unidirectional optical pulse propagation equation. Phys. Rev. Lett. 89 (28), (1–4) 283,902.

Kolesik, M., Moloney, J.V., Wright, E.M., 2001. Polarization dynamics of femtosecond pulses propagating in air. Phys. Rev. E 64, 046607.

Kolesik, M., Wright, E.M., Becker, A., Moloney, J.V., 2006. Simulation of third-harmonic and supercontinuum generation for femtosecond pulses in air. Appl. Phys. B 85 (4), 531–538.

Kolesik, M., Wright, E.M., Moloney, J.V., 2004. Dynamic nonlinear X-waves for femtosecond pulse propagation in water. Phys. Rev. Lett. 92, 2539011–4.

Kolesik, M., Wright, E.M., Moloney, J.V., 2005. Interpretation of the spectrally resolved far field of femtosecond pulses propagating in bulk nonlinear dispersive media. Opt. Express 13 (26), 10,729–10,741.

Kondo, Y., Nouchi, K., Mitsuyu, T., Watanabe, M., Kazansky, P.G., Hirao, K., 1999. Fabrication of long-period fiber gratings by focused irradiation of infrared femtosecond laser pulses. Opt. Lett. 24 (10), 646.

Koprinkov, I.G., 2004. Ionization variation of the group velocity dispersion by high-intensity optical pulses. Appl. Phys. B 79, 359.

Koprinkov, I.G., Suda, A., Wang, P., Midorikawa, K., 2000. Self compression of high intensity femtosecond optical pulses and spatiotemporal soliton generation. Phys. Rev. Lett. 84 (17), 3847–3850.

Koprinkov, I.G., Suda, A., Wang, P., Midorikawa, K., 2001. Reply. Phys. Rev. Lett. 87 (22), 229,402.

Kornelis, W., Biegert, J., Tisch, J.W.G., Nisoli, M., Sansone, G., Vozzi, C., Silvestri, S.D., Keller, U., 2003. Single-shot kilohertz characterization of ultrashort pulses by spectral phase interferometry for direct electric-field reconstruction. Opt. Lett. 28, 281–283.

Korobkin, V.V., Prokhorov, A.M., Serov, R.V., Shchelev, M.Y., 1970. Self-focusing filaments as a result of the motion of focal points. Pis'ma Zh. Eksp. Teor. Fiz. 11, 153.

Kortsalioudakis, N., Tatarakis, M., Vakakis, N., Moustaı̈zis, S.D., Tzortzakis, S., Franco, M., Prade, B., Mysyrowicz, A., Papadogiannis, N., Couairon, A., 2005. Enhanced harmonic conversion efficiency in the self-guided propagation of femtosecond ultraviolet laser pulses in argon. Appl. Phys. B 80 (2), 211–214.

Kosareva, O.G., Grigor'evskii, A.V., Kandidov, V.P., 2005a. Formation of extended plasma channels in a condensed medium upon axicon focusing of a femtosecond laser pulse. Quantum Electron. 35 (11), 1013–1014.

Kosareva, O.G., Panov, N.A., Kandidov, V.P., 2005b. Scenario of multiple filamentation and supercontinuum generation in a high-power femtosecond laser pulse. Atmos. Oceanic Opt. 18 (3), 204–211.

Kosareva, O.G., Kandidov, V.P., Brodeur, A., Chien, C.Y., Chin, S.L., 1997a. Conical emission from laser-plasma interactions in the filamentation of powerful ultrashort laser pulses in air. Opt. Lett. 22 (17), 1332–1334.

Kosareva, O.G., Kandidov, V.P., Brodeur, A., Chin, S.L., 1997b. From filamentation in condensed media to filamentation in gases. J. Nonlinear Opt. Phys. Mater. 6 (4), 485–494.

Kosareva, O.G., Kandidov, V.P., Golubtsov, I.S., Chin, S.-L., 2003. Conversion of high-power femtosecond laser pulse to supercontinuum in atmospheric air. In: Young, C.Y., Stryjewski, J.S. (Eds.), Atmospheric Propagation, vol. 4976. SPIE, pp. 159–170.

Kosareva, O.G., Nguyen, T., Panov, N.A., Liu, W., Saliminia, A., Kandidov, V.P., Aközbek, N., Scalora, M., Vallée, R., Chin, S.L., 2006a. Array of femtosecond plasma channels in fused silica. Opt. Commun. 267 (2), 511–523.

Kosareva, O.G., Panov, N.A., Aközbek, N., Kandidov, V.P., Luo, Q., Hosseini, S.A., Liu, W., Gravel, J.-F., Roy, G., Chin, S.L., 2006b. Controlling a bunch of multiple filaments by means of a beam diameter. Appl. Phys. B 82 (1), 111–122.

Kosmatov, N.E., Shvets, V.F., Zakharov, V.E., 1991. Computer simulation of wave collapses in the nonlinear Schrödinger equation. Physica D 52, 16.

Kou, L., Labrie, D., Chylek, P., 1993. Refractive indices of water and ice in the 0.65- to 2.5-gm spectral range. Appl. Opt. 32 (19), 3531.

Kozlov, M.V., McKinstrie, C.J., Xie, C., 2005. Moment equations for optical pulses in dispersive and dissipative systems. Opt. Commun. 251, 194 –208.

Krause, J.L., Schafer, K.J., Kulander, K.C., 1992. High-order harmonic generation from atoms and ions in the high intensity regime. Phys. Rev. Lett. 68, 3535–3538.

Kudriašov, V., Gaižauskas, E., Sirutkaitis, V., 2005. Beam transformation and permanent modification in fused silica induced by femtosecond filaments. J. Opt. Soc. Am. B 22 (12), 2619–2627.

Kulander, K.C., Schafer, K.J., Krause, J.L., 1993. Dynamics of short pulse excitation ionization and harmonic conversion. In: Piraux, B., L'Huillier, A., Rzazewski, K. (Eds.), Proceedings of the Workshop on Super-Intense Laser-Atom Physics (SILAP III), vol. 316. Plenum Press, New York, pp. 95–110.

Kumagai, H., Cho, S.-H., Ishikawa, K., Midorikawa, K., Fujimoto, M., Aoshima, S., Tsuchiya, Y., 2003. Observation of the complex propagation of a femtosecond laser pulse in a dispersive transparent bulk material. J. Opt. Soc. Am. B 20 (3), 597–602.

La Fontaine, B., Comtois, D., Chien, C.Y., Desparois, A., Génin, F., Jarry, G., Johnston, T.W., Kieffer, J.-C., Martin, F., Mawassi, R., Pépin, H., Risk, F.A.M., Vidal, F., Potvin, C., Couture, P., Mercure, H.P., 2000. Guiding large-scale spark discharges with ultrashort pulse laser filaments. J. Appl. Phys. 88 (2), 610–615.

La Fontaine, B., Vidal, F., Comtois, D., Chien, C.Y., Desparois, A., Johnston, T.W., Kieffer, J.C., Mercure, H.P., Pépin, H., Rizk, F.A.M., 1999a. The influence of electron density on the formation of streamers in electrical discharges triggered with ultrashort laser pulses. IEEE Trans. Plasma Sci. 27, 688–700.

La Fontaine, B., Vidal, F., Jiang, Z., Chien, C.Y., Comtois, D., Desparois, A., Johnston, T.W., Kieffer, J.-C., Pépin, H., 1999b. Filamentation of ultrashort pulse laser beams resulting from their propagation over long distances in air. Phys. Plasmas 6, 1615.

Ladouceur, H.D., Baronavski, A.P., Lohrmann, D., Grounds, P.W., Girardi, P.G., 2001. Electrical conductivity of a femtosecond laser generated plasma channel in air. Opt. Commun. 189, 107.

Lallemand, P., Bloembergen, N., 1965. Self-focusing of laser beams and stimulated Raman gain in liquids. Phys. Rev. Lett. 15, 1010–1012.

Lam, J.F., Lippmann, B., Tappert, F., 1977. Self-trapped laser beams in plasma. Phys. Fluids 20 (7), 1176–1179.

Landman, M., Papanicolaou, G.C., Sulem, C., Sulem, P.L., Wang, X.P., 1991. Stability of isotropic singularities for the nonlinear Schrödinger equation. Physica D 47 (3), 393–415.

Landman, M., Papanicolaou, G.C., Sulem, C., Sulem, P.L., Wang, X.P., 1992. Stability of isotropic self-similar dynamics for scalar-wave collapse. Phys. Rev. A 46, 7869–7876.

Lange, H.R., 1998. Self-guiding of ultrashort laser pulses in air. Thèse de doctorat, École Polytechnique, École Polytechnique, Palaiseau, France.

Lange, H.R., Chiron, A., Ripoche, J.-F., Mysyrowicz, A., Breger, P., Agostini, P., 1998a. High order harmonic generation and quasi-phase matching in xenon using self-guided femtosecond laser pulses. Phys. Rev. Lett. 81 (8), 1611.

Lange, H.R., Franco, M.A., Ripoche, J.-F., Prade, B.S., Rousseau, P., Mysyrowicz, A., 1998b. Reconstruction of the time profile of femtosecond laser pulses through cross-phase-modulation. IEEE J. Selected Top. Quant. Electron. 4 (2), 295–300.

Lange, H.R., Grillon, G., Ripoche, J.-F., Franco, M.A., Lamouroux, B., Prade, B.S., Mysyrowicz, A., Nibbering, E.T.J., Chiron, A., 1998c. Anomalous long-range propagation of femtosecond laser pulses through air: moving focus or pulse self-guiding? Opt. Lett. 23 (2), 120–122.

Lange, H.R., Ripoche, J.-F., Chiron, A., Lamouroux, B., Franco, M., Prade, B., Nibbering, E., Mysyrowicz, A., 1998d. Time-space self-compression of femtosecond laser pulses in air. In: Technical Digest of the CLEO/IQEC Conference. OSA, San Francisco, p. 243.

Lehmeier, H.J., Leupacher, W., Penzkofer, A., 1985. Nonresonant third order hyperpolarizability of rare gases and N_2 determined by third harmonic generation. Opt. Commun. 56 (1), 67–72.

Lehner, T., Auby, N., 2000. Stabilization of the Kerr effect by self-induced ionization: formation of optical light spatially localized structures. Phys. Rev. E 61 (2), 1996–2005.

LeMesurier, B.J., 2000. Dissipation at singularities of the nonlinear Schrödinger equation through limits of regularisations. Physica D 138, 334–343.

Lenzner, M., Krüger, J., Sartania, S., Cheng, Z., Spielmann, C., Mourou, G., Kautek, W., Krausz, F., 1998. Femtosecond optical breakdown in dielectrics. Phys. Rev. Lett. 80, 4076.

L'Huillier, A., Lompre, L.A., Mainfray, G., Manus, C., 1983. Multiply charged ions induced by multiphoton absorption processes in rare-gas atoms at 1.064 μm. J. Phys. B: At. Mol. Phys. 16, 1363–1381.

Li, M., Menon, S., Nibarger, J.P., Gibson, G.N., 1999. Ultrafast electron dynamics in femtosecond optical breakdown of dielectrics. Phys. Rev. Lett. 82, 2394–2397.

Li, R., Chen, X., Liu, J., Zhu, Y., Ge, X., Lu, H., Lin, L., Xu, Z., 2006. Pulse self-compression in the nonlinear propagation of intense femtosecond laser pulse in normally dispersive solids. In: Yamanouchi, K., Chin, S.L., Agostini, P., Ferrante, G. (Eds.), Progress in Ultrafast Intense Laser Science I, vol. 84. Springer, Berlin, pp. 259–273 (Chapter 14).

Liou, L.W., Cao, X.D., Kinstrie, C.J.M., Agrawal, G.P., 1992. Spatiotemporal instabilities in dispersive nonlinear media. Phys. Rev. A 46, 4202.

Liu, C.S., Tripathi, V.K., 2000. Laser frequency upshift, self-defocusing, and ring formation in tunnel ionizing gases and plasmas. Phys. Plasmas 7 (11), 4360.

Liu, J., Chen, X., Liu, J., Zhu, Y., Leng, Y., Dai, J., Li, R., Xu, Z., 2006a. Spectrum reshaping and pulse self-compression in normally dispersive media with negatively chirped femtosecond pulses. Opt. Express 14 (2), 979.

Liu, J., Chen, X., Zhu, Y., Leng, Y., Dai, J., Ge, X., Li, R., Xu, Z., 2006b. Compression of intense laser pulse through filamentation in an argon-filled cell. Chin. Phys. Lett. 23 (2), 374–376.

Liu, J., Li, R., Xu, Z., 2006c. Few-cycle spatiotemporal soliton wave excited by filamentation of a femtosecond laser pulse in materials with anomalous dispersion. Phys. Rev. A 74, 043801.

Liu, W., Luo, Q., Théberge, F., Xu, H.L., Hosseini, S.A., Sarifi, S.M., Chin, S.L., 2006d. The influence of divergence on the filament length during the propagation of intense ultra-short laser pulses. Appl. Phys. B 82, 373–376.

Liu, W., Théberge, F., Daigle, J.-F., Simard, P.T., Sarifi, S.M., Kamali, Y., Xu, H.L., Chin, S.L., 2006e. An efficient control of ultrashort laser filament location in air for the purpose of remote sensing. Appl. Phys. B 85, 55–58.

Liu, Y., Jiang, H., Gong, Q., 2006f. Spatiotemporal transformation of a focused femtosecond pulse in the absence of self-focusing. Opt. Lett. 31 (6), 832.

Liu, J., Duan, Z., Zeng, Z., Xie, X., Deng, Y., Li, R., Xu, Z., Chin, S.L., 2005a. Time-resolved investigation of low-density plasma channels produced by a kilohertz femtosecond laser in air. Phys. Rev. E 72, 026412.

Liu, J., Schroeder, H., Chin, S.L., Li, R., Xu, Z., 2005b. Nonlinear propagation of fs laser pulses in liquids and evolution of supercontinuum generation. Opt. Express 13 (25), 12248.

Liu, J., Schroeder, H., Chin, S.L., Li, R., Xu, Z., 2005c. Ultrafast control of multiple filamentation by ultrafast laser pulses. Appl. Phys. Lett. 87, 161105.

Liu, J., Schroeder, H., Chin, S.L., Li, R., Yu, W., Xu, Z., 2005d. Space-frequency coupling, conical waves, and small-scale filamentation in water. Phys. Rev. A 72, 053817.

Liu, W., Gravel, J.-F., Théberge, F., Becker, A., Chin, S.L., 2005e. Background reservoir: its crucial role for long-distance propagation of femtosecond laser pulses in air. Appl. Phys. B 80, 857–860.

Liu, W., Théberge, F., Arévalo, E., Gravel, J.-F., Becker, A., Chin, S.L., 2005f. Experiments and simulations on the energy reservoir effect in femtosecond light filaments. Opt. Lett. 30 (19), 2602–2604.

Liu, M., Guo, H., Tang, H., Qiu, Y., Deng, D., Kong, H.J., 2002a. Vector theory of ultrashort, intense, pulsed laser beams propagating in gaseous media. J. Korean Phys. Soc. 41 (5), 717–721.

Liu, W., Kosareva, O., Golubtsov, I.S., Iwasaki, A., Becker, A., Kandidov, V.P., Chin, S.L., 2002b. Random deflection of the white light beam during self-focusing and filamentation of a femtosecond laser pulse in water. Appl. Phys. B 75, 595–599.

Liu, W., Petit, S., Becker, A., Aközbek, N., Bowden, C.M., Chin, S.L., 2002c. Intensity clamping of a femtosecond laser pulse in condensed matter. Opt. Commun. 202, 189–197.

Liu, P., Smith, W.L., Lotem, H., Bechtel, J.H., Bloembergen, N., Adhav, R.S., 1978. Absolute two-photon absorption coefficients at 355 and 266 nm. Phys. Rev. B 17, 4620.

Liu, P., Yen, R., Bloembergen, N., 1979. Two-photon absorption coefficients in uv window and coating materials. Appl. Opt. 18, 1015.

Liu, W., Chin, S.L., 2005. Direct measurement of the critical power of femtosecond Ti: sapphire laser pulse in air. Opt. Express 13 (15), 5750–5755.

Liu, W., Chin, S.L., Kosareva, O., Golubtsov, I.S., Kandidov, V.P., 2003a. Multiple refocusing of a femtosecond laser pulse in a dispersive liquid (methanol). Opt. Commun. 225 (1–3), 193–209.

Liu, W., Kosareva, O., Golubtsov, I.S., Iwasaki, A., Becker, A., Kandidov, V.P., Chin, S.L., 2003b. Femtosecond laser pulse filamentation versus optical breakdown in H$_2$O. Appl. Phys. B 76, 215.

Liu, W., Luo, Q., Chin, S.L., 2003c. Competition between multiphoton/tunnel ionization and filamentation induced by powerful femtosecond laser pulses in air. Chinese Opt. Lett. 1 (1), 56.

Liu, W., Hosseini, S.A., Luo, Q., Ferland, B., Chin, S.L., Kosareva, O.G., Panov, N.A., Kandidov, V.P., 2004. Experimental observation and simulations of the self-action of white-light laser pulse propagating in air. N. J. Phys. 6, 6.

Liu, X., Du, D., Mourou, G., 1997. Laser ablation and micromachining with ultrashort laser pulses. IEEE J. Quant. Electron. 33, 1706–1716.

Lompre, L.A., Mainfray, G., Manus, C., Repoux, S., Thebault, J., 1976. Multiphoton ionization of rare gases at very high laser intensity (10^{15} W/cm^2) by a 30-ps laser pulse at 1.06 µm. Phys. Rev. Lett. 36 (16), 949–952.

Lotz, W., 1967a. An empirical formula for the electron-impact ionization cross-section. Z. Phys. 206, 205–211.

Lotz, W., 1967b. Ionization potentials of atoms and ions from hydrogen to zinc. J. Opt. Soc. Am. 57 (7), 873–878.

Lotz, W., 1968a. Binding energies of electrons in the next inner subshell of atoms and ions from boron to zinc. J. Opt. Soc. Am. 58 (2), 236–240.

Lotz, W., 1968b. Electron-impact ionization cross sections and ionization rate coefficients for atoms and ions from hydrogen to calcium. Z. Phys. 216, 241–247.

Lotz, W., 1968c. Subshell binding energies of atoms and ions from hydrogen to zinc. J. Opt. Soc. Am. 58 (7), 915–921.

Loy, M.M.T., Shen, Y.R., 1969. Small-scale filaments in liquids and tracks of moving foci. Phys. Rev. Lett. 22, 994–997.

Loy, M.M.T., Shen, Y.R., 1973. Study of self-focusing and small-scale filaments of light in nonlinear media. IEEE J. Quant. Electron. QE-9 (3), 409.

Lu, J.-Y., Greenleaf, J.F., 1992a. Experimental verification of nondiffracting x-waves. IEEE Trans. on Ultrason. Ferroelectr. Freq. Control 39 (3), 441–446.

Lu, J.-Y., Greenleaf, J.F., 1992b. Nondiffracting x waves-exact solutions to free-space scalar wave equation and their finite aperture realizations. IEEE Trans. on Ultrasonics, Ferroelectr. Freq. Control 39 (1), 19–31.

Lu, J.-Y., Greenleaf, J.F., 1994. A study of two-dimensional array transducers for limited diffraction beams. IEEE Trans. Ultrason. Ferroelectr. Freq. Control 41 (5), 724–739.

Lu, X., Xi, T., Li, Y., Zhang, J., 2004. Lifetime of the plasma channel produced by ultra-short and ultra-high power laser pulse in the air. Acta Physica Sinica 53 (10), 3404–3408.

Lugovoi, V.N., Prokhorov, A.M., 1968. A possible explanation of the small-scale self-focusing filaments. JETP Lett. 7, 117–119.

Luo, Q., Hosseini, S.A., Liu, W., Chin, S.L., 2004. Lasing action in air induced by ultrafast laser filamentation. Opt. Photon. News (September), 44–47.

Luo, Q., Hosseini, S.A., Liu, W., Gravel, J.-F., Kosareva, O.G., Panov, N.A., Aközbek, N., Kandidov, V.P., Roy, G., Chin, S.L., 2005a. Effect of beam diameter on the propagation of intense femtosecond laser pulses. Appl. Phys. B 80 (1), 35–38.

Luo, Q., Yu, J., Hosseini, S.A., Liu, W., Ferland, B., Roy, G., Chin, S.L., 2005b. Long-range detection and length estimation of light filaments using extra attenuation of terawatt femtosecond laser pulses propagating in air. Appl. Opt. 44 (3), 391.

Luo, Q., Liu, W., Chin, S.L., 2003. Lasing action in air induced by ultrafast laser filamentation. Appl. Phys. B 76, 337–340.

Luo, Q., Xu, H.L., Hosseini, S.A., Daigle, J.-F., Théberge, F., Sharifi, M., Chin, S.L., 2006. Remote sensing of pollutants using femtosecond laser pulse fluorescence spectroscopy. Appl. Phys. B 82 (1), 105–109.

Luther, G.G., Moloney, J.V., Newell, A.C., Wright, E.M., 1994a. Self-focusing threshold in normally dispersive media. Opt. Lett. 19 (12), 862–864.

Luther, G.G., Newell, A.C., Moloney, J.V., Wright, E.M., 1994b. Short pulse conical emission and spectral broadening in normally dispersive media. Opt. Lett. 19 (11), 789–791.

Manassah, J.T., Baldeck, P.L., Alfano, R.R., 1988. Self-focusing, self-phase modulation, and diffraction in bulk homogeneous material. Opt. Lett. 13 (12), 1090.

Mansfield, C.R., Peck, E.R., 1969. Dispersion of helium. J. Opt. Soc. Am. 59 (2), 199.

Mao, S.S., Quéré, F., Guizard, S., Mao, X., Russo, R.E., Petite, G., Martin, P., 2004. Dynamics of femtosecond laser interactions with dielectrics. Appl. Phys. A 79 (7), 1695–1709.

Marburger, J.H., 1975. Self-focusing: Theory. Prog. Quant. Electr. 4, 35–110.

Marburger, J.H., Dawes, E., 1968. Dynamical formation of a small-scale filament. Phys. Rev. Lett. 21, 556–558.

Marklund, M., Shukla, P.K., 2006. Filamentational instability of partially coherent femtosecond optical pulses in air. Opt. Lett. 31 (12), 1884.

Matijošius, A., Piskarskas, R., Gaižauskas, E., Dubietis, A., Di Trapani, P., 2004a. Space-time recovery of arbitrarily shaped wave-packets by means of three dimensional imaging technique. Nonlinear Analysis: Model. Control 9 (3), 259–270.

Matijošius, A., Trull, J., Di Trapani, P., Dubietis, A., Piskarskas, R., Varanavičius, A., Piskarskas, A., 2004b. Non-linear space–time dynamics of ultrashort wave-packets in water. Opt. Lett. 29 (10), 1123.

Matvienko, G., Stepanov, A., Zemlyanov, A., Kartashov, D., Bochkarev, N., Kirsanov, A., Geints, Y., Kabanov, A., 2005. The propagation of femtosecond radiation in the aerosol atmosphere. in: Technical Digest of the ICONO/LAT 2005 Conference. St Petersburg, Russia, pp. LAT-394.

Matvienko, G.G., Veretennikov, V.V., Krekov, G.M., Krekova, M.M., 2003. Remote sensing of atmospheric aerosols with a white-light femtosecond lidar. Atmos. Oceanic Opt. 16, 1013–1019.

Max, C.E., 1976. Strong self-focusing due to the ponderomotive force in plasmas. Phys. Fluids 19 (1), 74–77.

McGloin, D., Dholakia, K., 2005. Bessel beams: diffraction in a new light. Contemporary Phys. 46 (1), 15–28.

Méchain, G., 2005. Study of filamentation of femtosecond laser pulses in air. Thèse de doctorat, École Polytechnique, Palaiseau, France.

Méchain, G., Couairon, A., André, Y.-B., D'Amico, C., Franco, M., Prade, B., Tzortzakis, S., Mysyrowicz, A., Sauerbrey, R., 2004a. Long range self-channeling of infrared laser pulses in air: a new propagation regime without ionization. Appl. Phys. B 79, 379–382.

Méchain, G., Couairon, A., Franco, M., Prade, B., Mysyrowicz, A., 2004b. Organizing multiple femtosecond filamentation in air. Phys. Rev. Lett. 93 (3), 035003.

Méchain, G., D'Amico, C., André, Y.-B., Tzortzakis, S., Franco, M., Prade, B., Mysyrowicz, A., Couairon, A., Salmon, E., Sauerbrey, R., 2005a. Length of plasma filaments created in air by a multiterawatt femtosecond laser. Opt. Commun. 247, 171–180.

Méchain, G., Méjean, G., Ackermann, R., Rohwetter, P., André, Y.-B., Kasparian, J., Prade, B., Stelmaszczyk, K., Yu, J., Salmon, E., Winn, W., Schlie, L.A.V., Mysyrowicz, A., Sauerbrey, R., Wöste, L., Wolf, J.-P., 2005b. Propagation of fs-TW laser filaments in adverse atmospheric conditions. Appl. Phys. B 80, 785–789.

Méchain, G., Mysyrowicz, A., Depiesse, M., Pellet, M., 2005c. A virtual antenna produced in air by intense femtosecond laser pulses. In: Titterton, D.H., Kirkpatrick, S.M., Stoian, R., Appleby, R., Chamberlain, J.M., Krapels, K.A. (Eds.), Technologies for Optical Countermeasures II; Femtosecond Phenomena II; and Passive Millimetre-Wave and Terahertz Imaging II, vol. 5989. SPIE, p. 5989.

Méchain, G., Olivier, T., Franco, M., Couairon, A., Prade, B., Mysyrowicz, A., 2006. Femtosecond filamentation in air at low pressures: Part II: Laboratory experiments. Opt. Commun. 261, 322–326.

Méchain, G., Tzortzakis, S., Prade, B., Franco, M., Mysyrowicz, A., Leriche, B., 2003. Calorimetric detection of THz radiation from femtosecond filaments in air. Appl. Phys. B 77, 707–709.

Méjean, G., Ackermann, R., Kasparian, J., Salmon, E., Yu, J., Wolf, J.-P., Rethmeier, K., Kalkner, W., Rohwetter, P., Stelmaszczyk, K., Wöste, L., 2006. Improved laser triggering and guiding of megavolt discharges with dual fs-ns pulses. Appl. Phys. Lett. 88, 021101.

Méjean, G., Kasparian, J., Salmon, E., Yu, J., Wolf, J.-P., Bourayou, R., Sauerbrey, R., Rodriguez, M., Wöste, L., Lehmann, H., Stecklum, B., Laux, U., Eislöffel, J., Scholz, A., Hatzes, A.P., 2003. Towards a supercontinuum-based infrared lidar. Appl. Phys. B 77 (2–3), 357–359.

Méjean, G., Kasparian, J., Yu, J., Frey, S., Salmon, E., Wolf, J.-P., 2004. Remote detection and identification of biological aerosols using a femtosecond terawatt lidar system. Appl. Phys. B 78 (5), 535–537.

Midorikawa, K., Kawano, H., Suda, A., Nagura, C., Obara, M., 2002. Polarization properties of ultrafast white-light continuum generated in condensed media. Appl. Phys. Lett. 80 (6), 923.

Migus, A., Gauduel, Y., Martin, J.L., Antonetti, A., 1987. Excess electrons in liquid water: first evidence of a prehydrated state with femtosecond lifetime. Phys. Rev. Lett. 58, 1559–1562.

Mikalauskas, D., Dubietis, A., Danielius, R., 2002. Observation of light filaments induced in air by visible picosecond laser pulses. Appl. Phys. B 75, 899–902.

Miki, M., Aihara, Y., Shindo, T., 1996. Mechanisms of guiding ability of CO_2 laser-produced plasmas on pulsed discharges. J. Phys. D 29 (7), 1984–1996.

Miki, M., Shindo, T., Aihara, Y., 1993. Development of long gap discharges guided by a pulsed CO_2 laser. J. Phys. D 26 (8), 1244–1252.

Miki, M., Wada, A., 1996. Guiding of electrical discharges under atmospheric air by ultraviolet laser-produced plasma channel. J. Appl. Phys. 80 (6), 3208–3214.

Milsted Jr, C.S., Cantrell, C.D., 1996. Vector effects in self focusing. Phys. Rev. A 53 (5), 3536–3542.

Mishima, K., Hayashi, M., Yi, J., Lin, S.H., Selzle, H.L., Schlag, E.W., 2002. Generalization of Keldysh's theory. Phys. Rev. A 66 (3), 033401.

Mizrahi, V., Shelton, D.P., 1985. Dispersion of nonlinear susceptibilities of Ar, N_2 and O_2 measured and compared. Phys. Rev. Lett. 55 (7), 696.

Mlejnek, M., Kolesik, M., Moloney, J.V., Wright, E.M., 1999a. Optically turbulent femtosecond light guide in air. Phys. Rev. Lett. 83 (15), 2938–2941.

Mlejnek, M., Wright, E.M., Moloney, J.V., 1999b. Moving focus versus self-waveguiding model for long distance propagation of femtosecond pulses in air. IEEE J. Quant. Electr. 35 (12), 1771–1776.

Mlejnek, M., Wright, E.M., Moloney, J.V., 1999c. Power dependence of dynamic spatial replenishment of femtosecond pulses propagating in air. Opt. Express 4 (7), 223–228.

Mlejnek, M., Kolesik, M., Wright, E.M., Moloney, J.V., 2001. Recurrent femtosecond pulse collapse in air due to plasma generation: numerical results. Comput. Simulation 56 (6), 563–570.

Mlejnek, M., Wright, E.M., Moloney, J.V., 1998a. Dynamic spatial replenishment of femtosecond pulses propagating in air. Opt. Lett. 23 (5), 382–384.

Mlejnek, M., Wright, E.M., Moloney, J.V., 1998b. Femtosecond pulse propagation in argon—a pressure dependence study. Phys. Rev. E 58 (4), 4903–4910.

Moll, K.D., Gaeta, A.L., 2004. Role of dispersion in multiple-collapse dynamics. Opt. Lett. 29 (9), 995–997.

Moll, K.D., Gaeta, A.L., Fibich, G., 2003. Self-similar optical wave collapse: observation of the Townes profile. Phys. Rev. Lett. 90, 203902.

Moloney, J.V., Kolesik, M., 2007. Full vectorial, intense ultrashort pulse propagators: derivation and applications. In: Yamanouchi, K., Chin, S.L., Agostini, P., Ferrante, G. (Eds.), Progress in Ultrafast Intense Laser Science II, vol. 85. Springer, Berlin.

Moloney, J.V., Kolesik, M., Mlejnek, M., Wright, E.M., 2000. Femtosecond self-guided atmospheric light strings. Chaos 10 (3), 559–569.

Nagura, C., Suda, A., Kawano, H., Obara, M., Midorikawa, K., 2002. Generation and characterization of ultrafast white-light continuum in condensed media. Appl. Opt. 41 (18), 3735–3742.

Nathan, V., Guenther, A.H., Mitra, S.S., 1985. Review of multiphoton absorption in crystalline solids. J. Opt. Soc. Am. B 2 (2), 294–316.

Naudeau, M.L., Law, R.J., Luk, T.S., Nelson, T.R., Cameron, S.M., Rudd, J.V., 2006. Observation of nonlinear optical phenomena in air and fused silica using a 100 Gw, 1.54 μm source. Opt. Express 14 (13), 6194.

Newell, A.C., Moloney, J.V., 1992. Nonlinear Optics. Addison-Wesley, New-York.

Nguyen, N.T., Saliminia, A., Chin, S.L., Vallée, R., 2006. Control of femtosecond laser written waveguides in silica glass. Appl. Phys. B 85, 145–148.

Nguyen, N.T., Saliminia, A., Liu, W., Chin, S.L., Vallée, R., 2003. Optical breakdown versus filamentation in fused silica by use of femtosecond infrared laser pulses. Opt. Lett. 28 (17), 1591–1593.

Nibbering, E.T.J., Curley, P.F., Grillon, G., Prade, B.S., Franco, M.A., Salin, F., Mysyrowicz, A., 1996. Conical emission from self-guided femtosecond pulses in air. Opt. Lett. 21 (1), 62–64.

Nibbering, E.T.J., Grillon, G., Franco, M.A., Prade, B.S., Mysyrowicz, A., 1997. Determination of the inertial contribution to the nonlinear refractive index of air, N_2, and O_2 by use of unfocused high-intensity femtosecond laser pulses. J. Opt. Soc. Am. B 14 (3), 650–660.

Niday, T.A., Wright, E.M., Kolesik, M., Moloney, J.V., 2005. Stability and transient effects in nanosecond ultraviolet light filaments in air. Phys. Rev. E 72, 016618.

Nikogosyan, D.N., 1997. Properties of Optical and Laser-related Materials. Wiley, Chichester.

Nisoli, M., de Silvestri, S., Svelto, O., Szipöcz, R., Ferencz, K., Spielmann, C., Sartania, S., Krausz, F., 1997. Compression of high-energy laser pulses below 5 fs. Opt. Lett. 22 (8), 522–524.

Noack, J., Vogel, A., 1999. Laser-induced plasma formation in water at nanosecond to femtosecond time scales: calculation of thresholds, absorption coefficients, and energy density. IEEE J. Quant. Electron. 35 (8), 1156–1167.

Nurhuda, M., Suda, A., Hatayama, M., Nagasaka, K., Midorikawa, K., 2002a. Propagation dynamics of femtosecond laser pulses in argon. Phys. Rev. A 66 (2), 023811.

Nurhuda, M., Suda, A., Midorikawa, K., 2002b. Ionization-induced high-order nonlinear susceptibility. Phys. Rev. A 66, 041802(R).

Nurhuda, M., Suda, A., Midorikawa, K., 2002c. Saturation of dynamic nonlinear susceptibility of noble gas atom in intense laser field. RIKEN Review (October), 40.

Nurhuda, M., Suda, A., Midorikawa, K., 2004. Saturation of nonlinear susceptibility. J. Nonlinear Opt. Phys. Mater. 13 (2), 301–313.

Nurhuda, M., Suda, A., Midorikawa, K., Budiono, H., 2005. Control of self-phase modulation and plasma-induced blueshifting of high-energy, ultrashort laser pulses in an argon-filled hollow fiber using conjugate pressure-gradient method. J. Opt. Soc. Am. B 22 (8), 1757–1762.

Nurhuda, M., Suda, A., Midorikawa, K., Hatayama, M., Nagasaka, K., 2003. Propagation dynamics of femtosecond laser pulses in a hollow fiber filled with argon: constant gas pressure versus differential gas pressure. J. Opt. Soc. Am. B 20 (9), 2002–2011.

Nurhuda, M., van Groesen, E., 2005. Effects of delayed Kerr nonlinearity and ionization on the filamentary ultrashort laser pulses in air. Phys. Rev. E 71, 066502.

Olivier, T., Billard, F., Akhouayri, H., 2004. Nanosecond z-scan measurements of the nonlinear refractive index of fused silica. Opt. Express 12 (7), 1377.

Onda, S., Watanabe, W., Yamada, K., Itoh, K., Nishii, J., 2005. Study of filamentary damage in synthesized silica induced by chirped femtosecond laser pulses. J. Opt. Soc. Am. B 22 (11), 2437–2443.

Papazoglou, D., Zergioti, I., Tzortzakis, S., Sgouros, G., Maravelias, G., Christopoulos, S., Fotakis, C., 2005. Sub-picosecond ultraviolet laser filamentation-induced bulk modifications in fused silica. Appl. Phys. A 81 (2), 241–244.

Peck, E.R., 1983. Sellmeier fits with linear regression; multiple data sets; dispersion formulas for helium. Appl. Opt. 22 (18), 2906.

Peñano, J.R., Sprangle, P., Hafizi, B., Ting, A., Gordon, D.F., Kapetanakos, C.A., 2004. Propagation of ultra-short, intense laser pulses in air. Phys. Plasmas 11 (5), 2865–2874.

Peñano, J.R., Sprangle, P., Manheimer, W., Zigler, A., 2005. Transmission of intense femtosecond laser pulses into dielectrics. Phys. Rev. E 72, 036412.

Peñano, J.R., Sprangle, P., Serafim, P., Hafizi, B., Ting, A., 2003. Stimulated Raman scattering of intense laser pulses in air. Phys. Rev. E 68 (5), 056502.

Penetrante, B.M., Bardsley, J.N., Wood, W.M., Siders, C.W., Downer, M.C., 1992. Ionization-induced frequency shifts in intense femtosecond laser pulses. J. Opt. Soc. Am. B 9 (11), 2032–2040.

Penzkofer, A., Seilmeier, A., Kaiser, W., 1975. Parametric four-photon generation of picosecond light at high conversion efficiency. Opt. Commun. 14, 363–367.

Pépin, H., Comtois, D., Vidal, F., Chien, C.Y., Desparois, A., Johnston, T.W., Kieffer, J.C., La Fontaine, B., Martin, F., Rizk, F.A.M., Potvin, C., Couture, P., Couture, H.P., Bondiou-Clergerie, A., Lalande, P., Galimberti, I., 2001. Triggering and guiding high-voltage large-scale leader discharges with sub-joule ultrashort laser pulses. Phys. Plasmas 8 (5), 2532.

Perelomov, A.M., Popov, V.S., Terent'ev, M.V., 1966. Ionization of atoms in an alternating electric field. Sov. Phys. JETP 23 (5), 924–934.

Perry, M.D., Landen, O.L., Szöke, A., Campbell, E.M., 1988. Multiphoton ionization of the noble gases by an intense 10^{14} W/cm^2 dye laser. Phys. Rev. A 37 (3), 747–760.

Petit, S., Talebpour, A., Proulx, A., Chin, S.L., 2000a. Polarization dependence of the propagation of intense laser pulses in air. Opt. Commun. 175, 323–327.

Petit, S., Talebpour, A., Proulx, A., Chin, S.L., 2000b. Some consequences during the propagation of an intense femtosecond laser pulse in transparent optical media: a strongly deformed white light laser. Laser Phys. 10 (1), 93–100.

Pfeifer, T., Gallmann, L., Abel, M.J., Neumark, D.M., Leone, S.R., 2006. Circular phase mask for control and stabilization of single optical filaments. Opt. Lett. 31 (15), 2326.

Philip, J., D'Amico, C., Chériaux, G., Couairon, A., Prade, B., Mysyrowicz, A., 2005. Amplification of femtosecond laser filaments in Ti: sapphire. Phys. Rev. Lett. 95, 163901.

Pitts, T.A., Luk, T.S., Gruetzner, J.K., Nelson, T.R., McPherson, A., Cameron, S.M., Bernstein, A.C., 2004. Propagation of self-focusing laser pulses in atmosphere: experiment versus numerical simulation. J. Opt. Soc. Am. B 21 (11), 2008–2016.

Polesana, P., Dubietis, A., Porras, M.A., Kučinskas, E., Faccio, D., Couairon, A., Di Trapani, P., 2006. Near-field dynamics of ultrashort pulsed Bessel beams in media with Kerr nonlinearity. Phys. Rev. E 73, 056612.

Polesana, P., Faccio, D., Di Trapani, P., Dubietis, A., Piskarkas, A., Couairon, A., Porras, M.A., 2005. High localization focal depth and contrast by means of nonlinear Bessel beams. Opt. Express 13, 6160.

Polyakov, S., Yoshino, F., Stegeman, G., 2001. Interplay between self-focusing and high-order multiphoton absorption. J. Opt. Soc. Am. B 18 (12), 1891–1895.

Porras, M.A., Di Trapani, P., 2004. Localized and stationary light wave modes in dispersive media. Phys. Rev. E 69 (6), 066606.

Porras, M.A., Dubietis, A., Kučinskas, E., Bragheri, F., Degiorgio, V., Couairon, A., Faccio, D., Di Trapani, P., 2005a. From X- to O-shaped spatiotemporal spectra of light filaments in water. Opt. Lett. 30 (24), 3398–3400.

Porras, M.A., Parola, A., Di Trapani, P., 2005b. Nonlinear unbalanced O waves: nonsolitary, conical light bullets in nonlinear dissipative media. J. Opt. Soc. Am. B 22 (7), 1406.

Porras, M.A., Dubietis, A., Matijošius, A., Piskarskas, R., Bragheri, F., Averchi, A., Di Trapani, P., 2007. Characterization of anomalous conical emission of light filaments in media with anomalous dispersion. J. Opt. Soc. Am. B 24, 581–584.

Porras, M.A., Parola, A., Faccio, D., Dubietis, A., Di Trapani, P., 2004. Nonlinear unbalanced Bessel beams: stationary conical waves supported by nonlinear losses. Phys. Rev. Lett. 93 (15), 153902.

Porras, M.A., Trillo, S., Conti, C., Di Trapani, P., 2003a. Paraxial envelope X-waves. Opt. Lett. 28 (13), 1090.

Porras, M.A., Valiulis, G., Di Trapani, P., 2003b. Unified description of Bessel X-waves with cone dispersion and tilted pulses. Phys. Rev. E 68 (1), 016613.

Potenza, M.A.C., Minardi, S., Trull, J., Blasi, G., Salerno, D., Varanavicius, A., Piskarskas, A., Di Trapani, P., 2004. Three dimensional imaging of short pulses. Opt. Commun. 229, 38.

Poumellec, B., Sudrie, L., Franco, M., Prade, B., Mysyrowicz, A., 2003. Femtosecond laser irradiation stress induced in pure silica. Opt. Express 11 (9), 1070.

Prade, B., Franco, M., Mysyrowicz, A., Couairon, A., Buersing, H., Eberle, B., Krenz, M., Seiffer, D., Vasseur, O., 2006a. Spatial mode cleaning by femtosecond filamentation in air. Opt. Lett. 31 (17), 2601.

Prade, B., Franco, M., Mysyrowicz, A., Couairon, A., Buersing, H., Eberle, B., Krenz, M., Seiffer, D., Vasseur, O., 2006b. Spatial mode cleaning by femtosecond filamentation in air. In: Technical Digest of the CLEO/IQEC 2006 Conference. OSA, Long beach, CA, p. QTuB.

Press, W.H., Teukolsky, S.A., Vetterling, W.T., Flannery, B.P., 1992. Numerical Recipes. Cambridge University Press, Cambridge.

Proulx, A., Talebpour, A., Petit, S., Chin, S.L., 2000. Fast pulsed electric field created from the self-generated filament of a femtosecond Ti: sapphire laser pulse in air. Opt. Commun. 174, 305–309.

Rae, S.C., Burnett, K., 1992. Detailed simulations of plasma-induced spectral blueshifting. Phys. Rev. A 46 (2), 1084–1090.

Rairoux, P., Schillinger, H., Neirdeimer, S., Rodriguez, M., Ronneberger, F., Sauerbrey, R., Stein, B., Waite, D., Wedekind, C., Wille, H., Wöste, L., Ziener, C., 2000. Remote sensing of the atmosphere using ultrashort laser pulses. Appl. Phys. B 71, 573.

Raizer, Y.P., 1965. Heating of a gas by a powerful light pulse. Sov. Phys. JETP-USSR 21 (5), 1009.

Raizer, Y.P., 1966. Breakdown and heating of gases under influence of a laser beam. Sov. Phys. Uspekhi-USSR 8 (5), 650.

Raizer, Y.P., 1997. Gaz Discharge Physics. Springer, Berlin.

Rambo, P., Schwarz, J., Diels, J.-C., 2001a. High-voltage electrical discharges induced by an ultrashort-pulse UV laser system. J. Opt. A 3, 146–158.

Rambo, P., Schwarz, J., Diels, J.-C., 2001b. Interferometry with two-dimensional spatial and high temporal resolution. Opt. Commun. 197, 145–159.

Ranka, J.K., Gaeta, A.L., 1998. Breakdown of the slowly varying envelope approximation in the self-focusing of ultrashort pulses. Opt. Lett. 23 (7), 534–536.

Ranka, J.K., Schirmer, R.W., Gaeta, A.L., 1996. Observation of pulse splitting in nonlinear dispersive media. Phys. Rev. Lett. 77 (18), 3783–3786.

Reivelt, K., Saari, P., 2000. Optical generation of focus wave modes. J. Opt. Soc. Am. A 17 (10), 1785–1790.

Ripoche, J.-F., Grillon, G., Prade, B., Franco, M., Nibbering, E., Lange, R., Mysyrowicz, A., 1997. Determination of the time dependence of n_2 in air. Opt. Commun. 135, 310–314.

Robinson, P.A., 1997. Nonlinear wave collapse and strong turbulence. Rev. Mod. Phys. 62, 507–573.

Rodriguez, M., Bourayou, R., Méjean, G., Kasparian, J., Yu, J., Salmon, E., Scholz, A., Stecklum, B., Eislöffel, J., Laux, U., Hatzes, A.P., Sauerbrey, R., Wöste, L., Wolf, J.-P., 2004. Kilometric-range nonlinear propagation of femtosecond laser pulses. Phys. Rev. E 69, 036607.

Rodriguez, M., Sauerbrey, R., Wille, H., Wöste, L., Fujii, T., André, Y.-B., Mysyrowicz, A., Klingbeil, L., Rethmeier, K., Kalkner, W., Kasparian, J., Salmon, E., Yu, J., Wolf, J.-P., 2002. Triggering and guiding megavolt discharges by use of laser-induced ionized filaments. Opt. Lett. 27 (9), 772–774.

Rohwetter, P., Stelmaszczyk, K., Wöste, L., Ackermann, R., Méjean, G., Salmon, E., Kasparian, J., Yu, J., Wolf, J.-P., 2005. Filament-induced remote surface ablation for long range laser-induced breakdown spectroscopy operation. Spectrochimica Acta Part B 60, 1025–1033.

Rohwetter, P., Yu, J., Méjean, G., Stelmaszczyk, K., Salmon, E., Kasparian, J., Wolf, J.-P., Wöste, L., 2004. Remote LIBS with ultrashort pulses: characteristics in picosecond and femtosecond regimes. J. Anal. At. Spectrom. 19, 437–444.

Roskey, D.E., Kolesik, M., Moloney, J.V., Wright, E.M., 2006. The role of linear power partitioning in beam filamentation. Appl. Phys. B 86, 249–258.

Rothenberg, J.E., 1992a. Pulse splitting during self-focusing in normally dispersive media. Opt. Lett. 17 (8), 583–585.

Rothenberg, J.E., 1992b. Space–time focusing: breakdown of the slowly varying envelope approximation in the self-focusing of femtosecond pulses. Opt. Lett. 17 (19), 1340–1342.

Ruiz, C., Román, J.S., Méndez, C., Díaz, V., Plaja, L., Arias, I., Roso, L., 2005. Observation of spontaneous self-channeling of light in air below the collapse threshold. Phys. Rev. Lett. 95, 053905.

Saari, P., Reivelt, K., 1997. Evidence of X-shaped propagation-invariant localized light waves. Phys. Rev. Lett. 79 (21), 4135–4138.

Salerno, D., Jedrkiewicz, O., Trull, J., Valiulis, G., Picozzi, A., Di Trapani, P., 2004. Noise-seeded spatiotemporal modulation instability in normal dispersion. Phys. Rev. E 70, 065603.

Salières, P., l'Huillier, A., Antoine, P., Lewenstein, M., 1999. Studies of the spatial and temporal coherence of high order harmonics. Adv. At. Mol. Opt. Phys. 41, 83.

Saliminia, A., Chin, S.L., Vallée, R., 2005a. Ultra-broad and coherent white light generation in silica glass by focused femtosecond pulses at 1.5 μm. Opt. Express 13, 5731.

Saliminia, A., Vallée, R., Chin, S.L., 2005b. Waveguide writing in silica glass with femtosecond pulses from an optical parametric amplifier at 1.5 μm. Opt. Commun. 256, 422–427.

Saliminia, A., Nguyen, N.T., Chin, S.L., Vallée, R., 2004. The influence of self-focusing and filamentation on refractive index modifications in fused silica using intense femtosecond pulses. Opt. Commun. 241, 529–538.

Saliminia, A., Nguyen, N.T., Chin, S.L., Vallée, R., 2006. Densification of silica glass induced by 0.8 and 1.5 μm intense femtosecond laser pulses. J. Appl. Phys. 99, 093104.

Salo, J., Fagerholm, J., Friberg, A.T., Salomaa, M.M., 1999. Nondiffracting bulk-acoustic X waves in crystals. Phys. Rev. Lett. 83, 1171–1174.

Salo, J., Fagerholm, J., Friberg, A.T., Salomaa, M.M., 2000. Unified description of nondiffracting X and Y waves. Phys. Rev. E 62, 4261–4275.

Sansone, G., Benedetti, E., Calegari, F., Vozzi, C., Avaldi, L., Flammini, R., Poletto, L., Villoresi, P., Altucci, C., Velotta, R., Stagira, S., DeSilvestri, S., Nisoli, M., 2006. Isolated single-cycle attosecond pulses. Science 314 (5798), 443–446.

Schaffer, C.B., Brodeur, A., Garcia, J.F., Mazur, E., 2001a. Micromachining bulk glass by use of femtosecond laser pulses with nanojoule energy. Opt. Lett. 26 (2), 93.

Schaffer, C.B., Brodeur, A., Mazur, E., 2001b. Laser-induced breakdown and damage in bulk transparent materials induced by tightly focused femtosecond laser pulses. Meas. Sci. Technol. 12, 1784–1794.

Schillinger, H., Sauerbrey, R., 1999. Electrical conductivity of long plasma channels in air generated by self-guided femtosecond laser pulses. Appl. Phys. B 68, 753–756.

Schjødt-Eriksen, J., Moloney, J.V., Wright, E.M., Feng, Q., Christiansen, P.L., 2001. Polarization instability of femtosecond pulse splitting in normally dispersive self-focusing media. Opt. Lett. 26 (2), 78–80.

Schroeder, H., Chin, S.L., 2004. Visualization of the evolution of multiple filaments in methanol. Opt. Commun. 234, 399–406.

Schroeder, H., Liu, J., Chin, S.L., 2004. From random to controlled small-scale filamentation in water. Opt. Express 12 (20), 4768–4774.

Schumacher, D., 2002. Controlling continuum generation. Opt. Lett. 27 (6), 451.

Schwarz, J., Diels, J.-D., 2001. Analytical solution for uv filaments. Phys. Rev. A 65, 013806 1–10.

Schwarz, J., Rambo, P., Diels, J.-C., 2001. Measurements of multiphoton ionization coefficients with ultrashort ultraviolet laser pulses. Appl. Phys. B 72 (3), 343–347.

Schwarz, J., Rambo, P., Diels, J.-C., Kolesik, M., Wright, E.M., Moloney, J.V., 2000. Ultraviolet filamentation in air. Opt. Commun. 180, 383–390.

Schwarz, J., Rambo, P., Diels, J.-C., Kolesik, M., Wright, E.M., Moloney, J.V., 2002. Intense-field nonlinear optics: Long distance propagation of UV filaments. J. Mod. Opt. 49 (14–15), 2583–2597.

Sergeev, A., Vanin, E., Stenflo, L., Anderson, D., Lisak, M., Quiroga-Teixeiro, M.L., 1992. Nonlinear shaping of a two-dimensional ultrashort ionizing pulse. Phys. Rev. A 46, 7830–7836.

Shaw, M.J., Hooker, C.J., Wilson, D.C., 1993. Measurement of the nonlinear refractive index of air and other gases at 248 nm. Opt. Commun. 103, 153–160.

Shelton, D.P., 1990. Nonlinear susceptibilities of gases measured at 1064 and 1319 nm. Phys. Rev. A 42 (5), 2578–2592.

Shen, Y.R., 1984. The Principles of Nonlinear Optics. Wiley-Interscience, New York.

Shen, Y.R., Shaham, Y.J., 1965. Beam deterioration and stimulated Raman effect. Phys. Rev. Lett. 15, 1008–1010.

Shimoji, Y., Fay, A.T., Chang, R.S.F., Djeu, N., 1989. Direct measurement of the nonlinear refractive index of air. Opt. Lett. 6 (11), 1994–1996.

Shindo, T., Aihara, Y., Miki, M., Suzuki, T., 1993. Model experiments of laser-triggered lightning. IEEE Trans. Power Deliv. 8, 311–317.

Shlyonov, S.A., Kandidov, V.P., 2004a. Filament bunch formation upon femtosecond laser pulse propagation through the turbulent atmosphere. Part 1. Method. Atmos. Oceanic Opt. 17 (8), 565–570.

Shlyonov, S.A., Kandidov, V.P., 2004b. Filament bunch formation upon femtosecond laser pulse propagation through the turbulent atmosphere. Part 2. Statistical characteristics. Atmos. Oceanic Opt. 17 (8), 571–575.

Shon, N.H., Suda, A., Tamaki, Y., Midorikawa, K., 2001. High-order harmonic and attosecond pulse generations: bulk media versus hollow waveguides. Phys. Rev. A 63, 063806.

Shvets, G., Kaganovich, I., Startsev, E., 2002. Comment on generation of electromagnetic pulses from plasma channels induced by femtosecond light strings. Phys. Rev. Lett. 89 (13), 139301.

Silberberg, Y., 1990. Collapse of optical pulses. Opt. Lett. 15 (22), 1282–1284.

Sirutkaitis, V., Gaižauskas, E., Kudriashov, V., Barkauskas, M., Vaicaitis, V., Grigonis, R., Piskarskas, A.S., 2003. Self-guiding supercontinuum generation and damage in bulk materials induced by femtosecond pulses. In: Exarhos, G.J., Guenther, A.H., Kaiser, N., Lewis, K.L., Soileau, M.J., Stolz, C.J., Giesen, A., Weber, H. (Eds.), Laser-Induced Damage in Optical Materials: 2002 and 7th International Workshop on Laser Beam and Optics Characterization, vol. 4932. SPIE, pp. 346–357.

Skupin, S., Peschel, U., Etrich, C., Leine, L., Lederer, F., Michaelis, D., 2003. Simulation of femtosecond pulse propagation in air. Opt. Quant. Electron. 35, 573–582.

Skupin, S., Peschel, U., Etrich, C., Leine, L., Michaelis, D., Lederer, F., 2002. Intense pulses in air: breakup of rotational symmetry. Opt. Lett. 27 (20), 1812–1814.

Smith, W.L., Liu, P., Bloembergen, N., 1977. Superbroadening in H_2O and D_2O by self-focused picosecond pulses from a YAlG:Nd laser. Phys. Rev. A 15 (6), 2396–2404.

Sodha, M.S., Ghatak, A.K., Tripathi, V.K., 1976. Self-focusing of laser beams in plasmas and semiconductors. In: Wolf, E. (Ed.), Progress in Optics, vol. XIII of Lecture Notes in Mathematics. North-Holland, Amsterdam, pp. 171–265.

Sprangle, P., Peñano, J.R., Hafizi, B., 2002. Propagation of intense short laser pulses in the atmosphere. Phys. Rev. E 66 (4), 046418.

Sprangle, P., Peñano, J.R., Hafizi, B., Kapetanakos, C.A., 2004. Ultrashort laser pulses and electromagnetic pulse generation in air and on dielectric surfaces. Phys. Rev. E 69 (6), 066415.

Stegeman, G.I., Hagan, D.J., Torner, L., 1996. $\chi^{(2)}$ cascading phenomena and their applications to all-optical signal processing, mode-locking, pulse compression and solitons. Opt. Quant. Electron. 28 (12), 1691–1740.

Stegeman, G.I., Segev, M., 1999. Optical spatial solitons and their interactions: universality and diversity. Science 286 (5444), 1518–1523.

Stelmaszczyk, K., Rohwetter, P., Méjean, G., Yu, J., Salmon, E., Kasparian, J., Ackermann, R., Wolf, J.-P., Wöste, L., 2004. Long-distance remote laser-induced breakdown spectroscopy using filamentation in air. Appl. Phys. Lett. 85 (18), 3977–3979.

Stepanishen, P.R., 1999. Acoustic bessel bullets. J. Sound Vib. 222 (1),

Stepanishen, P.R., Sun, J., 1997. Acoustic bullets: Transient bessel beams generated by planar apertures. J. Acoust. Soc. Am. 102 (6), 3308–3318.

Stibenz, G., Zhavoronkov, N., Steinmeyer, G., 2006. Self-compression of millijoule pulses to 7.8 fs duration in a white-light filament. Opt. Lett. 31 (2), 274.

Stolen, R.H., Gordon, J.P., Tomlison, W.J., Haus, H.A., 1989. Raman response function of silica-core fibers. J. Opt. Soc. Am. B 6 (6), 1159–1166.

Stolen, R.H., Tomlison, W.J., 1992. Effect of the Raman part of the nonlinear refractive index on propagation of ultrashort optical pulses in fibers. J. Opt. Soc. Am. B 9 (4), 565–573.

Stuart, B.C., Feit, M.D., Herman, S., Rubenchik, A.M., Shore, B.W., Perry, M.D., 1996. Nanosecond-to-femtosecond laser-induced breakdown in dielectrics. Phys. Rev. B 53 (4), 1749–1761.

Stuart, B.C., Feit, M.D., Rubenchik, A.M., Shore, B.W., Perry, M.D., 1995. Laser-induced damage in dielectrics with nanosecond to subpicosecond pulses. Phys. Rev. Lett. 74 (12), 2248–2251.

Subbarao, D., Batra, K., Uma, R., 2003. Paraxial theory of slow self-focusing. Phys. Rev. E 68(6), 066403 1–14.

Subbarao, D., Uma, R., Singh, H., 1998. Paraxial theory of self-focusing of cylindrical laser beams. I. abcd laws. Phys. Plasmas 5 (9), 3440–3450.

Suda, A., Hatayama, M., Nagasaka, K., Midorikawa, K., 2005. Generation of sub-10-fs, 5-mj-optical pulses using a hollow fiber with a pressure gradient. Appl. Phys. Lett. 86, 111116.

Sudrie, L., 2002. Nonlinear propagation of femtosecond laser pulses in fused silica. Thèse de doctorat, Paris XI, Orsay University.

Sudrie, L., Couairon, A., Franco, M., Lamouroux, B., Prade, B., Tzortzakis, S., Mysyrowicz, A., 2002. Femtosecond laser-induced damage and filamentary propagation in fused silica. Phys. Rev. Lett. 89 (18), 186601.

Sudrie, L., Franco, M., Prade, B., Mysyrowicz, A., 1999. Writing of permanent birefringent microlayers in bulk fused-silica with femtosecond laser pulses. Opt. Commun. 171, 279.

Sudrie, L., Franco, M., Prade, B., Mysyrowicz, A., 2001. Study of damage in fused silica induced by ultra-short IR laser pulses. Opt. Commun. 191, 333.

Suzuki, M., 1985. General correction theorems on decomposition formulae of exponential operators and extrapolation methods for quantum monte-carlo simulations. Phys. Lett. A 113 (6), 299–300.

Suzuki, M., 1990. Fractal decomposition of exponential operators with applications to many-body theories and monte-carlo simulations. Phys. Lett. A 146, 319–323.

Suzuki, M., 1991. General theory of fractal path integrals with applications to many-body theories and statistical physics. J. Math. Phys. 32, 400.

Suzuki, M., 1993. General decomposition theory of ordered exponentials. Proc. Japan Acad. Ser. B 69 (7), 161.

Svelto, O., 1974. Self-focusing self-trapping and self-phase modulation of laser beams. Prog. Opt. 12, 1–51.

Takahashi, E., Nabekawa, Y., Nurhuda, M., Midorikawa, K., 2003. Generation of high-energy high-order harmonics by use of a long interaction medium. J. Opt. Soc. Am. B 20 (1), 158–165.

Talanov, V.I., 1964. Self-focusing of electromagnetic waves in nonlinear media. Izv. Vysshikh Uchebn. Zavedenii Radiofiz 7, 564–565.

Talanov, V.I., 1965. Self-focusing of wave beams in nonlinear media. JETP Lett. 2 (5), 138.

Talebpour, A., Abdel-Fattah, M., Bandrauk, A.D., Chin, S.L., 2001. Spectroscopy of the gases interacting with intense femtosecond laser pulses. Laser Phys. 11, 68–76.

Talebpour, A., Petit, S., Chin, S.L., 1999a. Re-focusing during the propagation of a focused femtosecond Ti: sapphire laser pulse in air. Opt. Commun. 171, 285–290.

Talebpour, A., Yang, J., Chin, S.L., 1999b. Semi-empirical model for the rate of tunnel ionization of N_2 and O_2 molecule in an intense Ti:sapphire laser pulse. Opt. Commun. 163, 29–32.

Tamaki, Y., Itatani, J., Nagata, Y., Obara, M., Midorikawa, K., 1999. Highly efficient, phase-matched high-harmonic generation by a self-guided laser beam. Phys. Rev. Lett. 82, 1422–1425.

Tamaki, Y., Itatani, J., Obara, M., Midorikawa, K., 2000. Optimization of conversion efficiency and spatial quality of high-order harmonic generation. Phys. Rev. A 62, 063802.

Tamošauskas, G., Šaulys, L., Dubietis, A., Piskarkas, A., 2005. Small scale laser-triggered electrical discharges and their application to characterization of plasma channel induced by light filaments. Lithuanian J. Phys. 45 (1), 37–42.

Tawara, H., Kato, T., 1987. Total and partial ionization cross sections of atoms and ions by electron impact. At. Data Nucl. Data Tables 36, 167–353.

Théberge, F., Aközbek, N., Liu, W., Becker, A., Chin, S.L., 2006a. Tunable ultrashort laser pulses generated through filamentation in gases. Phys. Rev. Lett. 97, 023904.

Théberge, F., Liu, W., Simard, P.T., Becker, A., Chin, S.L., 2006b. Plasma density inside a femtosecond laser filament in air: strong dependence on external focusing. Phys. Rev. E 74, 036406.

Théberge, F., Sharifi, S.M., Chin, S.L., Schröder, H., 2006c. Simple 3-D characterization of ultrashort laser pulses. Opt. Express 14 (21), 10125.

Théberge, F., Aközbek, N., Liu, W., Gravel, J.-F., Chin, S.L., 2005a. Third-harmonic beam profile generated in atmospheric air using femtosecond laser pulses. Opt. Commun. 245, 399–405.

Théberge, F., Liu, W., Hosseini, S.A., Luo, Q., Sharifi, S.M., Chin, S.L., 2005b. Long-range spectrally and spatially resolved radiation from filaments in air. Appl. Phys. B 81 (1), 131–134.

Théberge, F., Liu, W., Luo, Q., Chin, S.L., 2005c. Ultrabroadband continuum generated in air (down to 230 nm) using ultrashort and intense laser pulses. Appl. Phys. B 80 (2), 221–225.

Théberge, F., Luo, Q., Liu, W., Hosseini, S.A., Sharifi, M., Chin, S.L., 2005d. Long-range third-harmonic generation in air using ultrashort intense laser pulses. Appl. Phys. Lett. 87, 081108.

Tien, A.-C., Backus, S., Kapteyn, H., Murnane, M., Mourou, G., 1999. Short-pulse laser damage in transparent materials as a function of pulse duration. Phys. Rev. Lett. 82, 3883.

Tikhonchuk, V.T., 2002. Comment on generation of electromagnetic pulses from plasma channels induced by femtosecond light strings. Phys. Rev. Lett. 89 (20), 209301.

Tikhonenko, V., Christou, J., Luther-Davies, B., 1996. Three dimensional bright spatial soliton collision and fusion in a saturable nonlinear medium. Phys. Rev. Lett. 76 (15), 2698–2701.

Ting, A., Alexeev, I., Gordon, D., Fischer, R., Kaganovich, D., Jones, T., Briscoe, E., Peñano, J., Hubbard, R., Sprangle, P., 2005a. Measurements of intense femtosecond laser pulse propagation in air. Phys. Plasmas 12, 056705.

Ting, A., Gordon, D.F., Briscoe, E., Peñano, J., Sprangle, P., 2005b. Direct characterization of self-guided femtosecond laser filaments in air. Appl. Opt. 44 (8), 1474.

Tosa, V., Takahashi, E., Nabekawa, Y., Midorikawa, K., 2003. Generation of high-order harmonics in a self-guided beam. Phys. Rev. A 67, 063817.

Trull, J., Jedrkiewicz, O., Di Trapani, P., Matijosius, A., Varanavicius, A., Valiulis, G., Danielius, R., Kučinskas, E., Piskarskas, A., Trillo, S., 2004. Spatio-temporal 3d mapping of nonlinear X-waves. Phys. Rev. E 69 (2), 026607.

Trushin, S.A., Panja, S., Kosma, K., Schmid, W.E., Fuss, W., 2005. Supercontinuum extending from > 1000 to 250 nm, generated by focusing ten-fs laser pulses at 805 nm into ar. Appl. Phys. B 80, 399–403.

Turitsyn, S.K., 1985. Spatial dispersion of nonlinearity and stability of multidimensional solitons. Theoret. Math. Phys. 64, 226–232.

Tzortzakis, S., 2001. Filamentation of femtosecond laser pulses in transparent nonlinear media. Thèse de doctorat, École Polytechnique, Palaiseau.

Tzortzakis, S., Anglos, D., Gray, D., 2006a. Ultraviolet laser filaments for remote laser-induced breakdown spectroscopy (libs) analysis: applications in cultural heritage monitoring. Opt. Lett. 31 (8), 1139.

Tzortzakis, S., Papazoglou, D.G., Zergioti, I., 2006b. Long-range filamentary propagation of subpicosecond ultraviolet laser pulses in fused silica. Opt. Lett. 31, 796.

Tzortzakis, S., Bergé, L., Couairon, A., Franco, M., Prade, B., Mysyrowicz, A., 2001a. Break-up and fusion of self-guided femtosecond light pulses in air. Phys. Rev. Lett. 86, 5470–5473.

Tzortzakis, S., Lamouroux, B., Chiron, A., Moustaizis, S.D., Anglos, D., Franco, M., Prade, B., Mysyrowicz, A., 2001b. Femtosecond and picosecond ultraviolet laser filaments in air: experiments and simulations. Opt. Commun. 197, 131–143.

Tzortzakis, S., Prade, B., Franco, M., Mysyrowicz, A., Hüller, S., Mora, P., 2001c. Femtosecond laser-guided electric discharge in air. Phys. Rev. E 64, 057401.

Tzortzakis, S., Sudrie, L., Franco, M., Prade, B., Mysyrowicz, A., Couairon, A., Bergé, L., 2001d. Self-guided propagation of ultrashort IR laser pulses in fused silica. Phys. Rev. Lett. 87, 213902.

Tzortzakis, S., Franco, M., Prade, B., Mysyrowicz, A., 2000a. Time evolution of the plasma channel at the trail of a self-guided IR femtosecond laser pulse in air. Opt. Commun. 181, 123.

Tzortzakis, S., Lamouroux, B., Chiron, A., Franco, M., Prade, B., Mysyrowicz, A., Moustaizis, S.D., 2000b. Nonlinear propagation of subpicosecond ultraviolet laser pulses in air. Opt. Lett. 25, 1270–1272.

Tzortzakis, S., Franco, M.A., André, Y.-B., Chiron, A., Lamouroux, B., Prade, B.S., Mysyrowicz, A., 1999. Formation of a conducting channel in air by self-guided femtosecond laser pulses. Phys. Rev. E 60, R3505–R3507.

Tzortzakis, S., Méchain, G., Patalano, G., André, Y.-B., Prade, B., Franco, M., Mysyrowicz, A., Munier, J.-M., Gheudin, M., Beaudin, G., Encrenaz, P., 2002. Coherent subterahertz radiation from femtosecond infrared filaments in air. Opt. Lett. 27 (21), 1944–1946.

Tzortzakis, S., Méchain, G., Patalano, G., Franco, M., Prade, B., Mysyrowicz, A., 2003. Concatenation of plasma filaments created in air by femtosecond infrared laser pulses. Appl. Phys. B 76, 609–612.

Uman, M.A., 1987. The lightning discharge, vol. 39 of International Geophysics Series. Academic, Orlando, FL.

Valiulis, G., Kilius, J., Jedrkiewicz, O., Bramati, A., Minardi, S., Conti, C., Trillo, S., Piskarskas, A., Di Trapani, P., 2001. Space–time nonlinear compression and three-dimensional complex trapping in normal dispersion. In: OSA Trends in Optics and Photonics (TOPS), Technical Digest of the Quantum Electronics and Laser Science Conference (QELS 2001), vol. 57. Optical Society of America, Washington DC, 2001, pp. QPD10–1–2.

Van Engen, A.G., Diddams, S.A., Clement, T.S., 1998. Dispersion measurements of water with white-light interferometry. Appl. Opt. 37 (24), 5679–5686.

Vidal, F., Comtois, D., Chien, C.-Y., Desparois, A., La Fontaine, B., Johnston, T.W., Kieffer, J.-C., Mercure, H.P., Rizk, F.A., 2000. Modeling the triggering of streamers in air by ultrashort laser pulses. IEEE Trans. Plasma Sci. 28, 418–433.

Vidal, F., Johnston, T.W., 1996. Electromagnetic beam breakup: multiple filaments, single beam equilibria, and radiation. Phys. Rev. Lett. 77 (7), 1282–1285.

Vlasov, S.N., Piskunova, L.V., Talanov, V.I., 1989. Three dimensional wave collapse in the nonlinear schrodinger equation model. Sov. Phys. JETP 68, 1125.

Wang, D., Ushio, T., Kawasaki, Z.I., Matsuura, K., Shimada, Y., Uchida, S., Yamanaka, C., Izawa, Y., Sonoi, Y., Simokura, N., 1995. A possible way to trigger lightning using a laser. J. Atmos. Terr. Phys. 57 (5), 459–466.

Wen, S., Fan, D., 2002. Spatiotemporal instabilities in nonlinear kerr media in the presence of arbitrary higher-order dispersions. J. Opt. Soc. Am. B 19 (7), 1653–1659.

Wille, H., Rodriguez, M., Kasparian, J., Mondelain, D., Yu, J., Mysyrowicz, A., Sauerbrey, R., Wolf, J.P., Wöste, L., 2002. Teramobile: a mobile femtosecond-terawatt laser and detection system. Eur. Phys. J. Appl. Phys. 20, 183–190.

Williams, F., Varna, S.P., Hillenius, S., 1976. Liquid water as a lone-pair amorphous semiconductor. J. Chem. Phys. 64, 1549–1554.

Wise, F., Di Trapani, P., 2002. The hunt for light bullets—spatiotemporal solitons. Opt. Phot. News February 2, 28–32.

Wood, W.M., Siders, C.W., Downer, M.C., 1991. Measurement of femtosecond ionisation dynamics of atmospheric density gases by spectral blueshifting. Phys. Rev. Lett. 67 (25), 3523–3526.

Wood, W.M., Siders, C.W., Downer, M.C., 1993. Femtosecond growth dynamics of an underdense ionization front measured by spectral blueshifting. IEEE Trans. Plasma Sci. 21 (1), 20–33.

Wöste, L., Wedekind, C., Wille, H., Rairoux, P., Stein, B., Nikolov, S., Werner, C., Niedermeier, S., Ronneberger, F., Schillinger, H., Sauerbrey, R., 1997. Femtosecond atmospheric lamp. Laser und Optoelektronik 29 (5), 51–53.

Wu, A.Q., Chowdhury, I.H., Xu, X., 2005. Femtosecond laser absorption in fused silica: numerical and experimental investigation. Phys. Rev. B 72, 085128.

Wu, A.Q., Chowdhury, I.H., Xu, X., 2006. Plasma formation in fused silica induced by loosely focused femtosecond laser pulse. Appl. Phys. Lett. 88, 111502.

Wu, H.-C., Sheng, Z.-M., Zhang, J., 2004. Interactive dynamics of two copropagating laser beams in underdense plasmas. Phys. Rev. E 70, 026407.

Wu, Z., 2003. The refocusing behaviour of a focused femtosecond laser pulse in fused silica. J. Opt. A 5, 102–107.

Wu, Z., Jiang, H., Sun, Q., Yang, H., Gong, Q., 2003. Filamentation and temporal reshaping of a femtosecond pulse in fused silica. Phys. Rev. A 68, 063820.

Xi, T.-T., Lu, X., Zhang, J., 2006. Interaction of light filaments generated by femtosecond laser pulses in air. Phys. Rev. Lett. 96, 025003.

Xing, Q., Yoo, K.M., Alfano, R.R., 1993. Conical emission by four-photon parametric generation by using femtosecond laser pulses. Appl. Opt. 32 (12), 2087–2089.

Xu, H.L., Daigle, J.F., Luo, Q., Chin, S.L., 2006a. Femtosecond laser-induced nonlinear spectroscopy for remote sensing of methane. Appl. Phys. B 82, 655–658.

Xu, H.L., Liu, W., Chin, S.L., 2006b. Remote time-resolved filament-induced breakdown spectroscopy of biological materials. Opt. Lett. 31 (10), 1540.

Xu, S.Z., Jia, T.Q., Sun, H.Y., Li, C.B., Li, X.X., Feng, D.H., Qiu, J.R., Xu, Z.Z., 2006c. Mechanisms of femtosecond laser-induced breakdown and damage in MgO. Opt. Commun. 259, 274–280.

Yablonovitch, E., 1974a. Self-phase modulation and short-pulse generation from laser-breakdown plasmas. Phys. Rev. A 10 (5), 1888–1895.

Yablonovitch, E., 1974b. Self-phase modulation of light in a laser-breakdown plasma. Phys. Rev. Lett. 32 (20), 1101–1104.

Yablonovitch, E., Bloembergen, N., 1972. Avalanche ionization and the limiting diameter of filaments induced by light pulses in transparent media. Phys. Rev. Lett. 29 (14), 907–910.

Yamada, K., Watanabe, W., Toma, T., Itoh, K., Nishii, J., 2001. In situ observation of photoinduced refractive-index changes in filaments formed in glasses by femtosecond laser pulses. Opt. Lett. 26 (1), 19–21.

Yang, G., Shen, Y.R., 1984. Spectral broadening of ultrashort pulses in a nonlinear medium. Opt. Lett. 9, 510–512.

Yang, H., Zhang, J., Li, Y., Zhang, J., Li, Y., Chen, Z., Teng, H., Wei, Z., Sheng, Z., 2002a. Characteristics of self-guided laser-plasma channels generated by femtosecond laser pulses in air. Phys. Rev. E 66 (1), 016406.

Yang, H., Zhang, J., Yu, W., Li, Y.J., Wei, Z.Y., 2002b. Long plasma channels generated by femtosecond laser pulses. Phys. Rev. E 65 (1), 016406.

Yang, H., Zhang, J., Zhang, J., Zhang, L.Z., Li, Y.J., Teng, H., Li, Y.T., Wang, Z.H., Chen, Z.L., Wei, Z.Y., Ma, J.X., Sheng, Z.M., 2003. Third-order harmonic generation by self-guided femtosecond pulses in air. Phys. Rev. E 67 (1), 015401.

Yang, H., Zhang, J., Zhang, Q., Hao, Z., Li, Y., Zheng, Z., Wang, Z., Dong, Q., Lu, X., Wei, Z., Sheng, Z., Yu, J., Yu, W., 2005. Polarization-dependent supercontinuum generation from light filaments in air. Opt. Lett. 30 (5), 534.

Yau, T.-W., Lee, C.-H., Wang, J., 2000. Femtosecond self-focusing dynamics measured by three-dimensional phase-retrieval cross correlation. J. Opt. Soc. Am B 17 (9), 1626–1635.

Yu, J., Mondelain, D., Ange, G., Volk, R., Niedermeier, S., Wolf, J.-P., Kasparian, J., Sauerbrey, R., 2001. Backward supercontinuum emission from a filament generated by ultrashort laser pulses in air. Opt. Lett. 26 (8), 533–535.

Yu, J., Mondelain, D., Kasparian, J., Salmon, E., Geffroy, S., Favre, C., Boutou, V., Wolf, J.-P., 2003. Sonographic probing of laser filaments in air. Appl. Opt. 42 (36), 7117–7120.

Yu, W., Yu, M.Y., Zhang, J., Qian, L.J., Yuan, X., Lu, P.X., Li, R.X., Sheng, Z.M., Liu, J.R., Xu, Z.Z., 2004. Long-distance propagation of intense short laser pulse in air. Phys. Plasmas 11 (11), 5360.

Zemlyanov, A., Geints, Y., 2005a. Filamentation of a high-power frequency-modulated femtosecond laser pulse on a vertical atmospheric path. Atmos. Oceanic Opt. 18 (10), 778–782.

Zemlyanov, A., Geints, Y., 2005b. Filamentation of ultrashort laser radiation in aerosol. Atmos. Oceanic Opt. 18 (4), 294–298.

Zemlyanov, A., Geints, Y., 2005c. Integral parameters of high-power femtosecond laser radiation at filamentation in air. Atmos. Oceanic Opt. 18 (7), 514–519.

Zemlyanov, A.A., Geints, Y., 2006. Filamentation length of ultrashort laser pulse in presence of aerosol layer. Opt. Commun. 259, 799–804.

Zemlyanov, A.A., Geints, Y., 2007. Zonal model of nonstationary self-focusing of femtosecond laser radiation in air: effective beam characteristics evolution. Eur. Phys. J. D, in print.

Zhao, X.M., Diels, J.-C., 1995. How lasers might control lightning strokes. Laser Focus World 29 (11), 113.

Zhao, X.M., Diels, J.-C., Wang, C.Y., Elizondo, J.M., 1995a. Propagation dynamics of intense femtosecond pulses: multiple splittings, coalescence, and continuum generation. IEEE J. Quant. Electron. 31, 599.

Zhao, X.M., Rambo, P., Diels, J.-C., 1995b. Filamentation of femtosecond uv pulses in air. QELS 16, 178.

Zharova, N.A., Litvak, A.G., Mironov, V.A., 2002. On the collapse of wave packets in a medium with normal group velocity dispersion. JETP Lett. 75, 539.

Zharova, N.A., Litvak, A.G., Petrova, T.A., Sergeev, A.M., Yunakovskii, A.D., 1986. Multiple fractionation of wave structures in a nonlinear medium. JETP Lett. 44, 13.

Zheng, Z.-Y., Zhang, J., Hao, Z.-Q., Zhang, Z., Chen, M., Lu, X., Wang, Z.-H., Wei, Z.-Y., 2005. Paper airplane propelled by laser plasma channels generated by femtosecond laser pulses in air. Opt. Express 13 (26), 10616.

Zozulya, A.A., Diddams, S.A., 1999. Dynamics of self-focused femtosecond laser pulses in the near and far fields. Opt. Express 4 (9), 336.

Zozulya, A.A., Diddams, S.A., Clement, T.S., 1998. Investigations of nonlinear femtosecond pulse propagation with the inclusion of Raman, shock, and third-order phase effects. Phys. Rev. A 58, 3303–3310.

Zozulya, A.A., Diddams, S.A., Van Engen, A.G., Clement, T.S., 1999. Propagation dynamics of intense femtosecond pulses: multiple splittings, coalescence, and continuum generation. Phys. Rev. Lett. 82, 1430.